



LIBRARY
Michigan State
University

This is to certify that the

dissertation entitled

Pillaring of Layered Double Hydroxide with Polyoxometalates

presented by

Taehyun Kwon

has been accepted towards fulfillment of the requirements for

Ph.D degree in Chemistry

Date September 22, 1988

MSU is an Affirmative Action/Equal Opportunity Institution

0-12771

PLACE IN RETURN BOX to remove this checkout from your record. TO AVOID FINES return on or before date due.

DATE DUE	DATE DUE	DATE DUE

MSU is An Affirmative Action/Equal Opportunity Institution c1circ/detectus.pm3-p.

# PILLARING OF LAYERED DOUBLE HYDROXIDE WITH POLYOXOMETALATES

# By TAEHYUN KWON

#### **A DISSERTATION**

Submitted to

Michigan State University

in partiaL fulfillment of the requirements

for the degree of

**DOCTOR OF PHILOSOPHY** 

**Department of Chemistry** 

1988

#### **ABSTRACT**

# PILLARING OF LAYERED DOUBLE HYDROXIDE WITH POLYOXOMETALATES By Taehvun Kwon

Pure Zn/Al layered double hydroxides (LDHs) of the type Zn<sub>2</sub>Al(OH)<sub>6</sub>·A, where A = Cl-, NO<sub>3</sub>-, have been prepared by an induced hydrolysis method. Several polyoxometalates (POMs) have been intercalated in the Zn/Al LDH gallery by controlled ion-exchange reactions to form new classes of two-dimensional microporous solids. The following POMs have been successfully intercalated to yield pure phases as the sole reaction products : H<sub>2</sub>W<sub>12</sub>O<sub>40</sub>6-, α-SiV<sub>3</sub>W<sub>9</sub>O<sub>40</sub>7-, PMo<sub>2</sub>W<sub>9</sub>O<sub>39</sub>7-, BV(IV)W<sub>11</sub>O<sub>40</sub>7-, BCo(II)W<sub>11</sub>O<sub>39</sub>7-, BCu(II)W<sub>11</sub>O<sub>39</sub>7-, SiFe(III)(SO<sub>3</sub>)W<sub>11</sub>O<sub>39</sub>7-, SiW<sub>11</sub>O<sub>39</sub>8-, BW<sub>11</sub>O<sub>39</sub>9-, PW<sub>9</sub>O<sub>34</sub>9-, PV<sub>14</sub>O<sub>42</sub>9-, H<sub>2</sub>W<sub>12</sub>O<sub>42</sub>10-, NaP<sub>5</sub>W<sub>3</sub>OO<sub>110</sub>14-. The following POMs undergo partial exchange and yield incompletely exchanged reaction products : PCu(II)W<sub>11</sub>O<sub>39</sub>8-, BV(V)W<sub>11</sub>O<sub>40</sub>6-, BCo(III)W<sub>11</sub>O<sub>39</sub>6-, PV<sub>3</sub>W<sub>9</sub>O<sub>40</sub>6-, β<sub>1</sub>-SiW<sub>11</sub>O<sub>39</sub>8-, β<sub>2</sub>-SiW<sub>11</sub>O<sub>39</sub>8-, β<sub>-</sub>SiV<sub>3</sub>W<sub>9</sub>O<sub>40</sub>7-.

The intercalation reaction exhibits novel ion exchange selectivities. A complete exchange reaction takes place only under acidic reaction conditions. The  $\alpha$  isomer of Keggin-type POM (eg.  $\alpha$ -SiV<sub>3</sub>W<sub>9</sub>O<sub>40</sub><sup>7-</sup>) is more favorably intercalated than other stereo isomers. Such favorable ion exchange behavior for  $\alpha$ -Keggin POM can be explained in terms of the commensurate relationship of oxygen layers in the POM and the LDH hydroxyl lattice. The rhombohedral stacking pattern of the hydroxyl layer, which is more thermodynamically favorable than the hexagonal stacking polytype, is retained when the  $\alpha$ -isomer is intercalated. The minimum charge carried by the Keggin-type POM for complete exchange is observed to be 6-.

The POMs intercalated in LDH galleries are hydrolytically more stable than POM in the homogeneous solution. In the solid state, the POM-pillared LDH (LDH-POM) is generally stable up to about 200°C. An amorphous phase is formed around 300°C, and new crystalline inorganic phases are formed around 500°C.

FTIR studies indicate that the POMs in LDH galleries experience two major types of interactions: anion-anion repulsions and hydrogen bonding interaction with the LDH layer. These two competing interactions determine the direction of the  $\nu(M=O)$  band shift compared to normal potassium or ammonium salts. It has been observed that hydrogen bonding dominates, resulting in a red shift for the  $\nu(M=O)$  band.

LDH-POMs have been found to swell in water, the extent of swelling ranging from one to two mono layers. Non-pillared LDH intercalate are not swell in water.

LDH-POMs exhibit high surface areas, compared to a non-pillared LDH derivatives. This result indicates that extra space in the gallery has been introduced by pillars. The surface area of the LDH-POM depends on the charge of POM in the gallery. The highest surface area has been found for the Keggin-type POM with an 8- charge. The nonrigidity of the host layer could lead to low surface areas in the case of LDH-POMs in which the POMs carry higher charges than 8-.

LDH-POMs are photochemically reactive. They oxidize iso-propanol to acetone under irradiation by a Hg(Xe) lamp. The reactivity of the LDH-POM is different from that for POM in homogeneous solution. The higher the charge of POM in the gallery, the more space in the gallery, and the higher the photoreactivity of LDH-POM. The diffusivity of both the reactant and the products in the LDH gallery appears to determine the efficiency of the photoreaction.

# TO MY FAMILY

ii

#### **ACKNOWLEDGEMENTS**

I would like to thank Dr. T.J. Pinnavaia for patience, encouragement, and guidance offered throught the years of graduate school. I am also grateful to Dr. H.A. Eick for his editorial assistance in improving my writing.

I would like to express my gratitude to all past and present group members with whom I have come in contact with.

Finally, I would like to thank my parent and my wife for their financial support as well as encouragement.

# **TABLE OF CONTENTS**

Chapter		Page
LIST OF TA	BLES	xii
CHAPTER I	INTRODUCTION	1
A.	Pillaring of Lamellar Solids	1
В.	Layered Double Hydroxide (LDH)	2
	1. Structure	2
	2. Synthesis of LDH	5
	3. Ion-exchange Property of LDHs	6
	4. Comparison of LDH and Smectite Swelling Properties -	8
	5. Thermal Stability of LDHs	12
	6. Application of LDHs	14
C.	Polyoxometalate	15
	1. Structure and Property of Polyoxometalate	15
	2. Charge Distribution of POMs	27
	3. Photochemistry of POMs	30
D.	Adsorption onto Porous Materials	36
CHAPTER I	I. Experimental	40
A.	Materials	40
В.	Preparation of LDH-Cl and LDH-NO3	40
C.	Preparation of Guest Anions POMs	41
D.	Synthesis of LDH-POMs	47
E.	Physical Measurements	52
	1. X-ray Powder Diffraction	52
	2. Gas Adsorption Measurement	53
	3. Thermal Stability Study of LDH-POMs	53
	4 Nuclear Magnetic Resonance Studies	53

F.	Photocatalytic Reaction	54
G.	Elemental Analysis	54
H.	Transmission Electron Microscopy (TEM)	55
CHAPTER II	I. RESULT AND DISCUSSION	56
A.	Synthesis of LDH-Cl, NO3	56
В.	Synthesis of LDH-POMs	58
C.	Characterization of LDH-POMs	61
	1. Electron Microscope Studies	61
	2. X-ray Powder Diffraction (XRD) Studies	66
	3. Elemental Analysis	66
	4. Nuclear Magnetic Resonance (NMR) Studies	66
	5. Infared Spectroscopy Study	82
	a) Vibrations of Host Layer	82
	b) Vibrations of Guest POM Anion	84
	c) Vibrations of LDH-POMs	90
D.	Selectivities of Ion-Exchange Reaction and	
	Orientation of the Intercalated POMs	111
	1. Charge Selectivity	111
	2. Streo Selectivities	116
	3. Orientation of POMs in the Gallery	121
E.	Thermal Stabilities of LDH-POMs	123
F.	Adsorption Study of LDH-POMs	208
G.	Theoretical Calculation of Surface Area Pore Volume	219
H.	Photoreactivity of LDH-POMs	224
I.	Swelling Properties of LDH-POMs	228
J.	Proposed Mechanism of Ion-Exchange Reactio	228
Appendix A:	XRD pattern of LDH-NO3 and LDH-POMs	223

Appendix B: T-plots and D-R or D-A plots of LDH-POMs	242
References	251

## LIST OF TABLES

Table		Page
1	Some Natural Minerals of the Pyroaurite-Sjogrenite	5
2	pH values for Synthesis by the	
	Induced Hydrolysis Method	7
3	Classification of 2:1 Minerals according	
	to the Swelling in Water and the	
	Exchangeable Cation (after Suquet) <sup>39</sup>	13
4	Swelling of [Zn <sub>2</sub> Cr(OH) <sub>6</sub> )][C <sub>12</sub> H <sub>25</sub> SO <sub>4</sub> -·nH <sub>2</sub> O]	
	in n-Alcohol	13
5	Thermal Stability of [M(II) <sub>1-x</sub> M(III)(OH) <sub>2</sub> ][An-]	14
6	Heteropoly Tungstate and Molybdates with	
	α-Keggin Structure	19
7	Polarographic Half-Wave Potentials of	
	Lacunary Tungstosilicate Anions	23
8	Lacunary 1:11 and 2:17 Polyanion Ligands	26
9	Heteroatoms and Terminal Ligands observed	
	in (XM <sub>11</sub> )ZL and (X <sub>2</sub> M <sub>17</sub> )ZL	28
10	Heteroatoms of Z(XM <sub>11</sub> ) <sub>2</sub> and Z(X <sub>2</sub> M <sub>17</sub> ) <sub>2</sub> Complexes	29
11	Elemental Analysis Data for LDH-POM	69
12	Vibrational Frequency of XO4	86
13	Infrared Spectral Data of Free-POMs	
	and LDH-POMs	91
14	LDH-POM Intercalates for N2 Adsorption Studies	217
15	N2 Gas Adsorption Data and Calculated Values	223
16	Photochemical Reactivities of LDH-POMs	226

# LIST OF FIGURES

Figu	Figure	
1	Layer sequence in pyroaurite and sjogrenite.	
	The brucite-like layers are shaded	4
2	Basal spacings(A) of Na-saturated beidllite at different p/po	9
3	Change of approximate mean spacing between layers	
	of montmorillonite with reciprocal of square root	
	of concentration for Na-saturated clay (after Norrish).	
	x in NaCl solutions, o in Na2SO4 solution	11
4	Two types of MO6 octahedra. a) Type I and b) Type	16
5	The five Baker-Figgis isomers of the Keggin structure (a).	
	In $\beta$ -, $\gamma$ -, $\delta$ , and $\varepsilon$ -structures one, two, three and	
	four M3O13 groups (shown unshaded) have been	
	rotated by $\pi/3$	17
6	$\alpha$ and $\beta$ structure of heteropolyanions of the 12-series	20
7	Polyhedral models and relationships between the	
	different known tungstosilicates. This scheme is	
	based partly on structural determination by	
	single-crystal X-ray diffraction studies and partly	
	on proposed structures. Hydrolysis of the $\beta$ -SiW $_{12}$ O $_{40}$ <sup>4</sup> -	
	anion only gives $\beta_2$ -SiW <sub>11</sub> O <sub>39</sub> 8- and, then,	
	the $\gamma$ -SiW <sub>10</sub> O <sub>36</sub> <sup>8-</sup> anion	21
8	Polyhedral representation of a) $\alpha$ -SiV <sub>3</sub> W <sub>9</sub> O <sub>40</sub> <sup>7</sup> -	
	and b) β-SiV <sub>3</sub> W <sub>9</sub> O <sub>40</sub> 6	30

Figu	Figure	
9	XRD pattern of LDH-Cl prepared at different pH.	
	* represents a Zn5(OH)8Cl2 phase	57
10	Ir spectrum of LDH-NO3	59
11	XRD pattern of LDH-NaP5W30O110, prepared at pH = 7.4	60
12	XRD pattern of a) LDH-SiFe(SO3)W11O39 and	
	b) LDH-PW9O34. * represents an extra phase	62
13	Transmission electron microscope picture of LDH-POMs	64
	(top, left), LDH-NO3; (top, right), LDH-BCuW11O39;	
	(below, left), LDH-PMo2W9O39; (below, right),	
	LDH-PW9O34.	
14	Polyhedral representation of H <sub>2</sub> W <sub>12</sub> O <sub>42</sub> <sup>10</sup>	65
15	(top, left), An ORTEP view of [NaP5W30O110]14-	
	looking approximately along the virtual C5 symmetry	
	axis. Oxygen and tungsten atoms are represented as	
	large and small open circules, respectively, and	
	the sodium ion by the central closed circle. The	
	phophorus atoms are shown as closed circles.	
	(top, right), an idealized view along C5 axis	
	showing the WO6 octahedra in the upper half of	
	the anion. (below), The PW6O22 unit perpendicular to	
	the anion's virtual C5 axis. The phosphorus atom is	
	represented by the closed circle	68

Figure		Page
16	Solution 51V NMR spectra for a) LDH-SiV3W9O40 at	
	pH = 2.0 LiClO <sub>4</sub> solution and b) $\alpha$ -K <sub>6</sub> HSiV <sub>3</sub> W <sub>9</sub> O <sub>40</sub> at	
	pH = 1.7	71
17	Solid state <sup>29</sup> Si MAS NMR for a) LDH-SiV <sub>3</sub> W <sub>9</sub> O <sub>4</sub>	
	and b) $\alpha\text{-}K_6\text{HSiV}_3\text{W}_9\text{O}_{40}.$	72
18	Solid state 51V MAS NMR for LDH-SiV3W9O40	73
19	Solid state <sup>31</sup> P MAS NMR for a) LDH-PMo <sub>2</sub> W <sub>9</sub> O <sub>39</sub>	
	and b) K7PMo2W9O39	75
20	Solid state <sup>31</sup> P MAS NMR for a) LDH-PW9O34	
	and b) Na8HPW9O34	77
21	Solid state <sup>31</sup> P MAS NMR for a) LDH-PV <sub>14</sub> O <sub>42</sub>	
	and b) (NH4)9PV14O4	78
22	Solid state <sup>11</sup> B MAS NMR for a) LDH-BW <sub>11</sub> O <sub>39</sub>	
	and b) K9BW11O39	80
23	Solid state <sup>23</sup> Na MAS NMR for a) LDH-NaP5W30O110	
	and b) (NH4)14NaP5W30O110	81
24	Solid state <sup>31</sup> P MAS NMR for a) LDH-NaP5W30O110	
	and b)(NH4)14NaP5W30O110	83
25	Idealized structure of $\alpha$ -XM <sub>12</sub> (Keggin structure) (a)	
	and α-XM <sub>11</sub> (defect Keggin structure) (b)	
	(central XO4tetrahedron is not shown).	
	$(O_a = oxygen shared by 3 MO_6 octahedra and$	
	$XO_4$ tetrahedron. $O_b$ and $O_c$ = oxygen linked	
	to two different M atokms. Od = terminal unshared oxygen	85

Figure	<b>2</b>	Page
26	The polyhedral model of the PV <sub>14</sub> O <sub>42</sub> 9- anion	89
27	Ir spectra of 1) (NH4)6W12O40 and 2) LDH-H2W12O42	93
28	Ir spectra of 1) K6BVW11O40 and 2) LDH-BVW11O40	95
29	Ir spectra of 1) K6HSiV3W9O40 and 2) LDH-SiV3W9O40.	96
30	Ir spectra of 1) K8SiW11O39 and 2) LDH-SiW11O39	97
31	-	99
32	Ir spectra of 1) K7PMo2W9O39 and 2) LDH-PMo2W9O39.	100
	Ir spectra of 1) K9BW11O39 and 2) LDH-BW11O39	
33	Ir spectra of 1) K7BCuW11O39 and 2) LDH-BCuW11O39.	101
34	Ir spectra of 1) K7BCoW11O39 2) LDH-BCoW11O39	103
35	Ir spectra of 1) K7SiFe(SO3)W11O39 and	
	2) LDH-SiFe(SO <sub>3</sub> )W <sub>11</sub> O <sub>3</sub>	104
36	Ir spectra of 1) β-Na <sub>8</sub> HPW <sub>9</sub> O <sub>34</sub> and 2) LDH-PW <sub>9</sub> O <sub>34</sub>	113
37	Ir spectra of 1) (NH4)8Co2W12O42 and 2) LDH-Co2W12O42.	107
38	Ir spectra of 1) (NH4)9PV14O42 and 2) LDH-PV14O42	108
39	Ir spectra of 1) (NH4)10H2W12O42 2) LDH-H2W12O42	109
40	Ir spectra of 1) (NH4)14NaP5W30O110 and	
	2) LDH-NaP5W30O11	110
41	XRD pattern of LDH-PCuW11O39	112
42	XRD pattern of a) LDH-BCo(III)W11O39,	
	b) LDH-BV(V)W <sub>11</sub> O <sub>40</sub> and c) LDH-PV <sub>3</sub> W <sub>9</sub> O <sub>40</sub>	114
43	XRD pattern of a) LDH-β <sub>1</sub> -SiW <sub>11</sub> O <sub>39</sub> , b) LDH-β <sub>2</sub> -SiW <sub>11</sub> O <sub>39</sub> ,	
	c) LDH-β3-SiW <sub>11</sub> O <sub>39</sub> , d) LDH-α-SiW <sub>11</sub> O <sub>39</sub> ,	
	e) LDH-β-SiV <sub>3</sub> W <sub>9</sub> O <sub>4</sub>	118

Figu	igure	
44	XRD pattern of LDH-H2W12O40 at different temperatures	127
	a) 25°C, b) 120°C, c) 180°C: dotted line for the	
	rehydrated sample, solid line for dehydrated sample,	
	d) 225°C, e) 320°C, and f) 470°C.	
45	Ir spectra of LDH-H2W12O40 at different temperatures	130
46	DSC and TGA of LDH-H <sub>2</sub> W <sub>12</sub> O <sub>40</sub>	131
47	XRD pattern of LDH-SiV3W9O40 at different temperatures.	133
	a) 25°C, b) 165°C, c) 220°C: dotted line for the	
	rehydrated sample, solid line for the dehydrated sample,	
	d) 250°C, e) 360°C, and f) 500°C.	
48	Ir spectra of LDH-SiV3W9O40 at different temperatures	136
49	DSC and TGA of LDH-SiV <sub>3</sub> W <sub>9</sub> O <sub>40</sub>	138
50	XRD pattern of LDH-BV(IV)W11O39 at different temperatures	140
	a) 25°C, b) 150°C, c) 225°C: dotted line for the	
	rehydrated sample, solid line for the dehydrated	
	sample, d) 255°C, e) 360°C, and f) 470°C.	
51	Ir spectra of LDH-BV(IV)W11O40 at different temperatures.	143
52	DSC and TGA of LDH-BV(IV)W11O40	144
53	XRD pattern of LDH-BCo(II)W11O39 at different temperatures.	146
	a) 25°C. b) 185°C: dotted line for the rehydrated sample,	
	solid line for the dehydrated sample, c) 200°C: dotted	
	line for the rehydrated sample, solid line for the	
	dehydrated sample, d) 250°C, e) 360°C, and f) 500°C.	
54	Ir spectra of LDH-BCo(II)W11O39 at different temperatures.	149

Figure	<b>e</b>	Page
55	DSC and TGA of LDH-BCo(II)W11O39	151
56	XRD pattern of LDH-BCu(II)W11O39 at different temperatures.	153
	a) 25°C, b) 125°C, c) 160°C, d) 190°C: dotted line for	
	the rehydrated sample, solid line for the dehydrated	
	sample, e) 230°C, and f) 500°C.	
57	Ir spectra of LDH-BCu(II)W11O39 at different temperatures.	156
58	DSC and TGA of LDH-BCu(II)W11O39	157
59	XRD pattern of LDH-PMo2W9O39 at different temperatures.	159
	a) 25°C, b) 150°C, c) 205°C: dotted line for the	
	rehydrated sample, solid line for the dehydrated	
	sample, d) 340°C, and e) 500°C.	
60	Ir spectra of LDH-PMo2W9O39 at different temperatures	162
61	DSC and TGA of LDH-PMo <sub>2</sub> W <sub>9</sub> O <sub>3</sub> 9	164
62	XRD pattern of LDH-SiFe(III)(SO <sub>3</sub> )W <sub>11</sub> O <sub>39</sub> at	
	different temperatures	166
	a) 25°C, b) 150°C, c) 185°C, d) 200°C: dotted line	
	for the rehydrated sample, solid line for the	
	dehydrated sample, e) 303°C, and f) 500°C.	
63	Ir spectra of LDH-SiFe(SO <sub>3</sub> )W <sub>11</sub> O <sub>39</sub> at different temperatures.	169
64	DSC and TGA of LDH-SiFe(SO <sub>3</sub> )W <sub>11</sub> O <sub>39</sub>	170
65	XRD pattern of LDH-SiW <sub>11</sub> O <sub>39</sub> at different temperatures	172
	a) 25°C, b) 160°C. c) 180°C: dotted line for the	
	rehydrated sample, solid line for the dehydrated	
	sample d) 230°C e) 300°C and f) 500°C	

Figu	Figure	
66	Ir spectra of LDH-SiW11O39 at different temperatures	175
67	DSC and TGA of LDH-SiW <sub>11</sub> O <sub>39</sub>	176
68	XRD pattern of LDH-BW11O39 at different temperatures	178
	a) 25°C, b) 150°C, c) 180°C: dotted line for	
	the rehydrated sample, solid line for the dehydrated	
	sample, d) 210°C, e) 260°C, and f) 500°C.	
69	Ir spectra of LDH-BW11O39 at different temperatures	181
70	DSC and TGA of LDH-BW11O39	183
71	XRD pattern of LDH-Co <sub>2</sub> W <sub>12</sub> O <sub>42</sub> at different temperatures.	185
	a) 25°C, b) 120°C, c) 180°C: dotted line for the	
	rehydrated sample, solid line for the dehydrated	
	sample, d) 225°C, e) 320°oC, and f) 500°oC.	
72	Ir spectra of LDH-Co <sub>2</sub> W <sub>12</sub> O <sub>42</sub> at different temperatures	188
73	DSC and TGA of LDH-Co <sub>2</sub> W <sub>12</sub> O <sub>42</sub>	189
74	XRD pattern of LDH-PW9O34 at different temperatures	191
	a) 25°C, b) 110°C: dotted line for the rehydrated	
	sample, solid line for the dehydrated sample,	
	c) 175°C, d) 215°C, e) 320°C, and f) 500°oC.	
75	Ir spectra of LDH-PW9O34 at different temperatures	194
76	DSC and TGA of LDU DWoO24	106

Figu	re	Page
77	Ir spectra of LDH-PV14O42 at different temperatures	194
78	XRD pattern of LDH-PV14O42 at differrent temperatures	199
	a) 25°C, b) 125°C, c) 185°C, d) 320°C, and e) 500°C.	
79	DSC and TGA of LDH-PV14O42	202
80	XRD pattern of LDH-NaP5W30O110 at different	
	temperatures	204
	a) 25°C, b) 120°C: dotted line for the rehydrated	
	sample, solid line for the dehydrated sample,	
	c) 180°C: dotted line for the rehydrated sample,	
	solid line for the dehydrated sample, d) 250°C,	
	and e) 500°C.	
81	Ir spectra of LDH-NaP5W30O110 at different temperatures	207
82	DSC and TGA of LDH-NaP5W30O110	209
83	XRD pattern of LDH-H2W12O42 at different temperatures	211
	a) 25°C, b) 120°C, c) 180°C, d) 230°C, e) 320°C	
	and f) 500°C.	
84	Ir spectra of LDH-H2W12O42 at different temperatures	214
85	DSC and TGA of LDH-H <sub>2</sub> W <sub>12</sub> O <sub>42</sub>	215
86	N2 adsorption isotherm of LDH-POMs	216
87	T-curve of LDH-Cl	218
88	XRD pattern for wet samples of 1) LDH-PV14O42	
	and 2) LDH-NaP5W30O110, wet sample	22 <b>9</b>

#### **CHAPTER I**

#### INTRODUCTION

#### A. Pillaring of Lamellar Solids

The concept of pillaring lamellar solids was first introduced by Barrer and Mcleod in 1955<sup>1</sup> by showing that permanent porosity could be induced in smectite clay (e.g., montmorillonite) by replacing the interlayer Na<sup>+</sup> ions with alkylammonium ions. The alkylammonium ions functioned as molecular props or pillars between the silicates and provided the intracrystalline free spaces between the pillars. The pillaring agents range from thermally unstable organic or organometallic cations, e.g., bicyclic amine cations<sup>2</sup>,<sup>3</sup> and tris metal chelates<sup>4</sup>,<sup>5</sup> to thermally stable polyoxo cations,<sup>6-11</sup> e.g., Al<sub>13</sub>O<sub>4</sub>(OH)<sub>24</sub>(H<sub>2</sub>O)<sub>12</sub><sup>7+</sup>, and related chromium- and zirconium-polyoxocations. In fact, the term 'pillaring clay' is being used frequently in reference to clays interlayered with thermally stable polyoxy aggregates. Since the charge density of smectite clays is relatively low, the lateral distance between pillars is sufficiently large and the layers are sufficiently rigid to allow for the existence of free void volume between the pillars. Such pore volume then becomes available for adsorption and possible catalytic reaction of substrates sufficiently small to reach the intracrystalline pores. The adsorption study provides the insight of such porous materials.

A few pillarable host lattices other than smectite clay have been reported.  $\alpha$ Zirconium phosphate, in which the layers are cross-linked by bis-alkyl phosphonic
group, 12-14 are another example of a pillared lamellar solid. But, in general, pillared

lamellar solids are still quite rare. The major reason for such rarity is that there has not been found suitable host lattices which meets the basic requirements for a pillarable lattice, that is, 1) a reasonably low layer charge density, and 2) a reasonably rigid lattice layer.

In this work, the first pillared oxide structure other than smectite clays will be presented. The host lattice is a layered double hydroxide (LDH), which has about three to four times higher surface charge density (about 25-35 Å<sup>2</sup>/e) than smectite clay. Therefore, the guest anion should have high charge density to compensate the high surface charge density of the host layer. Polyoxometalates, which have a wide range of charge density and a variety of sizes, would be a suitable class of guest anions which meet this requirement.

#### B. Layered Double Hydroxide (LDH)

#### 1. Structure

There are many natural minerals and synthetic compounds having compositions of the type:

$$[M(II)_{1-x}M(III)_x(OH)_2]^{+x}[A^{n-}_x/_n\cdot yH_2O]$$
 where

$$M(II) = Mg$$
, Fe, Ni, Zn, Cu

$$M(III) = Al, Fe, Cr$$

$$A^{n-} = CO_3^{2-}$$
,  $SO_4^{2-}$ ,  $NO_3^-$ ,  $X = halides$ ,  $Fe(CN)_6^{3-}$ ,  $CrO_4^{2-}$ ,  $ClO_4^-$ , etc

They are referred to as pyroaurite-sjogrenite mineral groups, 15 hydrotalcite-like minerals, 16 mixed metal hydroxides, 17 and layered double hydroxides. 18 The latter term, abbreviated LDH, will be used in the present work.

They can be derived by the substitution of trivalent ion, M(III) into brucite-like layers, M(II)(OH)<sub>2</sub>. This introduction imparts a net positive charge on the sheet which is balanced by hydrated anions intercalated between the brucite-like layers.

The most common natural LDHs are hydrotalcite and manasseite polymorphs with composition [Mg6Al2(OH)16][CO3.4H2O]. They are actually stacking polymorphs that have the same basic layer structure. Mg and Al are randomly distributed among the octahedral sites. In hydrotalcite, the layers are stacked with rhombohedral symmetry (BC...CA...AB...BC for the brucite-like mainlayers), and three brucite-like layers are present per unit cell (c = 3c' = 23.4 Å). In manasseite, they are stacked with hexagonal symmetry (BC...CB...BC...) and two brucite layers are present per unit cell (c = 2c' = 15.6 Å).19,20 In nature the polymorphs are commonly intergrown. Manasseite generally forms the core and hydrotalcite the outer part of the grain. Thus, hydrotalcite appears to form later than the coexisting manasseite, and presumably, at lower temperature. To date, synthetic hydrotalcite has been prepared, but manasseite has never been synthesized.

The crystal structures of the Mg(II)/Fe(III) pyroaurite and sjogrenite polymorphs are the most extensively studied natural LDH's.20-23 They possess the same morphology as the Mg(II)/Al(III), hydrotalcite and manasseite polymorphs. In both compounds, brucite-like layers carrying a net positive charge alternate with layers in which the oxygen atoms of carbonate groups and water molecules are statistically distributed on a single set of sites. Adjacent brucite-like layers are stacked so that the hexagonal groups on the lower surface of one layer are directly above those on the upper surface of the layer below, as in gibbsite, and not as in brucite. The 2H (hexagonal) and 3R (rhombohedral) subgroups represent the two simplest sequences satisfying this condition. The sequence of the OH layers in pyrourite and sjogrenite are the same as with those of hydrotalcite and manasseite, respectively. The distance between two metal layers in pyroaurite equals c/3 = 7.80 Å. Because the brucite layers are only about 4.8 Å thick, a space of 3.0 Å is left between them. This space is occupied by a disordered interlayer, [1/8CO<sub>3</sub>·1/2H<sub>2</sub>O]0.25-. The distances parallel to the z-axis between layers are the same in both polymorphs: Mg + Fe layer to OH layer, 1.02 Å; between OH layers in the brucite layer, 2.04 Å; OH layer to interlayer, 2.88 Å. Fig. 1 shows the layer sequences in

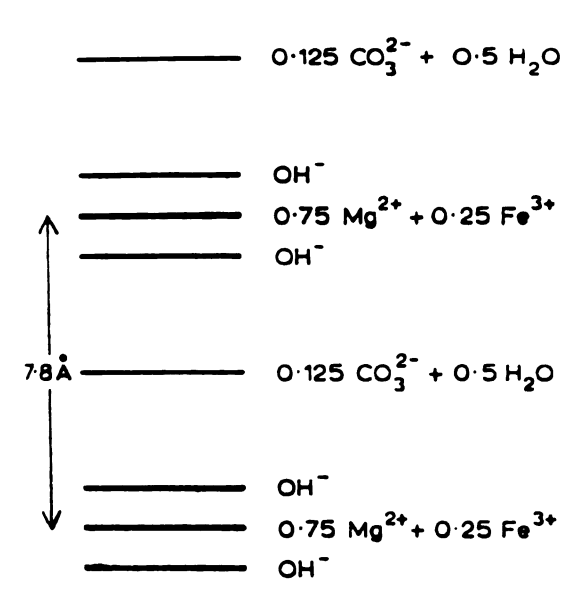


Fig. 1. Layer sequences in pyroaurite and sjogrenite.

The brucite-like layers are shaded.

pyroaurite and sjogrenite. Some natural minerals with the relevant crystal symmetries are given in Table 1.

Table 1. Some Natural Minerals of the Pyroaurite-Sjogrenite Group 22

N	ame	Approximate Composition		
3R-Typ	2H-Type	Hydroxide Sheet	Interlayer Sheet	
Pyroaurite	Sjogrenite	[Mg6Fe2(OH)	016]·[(CO3)(H2O)4]	
Hydrotalcite	Manasseite	[Mg6Al2(OH)	16]·[(CO3)(H2O)4]	
Stichtite	Barbertonite	[Mg6Cr2(OH)	16]·[(CO3)(H2O)4]	
Reevestite		[Ni6Fe2(OH)]	[6]·[(CO3)(H2O)4]	
Takovite		[Ni <sub>6</sub> Al <sub>2</sub> (OH)	16]·[(CO3)(H2O)4]	

#### 2. Synthesis of LDHs

Feitchnecht<sup>24</sup> has shown that a large number of synthetic LDHs can be prepared by titrating the solution containing divalent and trivalent cations with NaOH. Other workers have been involved in the modification and refinement of Feitchnecht's coprecipitation method.

Mortland and Gastusch<sup>25</sup> prepared the mixed Mg/Al hydroxides from the corresponding chlorides aged in a dialyzed medium, achieving in this way a much better crystallization and a high purity. They found that two mixed Mg/Al hydroxides having Mg/Al ratios of about 5:1 and 2:1 were formed from solution with Mg/Mg+Al molar ratios of 0.8 and 0.7, respectively. They have layer dimensions a = 3.048 Å, layer thickness 7.6 Å for the Al-rich compound and a = 3.072 Å, layer thickness 7.92 Å for the Al-poor compound.

Coprecipitation, followed by hydrothermal treatment, has been used by Miyata.<sup>26</sup> The hydrothermal treatment of freshly coprecipitated products results in highly crystalline LDHs in a relatively short period of time.

The hydrothermal and high temperature 'dry' technique was introduced by Roy et al.27 Solid MgO and Al<sub>2</sub>O<sub>3</sub>, which were the source of cations, were heated in the presence of H<sub>2</sub>O and CO<sub>2</sub> or N<sub>2</sub>O<sub>5</sub>, which were the source of CO<sub>3</sub><sup>2</sup>- and NO<sub>3</sub>- anions, respectively. The products were LDH-CO<sub>3</sub><sup>2</sup>- and LDH-NO<sub>3</sub>- respectively, where LDH stands for the positively charged Mg/Al brucite layer. This dry technique is useful when carbonate-free LDH is required.

Recently, R.M. Taylor<sup>28</sup> reported a new method, called "induced hydrolysis", which involves the hydrolysis of a cation in solution by a fully hydrolyzed and precipitated hydroxide of a second metallic cation. The term induced hydrolysis was coined because the fully hydrolyzed cation, that is, the hydroxide, caused complete hydrolysis of the second cation at a pH below that at which this reaction would normally occur. This technique utilized one cation typically M(III) as a hydroxide, formed from a solution of its chloride or nitrate salt. The advantage of this method is that crystalline compounds with reasonably sharp x-ray powder diffraction (XRD) patterns are formed within a few hours at room temperature. The pH values for precipitation of some typical LDH systems are listed in Table 2.

#### 3. Ion-exchange Property of LDHs

Since the exchangeability of the interlayer CO3<sup>2</sup>- of takovite [Ni3Al(OH)8]2·CO3·4H2O was first found by Bish,<sup>29</sup> a variety of anion exchanged LDHs have been prepared. Miyata<sup>30</sup> has reported quantitative studies of ion exchange properties of LDHs. The ion selectivities of monovalent anions are in the order of OH-> F-> Cl-> Br-> NO3-> I-. Ion selectivity of bivalent anions, which are higher than those of mono- valent anions, order as CO3<sup>2</sup>-> SO4<sup>2</sup>-. Such anion-exchanged forms of LDHs provide better XRD patterns than freshly precipitated LDHs.

Table 2. pH Values for Synthesis of LDHs by the Induced Hydrolysis Method

pН
6.9
7.4
7.5
8.4
7.4
7.4
4.0

#### 4. Comparison of LDH and Smectite Swelling Properties

The unidimensional swelling of smectite clays is their most interesting and important property. A number of polar molecules can be intercalated in multilayer form and thereby expand the galleries to substantial heights. The molecules may enter in stages, that is, one mono layer at a time.<sup>31</sup>

The adsorption of water on sodium beidellite is shown in Fig. 2.32 One mono layer is formed in the interlayer gallery at H<sub>2</sub>O partial pressures between approximately 0.1 to 0.6, and one more mono layer is built up to yield two mono-layers at partial pressures between 0.6 and 0.9. With sodium montmorillonite and hectorite the water layers can be built up infinitely and the clay layers are essentially exfoliated. Bradley et al.33 showed that water molecules could be sorbed in monomolecular sheets in montmorillonite, and that one, two, three, or four water layers were possible.

The occurrence of "steps" in the basal spacing of swelling minerals as a function of water content is now a generally accepted phenomenon. The first water to enter the interlayer positions is the result of hydration of the ions<sup>34</sup> after which the water forms distinct layers which increase in number. The water molecules of, at least, the first layers, are probably arranged in a hexagonal network<sup>35</sup> whose order is determined by hydrogen bonding to oxygens of the clay. This type of swelling is commonly referred to as Type 1,<sup>36</sup> short range swelling,<sup>37</sup> or crystalline swelling.<sup>38</sup> In this range, the adsorbed water increases to about 0.5g H<sub>2</sub>O/g clay while the interlayer spacing increases from 9.5 Å for the dry material to about 20 Å, corresponding to four layers of water. The mechanism of this Type 1, short range, or crystalline swelling has been explained in terms of the hydration energy of both interlayer cations and silicate layers.<sup>37</sup> When the interlayer cations in montmorillonite become hydrated, and the layer energy involved is able to overcome the attractive forces between layers, Type 1 swelling takes place. Since in the prototype minerals interlayer cations are absent, there is no cation hydration energy available to separate the layers and no swelling occurs in these types of minerals.

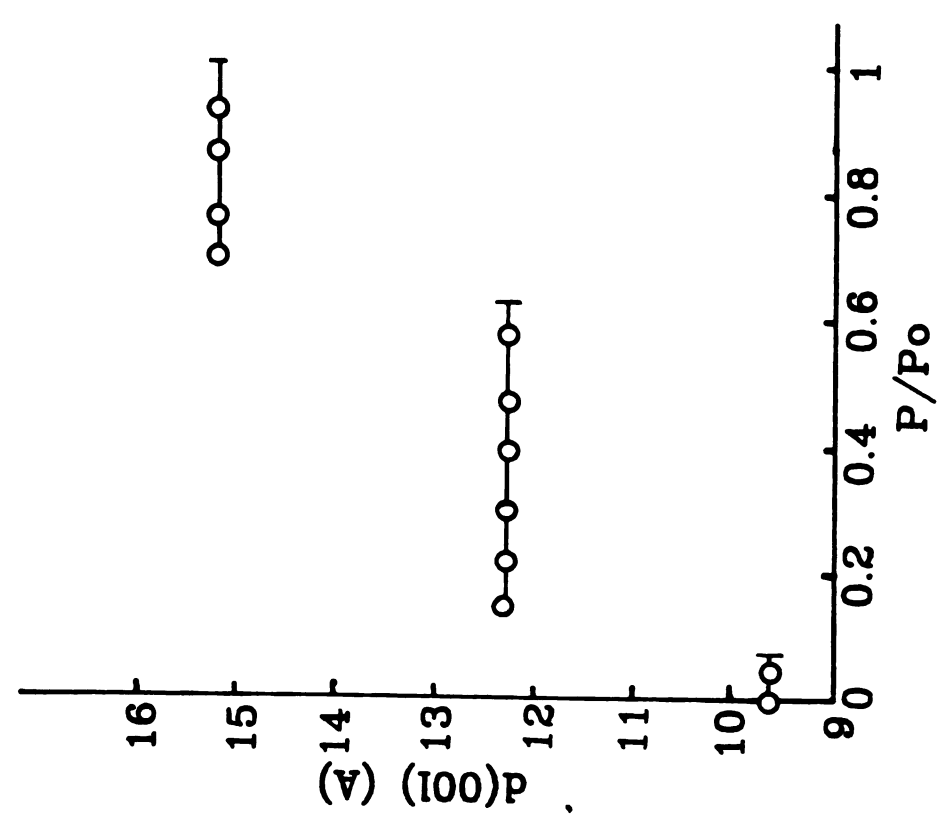
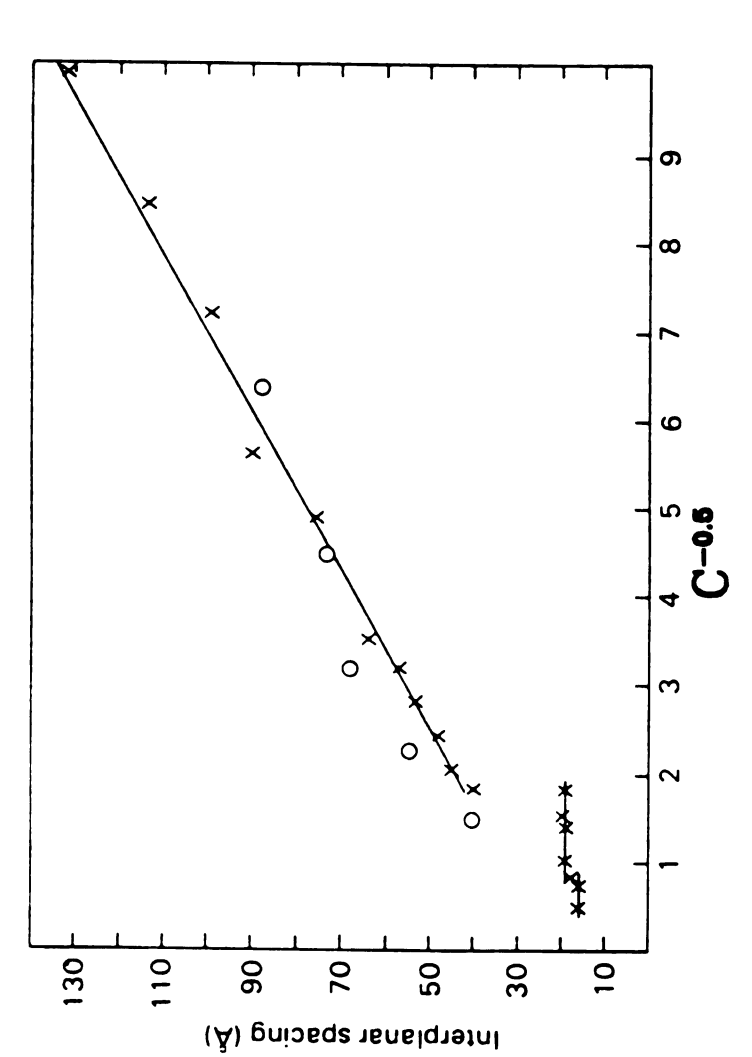


Fig. 2. Basal spacing (Å) of Na-saturated beidllite.

There is another type of swelling. Vermiculites and smectites when saturated with certain ions are capable of swelling to give much larger spacings between the layers than those normally observed with interlamellar complexes (Type 1). This type of swelling is called osmotic or type 2 swelling. 36 Its essential features are not only the large spacings observed but also the different nature of the forces between the layers. It is due to the diffuse double-layer repulsion by which the particles or the layers may be pushed further apart. In smectite the net negative layer charge is compensated by cations which are located on the layer surface in the dried clay. In the presence of water, these compensating cations have a tendency to diffuse away from the layer surface since their concentration will be smaller in the bulk solution. On the other hand, they are attracted electrostatically to the charged layers. The result of opposing trends is creation of an atmospheric distribution of compensating cations in a diffuse electrical double layer on the exterior layer surface of a clay particle. The compensating cations between the layers of the stack are confined to the narrow space between opposite layer surfaces. These forces are osmotic and result from a balance of electrostatic forces, van der Waals forces and the osmotic pressure of the interlamellar ions. The distance between the layers is not even approximately constant but shows a distribution covering a considerable range of distances. The transition from normal or Type 1 interlamellar swelling to Type 2 swelling is sharp. The swelling in the Type 2 is dependent on the concentration of electrolyte in the solution. The silicate-layer separation normally increases linearly as function of the reciprocal of the square root of the salt concentration.<sup>32</sup> Normal electrical double layers are presumably developed between the layers. As shown in Fig. 3, Norrish32 demonstrated that in Na-montmorillonite the individual layers dissociate completely as the water content is increased. The spacing first increases in steps corresponding to various organized structures of water molecules until 20 Å is reached and then jumps to 40 Å, after which it increases linearly. In the zone of large spacing (i.e. > 40 Å), single spacing is replaced by a statistical distribution. Osmotic swelling in the swellable



reciprocal of square root of concentration for Na-saturated clay (after Norrish, 1954)32. Fig. 3. Change of approximate mean spacing between layers of montmorillonite with x in NaCl solutions, o in Na2SO4 solutions.

minerals depends largely on the surface charge density and charge localization as well as the nature of the exchangeable cation. Table 3 shows the swelling property of expandable 2:1 minerals.39

There have been two reported cases of LDHs that swell. One of these is [Ca<sub>2</sub>Al(OH)<sub>6</sub>][OH-2H<sub>2</sub>O]<sup>40</sup> with a basal spacing of 7.4 Å. When it takes up water to produce [Ca<sub>2</sub>Al(OH)<sub>6</sub>][OH-6H<sub>2</sub>O], the basal spacing increases up to 10.7 Å indicative that one mono layer of water has been built up in the gallery. The other case is [Zn<sub>2</sub>Cr(OH)<sub>6</sub>][org.]<sup>41</sup> in which org. represents organic anions, for example, alkyl sulfates. Table 4 shows the swelling of [Zn<sub>2</sub>Cr(OH)<sub>6</sub>][org.] with polar organic solvents. The behavior is analogous to that of alkylammonium layer silicate.<sup>42</sup> The basal spacing after swelling of dodecyl sulfate with dodecyl alcohol corresponds to the value calculated for alkyl double layer (41.3 Å).

#### 5. Thermal Stability of LDHs

The thermal stability of LDHs are very important in their application for heterogeneous catalysts at elevated temperature. A thermal study of the hydrotalcite was done by G.W. Brindley and S. Kikkwa.<sup>43</sup> They reported that the XRD pattern showed little or no change up to 240°C, but at 260-280°C there was an abrupt decrease of basal spacing to 6.2-6.4 Å which was followed by a continued decrease until complete decomposition occurred at around 370°C. Following the abrupt basal spacing decrease to 6.4 Å at 260°C, and further decrease to 6.2 Å at 280°C, the mineral could be rehydrated to give the initial basal spacing. This initial collapse was due to decomposition of the CO3 groups, CO3<sup>2-</sup> ··· CO<sub>2</sub> + O<sup>2-</sup>; the oxygen anions remained between the hydroxide layers. The hydroxide layers were more closely packed than the bulky CO3 groups. At this state, the layers were sufficiently separated to permit water molecule penetration and reexpansion to the original spacing. The continued decrease in basal spacing to about 5.5 Å at higher temperature was attributed to hydroxide layer

Table 3. Classification of 2:1 Minerals according to the Swelling in Water and the Exchangeable Cation (after Suquet)39

Hydration state	Exchangeable Cation					
	Li	Na	K	Ca	Mg	Ba
Infinite	MBS	V MB	M			
3 water layers				MB(S)	MBS	MBS
2 water layers	V	BSV	M	(B)SV	(S)V	(S)V
1 water layer			BSV			
0 water layer			V			

M = Montmorillonite, B = Beidellite, S = Saponite,

V = Vermiculite

Table 4. Swelling of [Zn<sub>2</sub>Cr(OH)<sub>6</sub>][C<sub>12</sub>H<sub>25</sub>SO<sub>4</sub>-·nH<sub>2</sub>O] in n-Alcohol

swelling agent	d(Å)	swelling agent	d(Å)
С3Н7ОН	28.3	C <sub>10</sub> H <sub>21</sub> OH	38.2
С4Н9ОН	29.2	C <sub>12</sub> H <sub>25</sub> OH	41.1
С6Н13ОН	30.8	C <sub>14</sub> H <sub>29</sub> OH	42.4
C8H17OH	33.7	С16Н33ОН	44.9

decomposition and accommodation of O<sup>2</sup>- anions more or less within these layers. The minimum spacing of 5.5 Å approached that of brucite.

Generally speaking, the thermal stability of LDHs depends on both interlayer anions and the compositions of brucite-like layers. Table 5. shows the dehydroxylation temperature.

Table 5. Thermal stability of  $[M(II)_{1-x}M(III)(OH)_2][A^{n-1}]$ 

M(II)	M(III)	х	An-	Dehydroxylation temperature( <u>C</u> )	ref.
Mg	Al	0.25	SO <sub>4</sub> 2-	455	44
Mg	Al	0.25	CrO4 <sup>2</sup> -	460	44
Mg	Al	0.25	CO <sub>3</sub> 2-	440	44
Ni	Al	0.26	Cl-	300	45
Zn	Al	0.25	Cl-	280	45
Mg	Al	0.25	NO <sub>3</sub> -	455	45
Mg	Al	0.33	Cl-	430	45
Mg	Al	0.25	Cl-	415	45
Mg	Al	0.24	Cl-	400	45
Mg	Fe	0.25	CO <sub>3</sub> 2-	250	46

### 6. Application of LDHs

Synthetic LDHs, particularly carbonate derivatives, are utilized as acid adsorbents, 47 antipeptins, 48 Ziegler-Natta type catalyst supports, 49 in combination with a polyolefins as nontoxic and non smoke flame retardants, 50 catalyst precursors of syn gas-to-methanol production, 51 and catalyst precursors for the aldol condensation. 52 The pristine LDHs, e.g., [Zn<sub>2</sub>Cr(OH)<sub>6</sub>]X·nH<sub>2</sub>O have been tested for the triphase catalyst. 53 Thin films of LDHs deposited on electrodes have also been tested for the modification of electrode. 54

#### B. Polyoxometalate

#### 1. Structure and Properties of Polyoxometalates

Polyoxomelates are represented by the general formula  $^{55}$  [M<sub>m</sub>O<sub>y</sub>]P-(isopolyanions) and [X<sub>x</sub>M<sub>m</sub>O<sub>y</sub>]q-(x < m) (heteropolyanions), where M is usually molybdenum or tungsten, and less frequently vanadium, niobium or tantalum, or mixture of these elements in their highest oxidation states.

Such polyoxometalates form a structurally distinct class of complexes based predominantly, although not exclusively, upon quasi-octahedral-coordinated metal atoms (MO6). There are two types of polyoxometalates formed by two different MO6 units. Type I has only one terminal oxygen as shown in Fig. 4 a). On the other hand, Type II has two terminal oxygens as shown Fig. 4 b). Many W(VI) and Mo(VI) polyoxoanions are seen to be on larger, neutral MnO3n cages that encapsulate anionic subunits and are linked to them only by weak ( > 2.2 Å) bonds.56 For example, among the Type I class of polyoxoanions, W6O192- contains a W6O18 cage encapsulating O2-. Thus, W6O192can be expressed by  $(W_6O_{18})(O^2-)$ ,  $PM_{012}O_{40}^{3-}$  by  $(M_{012}O_{36})(PO_4^{3-})$ ,  $W_{10}O_{32}^{4-}$ by  $(W_{10}O_{30})(O^{2}-)_{2}$ ,  $P_{2}M_{01}8O_{62}6-$  by  $(M_{01}8O_{54})(PO_{4}^{3}-)_{2}$ , and so on. In the limit an infinitely large cage is formed by the linking of Type I MO6. Precisely such a compound is found in the MoO<sub>3</sub>·2H<sub>2</sub>O structure.<sup>57</sup> There is another type of polyoxoanions formed by the linking of Type II octahedra. For examples, consider Mo4O12(O2)24- in which the Mo4O<sub>12</sub> ring is encapsulating (O<sub>2</sub><sup>2</sup>-)<sub>2</sub>, expressed by (Mo4O<sub>12</sub>)(O<sub>2</sub><sup>2</sup>-)<sub>2</sub>,  $S_2Mo_5O_24^{4-}$  by  $(Mo_5O_{15})(SO_3^{2-})$ ,  $P_4W_8O_4O_1^{12-}$  by  $(W_8O_24)(PO_4^{3-})4$ , and so on. In the limit of a large ring of Type II polyanion one obtains an infinite chain structure of the composition MO<sub>3</sub>. Precisely such chains are found in the MoO<sub>3</sub> structure.<sup>58</sup>

The most extensively studied polyoxometalate compounds are those with Keggin structures, XM<sub>12</sub>O<sub>40</sub>n-. There are five possible isomers as shown in Fig. 5. Since Keggin reported the structure of 12-tungstophosphoric acid in 1933,<sup>59</sup> it has customarily

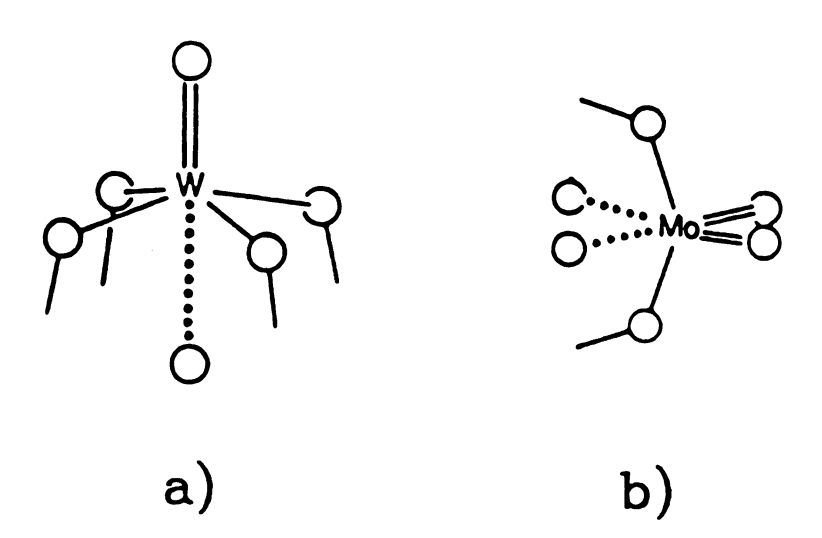
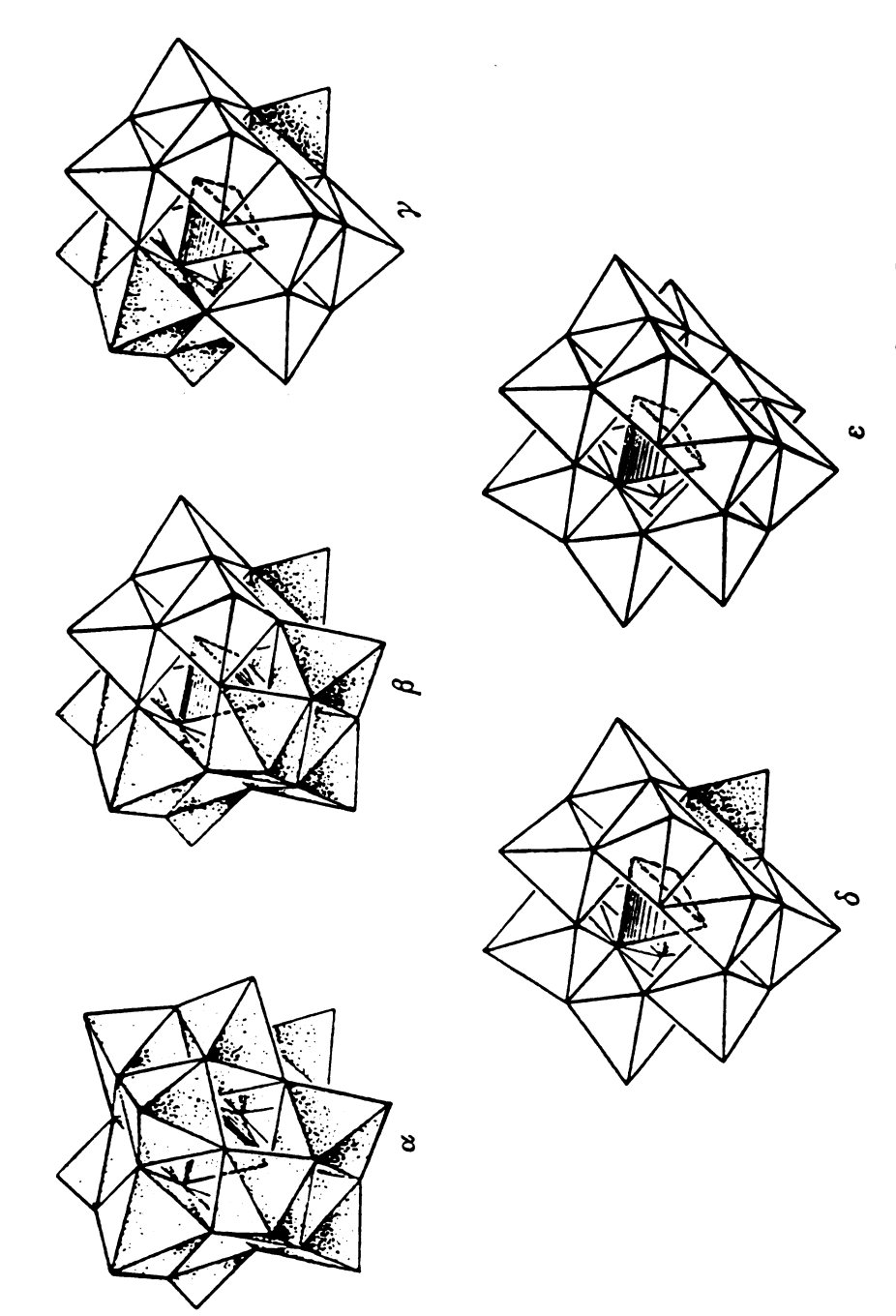


Fig. 4. Two types of  $MO_{\mbox{\scriptsize 6}}$  octahedra a) Type I and b) Type II.



structures one, two, three and four M3O13 groups (shown unshaded) have been rotated Fig. 5. The five Baker-Figgis isomers of the Keggin structure (a). In  $\beta$ -,  $\gamma$ -,  $\delta$ - and  $\epsilon$ by  $\pi/3$ .

been referred to as the  $\alpha$ -form. This structure is based on a central XO<sub>4</sub> tetrahedron surrounded by twelve MO<sub>6</sub> octahedra arranged in four groups of three edge shared octahedra, M<sub>3</sub>O<sub>13</sub> (M<sub>3</sub> triplet). These groups are linked by shared corners to each other and to the central XO<sub>4</sub> tetrahedron. The majority of heteropoly tungstates adopt either the Keggin structure or structures derived from fragments of that structure. Table 6 shows numerous heteropoly molybdates and tungstates with the  $\alpha$ -Keggin structure.

An isomer of the Keggin structure is known for several tungstates (X = B, Si, Ge,H<sub>2</sub>) and molybdates; these appear to contain the  $\beta$ -Keggin structure. Fig. 6 shows the  $\alpha$ and β-Keggin structures. The β-Keggin structure has one of the three edge-shared M3O13 triplets of the  $\alpha$ -structure rotated by  $60^{\circ}$  around the C3 axis (designated by R), thereby reducing the overall symmetry of the anion from Td to C3v. The new cornershared W-O-W linkage between the rotated group (R) and the rest of the anion involves a shorter W---W separation (3.65 vs 3.72 Å) and a more acute W-O-W angle(-145° vs 155°) than the a-structure. Both of these features may account for the lower stability of  $\beta$  vs  $\alpha$  i.e., increased coulombic repulsion  $^{60}$  and less favorable  $p_{\pi}$ - $d_{\pi}$  interactions,  $^{61}$ respectively. The  $\beta$ -structure is one of several proposed by Baker and Figgis;<sup>55</sup> the others involve the 60° rotation of two, three, and all four M<sub>3</sub>O<sub>13</sub> as shown in Fig. 5. All oxidized \beta-forms spontaneously isomerize to \alpha-forms at rates which vary from seconds for  $\beta\text{-PMo}_{12}$  at room temperature  $^{62}$  to hours for  $\beta\text{-SiW}_{12}$  at  $150^{\circ}\text{C.}^{63}$  The polarographic reduction waves for  $\beta$ -isomers parallel those for  $\alpha$ -isomers, but they exhibit slightly more positive potentials. It follows that the reduced \(\beta\)-structure is more stable than the  $\alpha$ -structure. The optical absorption spectra of reduced  $\beta$ -isomers are similar and are unlike those of the corresponding reduced  $\alpha$ -isomers.

When solutions of XW<sub>12</sub>O<sub>40</sub> are treated with base (pH > ca 5) a complex series of hydrolysis reactions ensues, leading to a variety of lacunary anions. Fig. 7 shows the reaction pathway as well as the species involved in each step.

Table 6. Heteropoly Tungstates and Molybdates with  $\alpha$ -Keggin Structure 54

Compound	X
[XW <sub>12</sub> O <sub>40</sub> ] <sup>n</sup> -	H, H <sub>2</sub> , B, Al, Ga(III) <sup>a</sup> , Si, Ge(IV), P(V),
	As(V), V(V)b, Cr(III), Mn(IV)c, Fe(III),
	Co(III), Cu(II), Cu(I), Zn, Se(IV)c, Te(IV),
	Sb(III)c, Bi(III)c
[XMo <sub>12</sub> O <sub>40</sub> ] <sup>n</sup> -	Si, Ge(IV), P(V), As(V), V(V)b, Ti(IV)c,
	Zr(IV)c, In(III)c, H2d, Mod

a Known as lacunary (GeW11) anion only.

b In mixed addenda (V + W, V + Mo) anions only.

c Confirmation desirable.

d Existence questionable.

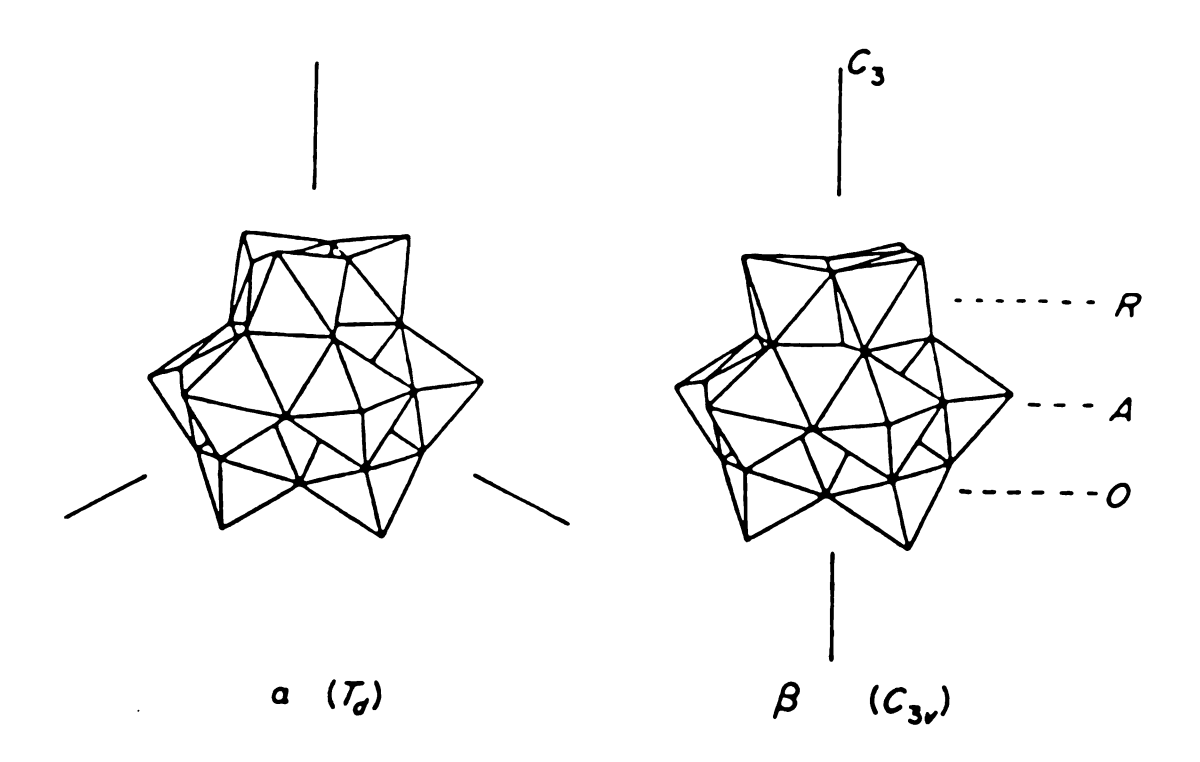


Fig. 6.  $\alpha$  and  $\beta$  structures of heteropolyanions of the 12-series

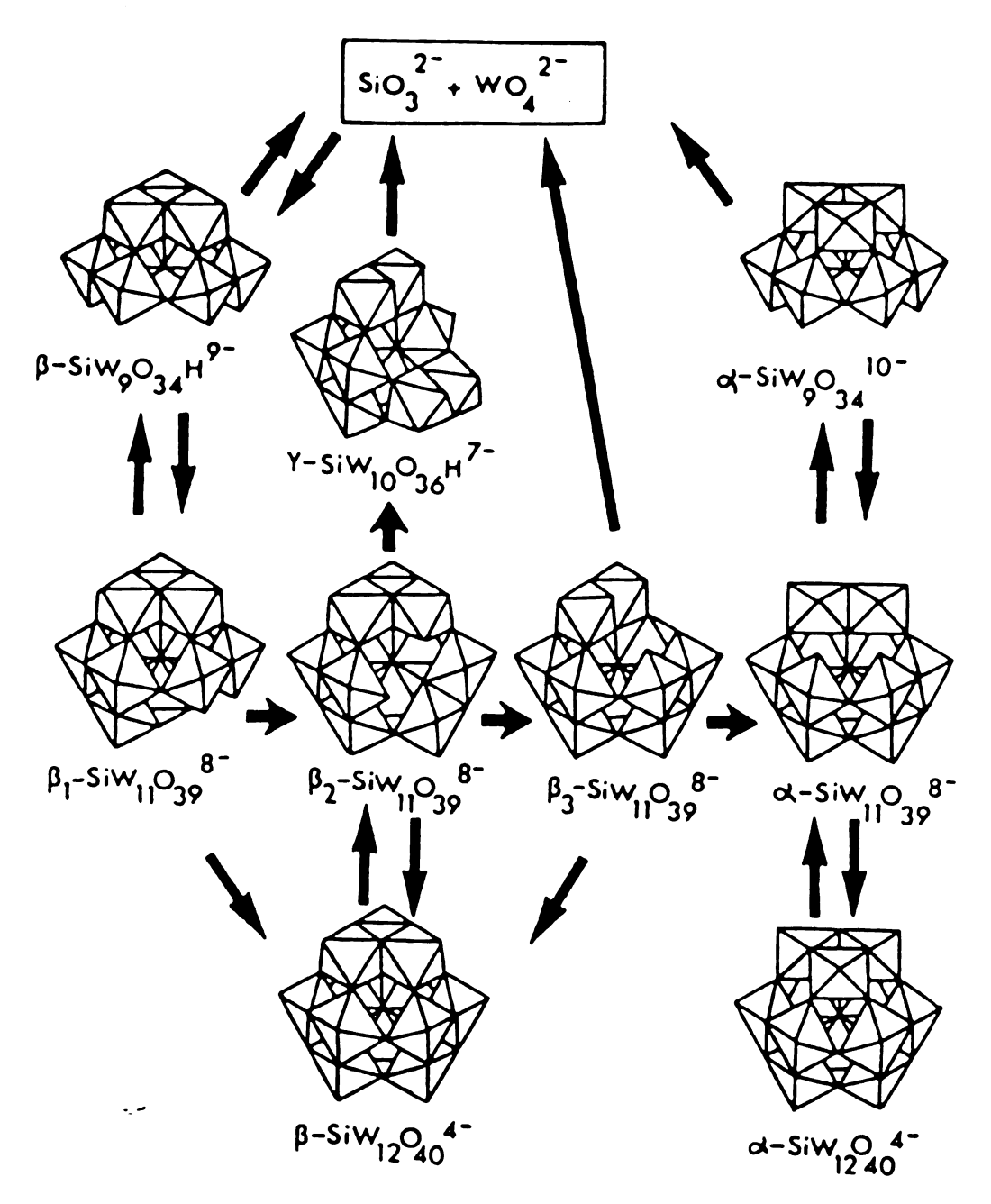


Fig. 7. Polyhedral models and relationships between the different known tungstosilicatas. This scheme is base partry on structural determination by single-crystal X-ray diffraction studies and partly on proposed structures. Hydrolysis of the  $\beta$ -SiW<sub>12</sub>O<sub>40</sub><sup>4-</sup> anion only gives  $\beta$ 2-SiW<sub>11</sub>O<sub>39</sub><sup>8-</sup> and , then, the  $\gamma$ -SiW<sub>10</sub>O<sub>36</sub><sup>8-</sup> anion.

Since each of the above polyanions is electrochemically reducible, the interconversions and isomerizations can be followed by polarography. The half-wave potentials of each tungstosilicate species are given in Table 7.

All of the lacunary anions, except  $\alpha$ -XW $_{11}$  and, perhaps, SiW $_{10}$  appear to be metastable in solution. But conditions of pH, temperature, etc., can be arranged so that decomposition and isomerization reactions are slow, and intermediate salts can be crystallized. The  $\beta$ -XW $_{12}$  structure can give rise to three isomeric XW $_{11}$  anions shown in Fig. 7. For X = Si and Ge all three isomers have been observed and isolated. Historically, the isomers were named to corresponding to the spontaneous direction of isomerization  $\beta_1 \longrightarrow \beta_3$ . The structure were assigned on the basis of electrostatic arguments.60 The structures show a diminution of the number of short W---W separations between rotated and unrotated W3 groups in the sequence  $\beta_1 \to \beta_2 \to \beta_3 \to \alpha$ . The properties of the  $\beta$ -SiW $_{11}$  isomers parallel those of  $\alpha$ -SiW $_{11}$  except that irreversible isomerization occurs in solution. Estimates of the half-lives of the SiW $_{11}$  isomers at pH = 5 and 25°C are  $\beta_1$ , 11hr;  $\beta_2$ , 7.5hr;  $\beta_3$ , 4.5hr.64

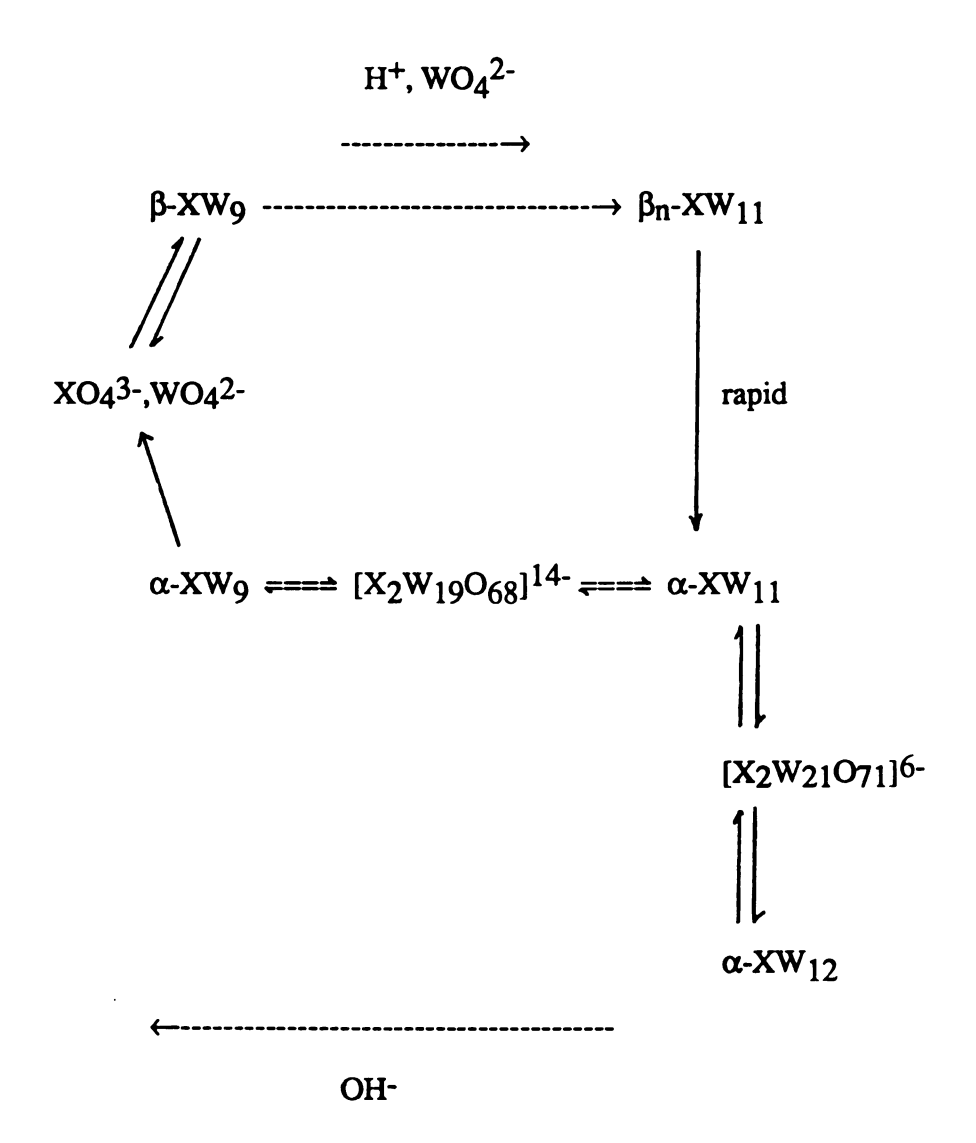
Alkaline degradation of  $\alpha$ -XW<sub>11</sub> and  $\beta$ -XW<sub>11</sub> at pH > 8 leads to  $\alpha$ -XW<sub>9</sub> and  $\beta$ -XW<sub>9</sub> anions, respectively, as shown in Fig. 7. There are no stable  $\beta$ -isomers of  $\alpha$ -[XW<sub>12</sub>O<sub>40</sub>]<sup>3</sup>- and  $\alpha$ -[XW<sub>11</sub>O<sub>39</sub>]<sup>7</sup>- (X = P, As). In aqueous solutions PW<sub>12</sub> has a limited stability range. At pH = 1.5 - 2, PW<sub>12</sub> is rapidly (and reversibly) converted to the lacunary PW<sub>11</sub> anion. The properties of further degradated species XW<sub>9</sub> (X = P, As) seem to parallel those of SiW<sub>9</sub> and GeW<sub>9</sub> in many, but not all aspects. The following scheme shows the presently known interconversions.

Table 7. Polarographic Half-Wave Potentials<sup>a</sup> of Lacunary Tungstosilicate Anions<sup>55</sup>

Anion	E <sub>1/2</sub> b (number of electrons)	
α-SiW9	-0.78 (4)	
β-SiW <sub>9</sub>	-0.80 (2)	-0.90 (2)
$\alpha$ -SiW <sub>11</sub>	-0.65 (2)	-0.91 (2)
$\beta_1$ -SiW $_{11}$	-0.63 (2)	-0.83 (2)
$\beta_2$ -SiW <sub>11</sub>	-0.63 (2)	-0.77 (2)
$\beta_3$ -SiW <sub>11</sub>	-0.69 (2)	-0.89 (2)

a Dropping mercury electrode; 1.0 M sodium acetate/acetic acid pH 4.7.

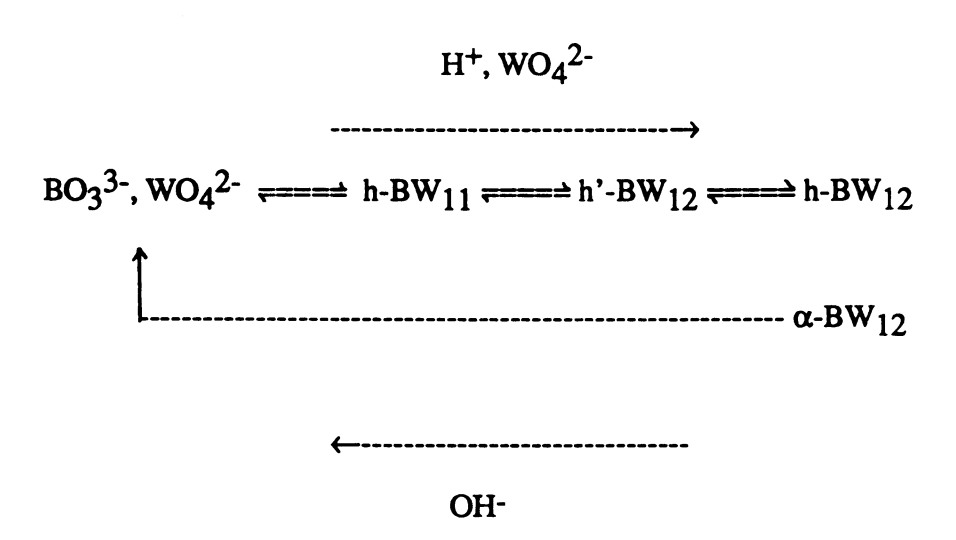
b vs. SCE



Besides the instability of  $\beta$ -[XW<sub>11</sub>O<sub>39</sub>]<sup>7</sup> and the non-existence (to date) of  $\beta$ -XW<sub>12</sub>, the above scheme differs from that of the tungstosilicates by the inclusion of X<sub>2</sub>W<sub>19</sub> (X = P) and X<sub>2</sub>W<sub>21</sub> (X = P, As) complexes.<sup>66</sup>

The only authenticated heteropolyanions containing boron are the tungstoborates.

The interconversion of isomers is shown below.67



Complexes are known in which the 'ligand' is a polyanion structure that is deficient in single MO6 octahedron. Metal ion binding occurs at the vacant site. Mono vacant Keggin derivatives form by far the largest and versatile class of lacunary polyanions, and their complexes have been intensively studied since the first examples were recognized in 1966.68 A list of polyanion ligands that have been observed in such complexes is given in Table 8.

Two global stochiometries are observed for the complexes, metal:'ligand' = 1:1 and 1:2. The 1:1 complexes are formed predominantly with 'octahedral' metal ions, with the polyanion ligand functioning in a dentate manner. In the 1:2 complexes the metal ion

Table 8. Lacunary 1:11 and 2:17 Polyanion Ligands<sup>a</sup>.55

Compound	X	Isomer
[XW <sub>12</sub> O <sub>39</sub> ] <sup>n</sup> -	P, As	α
	Si, Ge	$\alpha$ , $\beta_1$ , $\beta_2$ , $\beta_3$
	В	hb
	Al, Ga, Fe(III), Co(III)	$\alpha^{c}$
	Co(II), Zn, H <sub>2</sub>	$\alpha$ d
	Sb(III), Bi(III)	-e
[XMo11O39] <sup>n</sup> -	P. As, Si, Ge	α
$[X_2W_{17}O_{61}]^{10}$	P	$\alpha_1, \alpha_2$
	As	α

- a Species of which complexes have been isolated.
- b The free ligand has the currently unknown 'h' structure.
  - Complexes appear to contain the  $\alpha$  form.
- c α-structure not proved in every case, but considered very probable.
- d Free ligand not known.
- e True structure not known.

Table 9. Heteroatoms and Terminal Ligands observed in (XM<sub>11</sub>)ZL and (Z<sub>2</sub>M<sub>17</sub>)ZL Complexes.<sup>a</sup>, 55

Ligand, L	Heteroatom, Z	Refs.
O2-	W6+/5+, Mo6+/5+, V5+/4+	
	Ti4+, Sn4+, Nb5+, Rh3+,	69, 70, 71, 72
	Ge4+, Re7+/6+, Sb5+	73, 74
H <sub>2</sub> Ob	V3+, Cr3+, Mn2+/3+, Ni2+	68, 74, 75, 76
	Fe <sup>2+/3+</sup> , Co <sup>2+/3+</sup> , Cu <sup>2+</sup> ,	77, 78, 79, 80
	Zn <sup>2+</sup> , Al <sup>3+</sup> , Ga <sup>3+</sup> , In <sup>3+</sup> ,	81, 82,
	Rh3+	
	Ru3+/4+	83
N3-	Os6+	84
NO	Ru2+/3+	85
NH3, NCS-, NO2-,		
N3-, CN-, pyridine,	Co <sup>2</sup> +/ <sup>3</sup> +, Fe <sup>3</sup> +, Ni <sup>2</sup> +,	75, 86
pyrazine, thiourea	$Z_n$ 2+d	
Fe(CN)6 <sup>4</sup> -, SO3 <sup>2</sup> -	Fe2+	74

- a This table excludes complexes where ZL represents an organometallic moiety.
- b In several cases the pKs are such that stable hydroxometal derivatives are isoable.
- c Unsubstituted, 2- and 4-methyl, 3-cyano.
- d Not all metal-ligand combinations.

Table 10. Heteroatoms of  $Z(XM_{11})_2$  and  $Z(X_2M_{17})_2$  Complexes a, 55

Heteroatom, Zn+	Refs.	
Ce4+/3+, Pr3+, Nd3+, Sm3+, Eu3+, Ho3+	90	
Th4+, U5+/4+	91, 92, 93, 94	
Pr4+, Tb4+/3+, Pu4+/3+, Np4+, Am4+/3+,	95, 96, 97	
Cm <sup>4+/3+</sup> , Cf <sup>4+/3+</sup>		
In3+b	98	
La3+	99	
<u>Sr2+, Ba2 +</u>	100	

a All tungstates.

b Note that two types of complex, with six- and eight coordinate In<sup>3+</sup>, appear to be formed.

can be viewed as 8-coordinate. The sixth coordination site on the metal in the 1:1 complexes may be occupied by a variety of ligands L, as shown in Table 9.

A second type of complex shown in Table 10 is formed by the lacunary ligands XM<sub>11</sub> and X<sub>2</sub>M<sub>17</sub> with lanthanide and actinide cations. These complexes have the stoichiometry metal(ligand)<sub>2</sub> and the first examples were reported by Peacock and Weakley. 100 The high charge carried by the bis-ligand complexes enables the stabilization of 'unusual' oxidation states for the heteroatom, e.g., tetravalent Pr, Tb, Am, Cm, and Cf and pentavalent U.

## 2. Charge Distribution of Polyoxometalates

It is commonly asserted that heteropoly anions, particularly those with the almost spherical Keggin structure, are unsolvated in aqueous solution and do not participate in hydrogen bonding in the crystalline state. Various lines of experimental evidence, including viscosity 102 and diffusion studies, 102 and crystal structure determination, 104

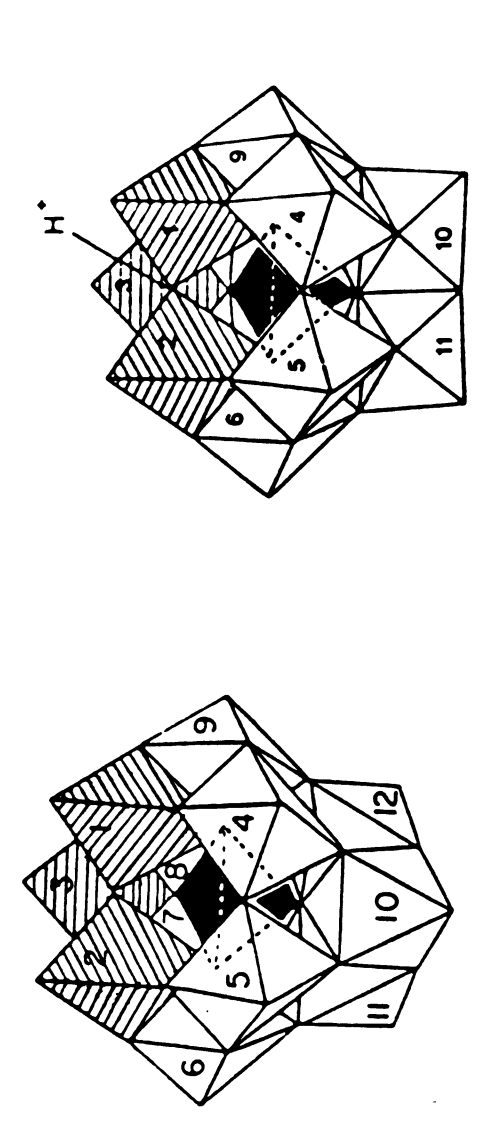


Fig. 8. Polyhedral representation of a)  $\alpha$ -SiV<sub>3</sub>W<sub>9</sub>O<sub>40</sub><sup>7</sup>- and b)  $\beta$ -SiV<sub>3</sub>W<sub>9</sub>O<sub>40</sub><sup>6</sup>-.

tend to support that assertion. 12-molybdosilicate and 12-molybdophophate anions are less susceptible to hydrogen bonding than is the perchlorate ion. 104 Since there is no apparent steric hindrance to heteroconjugation, these results confirm the very low surface charge density of such polyanions.

It has been known that the negative charge on the surface of the polyoxoanion is concentrated on specific oxygen atoms. Klemperer et al. 106 determined the protonated oxygen site of HV2W4O193- by 170 NMR. They observed an upfield shift of only the OV2 (bridging oxygen) resonance upon protonation of V2W4O194-. This change in chemical shift identified the OV2 oxygen in the V2W4O19<sup>4</sup>- cluster as the protonation site. All resonances except the OV2 resonance in V2W4O194- shifted downfield upon protonation of the cluster. This downfield shift reflects a strengthening of metal-oxygen bonds and concomitant reduction of negative charge on the oxygen atoms in HV<sub>2</sub>W<sub>4</sub>O<sub>19</sub><sup>3</sup>-. More recently, Klemperer et al. <sup>107</sup> reported the most basic site of oxygen atoms of cis-Nb2W4O194- by its alkylation reaction pattern. They concluded that the bridging oxygen (Nb-O-Nb) was the most basic site, i.e., site with most nucleophilicity. Also they found that charge delocalization substantially occurred in the anion when the product distribution was considered. The enhanced reactivity of Nb2W4O194- compared to that of W6O192- is additional supporting evidence for the idea of a charge delocalization. The OW2 oxygen in W6O192- were not alkylated by dimethyl sulfate in acetonitrile even after 2 days at ambient temperature. In contrast, the OW2 oxygens in Nb2W4O194- were alkylated under the same condition in less than 5 minutes.

It has been reported <sup>108</sup> that the protonation site of SiV<sub>3</sub>W<sub>9</sub>O<sub>40</sub>7- was assigned to the OV<sub>2</sub> oxygen (bridging oxygen) by <sup>51</sup>V NMR, as shown in Fig. 8.

## 3. Photochemistry of POMs

The photocatalytic process of polyoxoanions was first examined in detail by Papaconstantinou et al., 109 who subsequently demonstrated that reduced polyoxoanions

could be reoxydized by air, thereby completing a catalytic cycle. They suggested the following mechanism for the photooxidation of isopropanol by the polyoxoanion PW12O403-.110

hv
$$PW_{12}^{3-} + Me_{2}CHOH \xrightarrow{hv} PW_{12}^{4-} + Me_{2}COH + H^{+}$$

$$hv$$

$$PW_{12}^{4-} + Me_{2}COH \xrightarrow{hv} PW_{12}^{5-} + Me_{2}CO + H^{+}$$

$$PW_{12}^{5-} + PW_{12}^{3-} \xrightarrow{hv} 2PW_{12}^{4-}$$

$$2PW_{12}^{4-} + 1/2O_{2} + 2H^{+} \xrightarrow{hv} 2PW_{12}^{3-} + H_{2}O$$

$$PW_{12}^{5-} + 1/2O_{2} + 2H^{+} \xrightarrow{hv} PW_{12}^{3-} + H_{2}O$$

$$Me_2CHOH + 1/2O_2 \longrightarrow Me_2CO + H_2O$$

In the absence of O2, PW12<sup>4</sup>- can react with H+ according to

$$PW_{12}^{4-} + H^{+} ----- PW_{12}^{3-} + 1/2H_{2}$$

Therefore, the total reaction in the absence of O2 will be dehydrogenation:

hv 
$$R_1R_2CHOH \xrightarrow{} R_1R_2CO + H_2$$

Recently, Hill and Bouchard<sup>111</sup> reported that polyoxometalates (POMs) could be classified according to their photocatalytic reactivities:

Type I: Nb, Ta oxometalates, for example,  $M_6O_{19}^{8-}$  can not be photoreduced by any organic material even with u.v. light (< 290 nm)

Type II: These are readily photoreduced by a wide variety of organic substrates, but the reduced species are relatively and thermodynamically incapable of evolving hydrogen. Nearly all heteropoly and isopolymolybdates as well as polyvanadates are in this category. Thermal reoxidation of the reduced form of this type POM with O<sub>2</sub> is usually kinetically slow and sometimes thermodynamically unfavorable.

Type III: Nearly all heteropoly- and isopoly-tungstates undergo both facile photoreduction at 25°C by a variety of organic substrates, and the reduced forms undergo facile hydrogen evolution or air (O<sub>2</sub>) oxidation.

He suggested the following mechanism for the photooxidation of organic substrate by POMs.

Pn- + SH<sub>2</sub> ------ (P-H)<sup>n-</sup> + SH·

Pn- + SH<sub>2</sub> Pn-·SH<sub>2</sub>

hv

Pn-·SH<sub>2</sub> 
$$P^{(n+1)}$$
-·SH<sub>2</sub>+·

$$P^{(n+1)} \cdot SH_2^+ \cdot \cdots \rightarrow P^{(n+2)} + S + 2H^+$$
 $SH_2^+ \cdot \cdots \rightarrow HS \cdot + H^+$ 
 $P^{(n+2)} + S + H^+$ 
 $P^{(n+2)} + P^{(n+2)} \rightarrow P^{(n+1)} + S + H^+$ 

They emphasized that the two most likely mechanisms for the key substrate oxidation steps were radical hydrogen abstraction and electron transfer:

Substrate activation takes place in part by irradiation of the intermolecular charge transfer band of a POM-substrate complex, but also to some extent by a process most accurately characterized as hydrogen atom abstraction from the substrate by an intermolecular oxygen to metal charge transfer exited state of the POM.

The complex charge-transfer electron absorption manifold of some soluble metal oxide species, including heteropoly acids of Mo and W, is known to shift substantially to lower energy on going from water to organic solvents. These medium-induced bathochromic spectral shifts render some POM species highly photosenstive. Hill et al.  $^{112}$  reported the photoreactivity of 1,1,3,3,-tetramethyl urea (TMU)- $\alpha$ -H<sub>3</sub>PMo<sub>12</sub>O<sub>40</sub> the charge transfer complex. They observed that although the xmax was little perturbed on going from water ( $\lambda$ max = 310 nm) to TMU ( $\lambda$ max = 308 nm), the low energy absorption tail was quite shifted to the visible in TMU. The electronic interactions between the polyoxo moiety and the TMU moiety were responsible for the shifts in the

absorption spectrum. The shift were disrupted when the complex was dissolved in acetonitrile. Irradiation into this low energy absorption tail resulted in the oxidation of TMU and the production of the reduced POM 'heteropoly blue'.

Most recently, Fox et al.<sup>113</sup> reported a new mechanism for photooxidation of alcohols by POMs, which supports Hill's idea of POM-organic substrate complex formation. She claimed that the preassociation complex formation between alcohol and POM should precede photoactivation. She put forward several evidences for such a preassociation complex, including NMR and fluorescence life time measurements. This concept can explain the photoreactivity of POM-alcohol systems. The tightness of the preassociation complex is responsible for the reactivity. It depends on both alcohols and POMs. Less bulky alcohols favor the formation of such complexes and the following orders of reactivities are observed:

primary alcohol >> secondary alcohol >> tertiary alcohol

When V<sup>5+</sup> is substituted for W<sup>6+</sup> as in P<sub>2</sub>V<sub>5</sub>W<sub>15</sub>O<sub>62</sub>, the compound will bear three extra negative charges so that the electron density shifts toward the vanadium oxide terminal oxygen (-O<sub>4</sub>V $\equiv$ O<sup>-</sup>). The oppositely charged terminal oxygen will interfere electrostatically with the necessary complexation at the terminal VO site. Since negative charge is delocalized in the polyoxoanions by the bond alternation mechanism,<sup>56</sup> the tungsten sites should also exhibit diminished reactivity. The reactivity also depends on the heteroatom in the same type of POM. The order of decreasing reactivity is H > Fe >> Co, Si. The diminished reactivity has an electronic basis that allows for more efficient back electron transfer to the adsorbed oxidized species.

Papaconstantinou reported<sup>114</sup> that the rate of electron donation from alkyl radical to POM depended on the charge of the POMs and their reduction potentials. Increasing the negative charge on the complex and increasing the negative reduction potentials of the POM leads to a decrease in the electron transfer rate.

36

Fox finally proposed Scheme 1 for the photooxidation of 2-butanol by

PW<sub>12</sub>O<sub>40</sub>3-(1).113 She suggested that path a, the two electron, two proton route, was

more likely on the basis of several evidences. For example, the order of reactivity of

substrate paralleled that of substrate ionization potential.

C. **Adsorption onto Porous Materials** 

Since the pillared LDHs to be discussed in this work contain micropores, it is

appropriate to review briefly the method used to measure micropore volume and size.

The pore-types of porous materials are classified into three categories according

to their sizes:115

Macropores : widths > 500 Å

Mesopores : 20 Å < widths < 500 Å

Micropores: widths < 20 Å

Their adsorption mechanisms are different. The mesopore surface is the scene of

monomolecular and polymolecular adsorption of vapors, i.e., layer-by-layer coverage

ending in the volume filling of this pore type by the capillary condensation mechanism.

The specific surface areas of mesopore structures vary within the range 10 to 400 m<sup>2</sup>/g.

Adsorption on a microporous adsorbent involves not only the successive formation of

adsorption layers on the surface of the micropores, but also the filling of their adsorption

spaces. The concept of a surface area of microporous adsorbents loses its physical

significance.

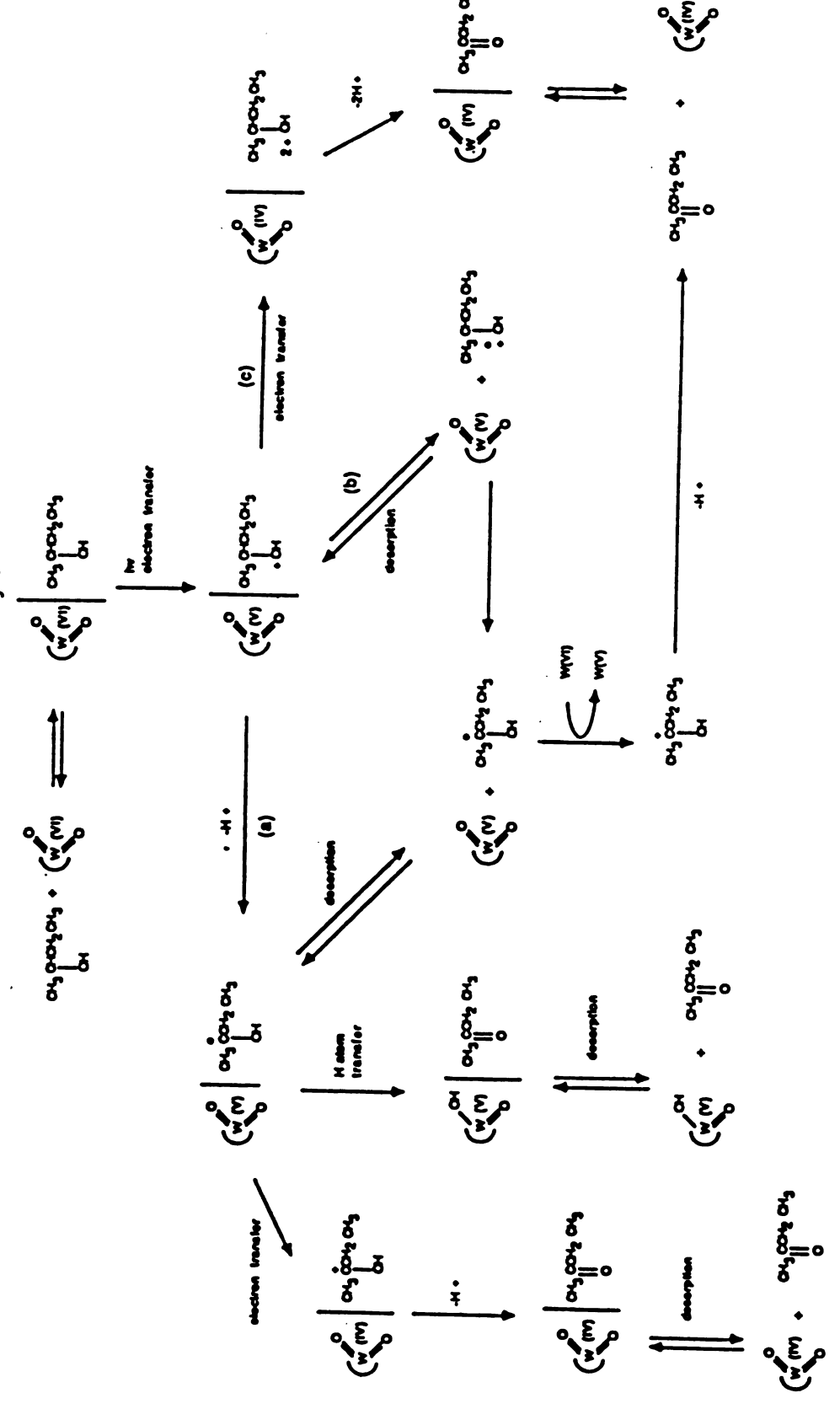
A characteristic feature of adsorption on microporous adsorbents is the substantial

increase in the adsorption energy and, consequently, the adsorption potentials in

micropores, as compared to the corresponding values for mesopores or nonporous

adsorbents of a similar chemical nature. An increase in adsorption energy in micropores





a) 1 is represented here as ( (VI) to clarity oxidation level at each stage of the sequence.

leads to a considerable increase in the value of vapor adsorption in the region of low equilibrium pressures.

There have been two equations extensively used to describe the adsorption of vapors onto microporous materials to determine the micropore volume. One of them is an empirical equation proposed by Dubinin and Radushkevich. 115 Their equation (D-R equation) is expressed as

$$a = a_0 \exp[-k(A/B)^2],$$

where  $a/a_0$  is a fraction of adsorption space filled at relative pressure  $p/p_0$ . A = RTln( $p/p_0$ ) and k and B are constants. The micropore volume ( $a_0$ ) is determined by plotting log a against  $log^2(p_0/p)$  (so called D-R plot). Marsh and Rand<sup>117</sup> demonstrated that this D-R plot extrapolation must be carried out with care, since, although the plot might show linear regions, it is very rarely linear over a wide pressure range. These deviations can be linearized by using a more generalized equation proposed by Dubinin and Astakhov.<sup>118</sup> It is expressed by an equation (D-A equation),

$$a = a_0 \exp[-(A/B)^n]$$

where  $a/a_0$  is the degree of pore filling, A is a differential molar work of adsorption, which is the negative value of Gibb's free energy of adsorption and is expressed by  $RTln(p_0/p)$ , B is a constant parameter which is a characteristic free energy of adsorption, and n is a constant. This D-A equation can also be expressed in another form,

$$\log[d(\log a)/dA] = \log(-nD) - (n-1)\log A$$

where D = 1/(2.303Bn)

By plotting log A against log[d(log a)/dA], n can be determined and then by plotting log a against A ao can be determined.

Brunauer et al. have proposed a method (so called MP method, micropore analysis method) for calculating, 119 on the basis of an experimental isotherm for vapor adsorption on a microporous adsorbent, the specific surface area, the pore volume and the volume distribution of the micropores according to their sizes. It is based on the so-called t-curve, which is a plot of the statistical thickness of the adsorbed film against p/p<sub>0</sub> for nonporous adsorbents. The statistical thickness t, which is the ordinate of the t-curve, is obtained by dividing the volume of nitrogen adsorbed as liquid at a given p/p<sub>0</sub> by the BET surface area. The isotherm of microporous material is converted into a V<sub>1</sub>(volume of liquid nitrogen adsorbed)-thickness plot (t-plot) in which the t values are read from a t-curve for standard nonporous material. By analyzing the t-curve, the surface area, pore volume and pore size distribution can be determined. If the t-plot is a linear, then the system consists of a nonporous material. If the t-plot is a non-linear, then the material is porous.

### CHAPTER II

#### **EXPERIMENTAL**

### A. Materials

Zinc nitrate hexahydrate, zinc chloride, aluminum nitrate nonahydrate, ammonium chloride, and sodium hydroxide were obtained from Fisher Scientific Company. Aluminum chloride hexahydrate, nitric acid, acetic acid, sodium molybdate dihydrate, ammonium acetate, and methanol were purchased from Mallinckrodt. Cobalt acetate tetrahydrate, tungstic acid (H2WO4), vanadyl sulfate trihydrate, and gold label iso-propyl alcohol were purchased from Aldrich Chemical Company. Ammonium hydroxide, potassium chloride, sodium metasilicate nonahydrate (Na2SiO3), and potassium bisulfite from J.T. Baker Chemical Company were used. Boric acid and hydrochloric acid were obtained from Columbus Chemical Company. Sodium metavanadate was purchased from Alfa-Products-Ventron. Sodium tungstate dihydrate was a gift from GTE Sylvania Company.

# B. Preparation of LDH-Cl and LDH-NO3

Pristine layered double hydroxides of the type Zn<sub>2</sub>Al(OH)<sub>6</sub>-Cl or -NO<sub>3</sub> (LDH-NO<sub>3</sub>, or -Cl) were prepared by a modification of the induced hydrolysis method of Taylor.<sup>28</sup> Deionized water, pre-boiled for 2 hours under N<sub>2</sub>, was used for the preparation of all solution. All manipulations were carried out under a N<sub>2</sub> atmosphere to avoid contact with CO<sub>2</sub>.

To 200 ml of 0.1M Al<sup>3+</sup> solution containing the desired anion in a 2-liter three neck round bottom flask was added 1M NaOH solution from a dropping funnel with vigorous stirring. The delivery of the NaOH solution was completed at pH = 7. The white slurry was stirred for one hour. Then, 200 ml of 0.3M Zn<sup>2+</sup> solution was added dropwise from a dropping funnel. As the Zn<sup>2+</sup> solution was added to the slurry, the pH of the reaction mixture dropped. The pH of the reaction mixture was adjusted to 6.2 by adding NaOH during the delivery of the Zn<sup>2+</sup> solution. After the complete delivery of the Zn<sup>2+</sup> solution, the slurry was boiled for one week under a N<sub>2</sub> atmosphere. The product was washed several times with water by centrifugation. After the final washing, the stock slurry was prepared by redispersing the product well into 800 ml of water. Even this latter operation was carried out under nitrogen.

An oriented film sample of the Zn<sub>2</sub>Al LDH was prepared on a glass slide for x-ray examination. About 50 mg of solid product was dissolved into 100 ml of 20% (v/v) HNO<sub>3</sub> for elemental analysis by atomic absorption.

## C. Preparation of Guest Anions POMs

All the guest anions were prepared according to literature methods. The details of syntheses are summarized below.

β-Na<sub>8</sub>HPW<sub>9</sub>O<sub>34</sub>·24H<sub>2</sub>O<sup>120</sup>: Sodium tungstate Na<sub>2</sub>WO<sub>4</sub>·2H<sub>2</sub>O (120 g, 0.36 mole) was dissolved in water (150 ml). Orthophosphoric acid, H<sub>3</sub>PO<sub>4</sub> (3 ml, 14.7M), and concentrated acetic acid (22 ml, 17.4M) were successively added to the solution. The desired white salt precipitated.

 $\alpha$ -K<sub>7</sub>PW<sub>9</sub>Mo<sub>2</sub>O<sub>39</sub>·nH<sub>2</sub>O<sup>120</sup> :  $\beta$ -Na<sub>8</sub>HPW<sub>9</sub>O<sub>34</sub>·24H<sub>2</sub>O (11 g, 3.9 mmole) was dissolved in an aqueous mixture of sodium molybdate, Na<sub>2</sub>MoO<sub>4</sub>·2H<sub>2</sub>O (20 ml, 1M) and HCl (16 ml, 1M). Then HCl (about 12 ml, 1M) was added dropwise until the pH was between 6 and 6.5. The desired product was precipitated by addition of solid KCl.

K7BCo(II)W<sub>11</sub>O<sub>39</sub>·nH<sub>2</sub>O<sup>121</sup>: Na<sub>2</sub>WO<sub>4</sub>·2H<sub>2</sub>O (36.3 g, 0.11 mole) was dissolved in 150 ml water and the pH adjusted to 6.3 with acetic acid. H<sub>3</sub>BO<sub>3</sub> (2 - 3 g, 0.03 - 0.05 mole) was added and the mixture was heated to 80 - 90°C. A solution containing 0.01 mole Co(II) was added dropwise, followed by the addition of KCl (15 - 20 g). Recrystallization from hot 2% KCl resulted in the formation of the desired product.

K7BCu(II)W11O390-nH2O82: This compound was prepared in exactly the same way as K7BCoW11O40H2, except that Cu(II) replaced Co(II). Fibrous, clear green crystals separated from the hot solution, followed on cooling by the separation of pale green cubic crystals.

α-K<sub>8</sub>SiW<sub>11</sub>O<sub>39</sub>·12H<sub>2</sub>O<sup>122</sup>: Na<sub>2</sub>WO<sub>4</sub>·2H<sub>2</sub>O (182 g, 0.55 mole) and 14.7 g of metasilicate, NaSiO<sub>3</sub>·9H<sub>2</sub>O were dissolved in 300 ml of cold water, HCl (195 ml, 4M) was added slowly, then the solution was boiled for an hour. The potassium salt was precipitated by addition of 75 g of solid KCl.

α-1,2,3,-K<sub>6</sub>HSiV<sub>3</sub>W<sub>9</sub>O<sub>40</sub><sup>123</sup>: NaVO<sub>3</sub> (5.5 g, 45 mmole) and 40 g of α-Na<sub>10</sub>SiW<sub>9</sub>O<sub>34</sub>·12H<sub>2</sub>O (15 mmole)<sup>78</sup> were mixed as dry powders and added to 400 ml of water at room temperature. The solution was stirred vigorously and 6M HCl was added dropwise to bring the pH to 1.5. A clear wine-colored solution developed. Solid KCl (50 g) was stirred into the solution to leave a clear solution. Methanol (1.5 L) was then added and the solution was allowed to age 60 hours, after which an orange precipitate was collected. The solid was dissolved in water at 65°C and filtered. The filtrate was cooled to 0°C to form 2.3 g of an orange-brown powdered product. Purity was checked by <sup>51</sup>V NMR.

K<sub>7</sub>SiFe(III)(SO<sub>3</sub>)W<sub>11</sub>O<sub>39</sub>·9H<sub>2</sub>O<sup>124</sup>: To a warm (60°C) solution of K<sub>5</sub>SiFe(III)(H<sub>2</sub>O)W<sub>11</sub>O<sub>39</sub>·14H<sub>2</sub>O<sup>124</sup> (10.0 g, 3.1 mmole) in 100 ml of water was added KHSO<sub>3</sub> (15.0 g, 0.125 mole). The solution was stirred at 60°C for 10 minutes and then cooled rapidly to 2°C. The sought salt separated upon adding 10 ml of methanol to the cold solution. It was not recrystallized.

(NH4)8Co2W12O42·20H2O126: Na2WO4·2H2O (180 g, 0.55 mole) was dissolved in 400 ml of water. The pH of the solution was adjusted to a value between 6.5 and 7.5 by addition of glacial acetic acid. A separate solution was prepared by dissolving cobaltous acetate tetrahydrate (24.9 g, 0.1 mole) in 125 ml of warm water to which a few drops of glacial acetic acid had been added. The sodium tungstate solution was brought to boil and the cobaltous acetate solution was added to it slowly with stirring. After all of the cobaltous acetate had been added, the solution was boiled for 10 minutes and then filtered hot to remove traces of insoluble matter. The solution was heated to boiling again and 135 g of ammonium acetate dissolved in a small amount of boiling water was added to it. Upon cooling, an 85% yield of dark emerald green cubic crystals separated. The product was recrystallized from hot acetic acid (0.5 ml of glacial acetic acid per 100 ml of water). Five recrystallizations gave a product which dissolved without leaving a solid residue.

(NH4)6H2W12O40-14H2O<sup>127</sup>: A slurry of tungstic acid, H2WO4 (90.8 g, 0.36 mole) in 240 ml of deionized water was stirred and heated to 80 - 90°C. While maintaining temperature, 10.5 ml of NH4OH (28%) was added during a period of 1 hour. Digestion was continued for 2 hours, and the mother liquor was separated from the ammonium metatungstate solution by filtration.

 $Na_{10}H_2W_{12}O_{42}\cdot 20H_2O^{128}$ : A solution of  $Na_2WO_4\cdot 2H_2O$  (50 g, 0.15 mole) and Al(NO<sub>3</sub>)<sub>3</sub>·9H<sub>2</sub>O (5.16 g, 14 mmole) in 20 ml water was adjusted to pH = 7.0 with 6M HNO<sub>3</sub>. A clear solution was formed after 10 - 15 minutes at the boiling temperature. The solution was filterd and evaporated on a steam bath to obtain crystals. The product was twice recrystallized and dried in air.

(NH4)14NaP5W30O110-31H2O<sup>129</sup>: Na<sub>2</sub>WO<sub>4</sub>·2H<sub>2</sub>O (250 g, 0.76 mole) was dissolved in 300 ml of boiling water. 85% H<sub>3</sub>PO<sub>4</sub> (400 g) was slowly added to it. The solution was transferred to a Pyrex glass-lined high pressure reactor, and heated to 120°C for 5 hours. After cooling, the ammonium salt was precipitated by the addition, with stirring, of 250 g of solid NH<sub>4</sub>Cl. The precipitate was separated by filtration, then redissolved into 400-500 ml of warm water (60°C). The salt was reprecipitated by addition of 200 g of solid NH<sub>4</sub>Cl, then redissolved into 700 ml of water. In general, in this step, a white insoluble deposit which formed was filtered out. The clear filtrate was then slowly cooled. The white crystals which formed first were the desired product.

K7BV(V)W11O40-7H2O130: The pH of a solution containing Na2WO4-2H2O (36.6 g, 0.11 mole) was adjusted to 6.3 with acetic acid and boric acid (2.47 g, 0.04 mole) was added. The solution was heated to 80-90°C and vanadyl(IV)sulfate trihydrate (2.17 g, 0.01 mole) was added, whereupon the color changed to dark red-brown. Solid KCl was added to the hot solution and the product was crystallized upon cooling. The salt was recrystallized from a 0.5M potassium acetate-acetic acid buffer (pH = 5).

(K,H)9[PV14O42]·nH2O<sup>131</sup>: NaVO<sub>3</sub> (4.5 g, 37 mmole) was dissolved in 250 ml of hot water and 6.2 ml of 1.5M H<sub>3</sub>PO<sub>4</sub> was added. The pH of the deep red solution was adjusted to 2-3 by 3M HNO<sub>3</sub>. The solution was warmed to 50°C, and an aqueous

solution at 50°C containing 10 g KCl was added slowly. After stirring, the solution was left standing overnight at room temperature to form fine black crystals.

β-K<sub>6</sub>HSiW<sub>9</sub>V<sub>3</sub>O<sub>40</sub>·3H<sub>2</sub>O<sup>132</sup>: Sodium metavanadate, NaVO<sub>3</sub> (6.4 g, 52 mmole) was dissolved in 900 ml of hot water and cooled to room temperature. To this colorless, homogeneous solution was added 8.4 ml (101 mmole) of 12M HCl. This resulted in a pale yellow, homogeneous solution (pH about 1.5). This was followed by the addition of solid A-β-Na<sub>9</sub>HSiW<sub>9</sub>O<sub>34</sub>·23H<sub>2</sub>O (48 g, 16.9 mmole) to the vigorously stirred solution. This solution rapidly developed a deep, cherry-red color as the SiW<sub>9</sub>O<sub>34</sub>·10- dissolved. The resulting homogeneous solution was reacdified with 2.8 ml (33.6 mmole) of 12M HCl, bringing the total H+ added to 134.6 mmole (8.0 equiv.). Next, solid KCl (60 g, 0.8 mole) was added and the solution was stirred until homogeneous. Methanol was added until the total volume was approximately 2 L. The resulting precipitate was separated by filtration and recrystallized overnight from a hot, saturated water/methanol solution at pH = 1.5. Filtration followed by air drying at 60°C yielded 37 g of the product. The solution 51V NMR contained a single peak at -570 ppm (1 g/4 ml of D<sub>2</sub>O<sub>2</sub> pH = 2.3).

 $\alpha$ -1,2,3,-K<sub>6</sub>PV<sub>3</sub>W<sub>9</sub>O<sub>40</sub>·4H<sub>2</sub>O<sup>123</sup>: NaVO<sub>3</sub> (6.1 g, 50 mmole) was added to 200 ml of 1.0M sodium acetate/acetic acid buffered at pH = 4.8. Na<sub>8</sub>HPW<sub>9</sub>O<sub>34</sub> (40 g, 15 mmole) was added and the solution was stirred at 25°C for 48 hours. The potassium salt was precipitated by the addition of 30 g of solid KCl. After the solution had been stirred for 30 min., methanol (500 ml) was added to produce a precipitate which was filtered. The product was examined by NMR. NMR (31P) -13.41 ppm. NMR(51V) -566.1 ppm at pH = 1.8, 30°C.

K8BW11O39-nH2O67: A mixture of Na2WO4·2H2O (36.3 g, 0.11 mole) and H3BO3 (3 g, 0.05 mole) was acidified by acetic acid to pH = 6.5. The potassium salt was

precipitated by addition of solid KCl. The product was filtered, washed with 100 ml of 50:50 water/methanol solution, and air dried.

β1-Na<sub>9</sub>SiW<sub>11</sub>O<sub>39</sub>·nH<sub>2</sub>O<sup>122</sup>: A suspension of Na<sub>9</sub>HSiW<sub>9</sub>O<sub>34</sub>·23H<sub>2</sub>O (5.8 g, 2.04 mmole) was added to 40 ml of 0.1M Na<sub>2</sub>WO<sub>4</sub> solution. Slow addition of 5 ml of 1M HCl reduced the solution pH to about 6.0. This was then followed by addition of 50 ml ethanol. The oily portion was decanted and the desired product was precipitated as a white powder by addition of ethanol.

β2-K8SiW<sub>11</sub>O<sub>39</sub>·12H<sub>2</sub>O<sup>122</sup>: Na<sub>2</sub>WO<sub>4</sub>·2H<sub>2</sub>O (182 g, 0.55 mole) was dissolved in 300 ml of water. The solution was cooled to 5°C and 165 ml of 4M HCl was added slowly. Then a solution containing 14.7 g of Na<sub>2</sub>SiO<sub>3</sub>·9H<sub>2</sub>O dissolved in 100 ml of water was added. The pH of solution was adjusted to 5.5 by adding 4M HCl. This value was maintained for about 1 hour (about 30 ml acid was needed). The potassium salt, contaminated with B-paratungstate, was precipitated by adding solid KCl. The precipitate was redissolved into water in an amount equal to 10 times the weight of salt. The insoluble salt was discarded and solid KCl was added to precipitate the desired product. The precipitate was filtered and washed with dilute KCl solution.

 $\beta_3$ -K<sub>8</sub>SiW<sub>11</sub>O<sub>39</sub>·12H<sub>2</sub>O<sup>122</sup>: This salt was obtained by the isomerization of  $\beta_2$ -SiW<sub>11</sub>O<sub>39</sub>·12H<sub>2</sub>O.  $\beta_2$ -K<sub>8</sub>SiW<sub>11</sub>O<sub>39</sub>·12H<sub>2</sub>O (30 g, 9.4 mmole) was dissolved into 300 ml of water. The pH of the solution was adjusted to 5.0 by adding HCl. After allowing the solution to age 4.5 hour at room temperature, the product, which was contaminated with  $\alpha$ -SiW<sub>11</sub>, was placed into water. The insoluble  $\alpha$ -isomer was discarded. The desired product was precipitated by adding solid KCl to the clear solution. The solution was filtered and washed with dilute KCl solution.

## D. Synthesis of LDH-POM's

The general method employed for the preparation of

Zn<sub>1-x</sub>Al(OH)<sub>2</sub> (=LDH)-POM was an ion exchange reaction. The pristine LDH-NO<sub>3</sub> was used as a starting material. The extent of the ion-exchange reaction was checked by infrared spectroscopy, which provided the characteristic bands of NO<sub>3</sub> at 1380 cm<sup>-1</sup> in case of incomplete reaction. All of the manipulations were carried out under a nitrogen atmosphere to prevent carbonate contamination.

LDH-BW11O39: A 50 ml (5.03 mequiv.) portion of boiling LDH-NO3 suspension was added dropwise to 100 ml (8.56 mequiv.) of K9BW11O39 solution at pH = 7.2. The pH of the reaction mixture was maintained at 6.2 by addition of dilute HNO3. After an hour of stirring at room temperature, the product was treated as usual way, in which the product was washed with deionized water by several centrifugations. The product was examined by ir spectroscopy and XRD.

LDH-PMo2W9O39: This was prepared in the same way as LDH-BW11O39 except that 10.6 milliequivalents of PMo2W9O39 were used.

**LDH-BV(IV)W11O40**: A 50 ml (5.03 mequiv.) portion of LDH-NO3 suspension was diluted to 110 ml and the pH was brought to 6 by addition of dilute HNO3. The boiling LDH-NO3 suspension was added dropwise to 50 ml (7.5 mequiv.) of K7BVW11O40 solution at pH = 5.0. The pH of the reaction mixture after 90 minutes of stirring at room temperature was adjusted to 6.0 by addition of dilute HNO3. The product was treated as above.

LDH-NaP5W30O110: A boiling 100 ml (2.6 mequiv.) portion of LDH-NO3 suspension at pH = 6.0 was added dropwise to 200 ml (4.08 mequiv.) of (NH4)14NaP5W30O110

solution. The pH of the reaction mixture after two hours of stirring was adjusted to 6.2 by adding dilute HNO3 during the reaction. The product was treated as above.

LDH-PV14O42: A 100 ml (2.6 mequiv.) portion of boiling LDH-NO3 suspension at pH = 6.0 was added dropwise to 100 ml (2.6 mequiv.) of (NH4)9PV14O42 solution at pH = 4.0. After an hour of stirring at room temperature, the product was treated as above.

**LDH-PW9O34**: A 100 ml solution (7 mequiv.) of  $\beta$ -NagHPW9O34 at pH = 7.6 was added dropwise to 60 ml (4.1 mequiv.) of LDH-NO3 suspension at room temperature. After complete delivery of PW9O34 solution, the pH of reaction mixture was 7.1. Dilute HNO3 was then added to the reaction mixture to bring its pH to 6. The final pH of the reaction mixture was 5.9. The product was treated as in the other cases.

LDH-SiFe(III)(SO<sub>3</sub>)W<sub>11</sub>O<sub>40</sub>: A 100 ml (3.55 mequiv.) of Fe(III)(SO<sub>3</sub>)W<sub>11</sub>O<sub>39</sub> solution at pH = 7.5 was added to 50 ml (2.51 mequiv.) of LDH-NO<sub>3</sub> suspension at room temperature. After 20 minutes of stirring, the pH of the reaction mixture was brought to 6.1 by adding dilute HNO<sub>3</sub>. The final pH of the reaction mixture after an additional 35 minutes of stirring was 6.2. The product was treated in the usual way.

LDH-α-SiV<sub>3</sub>W<sub>9</sub>O<sub>40</sub>: A boiling 150 ml (5 mequiv.) portion of LDH-NO<sub>3</sub> suspension at pH = 6.0 was added dropwise to 100 ml (7.1 mequiv.) of K<sub>6</sub>HSiV<sub>3</sub>W<sub>9</sub>O<sub>40</sub> solution at pH = 3.0. After an hour stirring, the product was washed twice with deionized water by centrifugation. The product was redispersed into 50 ml of water and then was added dropwise to 20 ml of solution containing 0.53 milliequivalents of K<sub>6</sub>HSiV<sub>3</sub>W<sub>9</sub>O<sub>40</sub> at pH = 3.0. After an hour stirring, the pH of reaction mixture was 5.7. The product was treated as usual.

LDH- $H_2W_{12}O_{40}$ : A boiling 80 ml portion (8.04 mequiv.) of LDH- $NO_3$  suspensiom at pH = 6.2 was added dropwise to 160 ml (10 mequiv.) of (NH4)6H2W12O40 solution at pH = 4.6. After 90 minutes of stirring, the product was washed twice with water by centrifugation. The product was redispersed into 50 ml of water and was added dropwise to 70 ml (4.5 mequiv.) of (NH4)6H2W12O40 solution at pH = 4.2. After an hour of stirring the product was treated as usual.

**LDH-BCO(II)W11O40**: A boiling 50 ml portion (5 mequiv.) of LDH-NO3 suspension at pH = 6.0 was added dropwise to 100 ml (7.5 mequiv.) of K7BCoW11O40 solution at pH = 6.0. After 90 minutes stirring, the pH of the reaction mixture was 6.7. The product was washed twice with water by centrifugation. The product was redispersed into 50 ml of water and was added to 100 ml (3.16 mequiv.) of BCoW11O40 solution at pH = 6.2. After an hour stirring, the product was treated as usual.

LDH-SiW11O39: A boiling 100 ml (5 mequiv.) portion of LDH-NO3 suspension at pH = 6.2 was added dropwise to 100 ml (7.6 mequiv.) of K8SiW11O39 solution at pH = 6.3. The pH of the reaction mixture was monitored by adding dilute HNO3 during the reaction so that after 90 minutes of stirring, the pH was 6. The product was washed twice with water by centrifugation. The product was redispersed into 50 ml of boiling water and was added dropwise to 80 ml (7 mequiv.) of SiW11O39 solution at pH = 6.3. The reaction condition was monitored by the addition of dilute HNO3 so that after an hour of stirring, the pH of the reaction mixture was 6.0. The final product was treated as usual.

LDH-BCu(II)W11O39: An 80 ml (8 mequiv) portion of boiling LDH-NO3 suspension at pH = 6.1 was added dropwise to 160 ml (10 mequiv.) of K3Na4BCuW11O40H2 solution at pH = 5.5. After 80 minutes of stirring, the pH of the reaction mixture was 5.5. The product was washed twice with water by centrifugation. It was redispersed into 50

ml of boiling water and was added dropwise to an 80 ml (4.3 mequiv.) solution of  $BCuW_{11}O_{39}$  at pH = 5.5. After another 80 minutes of stirring, the pH was 5.8. The product was treated as usual.

LDH-H2W12O42: A 50 ml (5 mequiv.) portion of boiling LDH-NO3 suspension at pH = 6.3 was added dropwise to 150 ml (7.6 mequiv.) of Na10H2W12O42 solution at pH = 6.2. After complete delivery of the LDH-NO3 slurry to the POM solution, the pH of the reaction mixture was brought to 6.0 by addition of dilute HNO3. After an hour stirring, the product was washed twice with water by centrifugation. The product was redispersed into 50 ml of water and was again added to 100 ml (3.9 mequiv.) of H2W12O42 solution at pH = 6.2. After 80 minutes of stirring, the pH of the reaction mixture was adjusted to 6.1 by addition of dilute HNO3 during stirring. The product was washed twice with water by centrifugation. The product was redispersed into 100 ml of water and was added dropwise to 150 ml (1.1 mequiv.) of H2W12O42 solution at pH = 6.2. The pH of the reaction mixture was adjusted to 5.9 by addition of dilute HNO3 with stirring. Finally, the slurry was treated as usual.

Reaction of LDH-NO3 with  $\beta$ -SiV<sub>3</sub>W<sub>9</sub>O<sub>40</sub>: A 5 ml of (0.5 mequiv.) portion of boiling LDH-NO3 slurry at pH = 6.1 was added dropwise to 20 ml (0.75 mequiv.) of  $\beta$ -K6HSiV<sub>3</sub>W<sub>9</sub>O<sub>40</sub> solution at pH = 2.3. After 80 minutes of stirring, the product was washed throughly with water by centrifugation. The exchange reaction was incomplete, as judged by XRD. Thus, the product was redispersed into 20 ml of water and was added again dropwise to 20 ml of the solution containing 0.75 milliequivalents of  $\beta$ -SiV<sub>3</sub>W<sub>9</sub>O<sub>40</sub> at pH = 3.6. After an hour stirring, the product was treated as usual.

Reaction of LDH-NO3 with  $\alpha$ -PV<sub>3</sub>W<sub>9</sub>O<sub>40</sub><sup>6-</sup>: A 10 ml (0.5 mequiv.) portion boiling LDH-NO3 suspension at pH = 6.1 was added dropwise to 20 ml (1.73 mequiv.) of  $\alpha$ -

 $K_6PV_3W_9O_{40}$  solution at pH = 3.6. After 75 minutes of stirring, the pH of the reaction mixture was 5.3. The excess of PV<sub>3</sub>W<sub>9</sub>O<sub>40</sub> was washed throughly with water by centrifugation. The reaction was incomplete, as verified by XRD. The incompletely exchanged product was redispersed into 20 ml of boiling water and was added dropwise to 20 ml of solution containing 1.3 milliequivalents of PV<sub>3</sub>W<sub>9</sub>O<sub>40</sub> at pH = 3.4. After an hour of stirring at room temperature, the product was routinely treated as usual.

Reaction of LDH-NO3 with BV(V)W11O40<sup>6-</sup>: A 15 ml (0.5 mequiv.) portion of boiling LDH-NO3 suspension at pH = 6 was added dropwise to 20 ml (0.75 mequiv) of K6BV(V)W11O40 solution at pH = 5. After an hour, the pH of the mixture was 5.6. The product was treated as above. The reaction was incomplete, as verified by XRD and ir. The incompletely exchanged product was redispersed into boiling 20 ml of water and was added dropwise to 20 ml of solution containing 1.2 milliequivalents of BV(V)W11O40 at pH = 5.3. After an hour of stirring, the excess BVW11O40 was throughly washed out with water by centrifugation. The product was examined by XRD, ir and 51V NMR. A sample for NMR experiment was prepared by dissolving the product in LiClO4 solution at pH = 2.0

Reaction of LDH-NO3 with BCo(III)W11O396-: A boiling 20 ml suspension containing 0.5 mequiv. of LDH-NO3 was added to a 20 ml solution containing 0.75 milliequivalents of  $K_6BCo(III)W11O39$  at pH = 5.5 and at ambient temperature. After 90 minutes of stirring, the product was washed in a routine way. The excess of BCo(III)W11O39 was contained in the supernatant. The pH of the reaction mixture at the end of the reaction was 6.1. The product was examined by XRD and ir spectroscopy.

Reaction of LDH-NO3 with  $\beta_1$ -Na<sub>8</sub>SiW<sub>11</sub>O<sub>39</sub>: A boiling 20 ml (0.39 mequiv.) portion of LDH-NO3 suspension at pH = 6.2 was added to 20 ml (0.61 mequiv.) of

 $SiW_{11}O_{39}$  solution at pH = 6.4. After an hour of stirring, the reaction product was treated as described previously.

Reaction of LDH-NO3 with  $\beta_2$ -K<sub>8</sub>SiW<sub>11</sub>O<sub>39</sub>: A boiling 20 ml (0.5 mequiv.) portion of LDH-NO3 suspension was added dropwise to SiW<sub>11</sub>O<sub>39</sub> solution containing 0.75 milliequivalents at pH = 7.6. After 30 minutes of stirring, the pH of the reaction mixture was lowered to 6.1 by addition of dilute HNO3. After an additional 15 minutes of stirring, the product was washed with water by centrifugation. The product was redispersed into 20 ml of water and added to a 20 ml solution containing 0.63 milliequivalents of SiW<sub>11</sub>O<sub>39</sub> at pH = 6.4. After 35 minutes of stirring, the pH of the reaction mixture was adjusted to 6 by adding dilute HNO3. After 50 minutes of stirring, the final product was collected and washed in the usual way.

Reaction of LDH-NO3 with  $\beta_3$ -K<sub>8</sub>SiW<sub>11</sub>O<sub>39</sub>: This reaction was carried out exactly in the same way as described for the  $\beta_1$ -SiW<sub>11</sub>O<sub>39</sub> intercalate. During reaction, the pH was adjusted to 6.1 by adding dilute HNO3.

## E. Physical Measurements

# 1. X-Ray Powder Diffraction

X-ray diffractograms were recorded using a Philips model APD 3720 diffractometer. Ni-filtered Cu  $K_{\alpha}$  radiation was used as the X-ray source. Typically, thin film sample was prepared by dropping a water slurry onto either a glass slide or a quartz sample holder, followed by air drying.

For the swelling experiments, samples were prepared on ceramic plates and kept wet to maintain the spacing characteristic of the most product.

## 2. Gas Adsorption Measurement

 $N_2$  gas adsorption at 77K was measured using either a Quantasorb Jr. Surface Area Analyzer or a Cahn electrical balance. Samples were outgassed under vacuum at the desired temperature, usually in the range  $120^{\circ}$ C to  $135^{\circ}$ C. He and  $N_2$  gas were passed through a trap maintained at dry ice temperature. Measurement performed in the Cahn balance provided data points at low  $p/p_0$ , which are useful especially for the micropore analysis of the material. The BET  $N_2$  surface areas were determined by the multiple point method in a  $p/p_0$  region where the data conformed to a linear BET plot.

## 3. Thermal Stability Study of LDH-POMs

Oriented film samples supported on either a glass slide or a quartz plate were heated at a given temperature for 5 hours in a Fisher Model 497 Isotemp Programmable Ashing Furnace in the open air. The heated samples were examined by X-ray diffraction and FTIR spectroscopy. The rehydration properties were studied by soaking the heated samples in water for one day, followed by air drying. Then, these rehydrated samples were reexamined by X-ray powder diffraction. Fourier transform infrared spectra of all samples were taken using an IBM model IR 40s. All sample were prepared by the standard KBr technique.

Differential scanning calorimetry and thermal gravimetric analysis were carried out on a Dupont 9900 thermal analyzer under N<sub>2</sub> purge. Temperature was ramped at a rate of 5°C/min from room temperature to 500°C.

# 4. Nuclear Magnetic Resonance Studies

A Bruker WH-180 spectrometer was used to obtain <sup>29</sup>Si, <sup>51</sup>V, <sup>31</sup>P, <sup>11</sup>B, and <sup>23</sup>Na at 35.77 MHz, 47.32 MHz, 72.88 MHz, 57.77 MHz, and 47.62 MHz, respectively. The WH-180 spectrometer was equipped with Nicolet NTCFT-180 computer software and a Doty solid state probe operated at the magic angle of 55°44'. In the case of solid samples, the sample spinning frequency was between 3.5 KHz and 5 KHz. TMS, VOCl3, 85% H3PO4, saturated H3BO3, and NaCl were used as references for Si, V, P, B, and

Na, respectively. The Na chemical shift of NaCl was taken to be 7.7 ppm relative to the infinitely dilute aqueous NaCl solution. The chemical shifts of other references were taken to be 0.0 ppm. The solution sample derived from LDH-SiV3W9O40 were prepared by dissolving the intercalate in acidic (pH = 1.5 - 2) LiClO4 aqueous solution.

# F. Photocatalytic Reaction

The pre-dispersed LDH-POM in H<sub>2</sub>O was transferred to a 45 ml of centrifuge tube and washed several times with isopropanol by centrifugation. The sample was redispersed in isopropanol and transferred to one of the chambers of an H-type photoreactor. The LDH-POM slurry was outgassed by pumping and refilled with Ar or O<sub>2</sub>. Photolysis was carried out with an Oriel 1Kw Hg(Xe) ozone-free lamp equipped with a 295 nm long pass filter and a water filter. The radiation was focused on the photoreactor by use of a secondary focussing lens. After 24 hours irradiation, the liquid reactant and products were separated from the solid LDH-POM by dipping the empty chamber of the H-type reactor into liquid nitrogen. After completely transferring the liquid, it was analyzed using a Varian aerograph model 920 gas chromatograph equipped with a 3 m carbopack B/3% sp-1500 column purchased from Supelco. Helium was used as a carrier gas with a flow rate of 0.25 ml/sec. The column-, detector- and injection-temperatures were 90°C, 180°C and 90°C, respectively. A thermocouple detector was used at a filament current of 200 mA. The solid LDH-POM used in the reaction was weighed after being dried under vacuum.

# G. Elemental analysis

Zinc and aluminum analyses of LDH-NO3 or -Cl were done at the inorganic chemistry laboratory of the Department of Toxicology at Michigan State University. The analysis of the other samples was done by Galbraith Laboratories

# H. Transmission Electron Microscopy (TEM)

Specimens for TEM were obtained by dropping a dilute slurry of the sample in water on copper grids. TEM was carried out a Jeol 100cx at the Center for Electron Optics at Michigan State University.

#### **CHAPTER III**

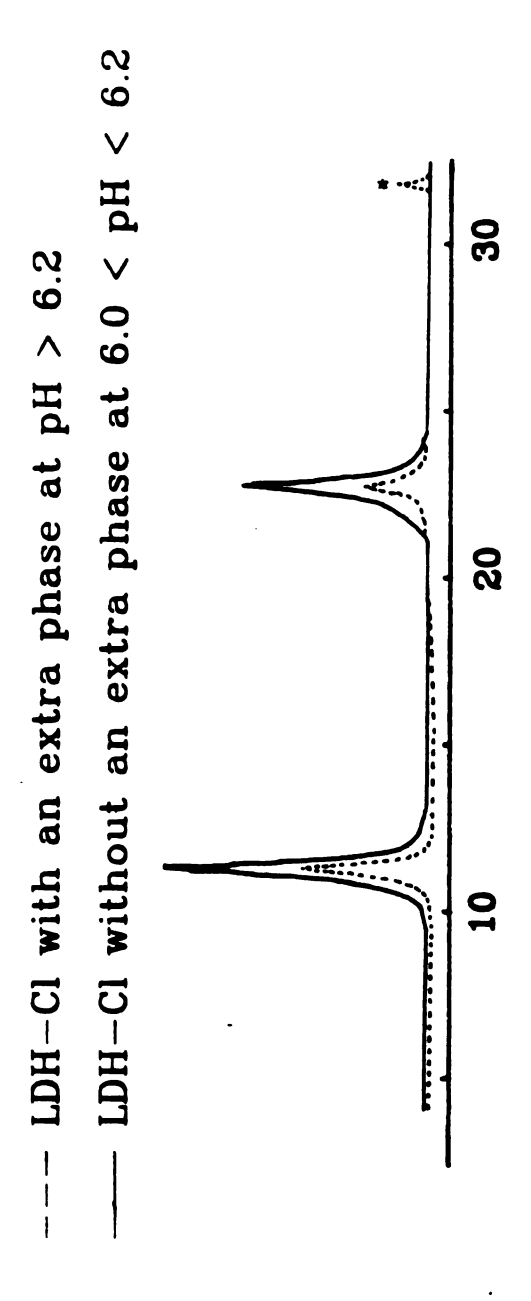
#### **RESULT AND DISCUSSION**

#### A. Synthesis of LDH-Cl, NO<sub>3</sub>

When a solution containing  $Zn^{2+}$  and  $Al^{3+}$  and  $Cl^{-}$  or  $NO3^{-}$  counter anions with Zn/Al = 3 is precipitated at pH = 10 by the addition of  $OH^{-}$ , a LDH phase  $Zn_{2}Al(OH)_{6}A$  and a secondary phase are formed upon hydrothermal treatment of the gel. The second phase is either  $Zn_{5}(OH)_{8}Cl_{2}$  or  $Zn_{5}(OH)_{8}(NO_{3})_{2}$ , as verified by their XRD patterns presented in Fig. 9. The ratio Zn/Al in the mixed solid product was 3. When the mixed product was redispersed in water and  $H^{+}$  was added to bring the pH to about 6, the second phase disappeared. That is, the second phase dissolved at this acidic condition. The excess  $Zn^{2+}$  resulting from the dissolution of second phase could be reprecipitated by adding  $OH^{-}$ .

When a solution containing  $Zn^2+$ ,  $Al^3+$  and Cl- with Zn/Al=3 was precipitated at pH = 6, no secondary phase was formed. The Zn/Al ratio in the solid precipitate was 2.

When a solution containing Zn/Al = 5 was precipitated at pH = 10 the second phase was observed again. Even a solution containing Zn/Al = 2 upon precipitation at pH = 10 exhibited the second phase. Therefore, the second phase is not due to excess Zn, but due to the coprecipitation of  $Zn_5(OH)_8A_2$  at a too high pH.



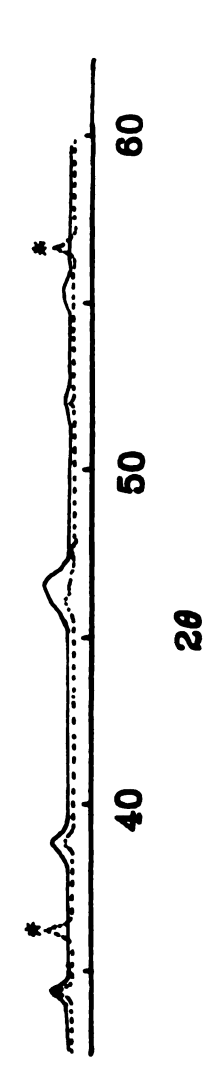


Fig. 9. XRD pattern of LDH-Cl prepared at different pH.

#### **B** Synthesis of LDH-POMs

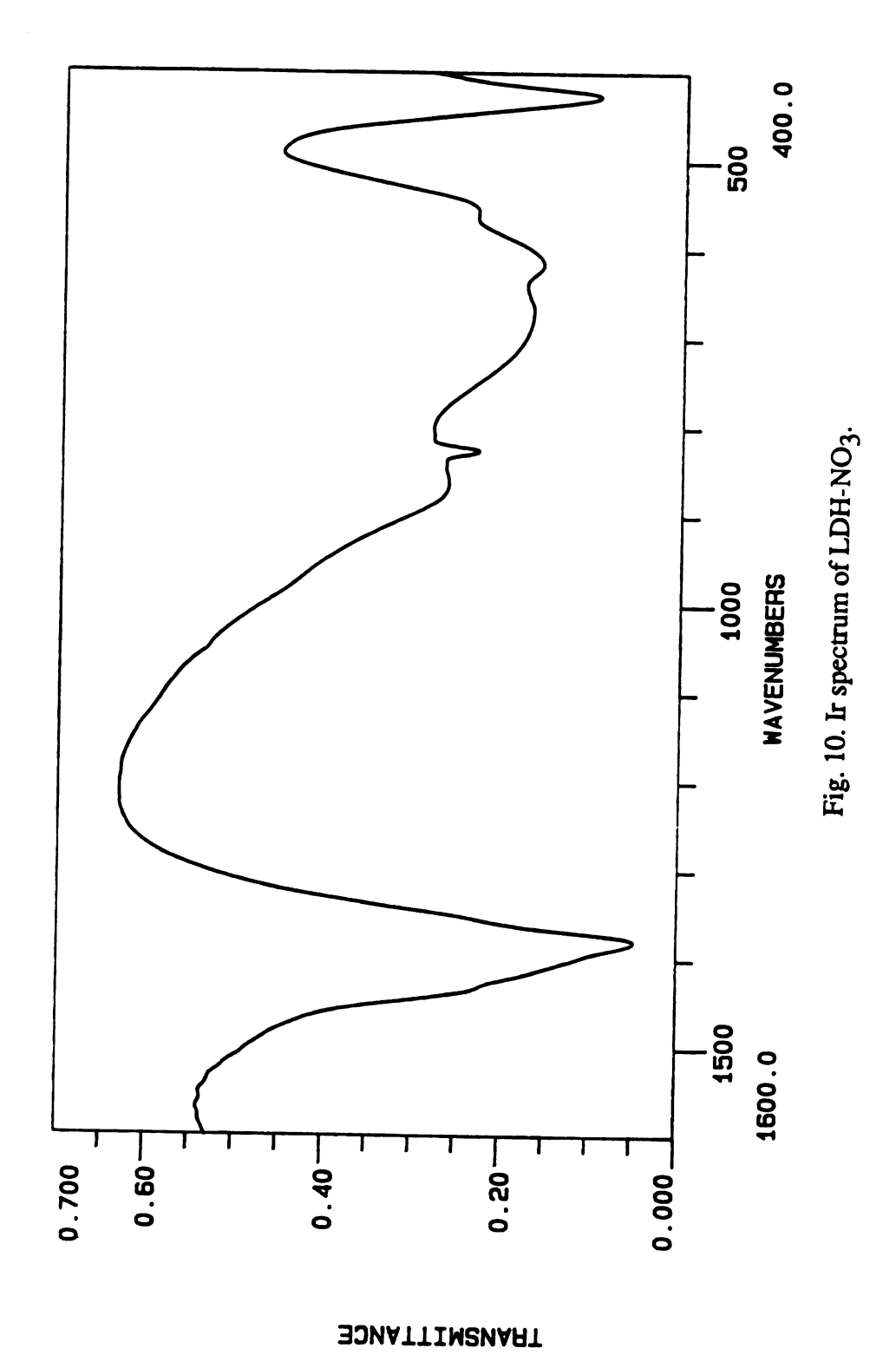
Ion-exchange was the general method employed for the preparation of LDH-POMs. The pristine LDH-NO3 was used as a starting material. This derivative is a high crystalline material, providing a highly crystalline exchange product. Because of the low ion exchange selectivity toward NO3-, the exchange reaction takes place easily. It is easy to check the extent of reaction, because the unexchanged NO3- can be detected easily by ir spectroscopy due to its characteristic N-O stretching absorption band at 1380 cm<sup>-1</sup>, as shown in Fig. 10.

When an exchange reaction is carried out, two major parameters should be considered in order to get high purity, crystalline products:

- 1) the pH of reaction mixture
- 2) the reaction temperature

Because LDH-NO3 is amphoteric, it is stable only within a limited pH range, i.e., 5.8 < pH < 10, otherwise it will dissolve. As discussed in the previous chapter, POMs are also generally hydrolytically unstable. However, they are quite stable within a certain pH range. The hydrolytic instabilities of both LDHs and POMs impose a restricted pH range on exchange reaction conditions. In addition to the hydrolytic instability problem, the product crystallinity can be affected by pH. In the case of LDH-NaP5W30O110, in which NaP5W30O110, unlike most POMs, is hydrolytically stable even under basic conditions at elevated temperature, the crystallinity of the product obtained at neutral pH is very much lower than that obtained under acidic condition, as is shown in Fig. 11. Furthermore, under basic conditions, the exchange reaction of POMs does not produce a completely exchanged crystalline product. Therefore, it is necessary to keep the reaction pH acidic.

The exchange reaction also depends on temperature. Exchange carried out at low temperature is always incomplete. When exchange is executed at elevated temperature, reaction occurs rapidly and completely. Therefore, it is desirable to carry out the



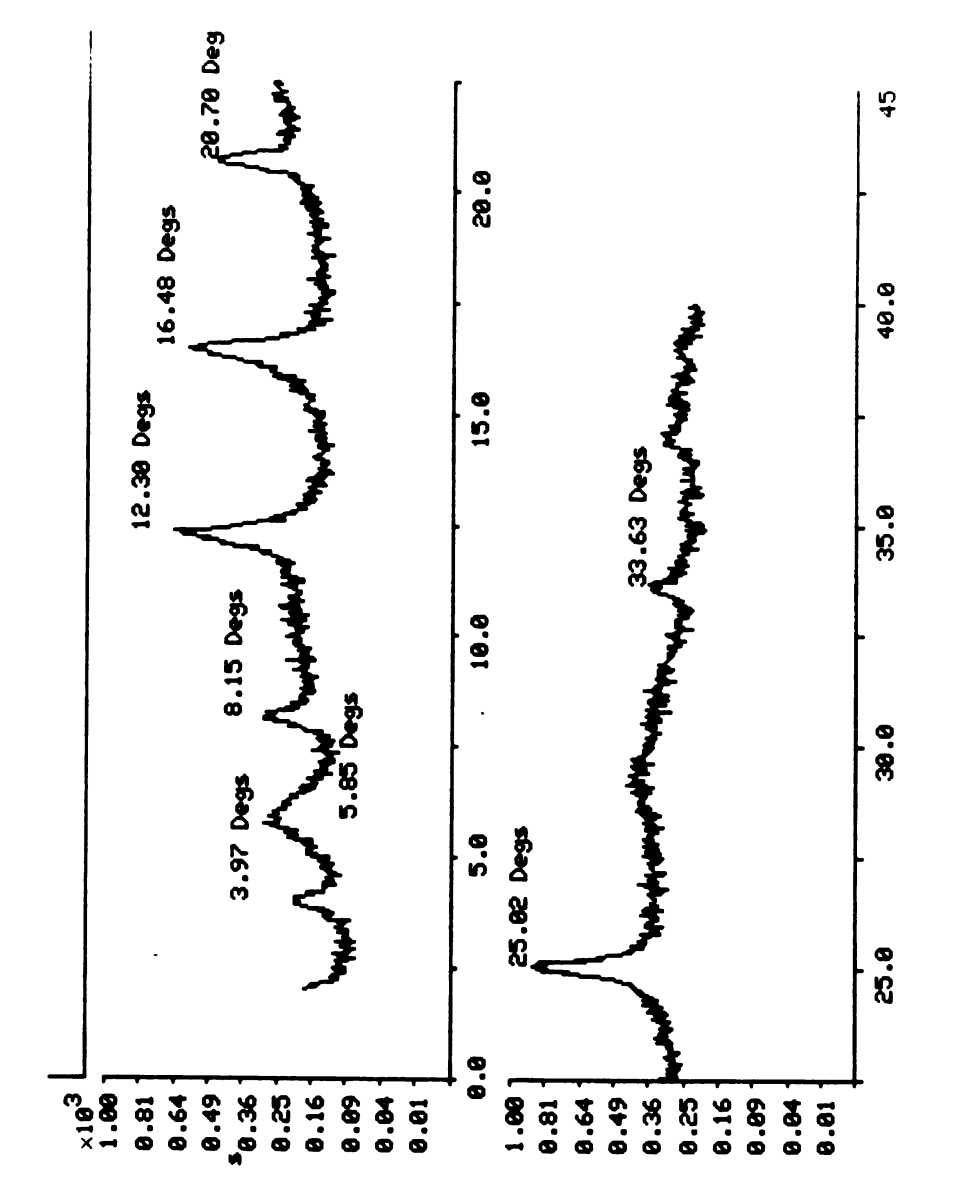


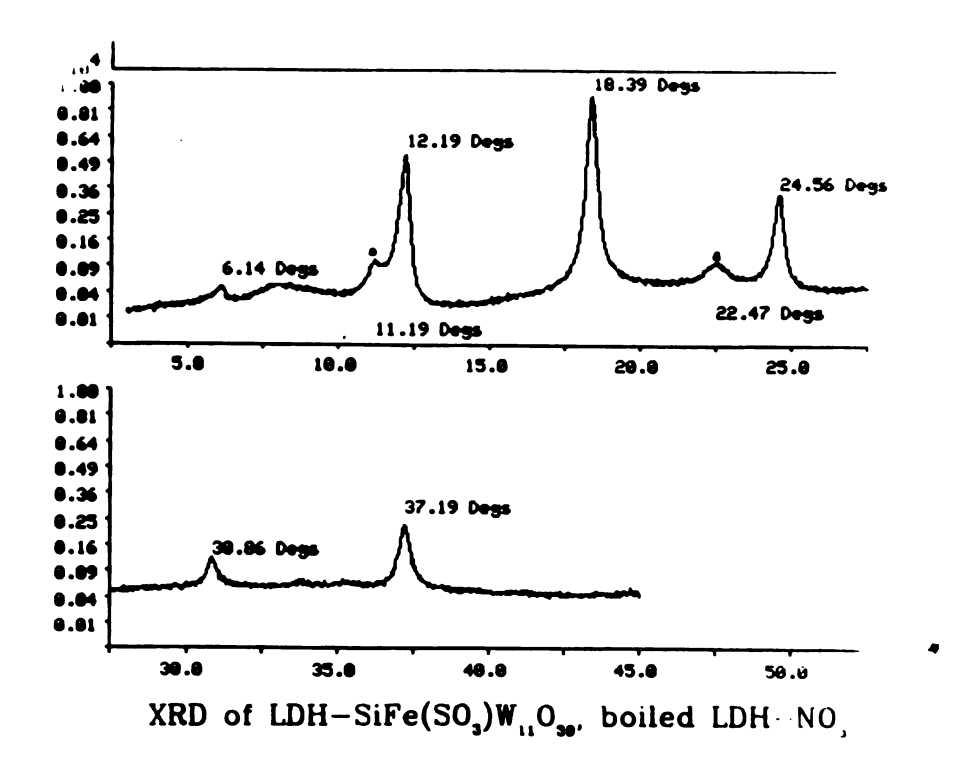
Fig. 11. XRD pattern of LDH-NaP<sub>5</sub>W<sub>30</sub>O<sub>110</sub> prepared at pH = 7.4.

exchange reaction at high temperature, provided that the POM is stable at this temperature. In general, an aqueous suspension of LDH-NO3 in boiling water is added dropwise to a POM solution at ambient temperature. When a drop of LDH-NO3 slurry is added to the POM solution, the local temperature at the contacting spot will be momentarily high enough to cause a fast exchange reaction, yet not cause POM decomposition. Once the POM is intercalated into the LDH gallery, it is hydrolytically stabilized. When a completely exchanged LDH-POM is heated in water to the boiling point, there is no indication of POM degradation in the gallery as demonstrated by ir and XRD. An exception is LDH-PV14O42, which is unstable under these conditions. In the case of LDH-SiFe(SO<sub>3</sub>)W<sub>11</sub>O<sub>39</sub>, if the hot LDH-NO<sub>3</sub> suspension is added to the POM solution, a two phase containing mixed product is formed. The XRD is shown in Fig. 12. The impurity phase LDH-SO3 intercalate ( $d_{001} = 7.98 \text{ Å}$ ) was formed from the decomposition of Si(SO<sub>3</sub>)W<sub>11</sub>O<sub>39</sub> to SO<sub>3</sub><sup>2</sup>-and SiW<sub>11</sub>O<sub>39</sub><sup>8</sup>-at such temperatures. An impurity phase is also obtained in case of LDH-PW9O34. Therefore, in those cases where POMs are not hydrolytically stable, the POM solution should be added to the LDH-NO3 slurry at room temperature to prevent impurity phase formation.

#### C. Characterization of LDH-POMs

#### 1. Electron Microscope Studies

The ion exchange reaction employed for the preparation LDH-POMs was a topotatic reaction, This was proved by an electron microscopy study of the products, LDH-POMs, and the starting material. The electron micrographs are provided in Fig. 13. The crystal shapes of the products are hexagonal, just as for the starting material, also the crystal sizes of the products are of the order of one micron, just as for the starting material. On the basis of these electron micrographs, it is obvious that the exchange reaction has taken place in a topotatic way.



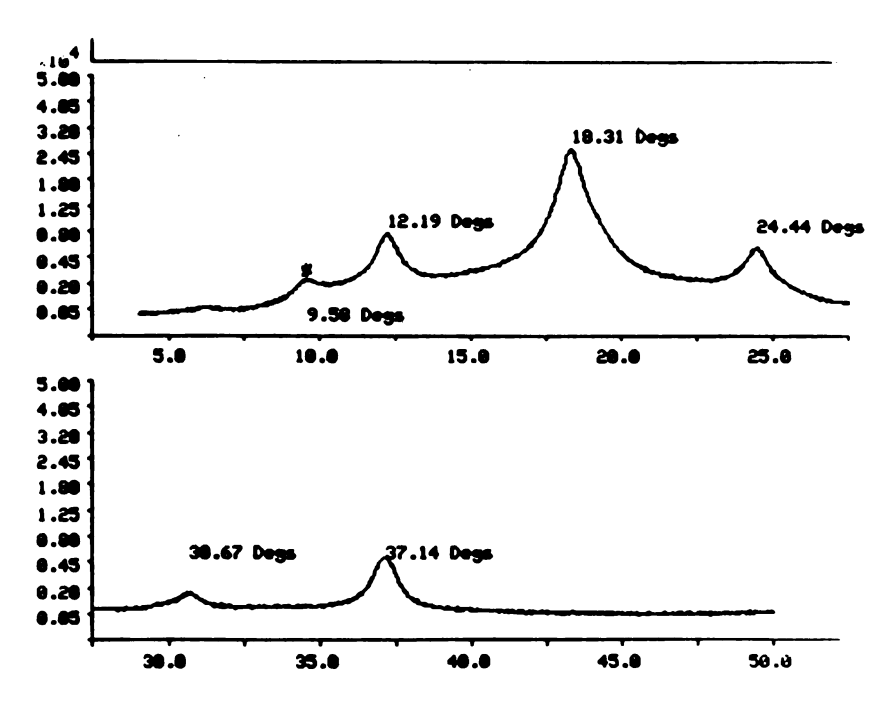
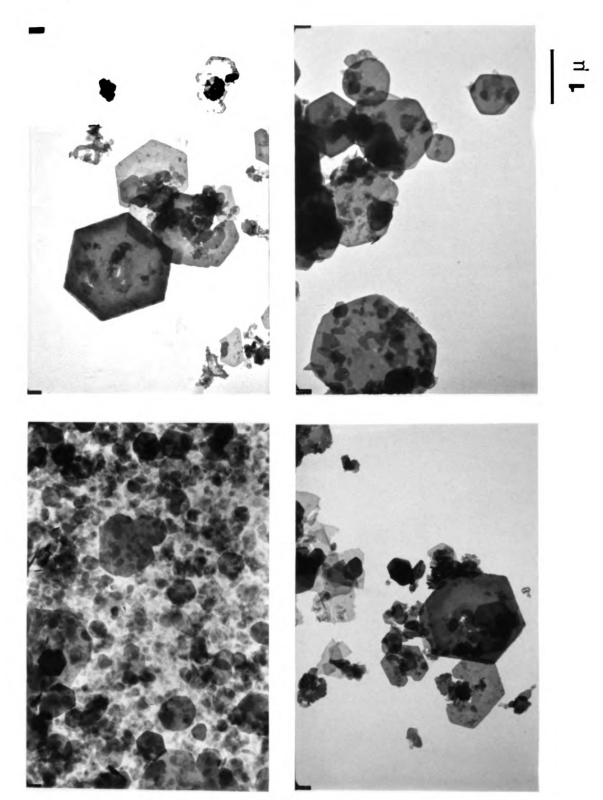


Fig. 12. XRD pattern of a) LDH-SiFe(SO<sub>3</sub>)W<sub>11</sub>O<sub>39</sub> and b) LDH-PW<sub>9</sub>O<sub>34</sub> prepared using a hot LDH-NO<sub>3</sub>. \* represents an impurity phase.

Fig. 13. Transmission electron microscope pictures for LDH-POMs. (top, left), LDH-NO3; (top, right), LDH-BCuW11O39; (below, left), LDH-PMo2W9O39; (below, right), LDH-PW9O34.



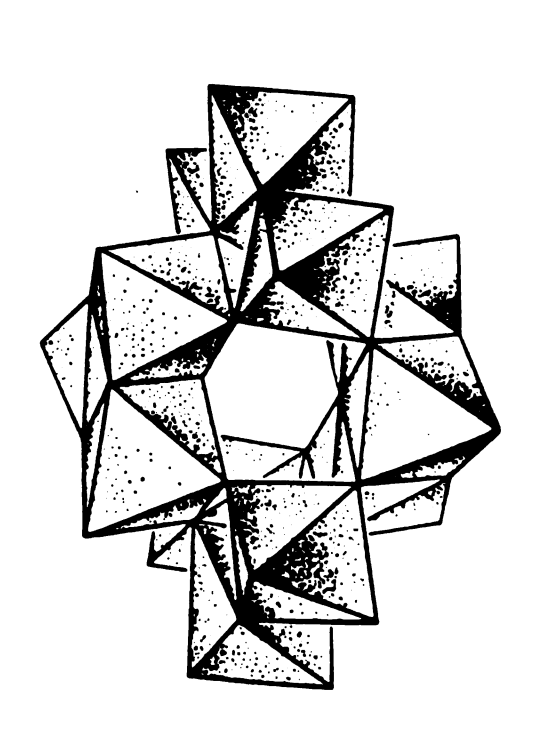


Fig. 14. Polyhedral representation of  $\rm H_2W_{12}O_{42}^{10}$ .

## 2. X-ray Powder Diffraction (XRD) Study

This technique is one of the most powerful methods for characterizing the LDH-POM intercalates. It provides information on the completeness of the exchange reaction, as well as on the phase homogeneity of the product, LDH-POM.

The XRD patterns of the LDH-POMs described in this work, which are provided in Appendix A, are divided into two categories. One is that in which the POM is of the Keggin-ion type. In this case the gallery height 14.8 A - 4.8 Å = 10 Å corresponds to the size of a POM consisting of four oxygen layers. In the second class of LDH-POM the POM is a non-Keggin-type, for example, LDH-H2W12O42 and LDH-NaP5W30O110. Although the basal spacing of the former is the same as that for an LDH-POM in which the POM is a Keggin-type, the structure of the H2W12O42 anion is not a Keggin-type, as shown in Fig. 14. When this anion is oriented in the gallery so that a mirror plane is parallel to the c direction, the resulting gallery height should give a value corresponding to four oxygen layers. In the case of LDH-NaP5W30O110, the gallery height is 16.5 Å, which corresponds to a value of seven oxygen layers. As given in Fig. 15, when this anion is oriented with the C5 axis parallel to the c direction, the resulting gallery height should correspond to seven oxygen layers.

#### 3. Elemental Analysis

Elemental analysis data (weight %) for some representative LDH-POMs are provided in Table 11.

## 4. Nuclear Magnetic Resonance (NMR) Studies

It has been demonstrated that NMR is a powerful technique for the elucidation of the structures of POMs. In this work, 29Si, 31P, 11B, 51V, and 23Na were accessible nuclei with our NMR facility. Even though this technique provides fine structural information, it was not applicable to any LDH-POMs containing paramagnetic atoms such as Co(II), Fe(III), and Cu(II). The following summarizes the NMR properties of each system accessible with our facility.

Fig. 15. a) An ORTEP view of [NaP<sub>5</sub>W<sub>30</sub>O<sub>110</sub>]<sup>14</sup>- looking approximately along the virtual C5 symmetry axis. Oxygen and tungsten atoms are represented as large and small open circles, respectively, and the sodium ion by the central closed circle. The phosphorus atoms are shown as closed circles that are almost entirely obscured by the inner pentagon of five tungsten atoms. b) An idealized view along C5 showing the WO6 octahedra in the upper half of the anion. c) The PW6O<sub>22</sub> unit view perpendicular to the anion's virtual C5 axis. Oxygen and tungsten atoms are represented by the large and small open circles, respectively, and the phosphorus atom by the closed circle.

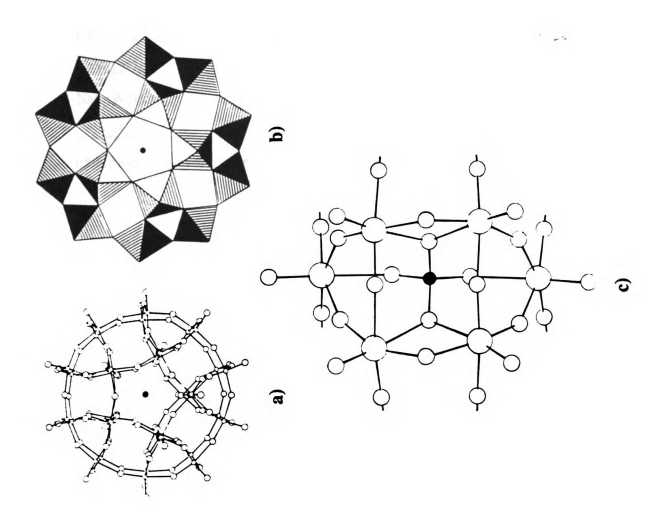


Table 11. Elemental Analysis Data for LDH-POMs

РОМ	wt % observed			wt % calcul	n*		
	Zn	Al	w	Zn	Al	w	
H2W12O40	14.8	3.1	41.6	15.6	3.9	40.0	22
SiW11O39	18.9	3.9	36.9	17.4	3.7	38.5	19
PW9O34	21.0	4.4	29.5	18.4	4.8	31.7	28
BW11O39	21.0	3.8	38.1	21.5	4.4	37.0	26
H2W12O42	19.2	3.5	38.7	21.2	4.4	35.8	38
NaP5W30O110	12.1	2.1	48.7	14.9	3.1	44.9	67

n\* represents a hydration number, as estimated from the TGA curves for each sample.

LDH-SiV<sub>3</sub>W<sub>9</sub>O<sub>40</sub>: The NMR spectra of this system could be obtained both in the state and in solution. For a solution spectrum, a sample was prepared by dissolving solid LDH- $SiV_3W_9O_{40}$  at pH = 2.0. At this pH the host layer was destroyed, but the anion SiV3W9O40 was stable. The 51V NMR spectra of LDH-SiV3W9O40 and that of the potassium salt in solution at pH = 1.7 are given in Fig. 16. The observed peak positions of the LDH-SiV3W9O40 and  $\alpha$ -K<sub>6</sub>HSiV<sub>3</sub>W<sub>9</sub>O<sub>40</sub> are -567 ppm and -572 ppm, respectively. The reported value for the potassium salt at 30°C is -573 ppm at pH = 1.5.122 The NMR chemical shift for the 51V has been reported to be sensitive to sample solution pH, so that  $\delta(51V)$  shifts to upfield (shielding) upon protonation. 133 Protonation increases the energy of a ligand-to-metal charge transfer, and hence decreases the absolute resonance frequency by reducing the deshielding contribution of the temperature-independent paramagnetism. Therefore, the small change in the chemical shift for the dissolved sample at pH = 2.0 means that the structure of the anion in the LDH-SiV3W9O40 is retained. The spectrum for the LDH-SiV3W9O40, has a single peak reasonably close to the peak position observed for the potassium salt, strongly suggestive that in the gallery the guest anion, SiV3W9O40 has the same structure as the potassium salt of the anion.

In the solid state state, the  $^{29}$ Si NMR spectra of both LDH-SiV3W9O40 and the potassium salt of the anion, as provided in Fig. 17, demonstrate that the anion structure under the two different surroundings is identical. There is only one peak at -84 ppm in both cases. The reported value is -84 ppm at pH = 1.5 and at  $^{30}$ °C.  $^{122}$ 

The solid state 51V MAS NMR of LDH-SiV3W9O40 does not provide clear structural information due to the complexity of the spectrum arising from spinning side bands, as shown in Fig. 18. On the basis of the above data it can be concluded that the structure of the guest anion in the LDH gallery is identical to that of the potassium salt.

LDH-PMo2W9O39: It has been reported that the peak position of the 31P NMR of this POM correlates with the structure of the POM.64 In the case of orthophosphate, PO43-,

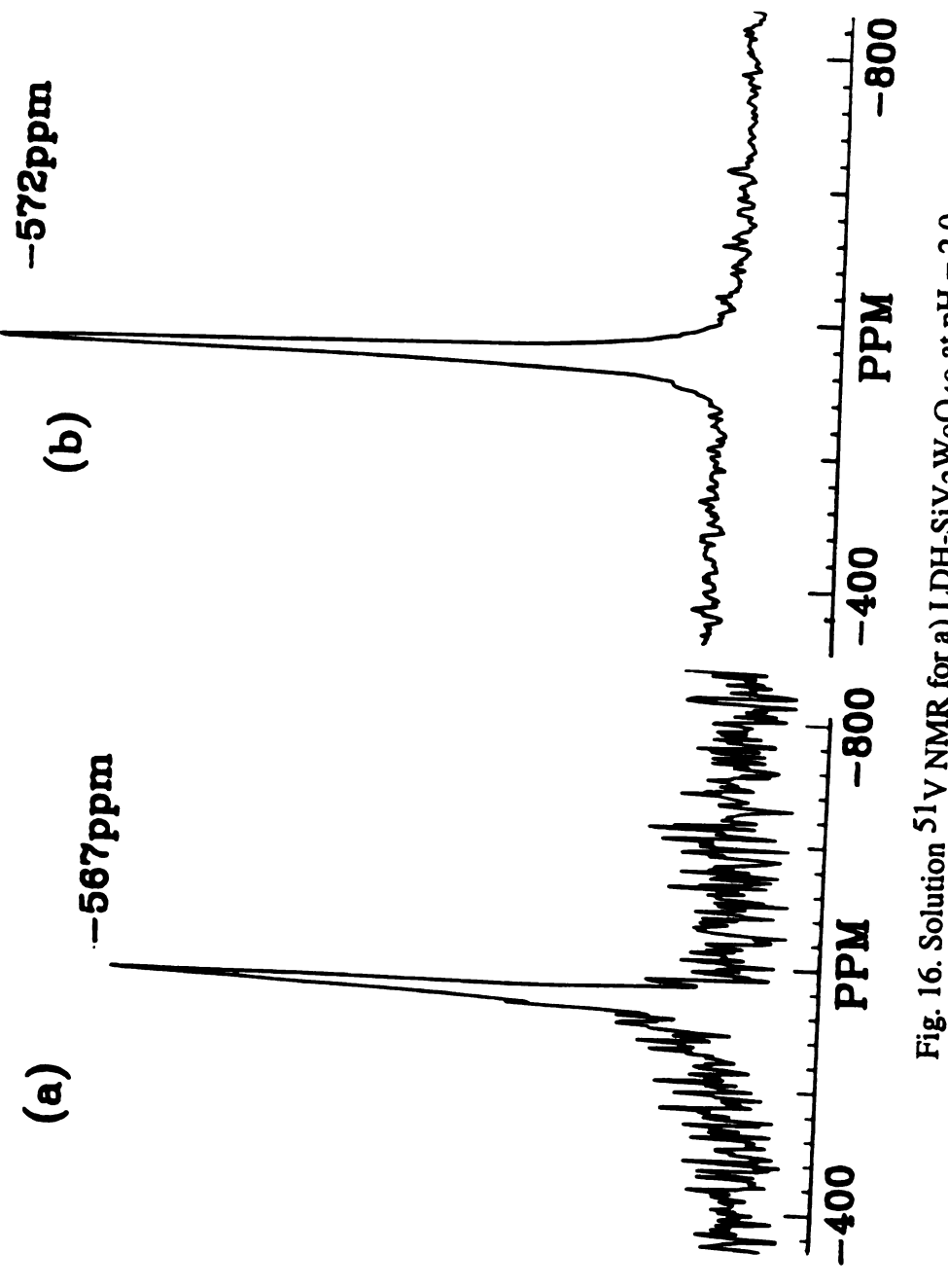
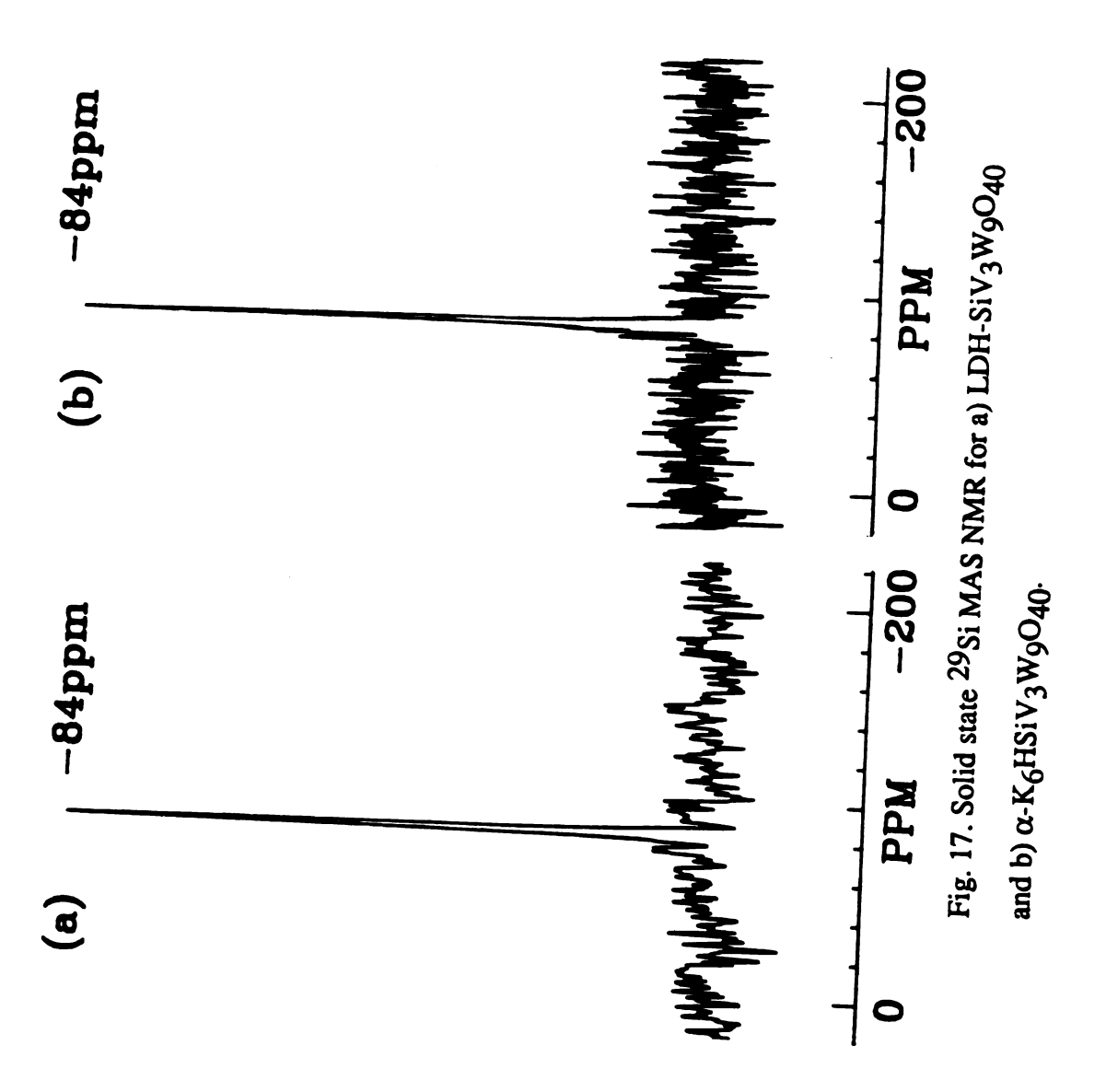


Fig. 16. Solution <sup>51</sup>V NMR for a) LDH-SiV<sub>3</sub>W<sub>9</sub>O<sub>40</sub> at pH = 2.0 LiClO<sub>4</sub> solution and b)  $\alpha$ -K<sub>6</sub>HSiV<sub>3</sub>W<sub>9</sub>O<sub>40</sub> at pH = 1.7.



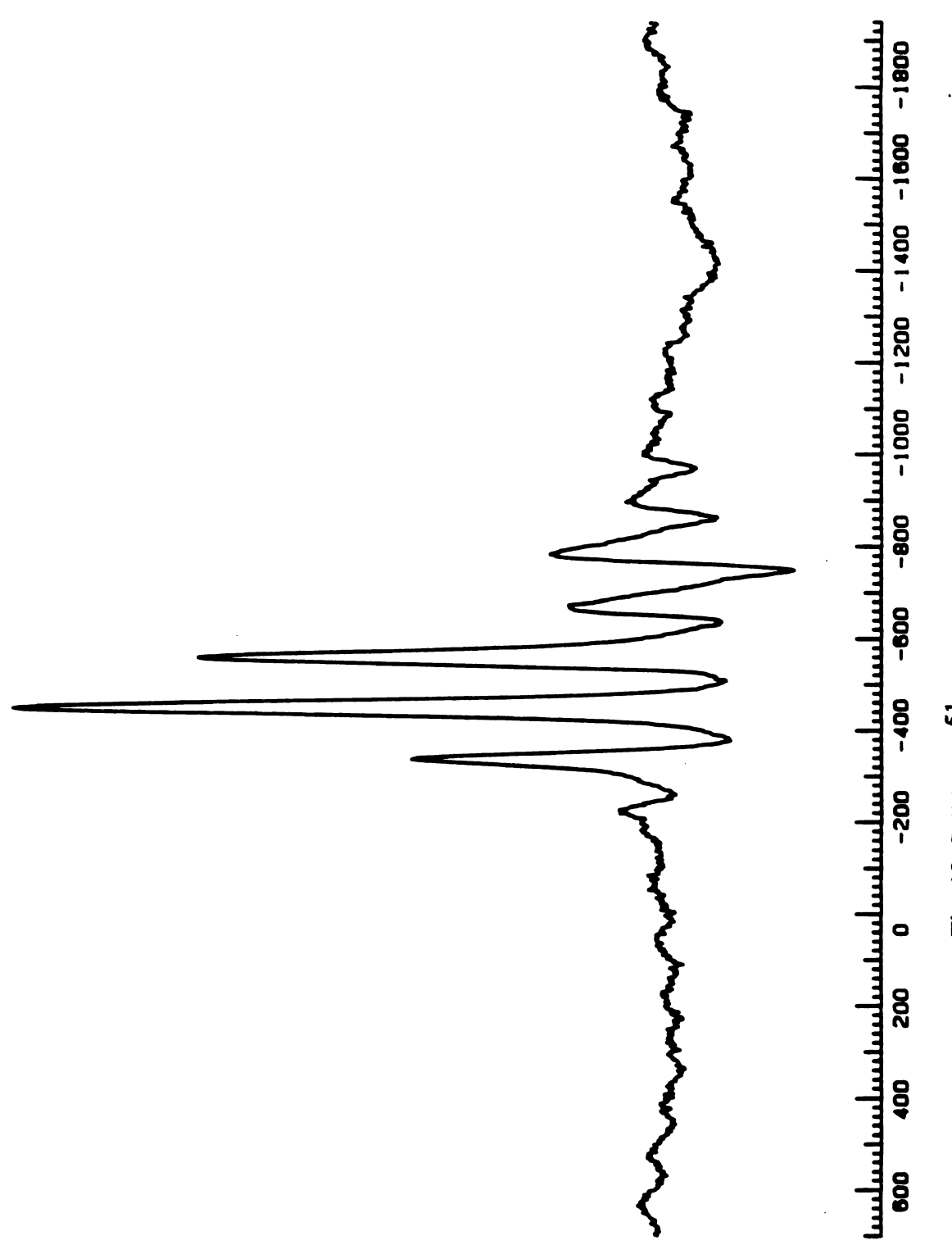


Fig. 18. Solid state <sup>51</sup>V MAS NMR for LDH-SiV<sub>3</sub>W<sub>9</sub>O<sub>40</sub>.

the  $\sigma$ -bond between a P atom and an oxygen atom is formed with sp<sub>3</sub> hybrid orbitals on the phosphorus atom. In addition to the  $\sigma$ -bond,  $\pi$  bonding forms through participation of the p orbitals of the oxygen atoms. This  $\pi$ -bond formation substantially reduces the positive charge on the P atom. Increasing the degree of  $\pi$ -interaction leads to deshielding of the P nucleus, and its resonance absorption is observed at lower field. Consequently, any interaction of the oxygen atoms with the external surroundings will influence the electron density around the P atom. This idea can be applied to the Keggin anion, PM12O40, in which each oxygen atom of PO4 is bounded to three metal atoms of the coordination sphere. The interaction of those atoms with phosphorus is influenced by the ability of the metal to remove electron density. Thus, oxygen atoms will shield the phosphorus atom to different degrees. In all cases except that of M = V, the 31P NMR line is shifted to higher field, reflecting a reduction of the  $\pi$ -interaction in the POM. The increase of  $\delta$  values according to the sequence PW<sub>12</sub> < PMo<sub>12</sub> < PV<sub>12</sub> is easily understood because the electron-accepter properties increase in the series V < Mo < W. It is also known that the greater the shielding, the higher the v(P-O) frequency.<sup>64</sup> With defect Keggin-type compounds, for example, PM11O39, occurrence of a hole (defect) leads to a weakening of the P-O bond and thus induces an increase in the  $\delta$  value. When the hole is filled by a cation that forms strong ionic bonding with the defect POM, for example, Zn<sup>2+</sup>, the oxygen atoms of the hole site are not substantially affected. Thus, the chemical shifts are similar to those of the parent "defect structure". On the other hand, if the hole is filled by a metal covalently bonded to the POM, the defect character is greatly attenuated, and the chemical shift approaches that of saturated Keggin-type compounds.

The solid state  $^{31}P$  MAS NMR spectra for LDH-PMo<sub>2</sub>W9O<sub>39</sub> and K7PMo<sub>2</sub>W9O<sub>39</sub> are provided in Fig. 19. Only one peak is observed at -10.8 ppm for LDH-PMo<sub>2</sub>W9O<sub>39</sub> and at -10.0 ppm for the potassium salt of anion. The reported value for the potassium salt is -9.4 ppm.<sup>64</sup> The chemical shift for the LDH-PMo<sub>2</sub>W9O<sub>39</sub> is slightly lower than that of the potassium salt. The P  $\pi$ -electron density in the PO<sub>4</sub>

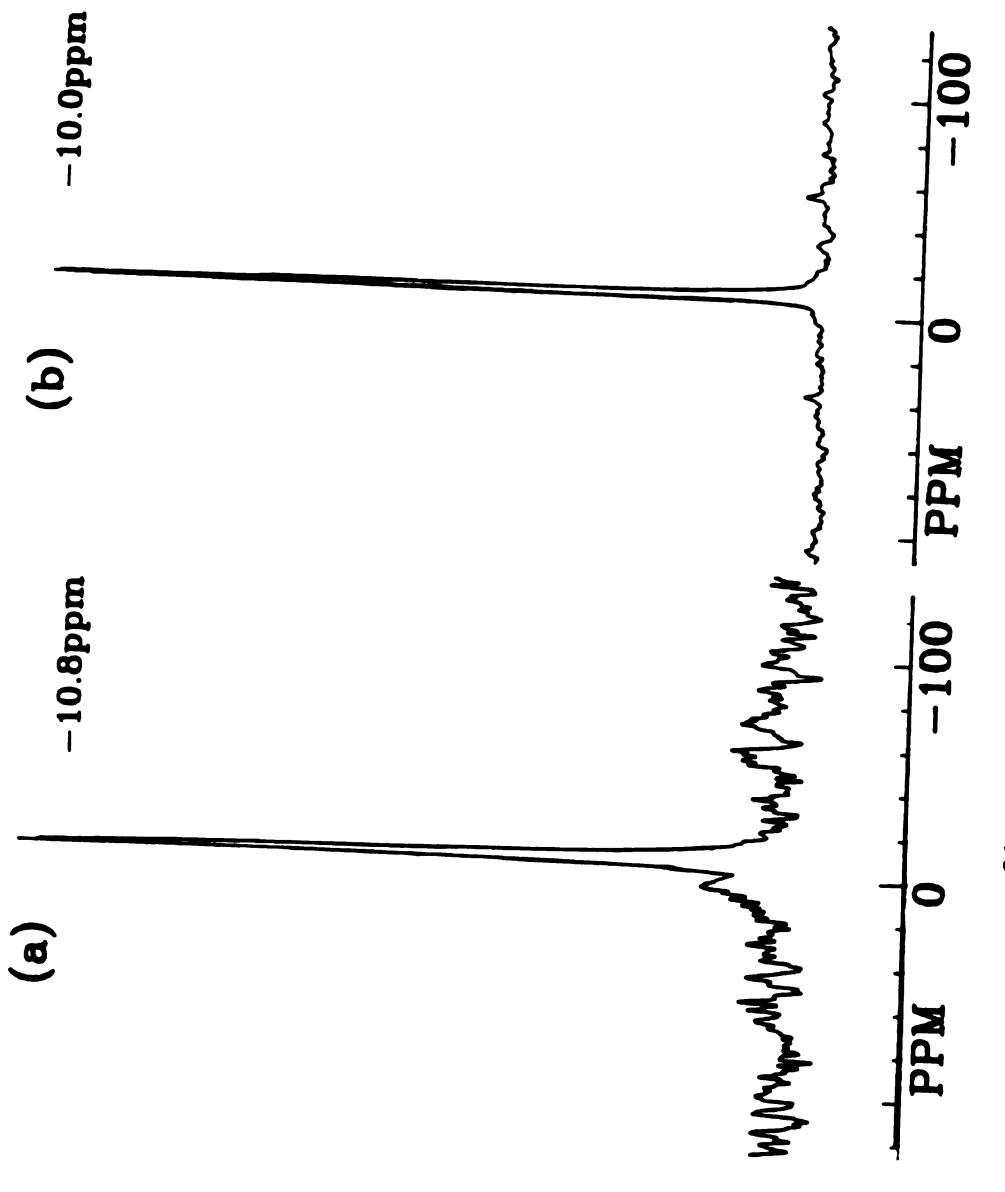


Fig. 19. Solid state <sup>31</sup>P NMR for a) LDH-PMo<sub>2</sub>W<sub>9</sub>O<sub>39</sub> and b) K<sub>7</sub>PMo<sub>2</sub>W<sub>9</sub>O<sub>39</sub>.

tetrahedron has been reduced upon intercalation of the anion in the LDH gallery. Hydrogen bonding between the POM anion and the hydroxyl layer may be a source of such electronic perturbation around the P nucleus.

On the basis of these NMR data, it is certain that the structures of the PMo2W9O39 anions in the LDH intercalate and in the potassium salt are identical.

LDH-PW9O34: The solid state 31P MAS NMR spectra for the LDH-PW9O34 and the potassium salt are shown in Fig. 20. In the case of LDH-PW9O34, there are two peaks at -13.3 ppm and at 0.4 ppm. The latter peak is due to an impurity and cannot be assigned to a POM containing a P atom. It has been observed that the size of impurity peak increases with aging. POMs containing phosphorus have not been observed to evidence such 31P chemical shifts. The major peak at -13.3 ppm for the LDH-PW9O34 is observed at lower δ region (higher field) than that of the corresponding potassium salt (-9.7 ppm). The hydrogen bonding between the anion and the hydroxyl layer in the LDH gallery may be responsible for the lower  $\delta$  value, as in the LDH-PMo<sub>2</sub>W<sub>9</sub>O<sub>34</sub> case. However, an alternative explanation is that the PW9O34 anion is transformed to a phosphorus containing POM which has the same size as the parent PW9O34. In this case the major peak at -13.3 ppm and the impurity peak at 0.4 ppm could arise from the POM containing a phosphorus atom and the phosphate anion, respectively. The hydrolysis of the PW9O34 anion in the gallery proceeds to some extent by aging. The latter argument is more plausible than the former. On the basis of the LDH-PW9O34 ir data, which will be discussed in the next section, the LDH product formed from the PW9O34 anion resembles that formed from PW9+ $_x$ O34+ $_y$  (0 <  $_x$  < 3).

LDH-PV14O42: The solid state <sup>31</sup>P MAS NMR spectra for both LDH-PV14O42 and (NH4)9PV14O42 are given in Fig. 21. Both spectra exhibit only one peak at -1.25 ppm for the LDH-PV14O42 and at -1.38 ppm for the ammonium salt. The similarity of these spectra suggests that the anion under the two different circumstances is identical.

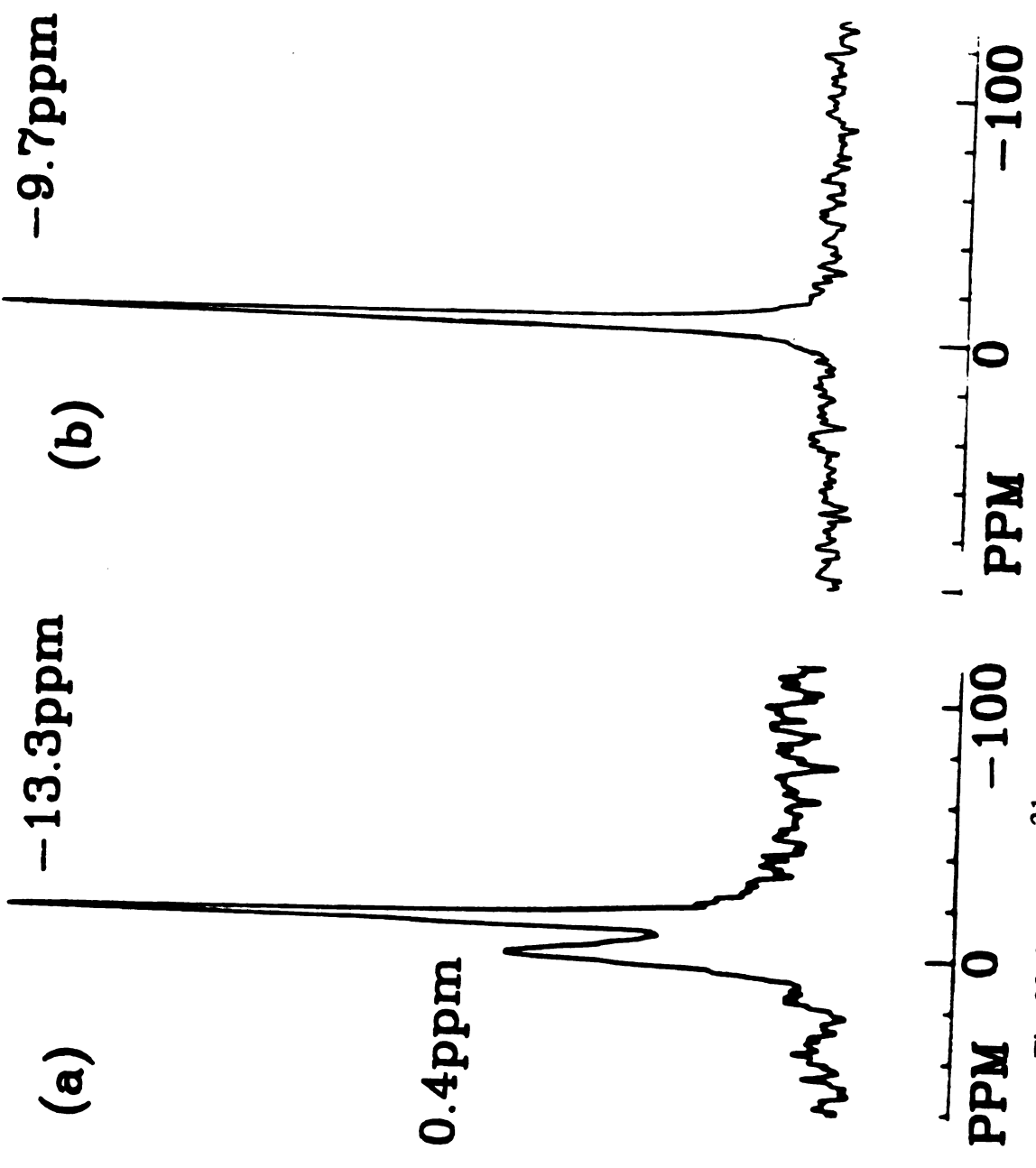


Fig. 20. Solid state <sup>31</sup>P MAS NMR for a)LDH-PW9O<sub>34</sub> and b) NagHPW9O<sub>34</sub>.

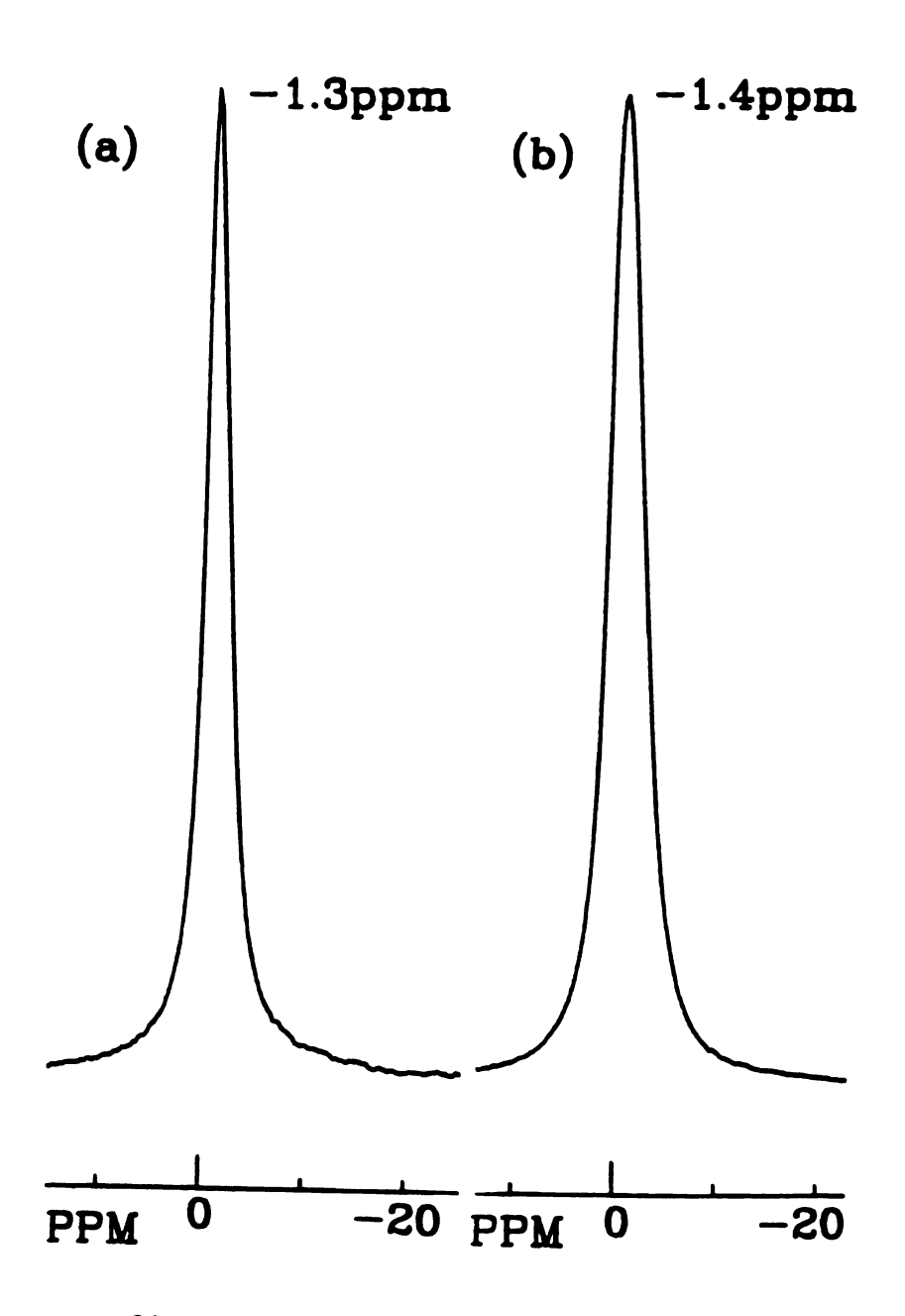


Fig. 21. Solid state  $^{31}\text{P}$  MAS NMR for a) LDH-PV $_{14}\text{O}_{42}$  and b) (NH $_4$ ) $_9\text{PV}_{14}\text{O}_{42}$ .

LDH-BW<sub>11</sub>O<sub>39</sub>: Boron atom has a spin 3/2. Thus, it has an electric quadruple moment which will lead to line broadening. The 11B solid state MAS NMR for both LDH-BW11O39 and K9BW11O39 are provided in Fig. 22. The spectrum for the potassium salt of the BW11039 anion shows a typical powder pattern containing a peak doublet. In this case, the quadruple interaction still contributes to the line broadening due to the asymmetric environment around the central B atom (C<sub>S</sub> symmetry). Therefore, even though the spectrum was obtained by the MAS technique, its shape still shows appreciable line broadening. On the other hand, in the case of LDH-BW11O39, the spectrum contains a much more narrow single line at -17.3 ppm. The reported chemical shift value for the BW12O405- anion in solution is -17.6 ppm relative to a saturated solution of boric acid. 134 Such a narrow single line indicates a highly symmetric environment around the B central atom in the BW11039 anion. Consequently, line broadening due to the quadruple interaction will vanish. The highly symmetric environment around the central B atom upon intercalation was indicated in the ir spectrum. Split bands assigned as v(B-O) due the low symmetry environment around the B atom in the potassium salt merged into one single band at 985 cm<sup>-1</sup> for the intercalated anion in LDH. The number of ir absorption bands for the potassium salt (C<sub>S</sub> symmetry) has been found to be greater than that for the intercalated anion, as given in Fig. 32.

The increased symmetry of the anion may be due to the filling of the vacancy in the defect Keggin structure with a group which may come from the hydroxyl layer (e.g., OH)

LDH-NaP5W30O110: The solid state <sup>23</sup>Na MAS NMR spectra of both LDH-NaP5W30O110 and the ammonium salt are given in Fig. 23. These spectra also show a typical powder pattern. The similarity of the two spectra suggests an identical anion structure under the two different circumstances. The slight line broadening that occurs upon intercalation may be due to a less symmetrical surrounding around the Na nucleus due to shift of the Na atom out of the central position in the POM. The shift in Na+

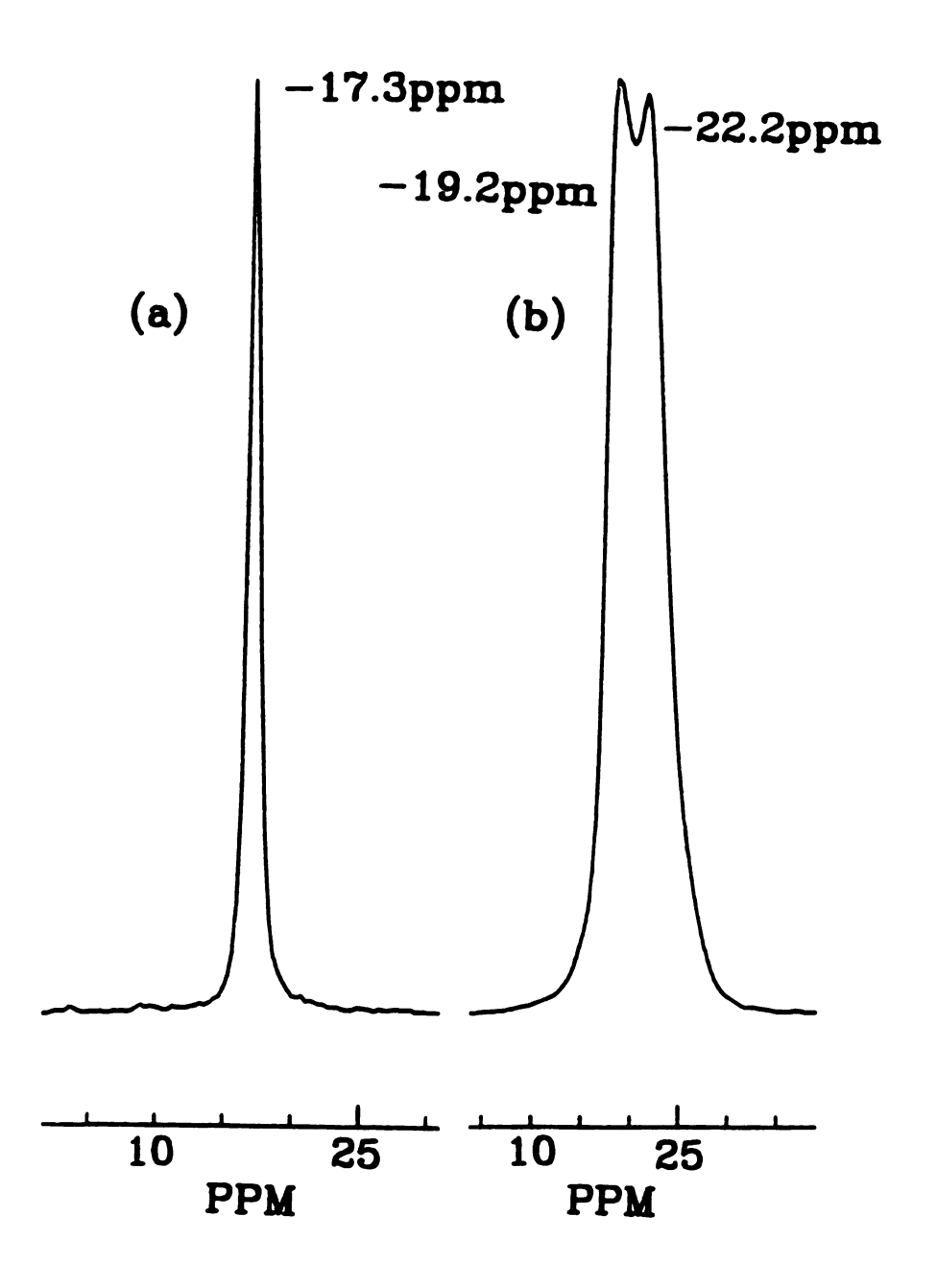


Fig. 22. Solid state  $^{11}\text{B}$  MAS NMR for a) LDH-BW $_{11}\text{O}_{39}$  and b) K9BW $_{11}\text{O}_{39}$ .

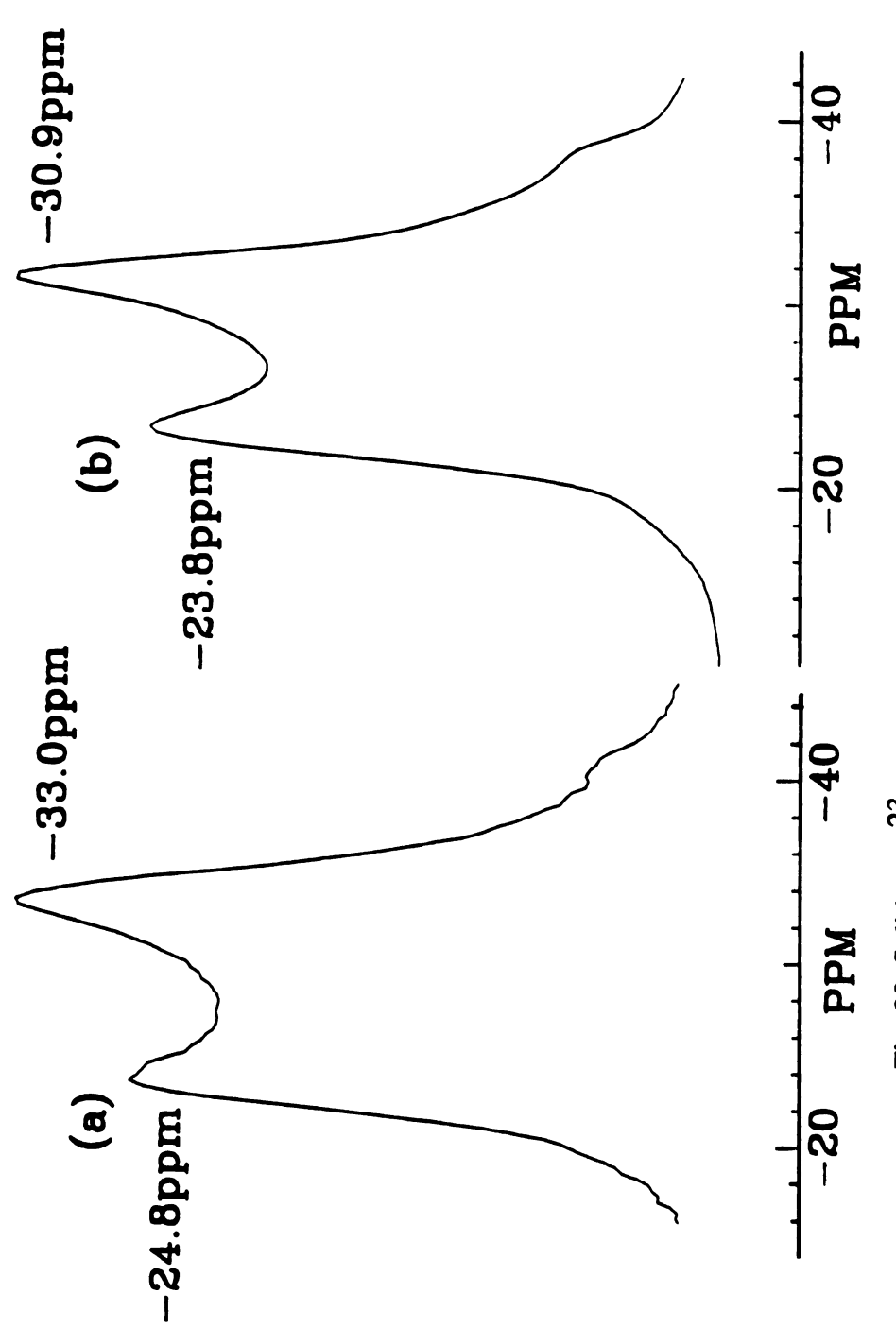


Fig. 23. Solid state  $^{23}$ Na MAS NMR for a) LDH-NaP<sub>5</sub>W<sub>30</sub>O<sub>110</sub> and b) (NH4)<sub>14</sub>NaP<sub>5</sub>W<sub>30</sub>O<sub>110</sub>.

position may arise because of interaction of the POM with the hydroxyl layer in the gallery. For instance, H-bonding may result in an increase in the electric field gradient around Na nucleus. Thus, the quadruple interaction will be increased and the line will be broadened.

The solid state <sup>31</sup>P MAS NMR spectra of both LDH-NaP5W30O110 and the ammonium salt of the POM are provided in Fig. 24. Since both spectra show a single peak at -9.8 ppm for LDH-NaP5W30O110 and at -9.7 ppm for the ammonium salt, it is obvious that the POMs in the different environments are identical.

#### 5. Infrared Spectroscopic Studies

The ir spectra of LDH-POMs should consist two main components. One should be the contribution of the host layer, which is a layered octahedral metal hydroxide lattice. The other should be the contribution of the guest POM anion.

#### a) Vibrations of the host layer

Information on the octahedral layers can be obtained from lattice vibrations. In principle, these vibrations can be assigned to the translational motions of the oxygen layers. A vibrational study of layers having the composition M(II)<sub>2</sub>M(III)(OH)<sub>6</sub> was done by Serna et al..<sup>135</sup> They assumed that the layer had ideal D<sub>3d</sub> symmetry. Under this assumption, seven ir active modes, namely, 3A<sub>2u</sub> + 4E<sub>u</sub>, are possible. Only five vibrations (2A<sub>2u</sub> + 3E<sub>u</sub>) can be observed above 250 cm<sup>-1</sup>. Within the frequency range accessible with our IBM-40 FTIR instrument, that is, above 400 cm<sup>-1</sup>, only three bands are observable. The most distinctive band, a M(II)-O-M(III) stretch, occurring in the range 460-410 cm<sup>-1</sup> is dependent on the metals occupying the octahedral interstices. For example, a strong band is observed at 435 cm<sup>-1</sup> for Ni<sub>2</sub>Al(OH)<sub>6</sub>·1/2CO<sub>3</sub>, 455 cm<sup>-1</sup> for Mg<sub>2</sub>Al(OH)<sub>6</sub>·1/2CO<sub>3</sub> and 430 cm<sup>-1</sup> for Fe<sub>2</sub>Al(OH)<sub>6</sub>·1/2CO<sub>3</sub>. For our Zn<sub>2</sub>Al(OH)<sub>6</sub>·NO<sub>3</sub> system, the band is observed at 427 cm<sup>-1</sup>. The other two bands for Zn-O-Al stretching occur at 678 and 558 cm<sup>-1</sup> as shown in Fig. 10. The other type of layer contribution is a δ(OH) vibration at about 620 cm<sup>-1</sup>.

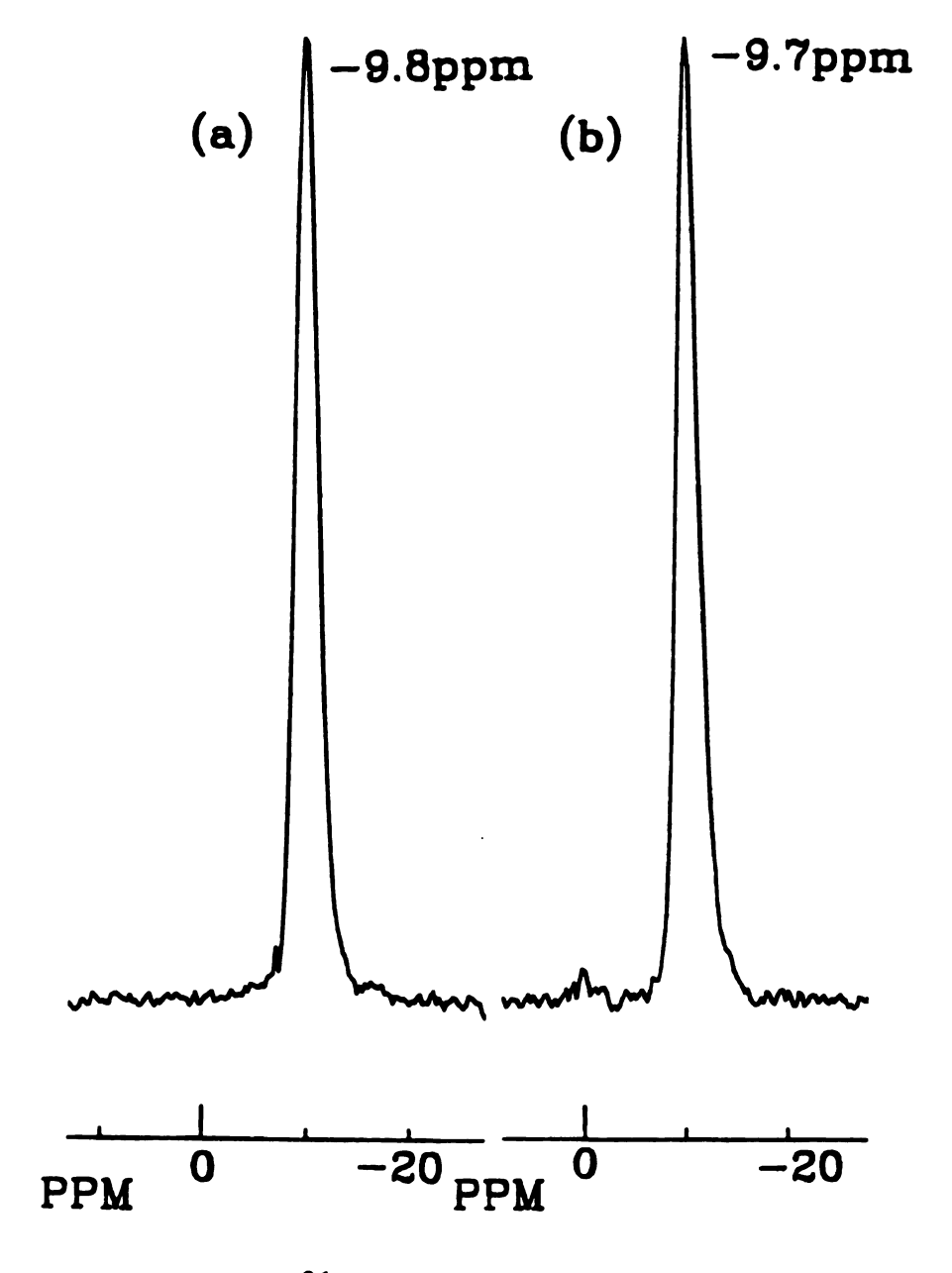


Fig. 24. Solid state  $^{31}$ P MAS NMR for a) LDH-NaP<sub>5</sub>W<sub>30</sub>O<sub>110</sub> and b) (NH4)<sub>14</sub>NaP<sub>5</sub>W<sub>30</sub>O<sub>110</sub>.

## b) Vibrations of guest POM anion

Ir spectroscopy is extensively used in polyoxometalate chemistry for structural elucidation. Especially, the vibrational spectra of Keggin structured POMs (XM12O40) have been extensively studied by Rocchiccioli-Deltcheff et al..135 As discussed in the introduction chapter, the α-Keggin structure consists of one XO<sub>4</sub> tetrahedron surrounded by four M3O13 (M3 triplet) sets formed by three edge-sharing octahedra. These structural features are illustrated in Fig. 25. Theoretically, there are 22 ir active modes. 135f) These modes belong to vibrations of the T<sub>2</sub> type. In view of the complexity of this anion, many vibrations may not be observed on account of either random degeneracy, low intensity of the bands, or occurrence beyond the measurable range limit.

Three major groups contribute to the POM spectrum, namely, the 12 terminal M=Od bonds, the 24 bridging M-O-M bonds and one central XOa4 tetrahedron. In the bridging M-O-M groups, there are two types of bonding in the bridging M-O-M groups: 12 almost linear M-Oc-M "intra" bridging bonds 135b) contained within four M3 triplets: 12 bent M-Oh-M "inter" bridging bonds connecting the four M3 triplets to each other. The band due to the M=O<sub>d</sub> group occurs in the 1100-900 cm<sup>-1</sup> range. For example, the band v(W=O) is observed at 935 cm<sup>-1</sup> for  $H_2W_{12}O_{40}^{6}$ , 960 cm<sup>-1</sup> for  $BW_{12}O_{40}^{5}$ ,  $982 \text{ cm}^{-1}$  for  $\text{SiW}_{12}\text{O}_{40}^{4-}$  and  $985 \text{ cm}^{-1}$  for  $\text{PW}_{12}\text{O}_{40}^{3-}$ . 136 d) The valence vibrations of the second M-O-M group (symmetry C<sub>2v</sub>) are observed in the range of 900 - 200 cm 1. Three bands can be observed, namely, the symmetric and asymmetric valence vibrations  $v_{asy}$  and  $v_{sy}$  and one deformational vibration  $\delta$  when  $v_{asy} > v_{sy}$ . <sup>137</sup> In general, two bands at 920 - 850 cm<sup>-1</sup> and 800 - 750 cm<sup>-1</sup> are assigned to the antisymmetric valence vibrations of M-Ob-M and M-Oc-M, respectively. The latter band is usually strong. The vibrations of the tetrahedral XO4 group in the anion appear in the region of 1100 - 800 cm<sup>-1</sup> (A<sub>1</sub> and T<sub>2</sub>) and 600 - 400 cm<sup>-1</sup> (E and T<sub>2</sub>). Only three with T2 symmetry are ir active modes. They include two vibrational modes v3 and v4 which

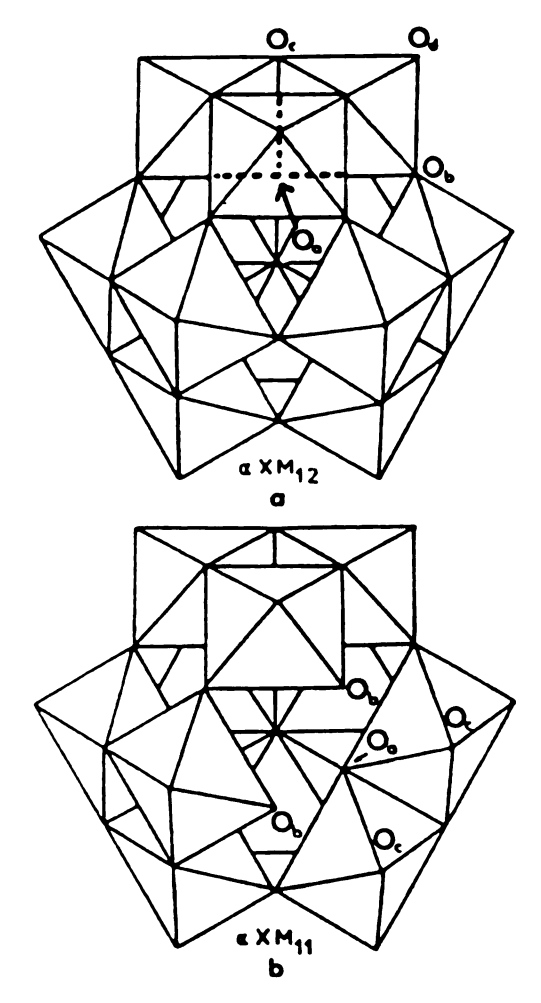


Fig. 25. Idealized structures of  $\alpha$ -XM $_{12}$  (Keggin structure) (a) and  $\alpha$ -XM $_{11}$  (defect Keggin structure) (b) (the central XO<sub>4</sub> tetrahedron is not shown). (O<sub>a</sub> = oxygen shared by 3 MO<sub>6</sub> octahedra and the XO<sub>4</sub> tetrahedron, O<sub>b</sub> and O<sub>c</sub> = oxygen linked to two different M atoms, O<sub>d</sub> = terminal unshared oxygen).

represent a stretching and a deformation motion, respectively. In general,  $v_3 > v_4$ . Table 12 provides the vibrational frequencies of the most frequently occurring XO4.

Table 12. Vibrational Frequency of XO<sub>4</sub>.135 d)

X	В	Si		Ge		P		A	s
M	W	W	Mo	W	Мо	W	Mo	W	_ Mo
v(cm <sup>-1</sup> )	920	930	910	815	802	1080	1070	915	900
	x	x	x	460	460	598	598	472	472

x: Complicated bands in the region of 500-530 cm<sup>-1</sup>.

Except for X = P, the X-O<sub>a</sub> band assigned as  $v_{asy}(X-O_a)$  often has a discussed shape. It is rather broad because of band mixing with  $v(M-O_b-M)$ . In the case of X=P,  $v_{asy}(P-O_a)$  is well resolved from other bands, thereby providing an accurate assignment.

In the case of a lacunary Keggin structure, XM11O39, the symmetry will decrease from T<sub>d</sub> to C<sub>s</sub>. The decrease in symmetry will result in band broadening and the splitting of degeneracies, thereby increasing the number of bands. However, such splittings do not take place as much as expected.<sup>135</sup> c),e) A general decrease of stretching frequencies is observed on account of a weakening of the anion cohesion. In particular, the strong band around 800 cm<sup>-1</sup> attributed to vasy(M-O<sub>b</sub>-M) is split into two bands at 797 and 725 cm<sup>-1</sup> for SiW11O39 and into two bands at 810 and 725 cm<sup>-1</sup> for PW11O39. For the PM11O39 anion, vs(P-O<sub>a</sub>), which is well separated from the other bands of the spectra for PM12O40 as explained above, is split into two components. The two bands occur at 1060 and 1040 cm<sup>-1</sup> for PM011O39 and at 1085 and 1040 cm<sup>-1</sup> for PW11O39. This splitting is also due to the symmetry decrease of the PO4 tetrahedron.

When a lacunary POM XM<sub>11</sub>O<sub>39</sub> forms complexes of the type XM<sub>11</sub>M'O<sub>39</sub>, in which M' are the 3d series ions, AlIII, SnIV or BIII, the ir spectra of these complexes show that the ligands retain a structure related to the Keggin structure. 135 e) Complexation always induces an increase in stretching frequencies, but the shifted

frequencies remain lower than the frequencies observed for  $XM_{12}O_{40}$ . This increase shows a strengthening of the anion cohesion and an opening of bridge angles relative to those of the free ligand, because the  $d_{\pi}$ - $p_{\pi}$  interaction of the M-O-M bond is enhanced by increasing the bridge angle M-O-M. In the case of PM11O39, the v3 PO<sub>4</sub> splitting value,  $\Delta v$ , is always lower than that of the free ligand. Therefore the filling of the vacant site by an M' atom restores to some extent the symmetry of the central tetrahedron, owing to the interaction between the M' and O<sub>a</sub> atoms. 135e)

When a XM11O39 degradates further to XM9O34, the symmetry changes from  $C_S$  to  $C_{3v}$ . The general decrease of stretching frequencies is also observed when XM12O40 changes to XM11O39. For example,  $v(W=O_d)$ s are observed at 985 cm<sup>-1</sup> for PW12O40,135 d) 950 cm<sup>-1</sup> for PW11O39135 c) and 931 cm<sup>-1</sup> for PW9O34.137 Furthermore,  $v(P-O_a)$  decreases in the same way; 1080 cm<sup>-1</sup> for PW12O40,135 d) 1085 and 1040 cm<sup>-1</sup> for PW11O39,135 c) and 1056 and 1002 cm<sup>-1</sup> for  $\alpha$ -PW9O34.138

When some of the tungstens in the XW12O40 Keggin structure are substituted by Mo or V, for example,  $SiW_{12-x}Mo_xO_{40}$  (x = 1 - 3), their ir spectra are intermediate between that of  $SiW_{12}O_{40}$  and that of  $SiM_{012}O_{40}$ , without the appearance of new bands due to the decrease of the molecular symmetry. 135 d) The band around 800 cm<sup>-1</sup> attributed to  $v(M-O_b-M)$  still remains discussed without splitting as is observed for  $SiW_{12}O_{40}$  and  $SiM_{012}O_{40}$ .

The detailed description of the ir spectroscopic features of each LDH-POM will be presented below (cf. Table 13). However, a few general conclusions will be provided first. Generally speaking, when POMs are intercalated into the gallery of the LDH, their ir bands shift either to higher or lower frequencies. Rocchiccioli-Deltcheff has disscussed the influence of counterions on the vibrational spectra of POMs in the solid state. 135 b) He defined two opposing effects, labelled effect A and effect B. The former leads to an increase in the stretching frequencies, for example,  $v(M=O_d)$ , with respect to the reference spectra (effect As) and a decrease in the vibrational frequency for the bending

motion of the bridging M-O-M (effect Ab), whereas the latter leads to an decrease in the the stretching frequencies. For example, the anion-anion interaction belongs to effect A and hydrogen bonding belongs to effect B. Therefore, the band shifts will be determined by these two competing effects. When effect A is predominant, a blue shift will result in  $V(M=O_d)$ . When they contribute equally, there will be no band shifts.

Generally speaking, in this work, red shift of vasv(M=O<sub>d</sub>) for the POMs in the gallery were observed most commonly due to the predomination of hydrogen bonding between M=O in POMs and the hydroxyl group in the host layer. The size of the POMs in the gallery can be calculated by subtracting the thickness of the hydroxyl layer (4.8 Å) from the basal spacings of the LDH-POMs determined from the XRD data. The size of the intercalated Keggin type POM is about 9.6 Å to 9.8 Å, which is smaller than that obtained for POMs (10.4 Å) in crystallographic studies. 135b) This observation strongly suggests that the interaction between the guest POM and the host hydroxyl layer is strong. Such a strong interaction causes d-spacing contraction, with resulting stabilization of POMs in the gallery. Most POMs except PV14O42 are stable in the gallery even in boiling water. In this latter case, a blue shift of the  $v(V=O_d)$  band was observed when the compound was in the gallery. This blue shift arises from the predomination of the anion-anion interactions in the gallery. These interactions cause an increase in the potential energy of POM network, thereby increasing the vibrational frequency. In fact, PV14O42 is not a keggin structure but is a derivative, having two more V=Od units located on opposite sides of the C3 axis of the original Keggin structure as shown in Fig. 26. The distance between these two V=Od is about 13.4 A.139 The resulting shape resembles a football. The long axis is about 13.4 Å and the short axis 10.4 Å. The PV14O42 ion is oriented in the gallery so that the long axis is parallel to the hydroxyl layer. Such orientation will result in a decrease of the distance between POMs, thereby enhancing the anion-anion interaction.

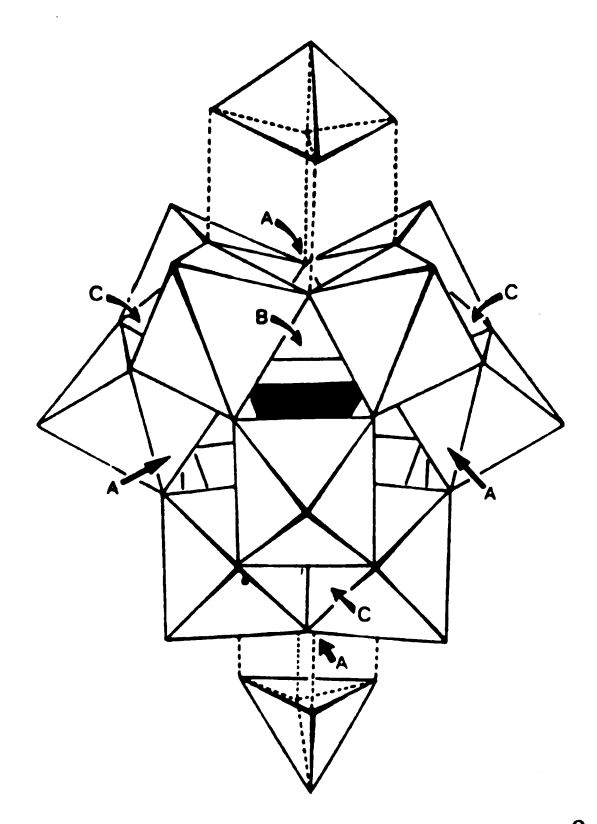


Fig. 26. The polyhedral model of the  $PV_{14}O_{42}^{9-}$  anion.

In order to explain the anon-anion interaction in the gallery, we define a new quantity, the average distance between the POMs in the gallery. This quantity is obtained on the basis of the hexagonal array of the POM in the gallery. Its detail will be discussed in the other section. In the case of PV14O42, which has a football like shape, the average distance is 13.2 Å, which is smaller than the longest axis (13.4 Å) and larger than the shortest axis (10.4 Å). Thus, two neighboring POMs can be oriented so that they can contact each other. Rocchiccioli-Deltcheff et al135 b) reported that the interaction would be effective if the distance between POMs is less than 6 Å. Therefore, the perturbation will spread over the POM framework. This anion-anion interaction results in unusual behavior, such as the instability of POMs in the gallery at high temperature in water, its thermal instability in the solid state, and a blue shift of the  $v(V=O_d)$  band on intercalation.

#### c) Vibrational Study of LDH-POMs

The details of each system are discussed below. All band positions with their assignments except those for NaP5W30O110 and LDH-NaP5W30O110 are listed in Table. 13.

LDH-H<sub>2</sub>W<sub>12</sub>O<sub>40</sub><sup>6-</sup>: When H<sub>2</sub>W<sub>12</sub>O<sub>40</sub> is intercalated into the LDH, it experiences two opposing effects, that is, effect A and effect B as discussed above. In this case, effect B is predominant, inducing a red shift (about 11 cm<sup>-1</sup>) for the band assigned as  $v(W=O_d)$ , even though the average distance between the POMs in the gallery is short enough (10.7 Å) to promote a effect A. The ir spectra of POMs under the two different surroundings are shown in Fig. 27. There is also a red shift of  $v(W-O_c-W)$  from 760 cm<sup>-1</sup> for the NH<sub>4</sub>+ salt to 757 cm<sup>-1</sup> for H<sub>2</sub>W<sub>12</sub>O<sub>40</sub> in the intercalated state. The red shift of this band is due to the effect Ab and effect B, as was pointed out by Rocchiccioli-Deltcheff. 135 b) The unlisted bands are  $\delta(OH)$  at 620 cm<sup>-1</sup> and v(Zn-O-Al) at 427 cm<sup>-1</sup>.

LDH-BVW<sub>11</sub>O<sub>40</sub>7-: In this complex there is almost no observable shift for  $\nu(W=O_d)$  even though the average distance between the POMs in the gallery is 11.6 Å. Therefore,

Table 13

Infrared Spectral Data of Free-POMs and LDH-POMs

Compounda		Assignmentb				
(NH4)6H2W12O42	vas(X-O <sub>a</sub> ) <sup>c</sup> -	<u>vas(M=Od)</u> 936	ν(M-O-M) 901, 871,	<u>Δν</u> <u>d</u>		
LDH-H <sub>2</sub> W <sub>12</sub> O <sub>40</sub>	-	925	760 895, 757	11		
K7BVW11O40	990, 908	947	885, 811, 693, 673	-		
LDH-BVW <sub>11</sub> O <sub>40</sub>	998, 905	949	807, 695 668	-2		
K6HSiV3W9O40 LDH-SiV3W9O40	1007 1003	915, 965 913, 959	782, 634 780	- e		
$\alpha$ -K <sub>8</sub> SiW <sub>11</sub> O <sub>39</sub>	995	960	891, 799	-		
LDH-SiW <sub>11</sub> O <sub>39</sub>	1001	955	728 791, 762 715	5		
K7PMo2W9O39	1082, 1046	945	897, 855	-		
LDH-PMo2W9O39	1033 1081, 1050	946	811, 734 803, 745	-1		
K9BW11O39	995, 917	954	884, 870 836, 811 788, 751	-		
LDH-BW <sub>11</sub> O <sub>39</sub>	985	939	719 896, 786 783, 716	5		
K7BCuW11O39	987, 907	940	875, 810 711	-		
LDH-BCuW <sub>11</sub> O <sub>39</sub>	986	937	897, 807 710	3		
K7BCoW11O39	984, 912	940	885, 820 775	-		
LDH-BCoW <sub>11</sub> O <sub>39</sub>	984	937	897, 815 782	3		
K7SiFe(SO3)W11O39	996	953	885, 797	-		
LDH-SiFe(SO <sub>3</sub> )W <sub>11</sub> O <sub>39</sub>	1000	952	727 903, 784 716	1		
β-Na <sub>8</sub> HPW <sub>9</sub> O <sub>34</sub>	1055, 1014	936	882, 819	-		
LDH-PW9O34	1083, 1057	947	748 809, 685	-11		

Table 13 continued

(NH4)8Co2W12O42	-	937	881, 790	-
LDH-Co <sub>2</sub> W <sub>12</sub> O <sub>42</sub>	-	917	752, 872, 787 735,	20
(NH4)9PV <sub>14</sub> O <sub>42</sub>	1060	938	867, 810 810, 770	-
LDH-PV <sub>14</sub> O <sub>42</sub>	1057	943	805, 757	-5
(NH4)10H2W12O42	-	950, 934	871, 861 765, 699	-
LDH-H2W12O42		932	863, 798, 702	e

- a Hydrated waters were omitted for simplicity and the data for (NH4)14NaP5W30O110 and LDH-NaP5W30O110 are not listed because of the ambiguity of band assignments.

  Their band positions are in the text.
- Band assignments were done only for three characteristicvibrations modes of POMs.
- c Frequency unit is cm<sup>-1</sup>.
- d  $\Delta v$  is obtained by substracting  $v(M=O_d)$  of free POM from that of LDH-POM.
- e Details are in the text.

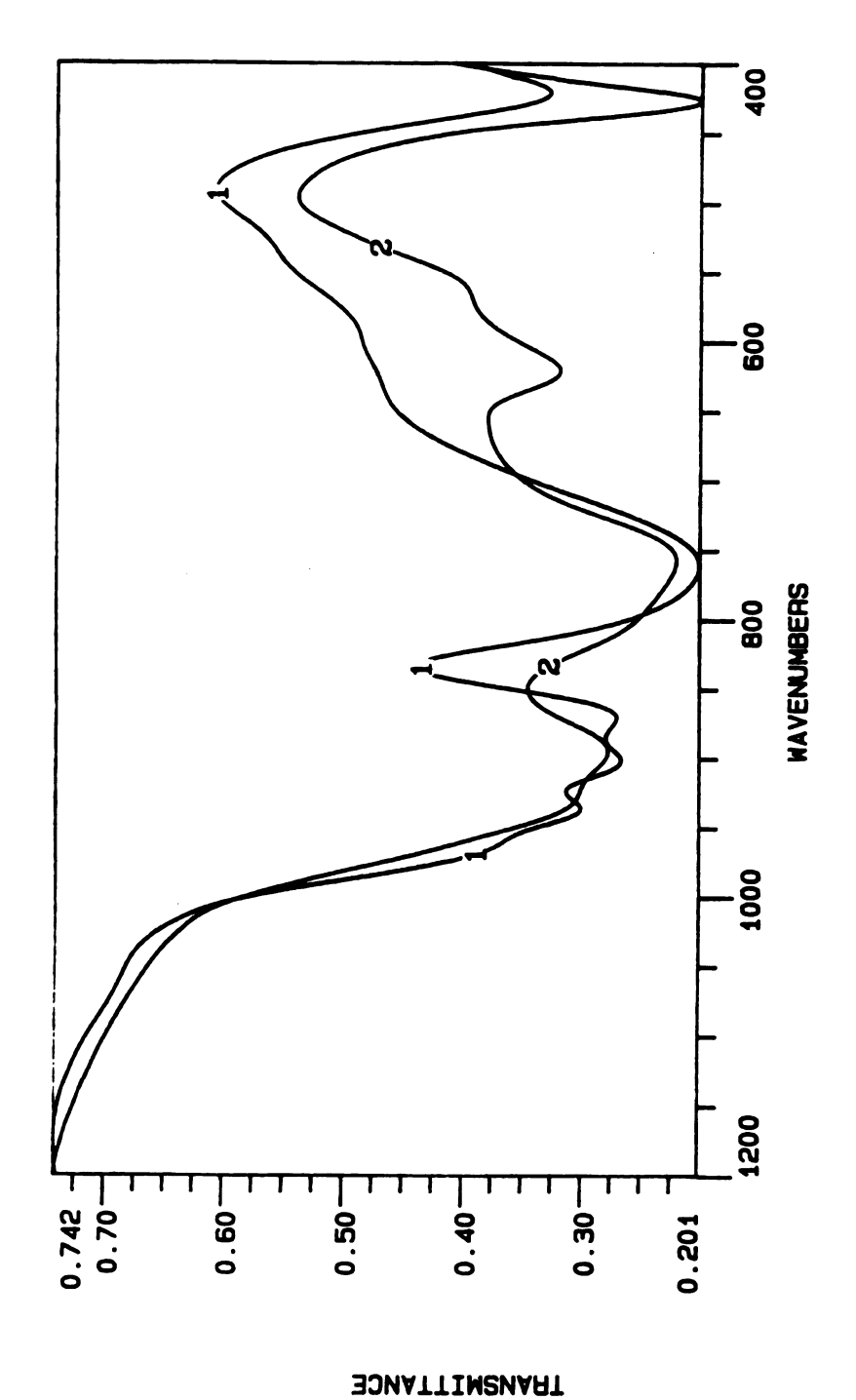


Fig. 27. Ir spectra of 1) (NH<sub>4</sub>)<sub>6</sub>H<sub>2</sub>W<sub>12</sub>O<sub>40</sub> and 2)LDH-H<sub>2</sub>W<sub>12</sub>O<sub>40</sub>.

the two opposing effects are almost balanced. A band for  $\nu(W-O_c-W)$  shifts from 811 cm<sup>-1</sup> for the K+ salt to 807 cm<sup>-1</sup> for the intercalated anion due to effect A and effect B. The unlisted remaining bands are  $\delta(OH)$  at 623 cm<sup>-1</sup>, an unassigned band at 559 cm<sup>-1</sup> and  $\nu(Zn-O-Al)$  at 427 cm<sup>-1</sup>. The ir spectra under the two different environment are very similar, as presented in Fig. 28.

**LDH-SiV3W9O40**<sup>7-</sup>: There are two strong bands assigned as  $v(M=O_d)$  at 965 and 915 cm<sup>-1</sup>. They are shifted from 959 and 913 cm<sup>-1</sup> for the K+ salt, respectively. The former bands shift more than the latter. The most basic sites of SiV3W9O40<sup>7-</sup>, that is, the oxygen atoms bound at V atoms, prefer to hydrogen bond with the hydroxyl group of the layer. Therefore, V=O<sub>d</sub> will participate in the hydrogen bonding more strongly than W=O<sub>d</sub>, with the result that the shift is greater than those of other W=O<sub>d</sub>. As a result, a band at 959 cm<sup>-1</sup> for LDH-SiV3W9O40 and a band at 965 cm<sup>-1</sup> for the K+ salt of SiV3W9O40 can be assigned as  $v(V=O_d)$ . As in the other cases,  $v(M-O_c-M)$  shifts from 782 cm<sup>-1</sup> in the K+ salt to 780 cm<sup>-1</sup> for the anion in the gallery due to effect Ab and effect B. The unlisted remaining bands are  $\delta(OH)$  at 622 cm<sup>-1</sup>, an unassigned band at 549 cm<sup>-1</sup> and v(Zn-O-Al) at 428 cm<sup>-1</sup>. The similar ir spectra for SiV3W9O40 under the two different environments, as shown in Fig. 29, indicate identical anion structures.

LDH-SiW11O39<sup>8-</sup>: In this case the B effect is predominant, so the  $v(W=O_d)$  band in the K+ salt at 960 cm<sup>-1</sup> shifts to 955 cm<sup>-1</sup> for the anion in the LDH. The average distance between the POM in the gallery is 12.4 Å. As in the other cases, there are red shifts in the  $v(W-O_c-M)$  band from 799 and 728 cm<sup>-1</sup> for the K+ salt to 791 and 715 cm<sup>-1</sup> for the LDH intercalated anion, as shown in Fig. 30. The band splitting of  $v(W-O_c-W)$  is conserved, suggestive that the POM in the gallery still has a lacunary Keggin structure. The unlisted remaining bands are  $\delta(OH)$  at 621 cm<sup>-1</sup>, an unassigned band at 545 cm<sup>-1</sup> and v(Zn-O-Al) at 429 cm<sup>-1</sup>. The similarities in the ir spectra of the anion under the two different environments confirms their identical structures.

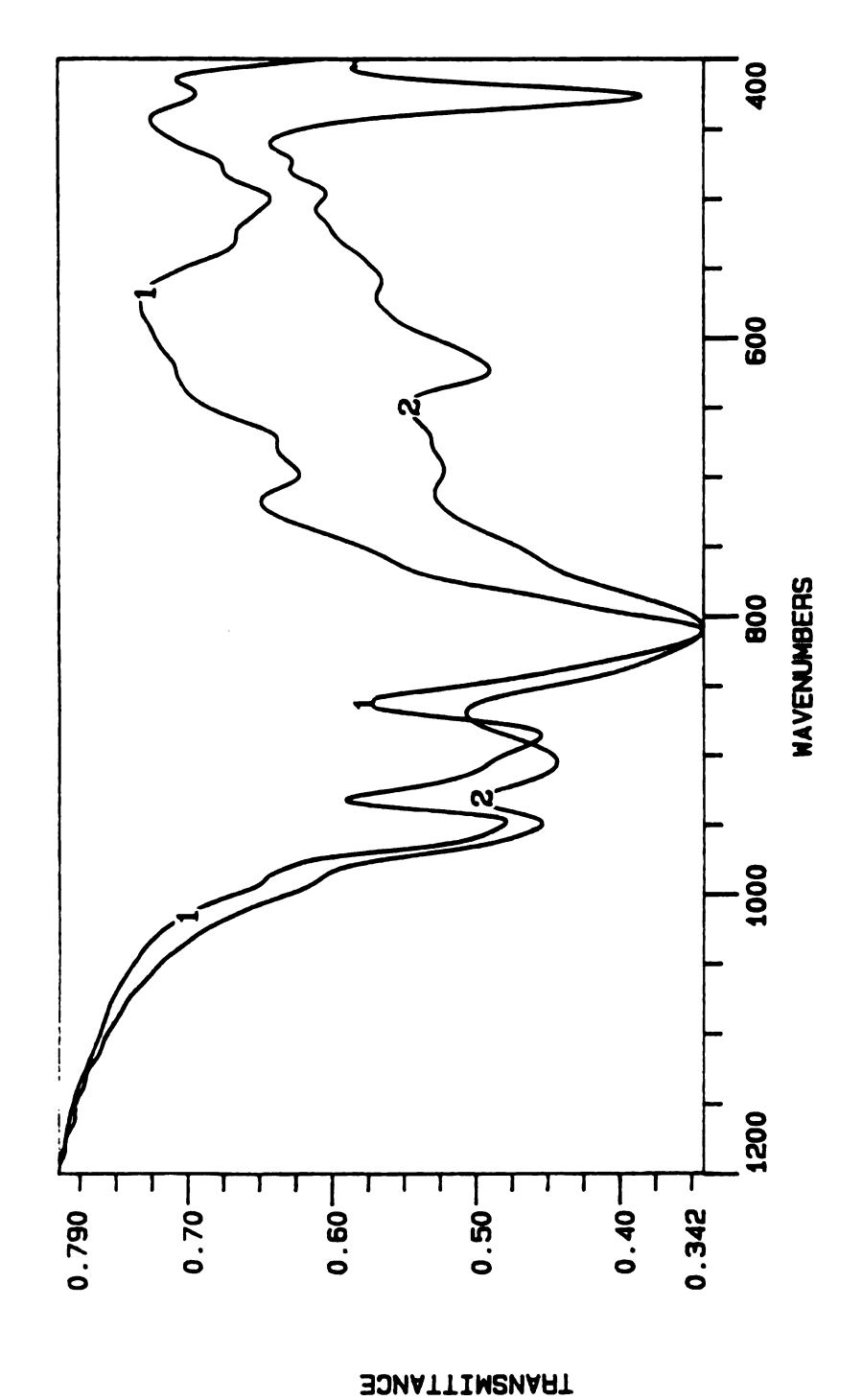


Fig. 28. Ir spectra of 1)  $K_6BVW_{11}O_{40}$  and 2) LDH-BVW $_{11}O_{40}$ .

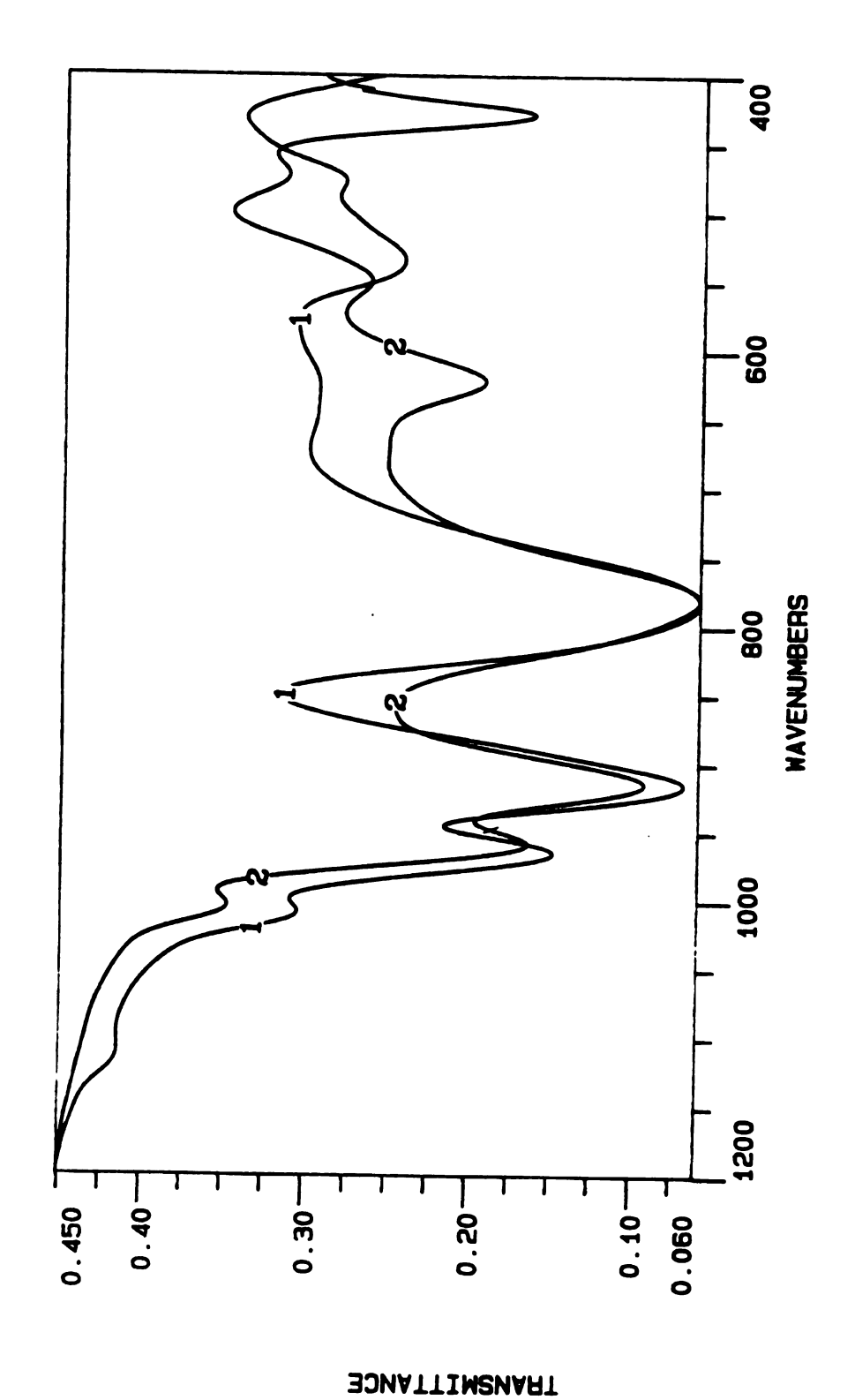


Fig. 29. Ir spectra of 1)  $\alpha$ -K<sub>6</sub>HSiV<sub>3</sub>W<sub>9</sub>O<sub>40</sub> and 2) LDH-SiV<sub>3</sub>W<sub>9</sub>O<sub>40</sub>.

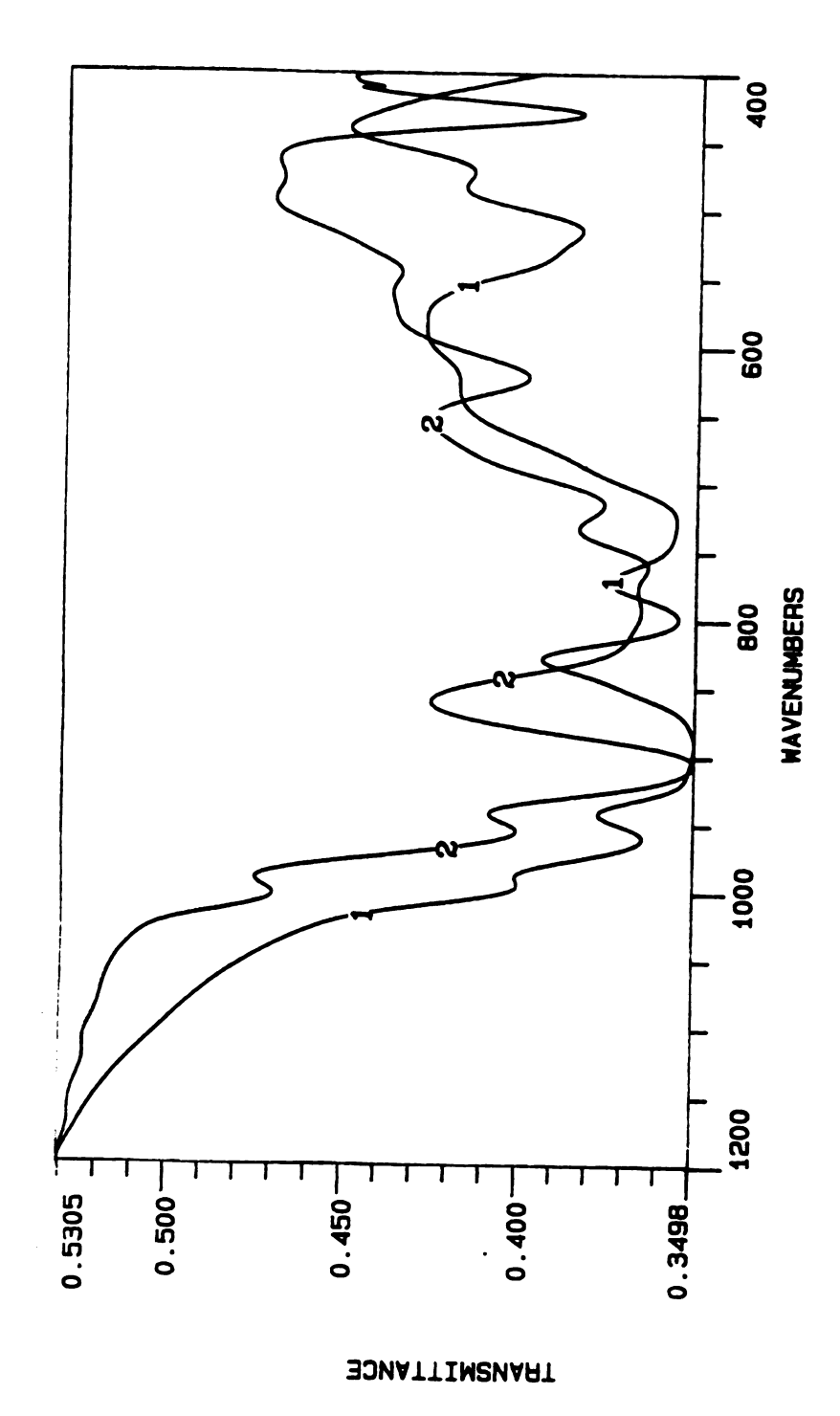


Fig. 30. Ir spectra of 1) K8SiW11O39 and 2) LDH-SiW11O39.

LDH-PMo<sub>2</sub>W<sub>9</sub>O<sub>39</sub><sup>7-</sup>: In this complex two opposing effects are well balanced, so no band shift is observed. However, similar to other cases, there is a red shift in  $\nu$ (M-O-M) from 811 cm<sup>-1</sup> for the K+ salt to 803 cm<sup>-1</sup> for the intercalated anion due to an effect Ab and an effect B. The three well-resolved bands attributed to  $\nu$ (M-O<sub>C</sub>-M) are merged into two bands for the intercalated ion, as given in Fig. 31. The unlisted remaining bands are  $\delta$ (OH) at 621 cm<sup>-1</sup>,  $\nu$ (Zn-O-Al) at 559 and 427 cm<sup>-1</sup>, and an unassigned band at 519 cm<sup>-1</sup>.

LDH-BW11O39<sup>9-</sup>: In this complex, the effect B is predominant so  $v(W=O_d)$  shifts from 954 cm<sup>-1</sup> in the K+ salt to 939 cm<sup>-1</sup> in the intercalated anion. The average distance between the POMs in the gallery is 13.2 A. In the K+ salt there are several bands corresponding to  $v(W-O_c-W)$ , as listed in Table 13. The other band positions at 625 cm<sup>-1</sup>, 513 and 479 cm<sup>-1</sup> are unassigned, see Fig. 32. Due to effect Ab and effect B, the two bands at 788 and 719 cm<sup>-1</sup> in the K+ salt are shifted to 783 and 716 cm<sup>-1</sup> in the intercalated anion. The remaining bands are  $\delta(OH)$  at 620 cm<sup>-1</sup> and v(Zn-O-Al) at 562 and 427 cm<sup>-1</sup>.

LDH-BCu(H<sub>2</sub>O)W<sub>1</sub>1O<sub>3</sub>9<sup>7-</sup>: In this complex the effect B is predominant, so  $v(W=O_d)$  shifts from 940 cm<sup>-1</sup> in the K+ salt to 937 cm<sup>-1</sup> in the intercalated anion, as provided in Fig. 33. As in other examples,  $v(W-O_c-W)$  bands shift to lower frequencies due to effect Ab and B. The remaining bands are  $\delta(OH)$  at 622 cm<sup>-1</sup>, v(Zn-O-Al) at 562 and 426 cm<sup>-1</sup>, and an unassigned band at 495 cm<sup>-1</sup>. The similarities of the ir spectra of POMs under two different environments suggests the structure of the POM is conserved in the layer. LDH-BCo(H<sub>2</sub>O)W<sub>1</sub>IO<sub>3</sub>9<sup>7-</sup>: This complex exhibits a dominant B effect, so a red shift (3 cm<sup>-1</sup>) is observed; see Table 12. As in the other cases,  $v(W-O_c-W)$  at 820 cm<sup>-1</sup> for the K+ salt shifts to a lower frequency, 815 cm<sup>-1</sup>, in the LDH intercalate due to effect Ab and B. The unlisted remaining bands are  $\delta(OH)$  at 623 cm<sup>-1</sup> and v(Zn-O-Al) at 562 and 427 cm<sup>-1</sup>. A band at 492 cm<sup>-1</sup> can be assigned as  $\delta(B-O_a)$  shifted from 499 cm<sup>-1</sup> for the

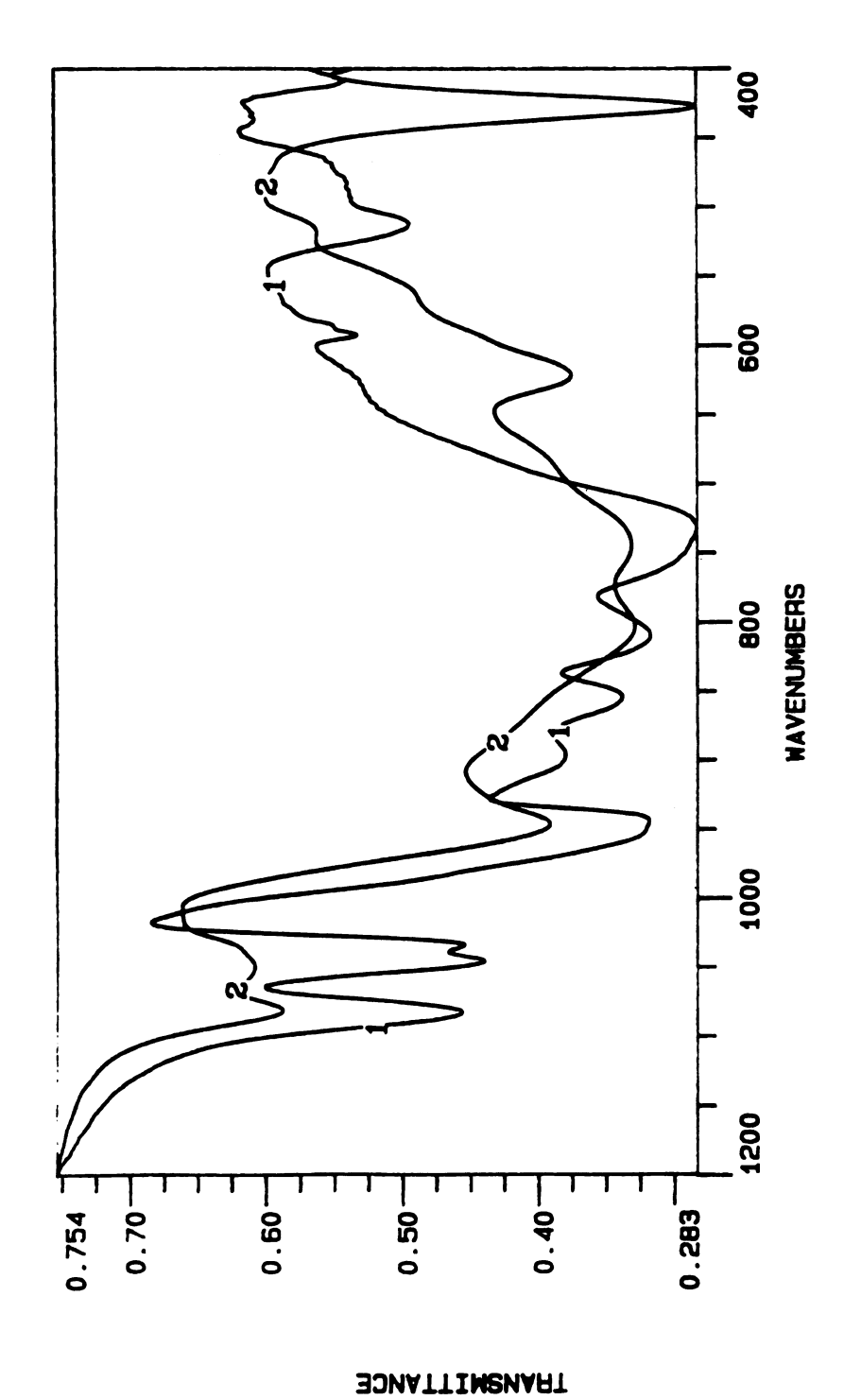


Fig. 31. Ir spectra of 1) K7PMo2W9O39 and 2) LDH-PMo2W9O39.

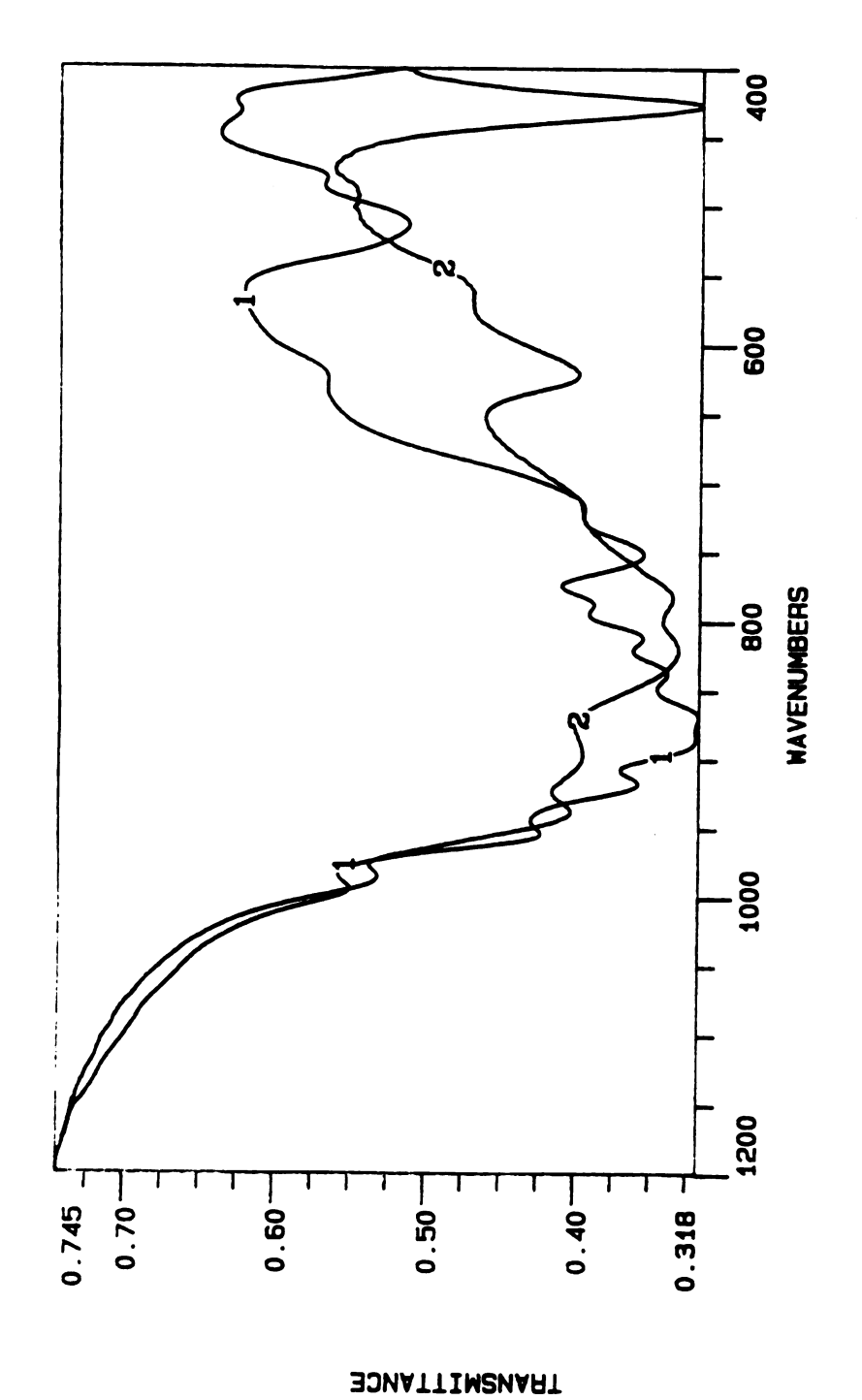


Fig. 32. Ir spectra of 1) K9BW11O39 and 2) LDH-BW11O39.

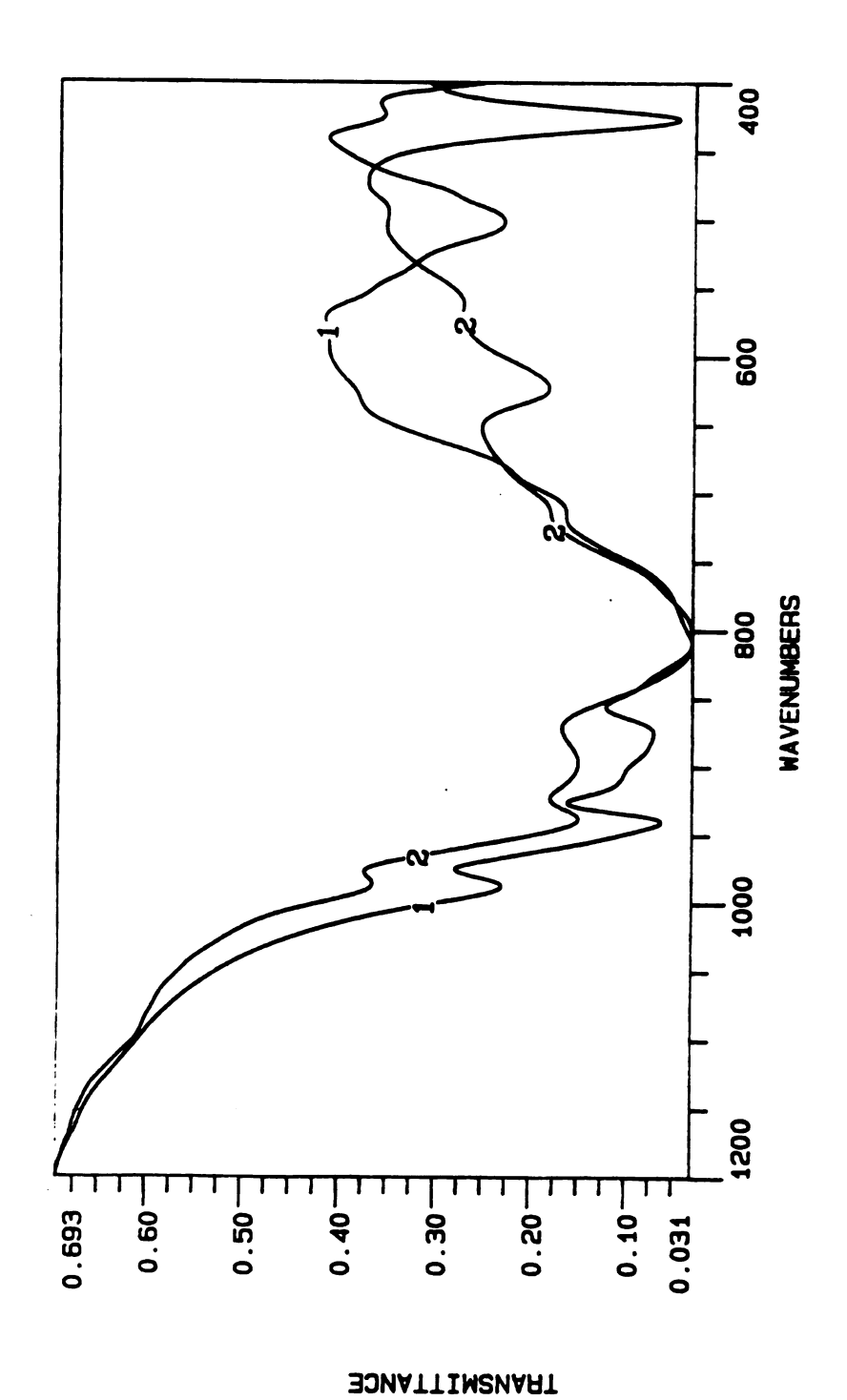


Fig. 33. Ir spectra of 1) K<sub>7</sub>BCuW<sub>11</sub>O<sub>39</sub> and 2) LDH-BCuW<sub>11</sub>O<sub>39</sub>.

K<sup>+</sup> salt. The similarities of the ir spectra of the POM under the two different circumstances are apparent in Fig. 34.

LDH-SiFe(SO<sub>3</sub>)W<sub>11</sub>O<sub>39</sub>7-: In this system, there is almost no band shift in  $\nu(W=O_d)$ , reflective that the two opposing effects are well balanced. However, as in the other cases, there are red shifts of  $\nu(W-O_c-W)$  from 797 and 727 cm<sup>-1</sup> in the K<sup>+</sup> salt to 784 and 716 cm<sup>-1</sup> in the intercalated anion. The other bands are  $\delta(OH)$  at 621 cm<sup>-1</sup> and  $\nu(Zn-O-Al)$  at 543 and 427 cm<sup>-1</sup>. The similarities of the ir spectra of the POM under the two different surroundings can be easily noticed in Fig. 35.

LDH-PW9O349-: Remarkable blue shifts are observed in this system. The v(P-O<sub>2</sub>) bands shift from 1055 and 1014 cm<sup>-1</sup> in the Na+ salt to 1083 and 1057 cm<sup>-1</sup> in the intercalated anion. Such blue shifts indicate strengthening of the P-Oa bond of the POM in the gallery. The v(W=O<sub>d</sub>) also exhibits a blue shift from 936 cm<sup>-1</sup> in the Na<sup>+</sup> salt to 947 cm<sup>-1</sup> in the intercalated anion. Such blue shifts may not be due to effect A because the average distance between the POMs in the gallery is 13.2 Å, as in the LDH-BW11O39 where an effect B was found to dominate. In general, it has been observed that v(W=O<sub>d</sub>) depends on the degree of the degradation of XM<sub>12</sub>O<sub>40</sub>, that is,  $v(XM_{12}O_{40}) > v(XM_{11}O_{39}) > v(XM_9O_{34})$ . From consideration of the band positions, it is plausible to suggest that the anion in the gallery is stabilized by forming a XM<sub>11</sub>M'O<sub>39</sub>-like surrounding. The band broadening in the 1000 - 650 cm<sup>-1</sup> region, which corresponds to the v(M-O-M) range, may be attributed to such an unusual surrounding of PW9O34 in the gallery. As shown in Fig. 36 the differences in the ir spectra of the anion under the two different circumstances are easily recognizable. The unlisted remaining bands are  $\delta(OH)$  at 620 cm<sup>-1</sup> and  $\nu(Zn-O-Al)$  at 565 and 428 cm<sup>-1</sup>. LDH-Co2W12O428-: In this case, the B effect is remarkably predominant so that v(W=O<sub>d</sub>) shifts from 937 cm<sup>-1</sup> in the NH<sub>4</sub>+ salt to 917 cm<sup>-1</sup> in the intercalated anion. There are also red shifts in v(W-O<sub>C</sub>-W) bands as in the other cases. Remaining bands include unassigned bands at 520 and 488 cm<sup>-1</sup>,  $\delta$ (OH) at 625 cm<sup>-1</sup> and  $\nu$ (Zn-O-Al) at

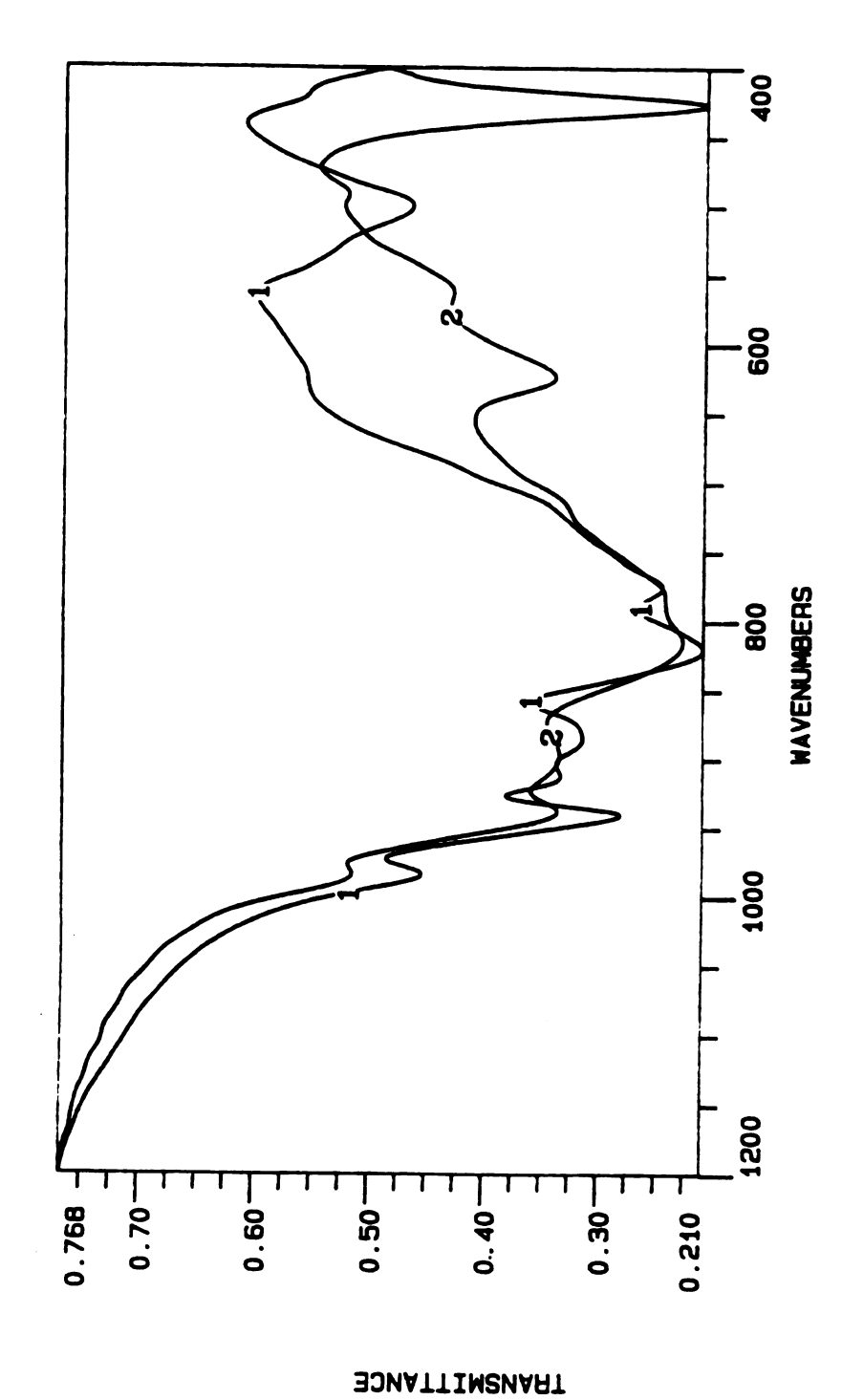


Fig. 34. Ir spectra of 1) K<sub>7</sub>BCoW<sub>11</sub>O<sub>39</sub> and 2) LDH-BCoW<sub>11</sub>O<sub>39</sub>.

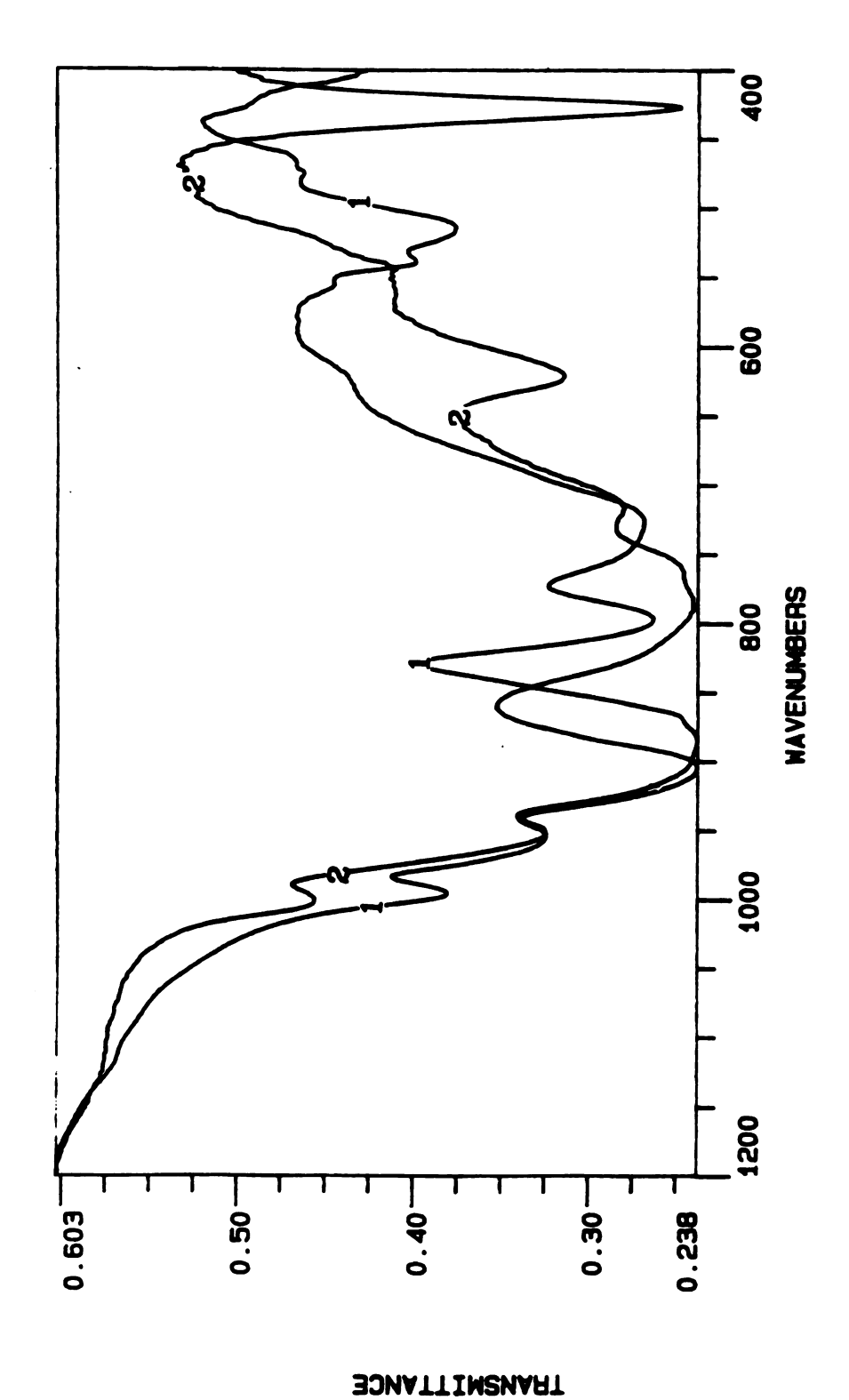


Fig. 35. Ir spectra of 1) K<sub>7</sub>SiFe(SO<sub>3</sub>)W<sub>11</sub>O<sub>39</sub> and 2) LDH-SiFe(SO<sub>3</sub>)W<sub>11</sub>O<sub>39</sub>.

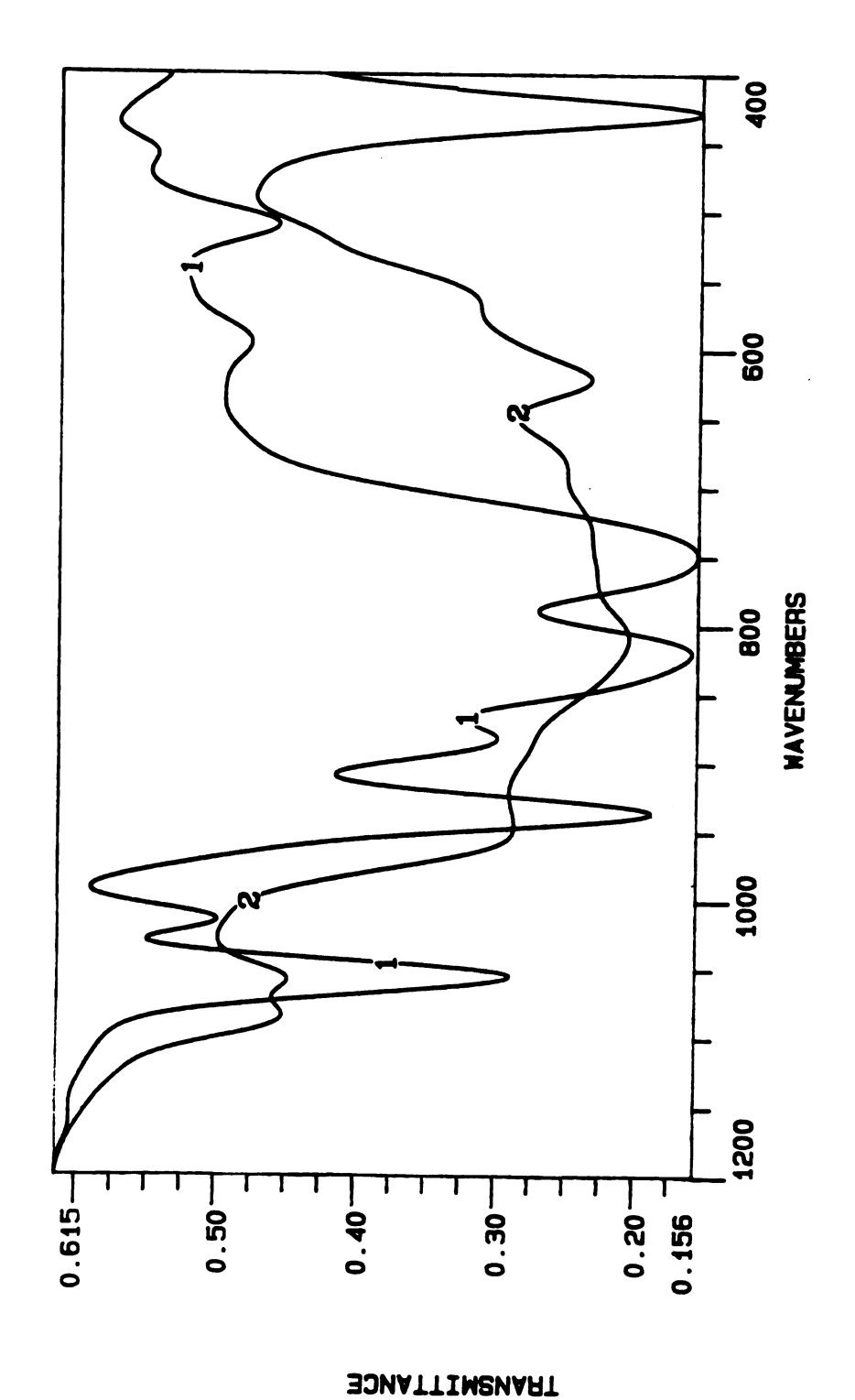


Fig. 36. Ir spectra of 1) \(\beta\)-NagHW9O34 and 2) LDH-PW9O34.

428 cm<sup>-1</sup>. The ir spectra of the anion under the two different circumstances are presented in Fig. 37.

LDH-PV<sub>14</sub>O<sub>42</sub>9-: This system was discussed previously. The unlisted remaining bands are  $\delta$ (OH) at 612 cm<sup>-1</sup> and  $\nu$ (Zn-O-Al) at 565 and 427 cm<sup>-1</sup>. The ir spectra of the anion under the two different circumstances are given in Fig. 38.

LDH-H<sub>2</sub>W<sub>12</sub>O<sub>42</sub><sup>10</sup>-: This is another system in which the effect B dominates. The NH<sub>4</sub>+ salt of the anion evidences two  $\nu(W=O_d)$  bands due to the two different W=O<sub>d</sub>s. One of them is engaged in hydrogen bonding with crystalline water. This bonding lowers  $\nu(W=O_d)$  to 934 cm<sup>-1</sup>, as discussed by Kiss. <sup>140</sup> Thus, the band at 950 cm<sup>-1</sup> corresponds to the non-hydrogen bonded W=O<sub>d</sub>. This band shifts to 932 cm<sup>-1</sup> in the LDH-H<sub>2</sub>W<sub>12</sub>O<sub>42</sub>, a value which is almost the same as that of the hydrogen bonded W=O<sub>d</sub>. Therefore, the ir spectrum of the intercalated anion in the LDH gallery shows only one W=O<sub>d</sub> band, as in the case of an anion in a highly hydrated state. As a result, it is obvious that the hydrogen bonding for W=O<sub>d</sub> in the POM is driven by its intercalation into the gallery. For the NH<sub>4</sub>+ salt, the remaining bands are  $\delta(W$ -OH) at 610, 555 and 532 cm<sup>-1</sup> and  $\delta(W$ -O-W) at 498 and 435 cm<sup>-1</sup>. The bands for LDH-H<sub>2</sub>W<sub>12</sub>O<sub>42</sub> are  $\delta(OH)$  at 618 cm<sup>-1</sup>,  $\nu(Zn$ -O-Al) at 560 and 427 cm<sup>-1</sup>, and  $\delta(W$ -O-W) at 493 cm<sup>-1</sup>. The ir spectra of the anion under the two different environments are provided in Fig. 39.

LDH-NaP5W30O110<sup>14-</sup>: Even though the band assignments for this system cannot be made clearly due the complexity of the anion, the band shapes and positions of the NH4+ salt of the anion and its LDH intercalate are very similar, as is shown in Fig. 40. Therefore, the two opposing effects must be well balanced. The structure of the POM in the gallery should be identical with that in the NH4+ salt. Bands positions are as follows: (NH4)14NaP5W30O110: 1164, 1079, 1017, 985, 935, 911, 778, 737, 656, 573, 541, 473, 464 cm-1

LDH-NaP5W30O110: 1165, 1080, 1018, 984, 936, 915, 787, 737, 618, 574, 545, 466, 427 cm<sup>-1</sup>

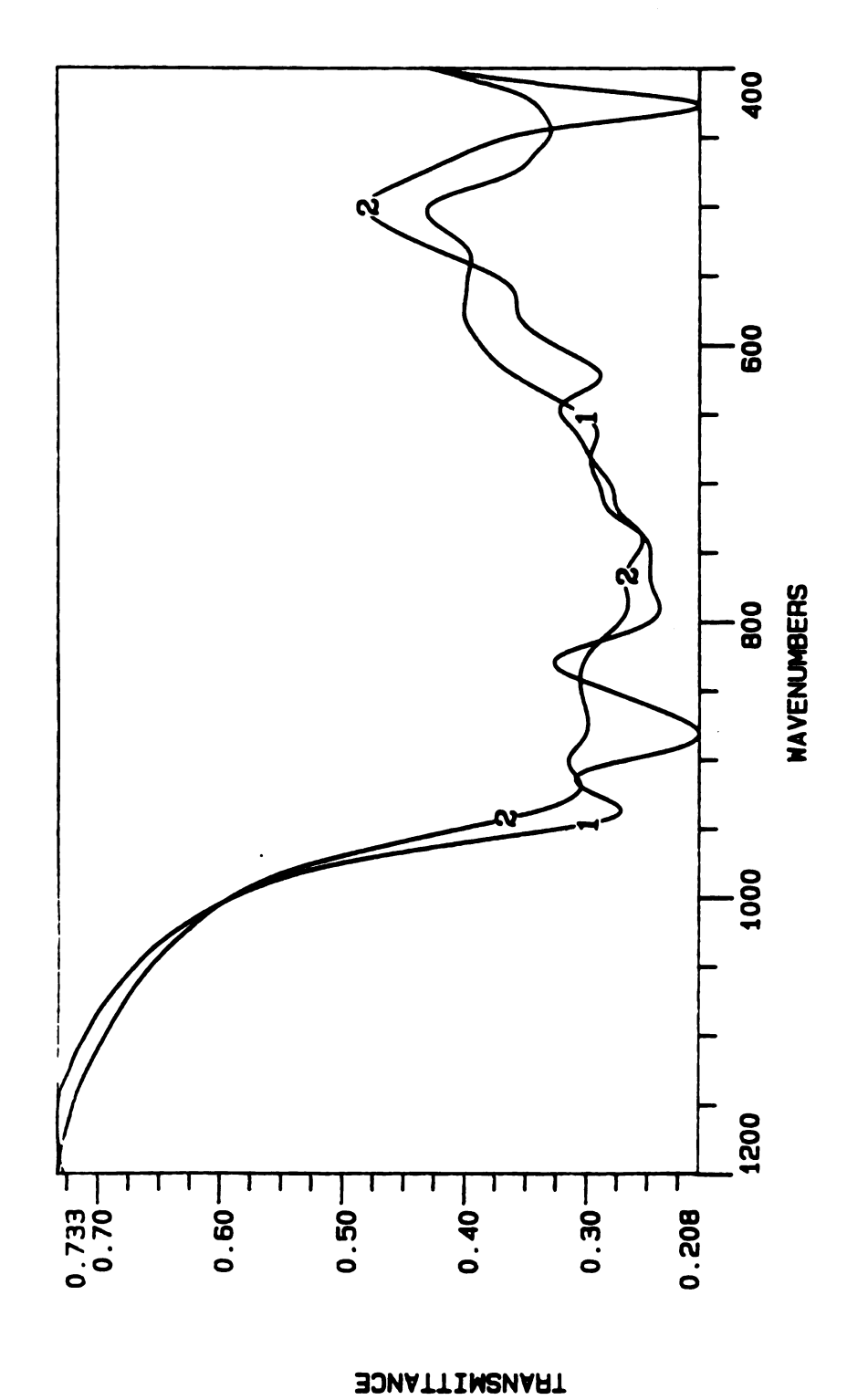
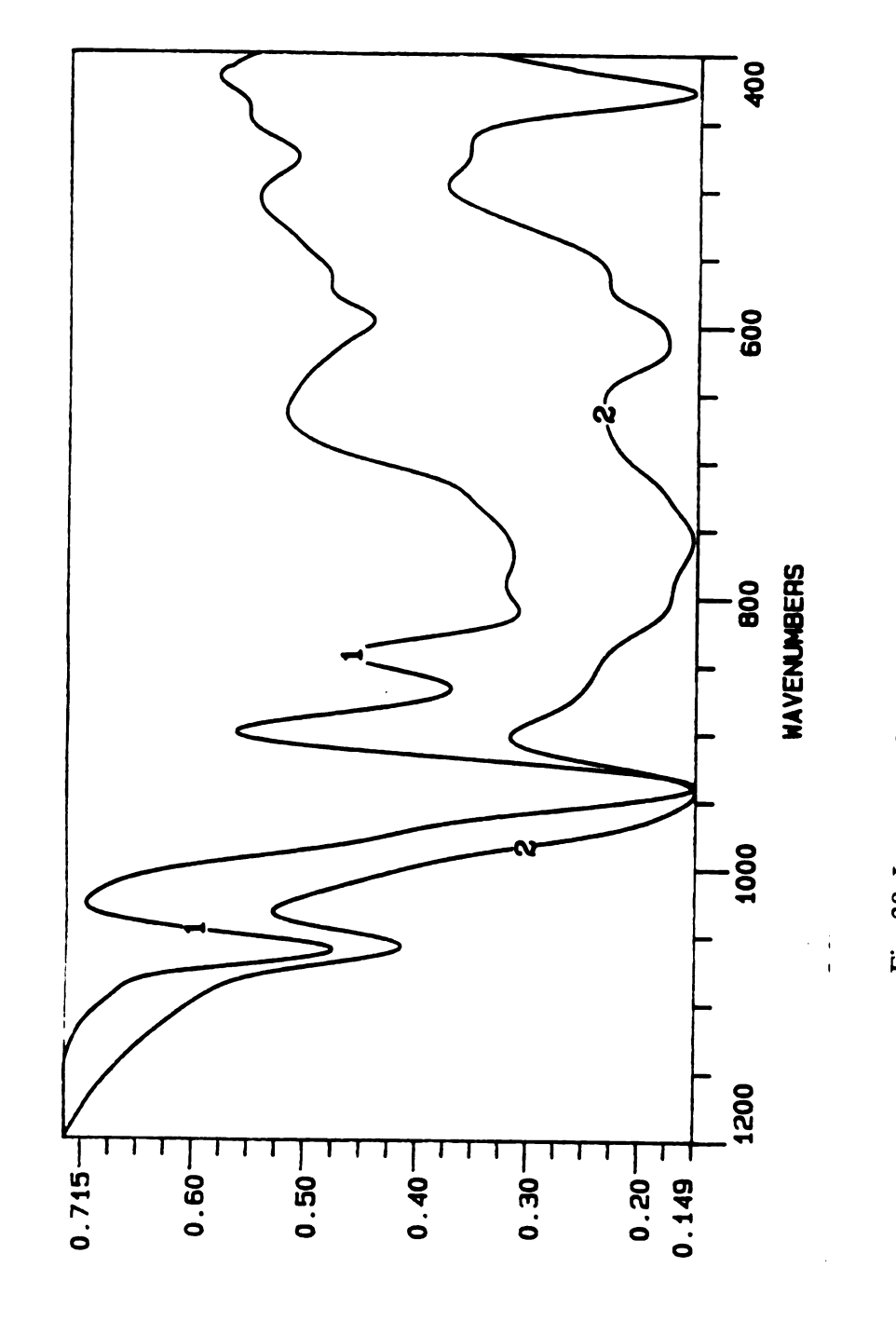


Fig. 37. Ir spectra of 1) (NH4)8Co<sub>2</sub>W<sub>12</sub>O<sub>42</sub> and 2) LDH-Co<sub>2</sub>W<sub>12</sub>O<sub>42</sub>.



THANSMITTANCE

Fig. 38. Ir spectra of 1) (NH4)9PV  $_{14}$ O $_{42}$  and 2) LDH-PV  $_{14}$ O $_{42}$ .

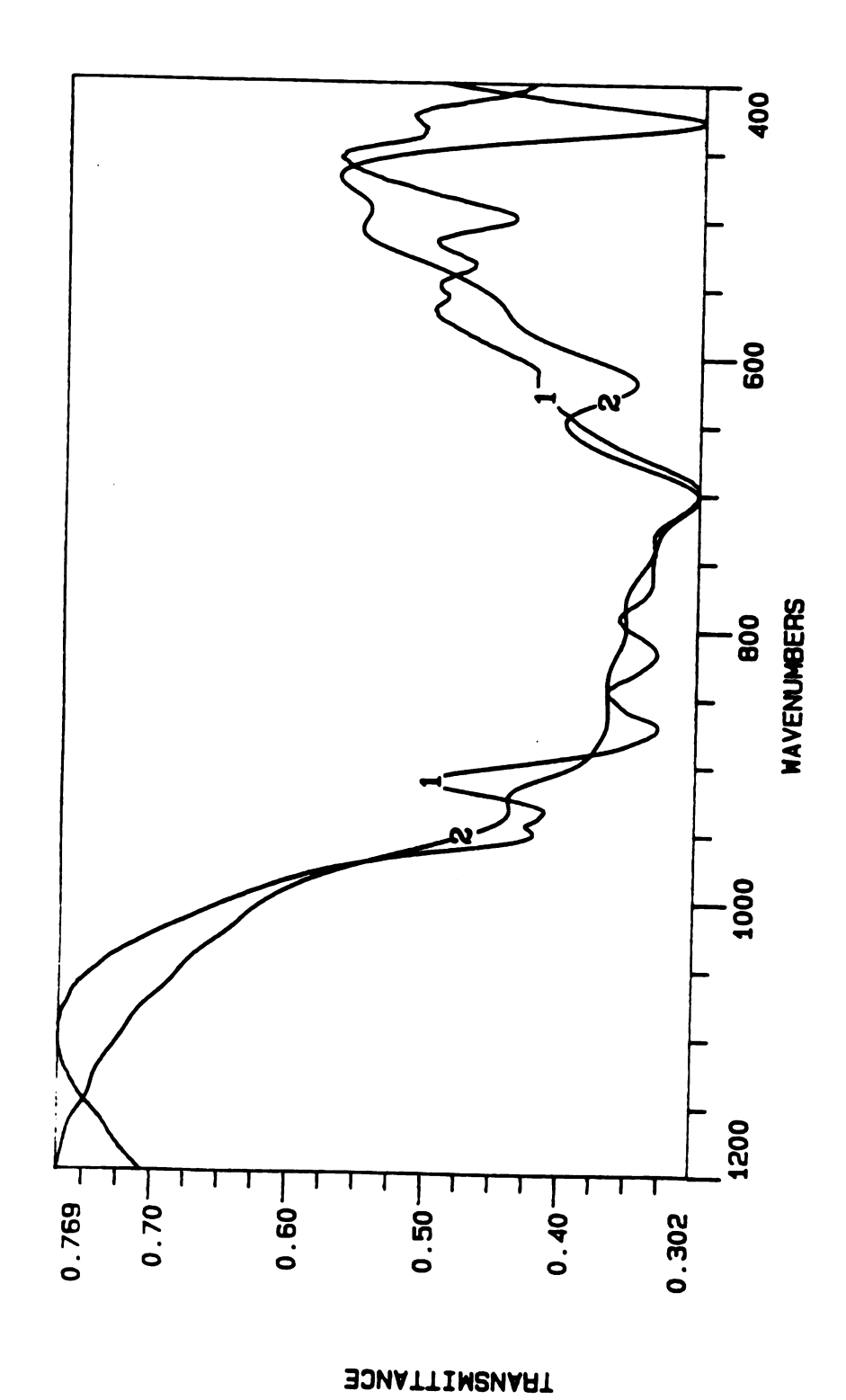


Fig. 39. Ir spectra of 1) (NH4)10W12O42 and LDH-H $_2$ W $_{12}$ O $_{42}$ .

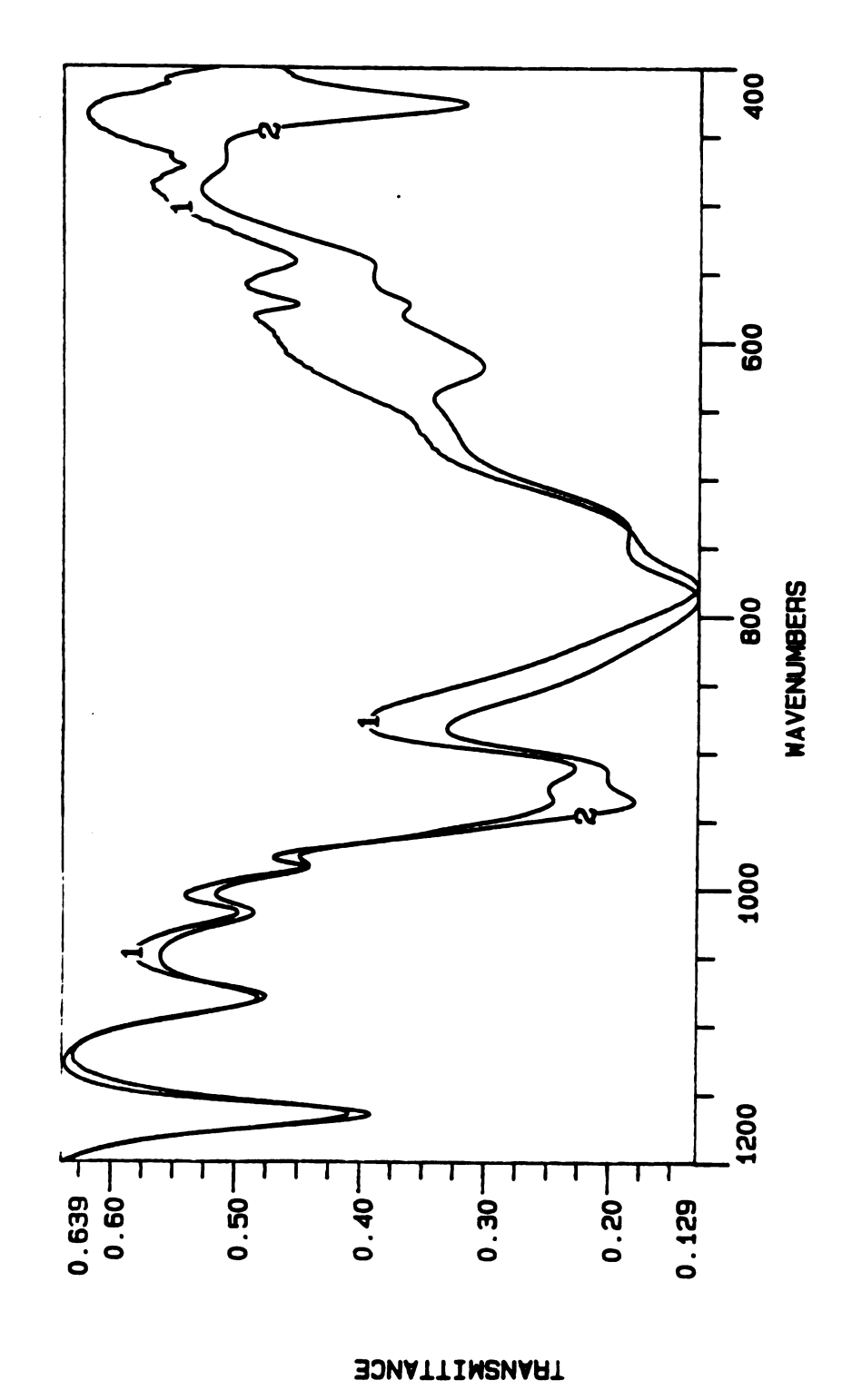


Fig. 40. Ir spectra of 1) (NH4) $_{14}$ NaP $_{5}$ W $_{30}$ O $_{110}$  and 2) LDH-NaP $_{5}$ W $_{30}$ O $_{110}$ .

In the latter case the bands due to the LDH layer are  $\delta(OH)$  at 618 cm<sup>-1</sup> and  $\nu(Zn\text{-O-Al})$  at 427 cm<sup>-1</sup>.

# D. Selectivities of ion exchange reaction and orientation of the intercalated POMs

# 1. Charge Selectivity

As discussed in the introduction chapter, the higher the charge of the anions, the more the ion is preferred by the LDH. For example, the charge density of PW12O40<sup>3</sup>- is lower than that of ClO4<sup>-</sup>. Such low charge densities are unfavorable for intercalation in LDH. As will be discussed in the gas adsorption study section, the minimum charge for the intercalation of POM with a Keggin structure is 4.8 - 5.0. This calculation was based on a comparison of the surface charge density of the LDH and POM. However, in this calculation any repulsive interactions between POMs in the gallery were not taken into account. When repulsions are taken into account, the POMs repel each other in the same gallery.

When POMs having a 5- charge were allowed to react with LDH-NO3, only partial ion exchange was observed, even when a large excess of POMs was used. Fig. 41 shows the existence of two phases, one for the LDH-POM and the other for unexchanged LDH-NO3. Such partial ion exchanges occurred even with POMs having 6- charge, but H2W12O406- was an exception even though very small amount of unexchanged NO3-was detected by ir spectroscopy. Fig. 42 illustrates the XRD of LDH-POMs with POM = BV(V)W11O406-, BCo(III)W11O396- and PV3W9O406-. The same types of XRD patterns are shown with that of Fig. 41, except that the peaks due to LDH-NO3 phase are much weaker. The decreased intensities of LDH-NO3 peaks indicate a smaller amount of this phase present here than in LDH-POM5-. Therefore, the POM6- is more favorably intercalated into the LDH lattice than POM5-. The more favorable ion exchange reaction of H2W12O406- relative to other POMs having the same charge can not be explained by

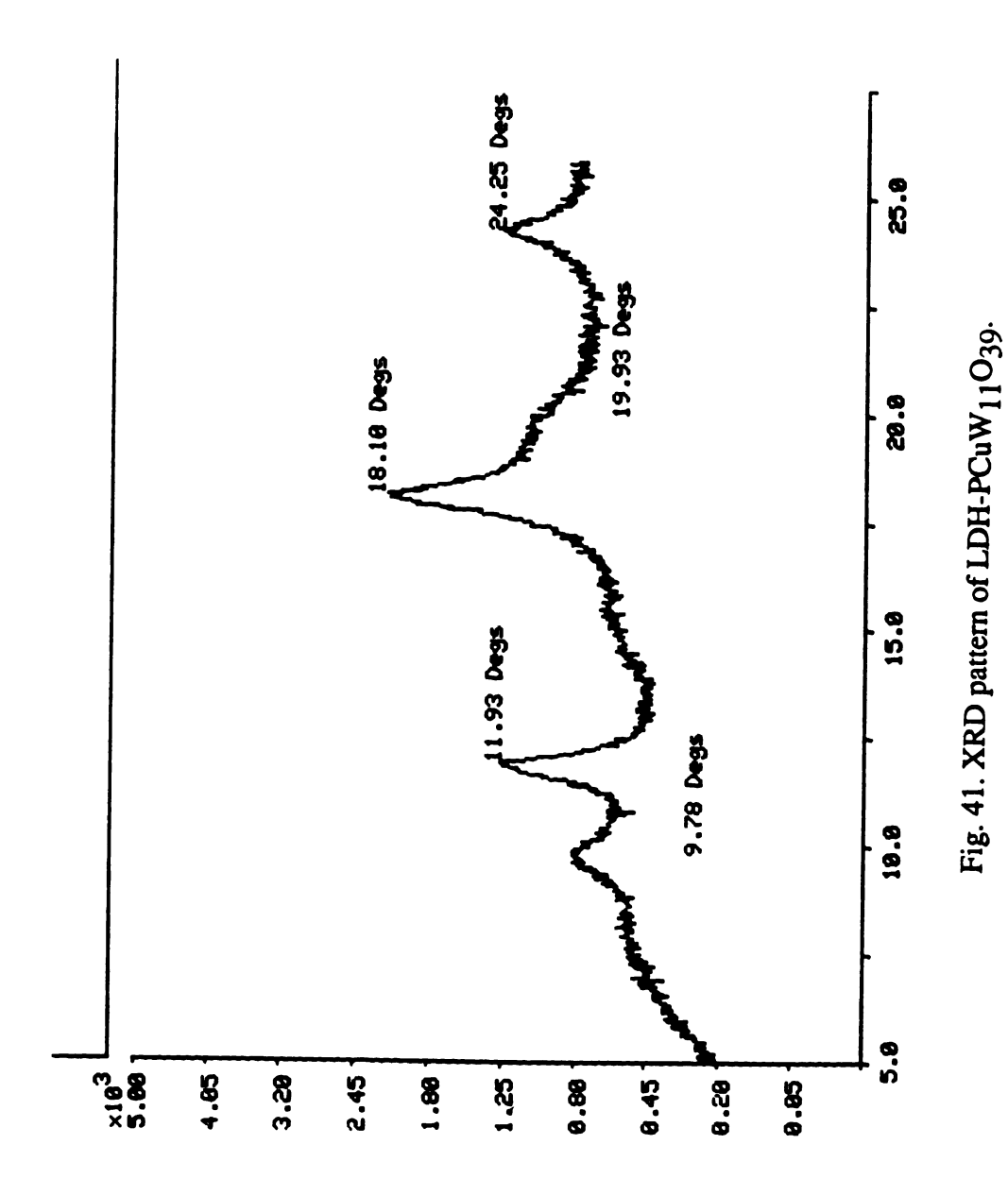
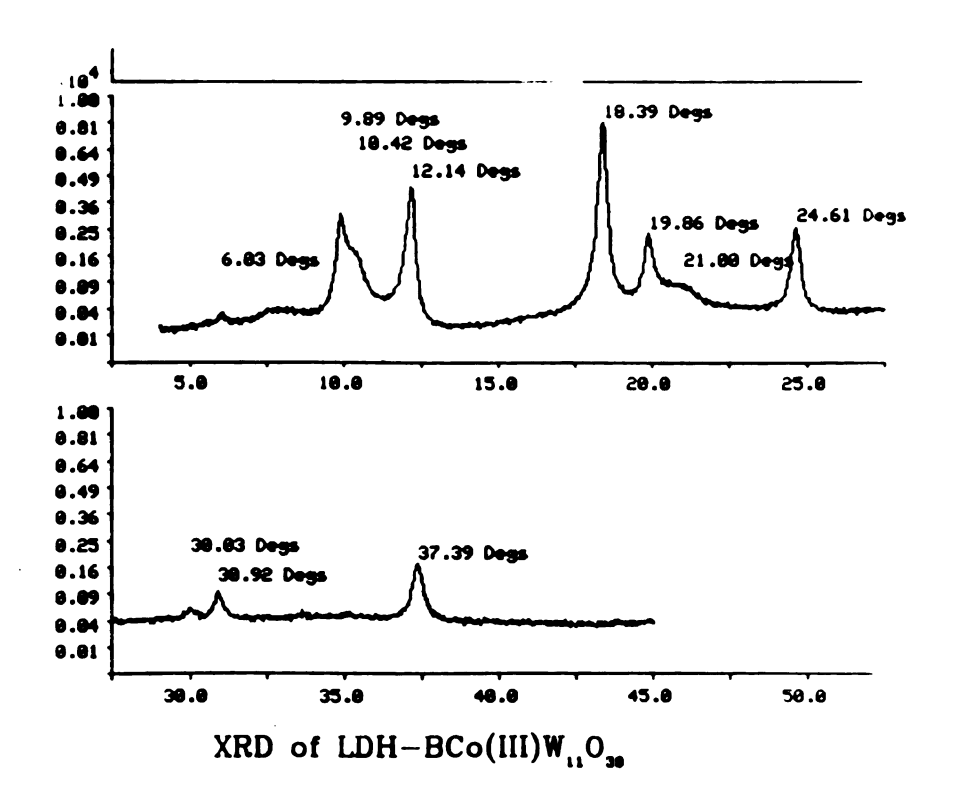
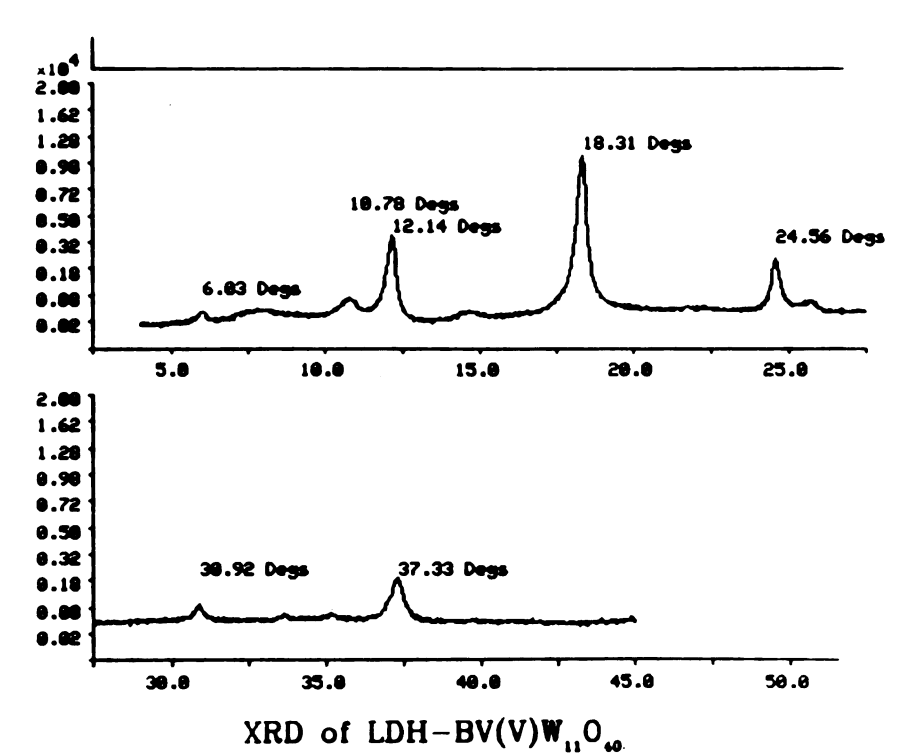
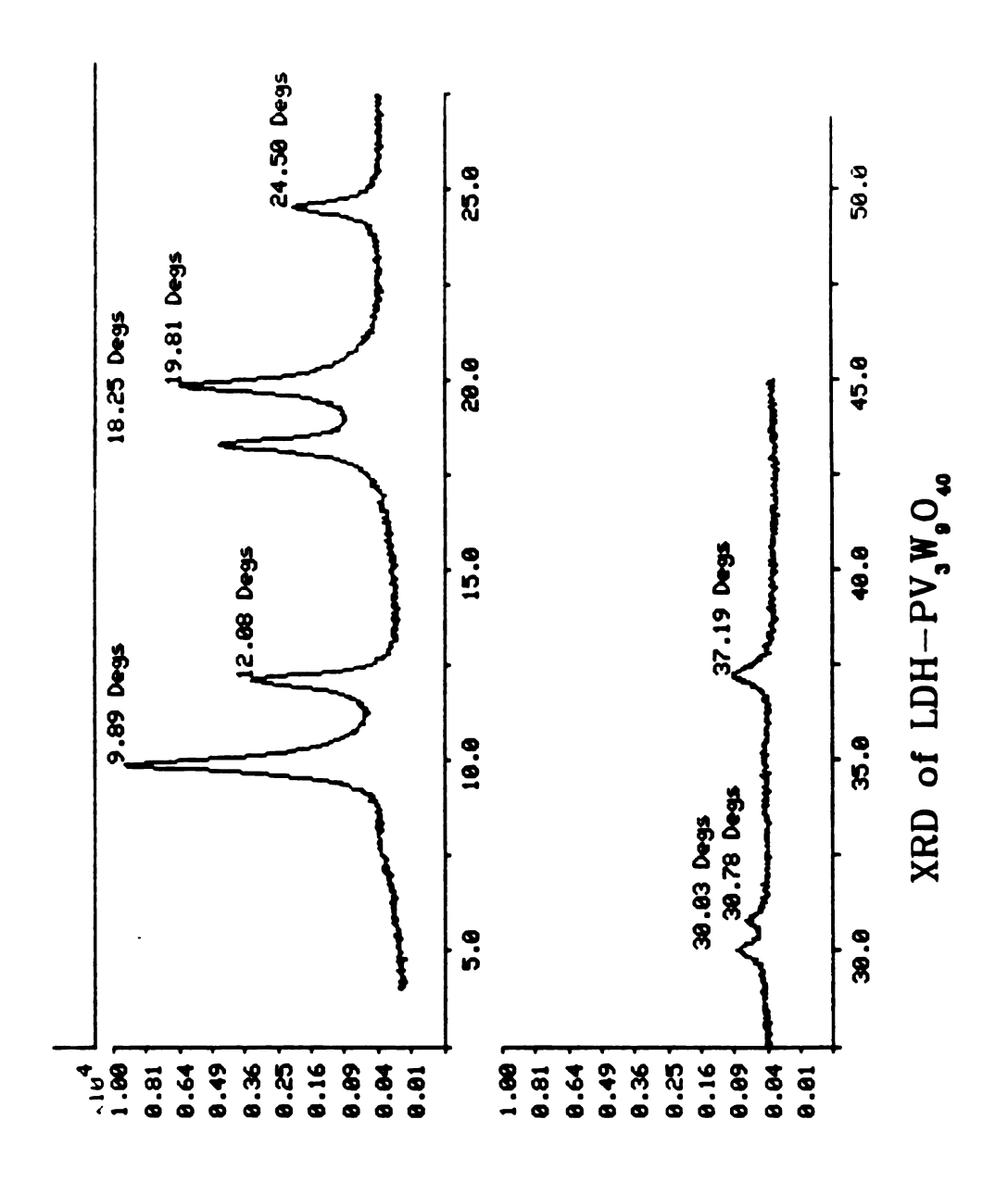


Fig. 42. XRD pattern of a) LDH-BCo(III)W  $_{11}{\rm O}_{39}$ , b) LDH-BV(V)W  $_{11}{\rm O}_{40}$  and c) LDH-PV3W9O40.







surface charge density consideration alone. There must be other factors governing the ion exchange reaction, for example, the hydration energy of the POM. If the energy gained by the intercalation of H<sub>2</sub>W<sub>12</sub>O<sub>40</sub>6- is greater than those of other POMs having same charge, the former must be more favorably intercalated than the latter.

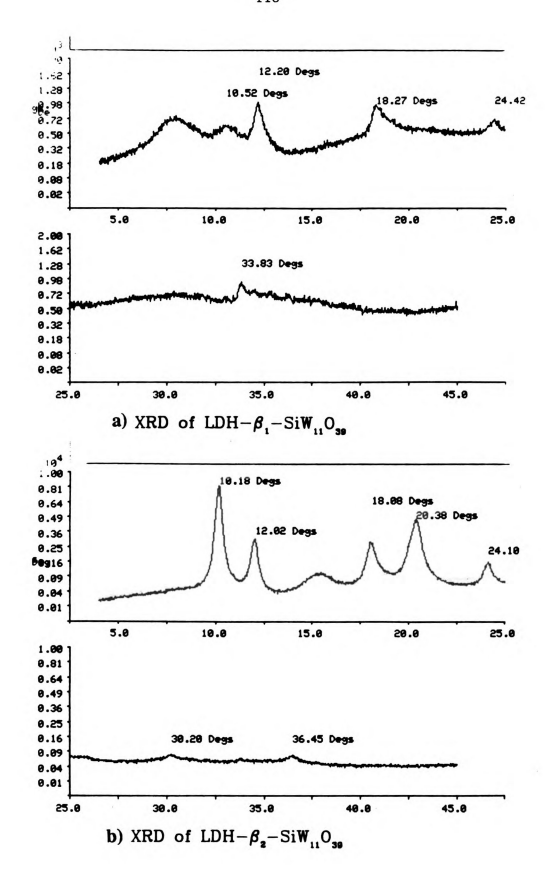
#### 2. Stereo Selectivities

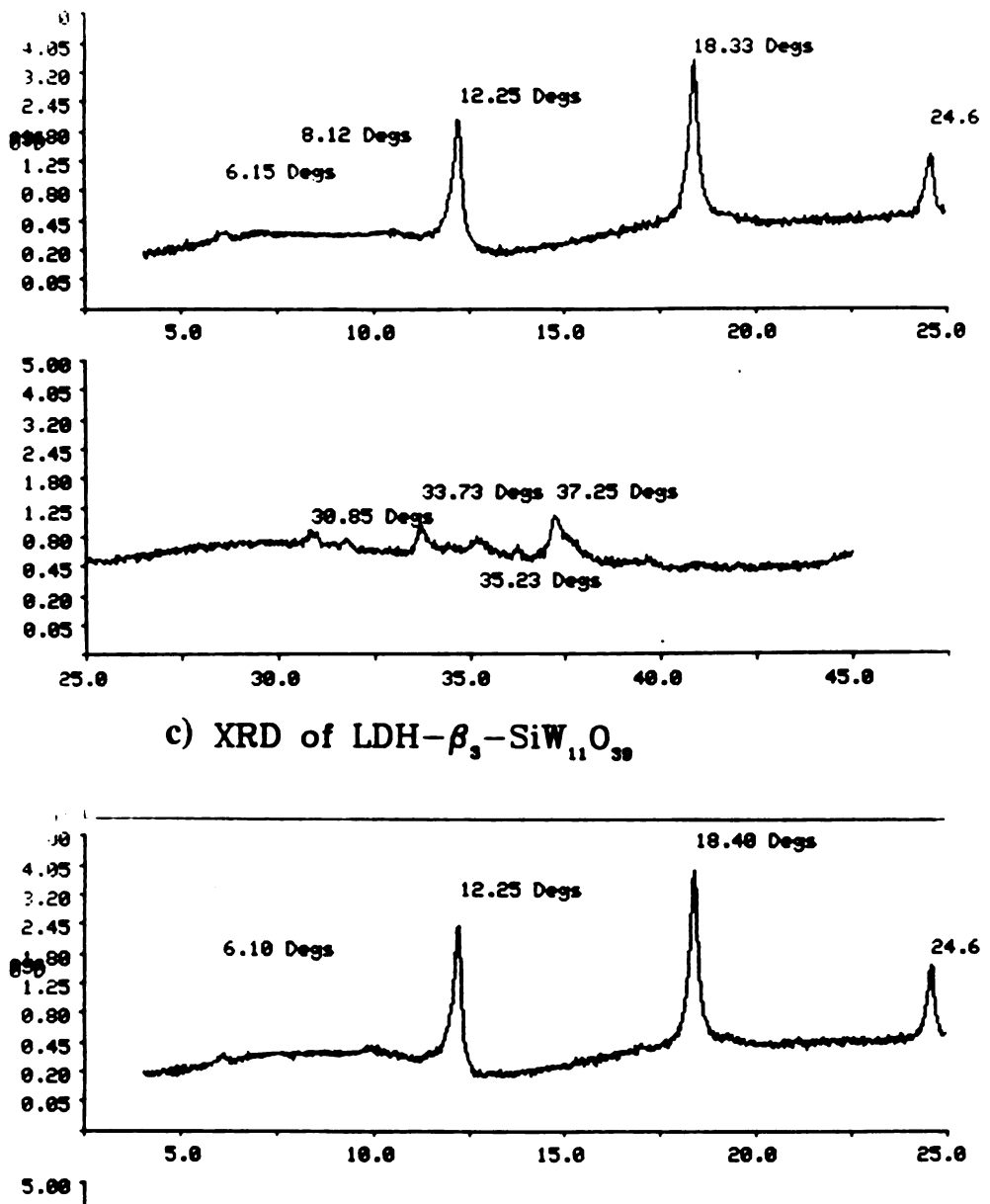
Except for  $\beta_3$ -SiW $_{11}O_{39}$ , when  $\beta$ -12- and  $\beta$ -11-POM with Keggin structure POMs reacted with LDH-NO3, incomplete exchange was observed. The XRDs of the partially exchanged LDH- $\beta$ -SiV $_3$ W $_9$ O $_{40}$ , LDH- $\beta_1$ - and  $\beta_2$ -SiW $_{11}O_{39}$  and also fully exchanged LDH- $\beta_3$ -SiW $_{11}O_{39}$  are shown in Fig. 43. In contrast to the above  $\beta$ -POMs ,  $\alpha$ -POMs such as  $\alpha$ -SiV $_3$ W $_9$ O $_{40}$  and  $\alpha$ -SiW $_{11}O_{39}$  are completely intercalated between the brucite-like lattice layers.

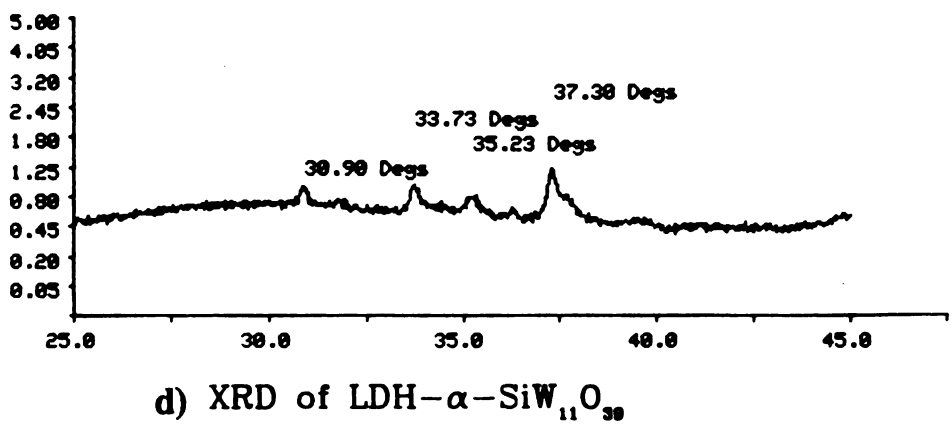
As discussed in the introduction, there are two observed stacking polymorphs for naturally occurring LDHs. One has a three-layer rhombohedral oxygen stacking symmetry, represented by (BC)(CA)(AB)(BC)..., the other has a two-layer hexagonal oxygen stacking symmetry, represented by (BC)(CB)(BC)(CB).... For the synthetic LDHs, only the three-layer rhombohedral stacking pattern, which is a low temperature product, has been observed. Thus, it is reasonable to expect this polymorphorism for LDH-POMs. The oxygen stacking symmetry of the 3-layer polymorph is so much more favorable than that the two-layer polymorph that the latter has not been observed in the laboratory.

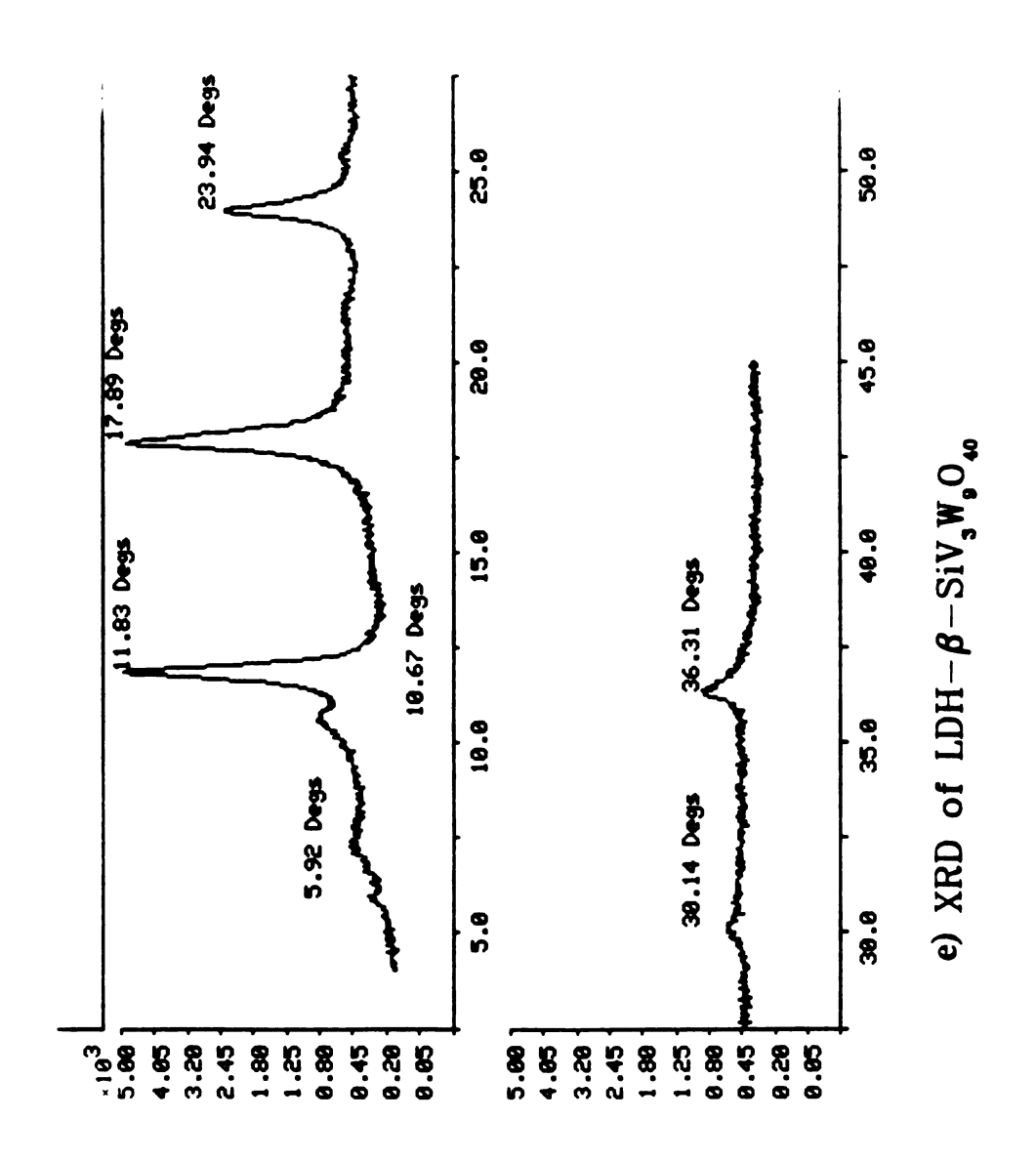
It is necessary to consider possible commensurate stacking symmetry relationships between the surface oxygens of POMs and the oxygen sheets of the brucite layers, i.e., the stereo relationship between the top and bottom oxygen sheets of POMs and the brucite hydroxyl. The resulting symmetry with LDH-α-POMs is always rhombohedral, when the POM in the gallery is oriented so that C<sub>2</sub> axis is orthogonal to the LDH layer. This orientation provides the maximum contact between the POM and LDH layer. The stacking pattern yields (BC)((CA))(AB)((BC))(CA)..., where the oxygen

Fig. 43. XRD pattern of a) LDH- $\beta_1$ -SiW $_{11}$ O $_{39}$ , b) LDH- $\beta_2$ -SiW $_{11}$ O $_{39}$ , c: LDH- $\beta_3$ -SiW $_{11}$ O $_{39}$ , d) LDH- $\alpha$ -SiW $_{11}$ O $_{39}$  and LDH- $\beta$ -SiV $_3$ W $_9$ O $_{40}$ .









layers contained within the double parentheses correspond to the top and bottom oxygen sheets of the POM in contact with the oxygen sheets of the brucite layers. Each oxygen sheet consists of eight oxygen atoms. With  $\beta$ -POM, either of the oxygen sheets from the POM consists of only six oxygen atoms. This six oxygen atom sheet is not commensurate with the hydroxyl group of the brucite-like layer, resulting in higher d-spacings, e.g., d(LDH-α-SiV<sub>3</sub>W<sub>9</sub>O<sub>40</sub>), 14.4 Å; d(LDH-β-SiV<sub>3</sub>W<sub>9</sub>O<sub>40</sub>), 14.8 Å. The reduced contact area between the POM and the LDH layer also makes the β-isomers' ion exchange tendencies less favorable. When one of the six oxygen atoms, which initially define the top or bottom faces of the POM, is removed from the β-12-Keggin structure, it results in the same sequence with LDH-\(\beta\_3\)-SiW<sub>11</sub>O<sub>39</sub>. The mismatching of the oxygen layers is vanished, so a favorable stacking is resulted as in the LDH- $\alpha$ -POM. The ion exchange behavior of  $\beta_3$ -SiW<sub>11</sub>O<sub>30</sub> is similar to that of  $\alpha$ -isomer. Therefore, complete exchange occurs with the b3 isomer. Its d-spacing also changes to a lower value (14.4 Å) as in the  $\alpha$ -isomer intercalates. However, the other two  $\beta$ -11-isomer intercalates result in the same sequence with the  $\beta$ -SiV<sub>3</sub>W<sub>9</sub>O<sub>40</sub> intercalate. Thus, only partial exchange occurs with these isomers.

## 3. Orientation of Keggin-Type POMs in the Gallery

As seen in Fig. 8, the structure of the  $\alpha$ - and  $\beta$ - isomer of SiV<sub>3</sub>W<sub>9</sub>O<sub>40</sub> contain three vanadium atoms located adjacent to each other. Rotated M<sub>3</sub> triplet unit is located on the opposite side. The ion exchange behavior difference between  $\alpha$ - and  $\beta$ -isomers described in the previous section indicates that the orientation of the Keggin-type POM in the gallery must be such that the  $\alpha$ - and  $\beta$ -isomers can be differentiated. There are two possible orientations, i.e., either C<sub>3</sub> or C<sub>2</sub> axis is orthogonal to the LDH layer. As discussed previously, the most possible orientation is one in which C<sub>2</sub> axis is perpendicular to the LDH-layer. Therefore, in LDH-SiV<sub>3</sub>W<sub>9</sub>O<sub>40</sub> C<sub>3</sub> axis is tilt along c direction. Such an orientation will be extended to other systems such as  $\alpha$ - and  $\beta$ -

isomers of 11-Keggin structures. These have been already discussed in the previous section.

In para-tungstate, H<sub>2</sub>W<sub>12</sub>O<sub>42</sub>, there are two M<sub>3</sub> triplets on opposite sides connected by two other types of units, as shown in Fig. 14. On the basis of the XRD study (d<sub>001</sub> = 14.1 Å) these two M<sub>3</sub> triplet must directly contact the brucite layer. The oxygen layer stacking arrangement of the whole system approximates rhombohedral symmetry even though two M<sub>3</sub> triplets are not exactly superimposed, but are shifted by about half an oxygen perpendicular to the direction connecting two M<sub>3</sub> triplets.

In the case of PV<sub>14</sub>O<sub>42</sub>, whose structure is shown in Fig. 26, there are two more V=O units than in Keggin-type POMs. These V=O units are located along the C<sub>2</sub> axis of the PV<sub>12</sub>O<sub>40</sub> ion. On the basis of both commensuration of the oxygen sheets of PV<sub>14</sub>O<sub>42</sub> in the brucite layer and d-spacing consideration (d = 14.4 Å) the orientation of this ion must be different from those of the other Keggin-type POMs. Therefore, the C<sub>2</sub> axis connecting the two extra V=O units is parallel to the brucite layer lattice.

The compound NaP5W30O110, whose structure is shown in Fig. 15, is oriented in the gallery so that the C5 axis of molecule is perpendicular to the brucite layer, as judged from the observed d-spacing ( $d_{001} = 21.3 \text{ Å}$ ). This orientation provides the maximum contact between the brucite layer and NaP5W30O110 and the minimum d-spacing.

With PW9O34, whose structure is shown in Fig. 7, there is only one way to explain the observed d-spacing (d001 = 14.5 Å), a value almost the same as those of the other Keggin-type POMs. The face, which is formed by removing three WO2 units, and the M3 triplet face located on the opposite side of this face are not contacting the brucite layer.

In other cases in which one W=O was replaced by Mn+(O, H2O, or SO3), where M is Cu(II), Co(II), V(IV), or Fe(III), their gallery orientations are uncertain. But with BCo(II)(H2O)W11O39, there was a color change from pinkish to greenish during the

heating of the sample under vacuum. This phenomenon is reversible. There is no d-spacing change during the dehydration process. This color change indicates the coordination number of Co(II) has changed from six to five. This type of color change in related molecules has been observed during removal of coordinated water in homogeneous solution by azeotropic boiling or by blowing hot nitrogen through their solid samples. 141 From the above observations made on LDH-BCo(II)W11O39, the side of the ion containing such coordinated water in the POM frame must not be contacting the brucite layer but must be positioned in the middle of the gallery.

## E. Thermal stabilities of LDH-POMs

Generally speaking, LDH-POMs are stable up to 200°C even though their thermal stabilities are dependent on the POMs in the gallery. Both LDH-H2W12O42 and LDH-PV14O42 are exceptional cases, because neither is thermally stable even at low temperature. They undergo degradation of POMs in the gallery, resulting in unassignable XRD patterns.

When samples are heated at certain temperatures, water molecules occupying the free space between POMs in the gallery are removed from LDH-POMs. As the water molecules are removed, their XRD patterns are also changed. Both the relative intensities of peaks and their peak positions are affected by dehydration. In general, the relative intensity of the 001 reflection increases, while the other 001 reflections decrease in intensity as the heating temperature increases. Specially, the relative intensity of 002 reflection decreases much more than those of the others. Peak broadenings are also observed as temperature increases. The higher the charge on the POM in the gallery, the greater the changes in the XRD patterns upon heating. When samples are dehydrated at temperatures where they are stable and then rehydrated by soaking in water, XRD peak positions and relative intensities are reestablished, even though absolute intensities are not regained. A slight decrease in d-spacing of the dehydrated sample is generally

observed. Such changes result only from the change water content in the gallery. The dehydration and rehydration process are reversible even though the rate of rehydration is dependent on the POMs in the system. Differences in scattering contributions of water molecules is the source of changes in XRD intensities. When water molecules are removed, there is no water contribution to peak intensity. When the system is rehydrated, the water contribution is restored. In order for the water molecules to contribute to the XRD pattern of system, they should be positioned regularly in the gallery. In the rehydrated system the water molecules reoccupy gallery positions equivalent to those for an unheated sample. Therefore, the same type of XRD pattern as that observed for an unheated sample is obtained.

The following noteworthy observations for LDH-POMs are summarized: 1) the higher the charge of the POM in the gallery, the more the XRD peaks are broadened, 2) the XRD pattern upon dehydration and rehydration processes is reversible, 3) upon dehydration the d-spacing decreases, 4) the calculated surface areas and pore volumes for systems containing POMs with more than 9- charge are much larger than the observed values.

Layer nonrigidity will result in layer sagging when LDH-POMs are dehydrated. The higher the charge of POMs in the gallery, the greater distance between the POM pillars and the more the layer will sag. When systems with sagged layers are rehydrated, the layer will reswell much like the swelling of a sponge. The decrease in the absolute intensities of the XRD peaks comes from the decrease in the regularity of the lattice array, which arises partially from layer sagging. Severe layer sagging may result in bond breaking in the layer network. Such partial bond breakings will also give rise to a decrease in the crystal size, which, in turn, will result in both peak broadening and a decrease in peak intensity. When such fractured crystals are rehydrated, bond reformation does not occur. Therefore, complete recovery of absolute peak intensities is not observed.

When LDH-POMs are heated at about 500°C, new inorganic phases appears. The only assignable major phase is a ZnWO4 type phase which appears for all complexes except LDH-PV14O42, in which the only a Zn2V2O7-type phase can be identified.

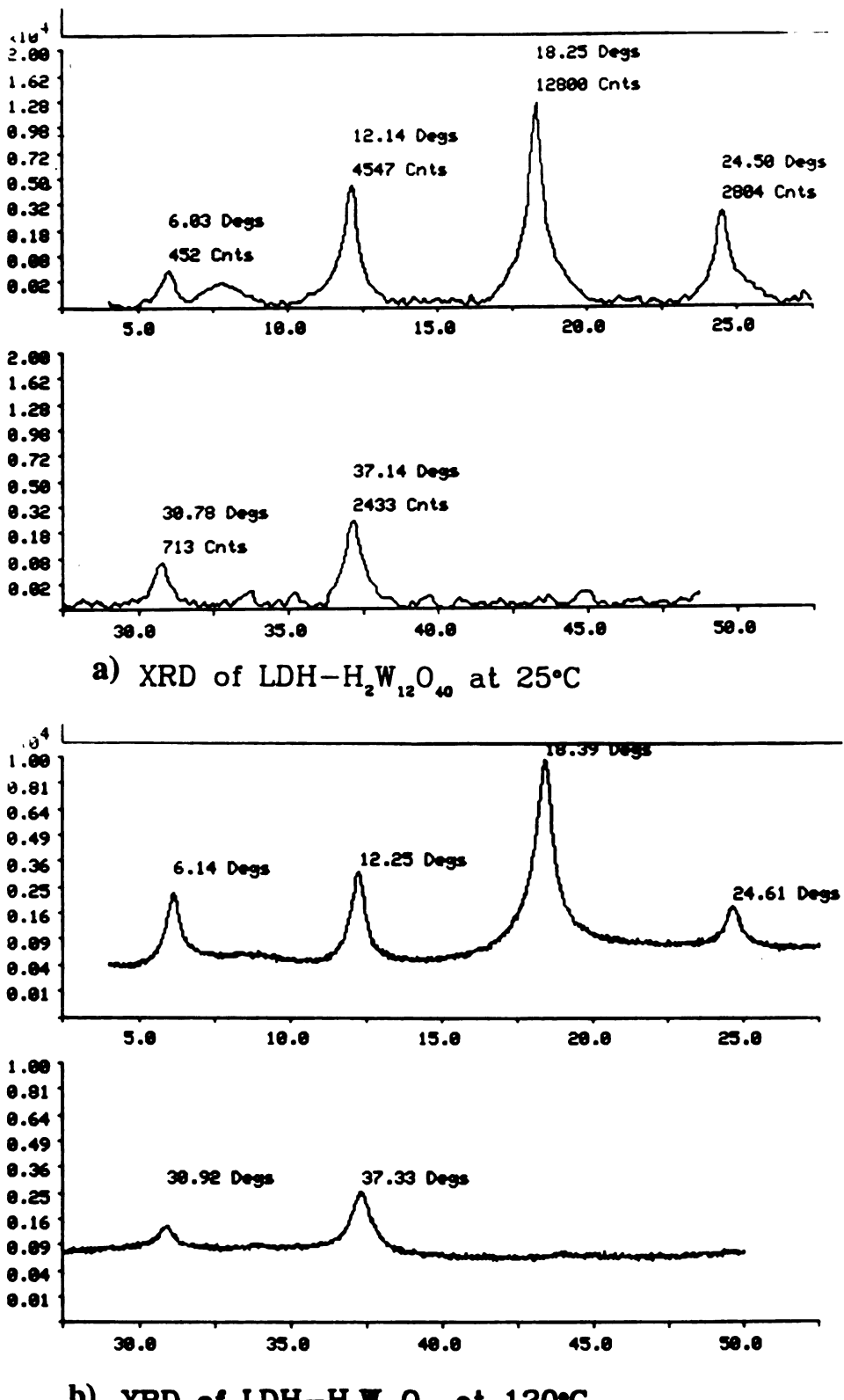
The thermal stability of LDH-POMs is discussed below.

LDH-H2W12O40: This complex is stable to  $180^{\circ}$ C, and samples heated below this temperature can be rehydrated. XRDs at different temperatures are shown in Fig. 44. By  $225^{\circ}$ C, the decomposition of  $H_2W_{12}O_{40}$  has occurred. The ir spectra in Fig. 45 and the XRD study shown in Fig. 45 verify the decomposition temperature. Only one unidentified peak at  $2\theta = 6.9$  remains in the sample heated to  $225^{\circ}$ C. The ir pattern of this sample becomes simpler below  $1000 \text{ cm}^{-1}$  and structure due to POM frequencies is no longer observed. The peak at  $426 \text{ cm}^{-1}$ , which is attributed to an Al-O-Zn stretching motion, disappears after heating this temperature. An amorphous phase is observed up to  $450^{\circ}$ C. At  $470^{\circ}$ C, crystalline inorganic phases appear.

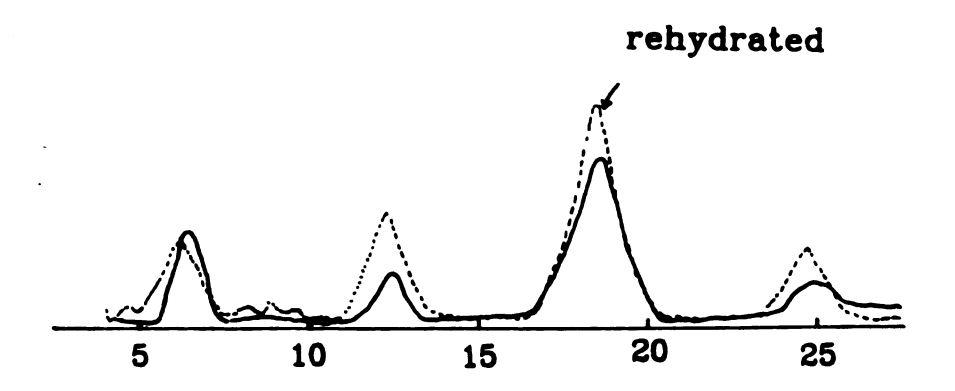
TGA and DSC data indicative of phase changes upon heating are shown in Fig. 46. The dehydration processes occur up to 216°C, followed by layer dehydroxylation up to 354°C. An exothermic peak starting at 446°C corresponds to the formation of new inorganic crystalline phases.

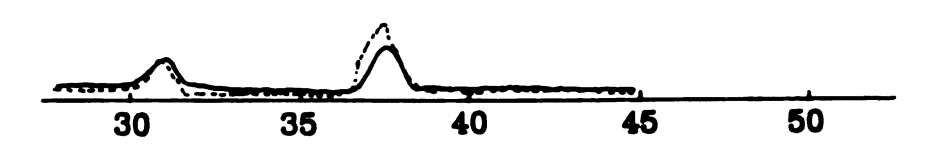
**LDH-SiV3W9O40**: This complex is stable up to  $220^{\circ}$ C. As shown in Fig. 47 rehydration of the heated sample is possible. The POM SiV3W9O40 decomposes at  $250^{\circ}$ C, as verified by ir spectroscopy and XRD data. The ir spectrum, presented in Fig. 48, shows a reduction in the number of bands below  $1000 \text{ cm}^{-1}$  and disappearance of the  $428 \text{ cm}^{-1}$  band due to the degradation and disappearance of both the POM and the hydroxyl layer upon heating. Therefore, the Zn-OH-Al lattice network is absence. There are only two detectable XRD peaks at  $2\theta = 6.56^{\circ}$  and  $19.03^{\circ}$  in the  $220^{\circ}$ C specimen, but these peaks cannot be related each other. Therefore, more than one unidentifiable phases must exist. An amorphous phase is observed below  $450^{\circ}$ C. The shape of ir

Fig. 44. XRD pattern of LDH-H<sub>2</sub>W<sub>12</sub>O<sub>40</sub> at different temperatures. a) 25°C, b) 120°C, c) 180°C: dotted line for the rehydrated sample, solid line for the dehydrated sample, d) 225°C, e) 320°C and f) 470°C

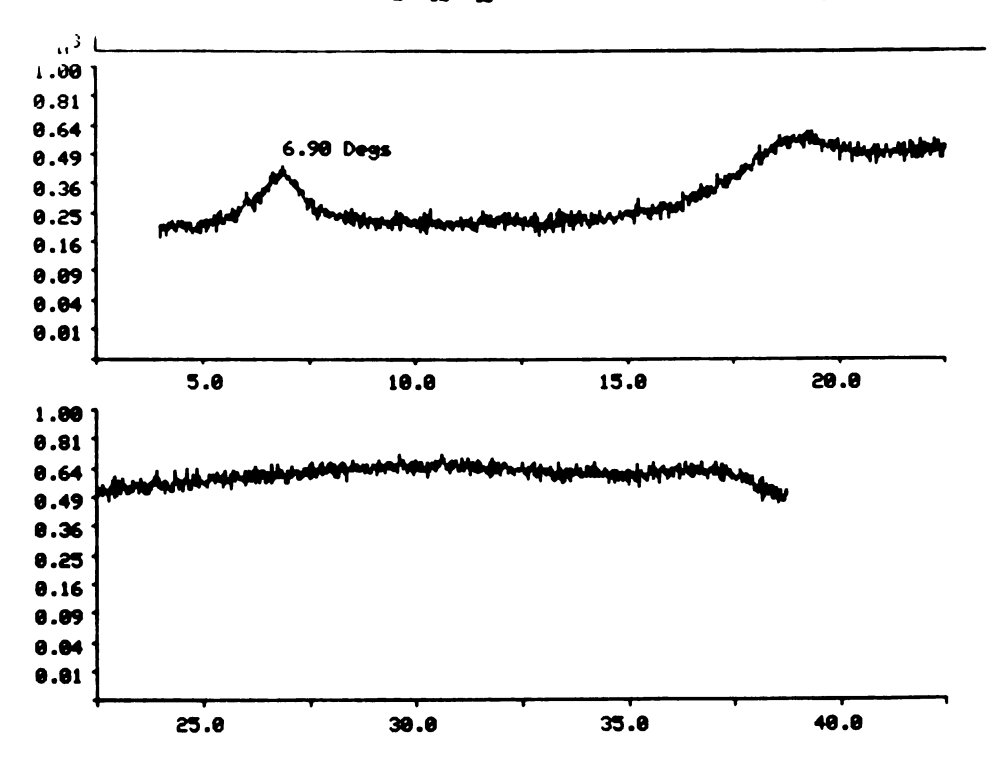


b) XRD of LDH-H<sub>2</sub>W<sub>12</sub>O<sub>40</sub> at 120°C

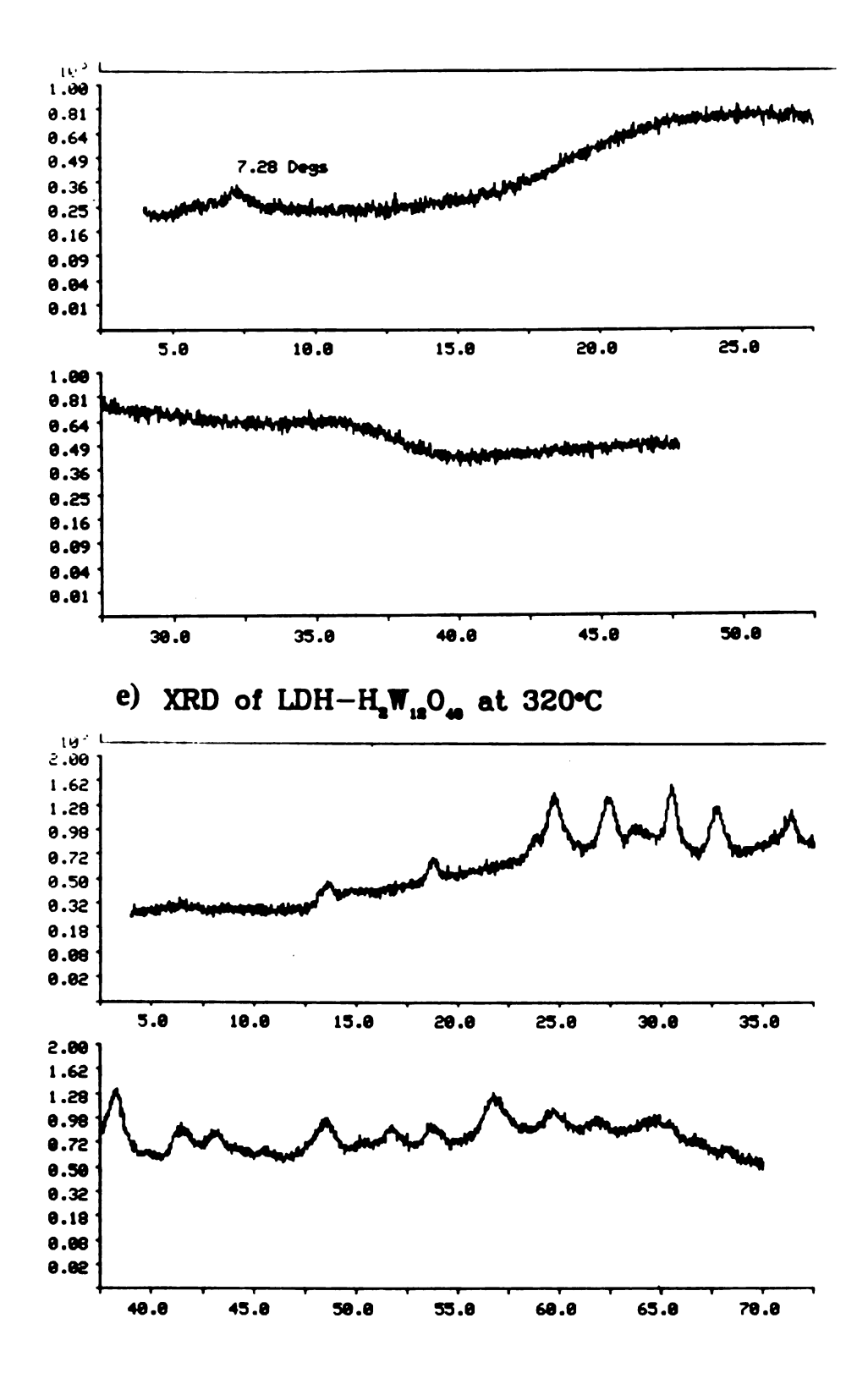




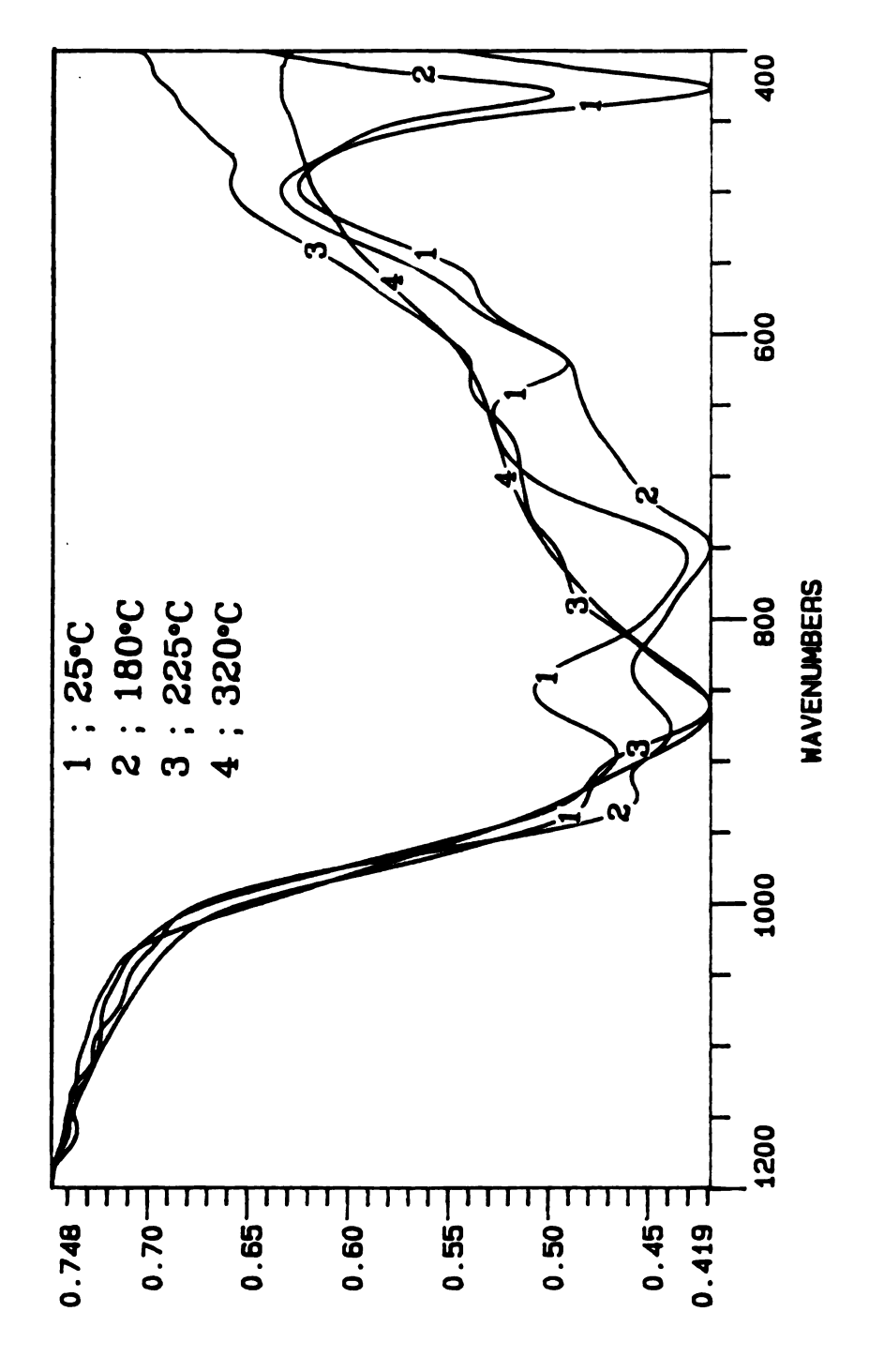
c) XRD of LDH- $H_2W_{12}O_{40}$  at 180°C and rehydrated.



d) XRD of LDH- $H_2W_{12}O_{40}$  at 225°C



f) XRD of LDH- $H_2W_{12}O_{40}$  at 470°C



THANSMITTANCE

Fig. 45. It spectra of LDH- $H_2W_{12}O_{40}$  at different temperatures.

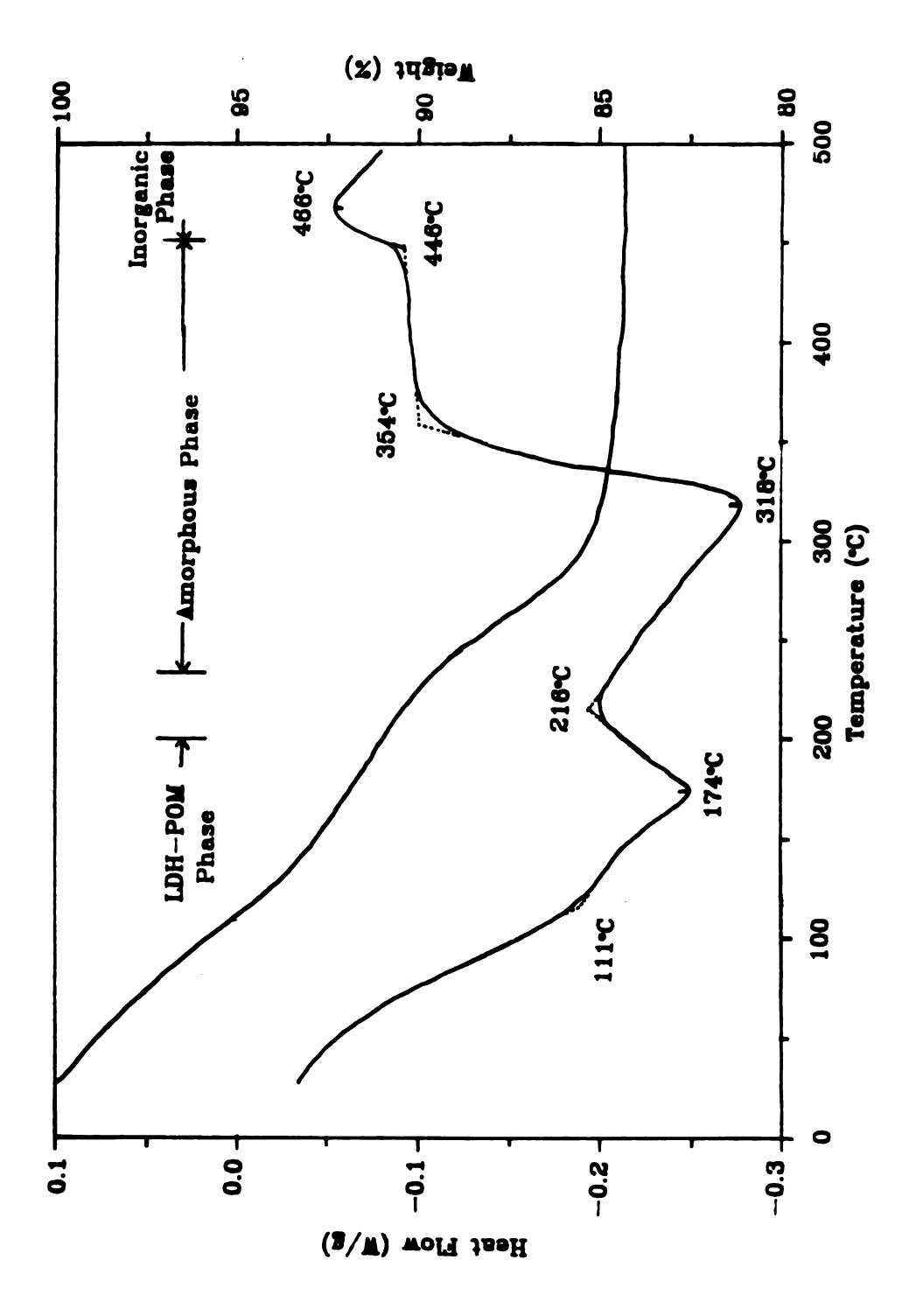
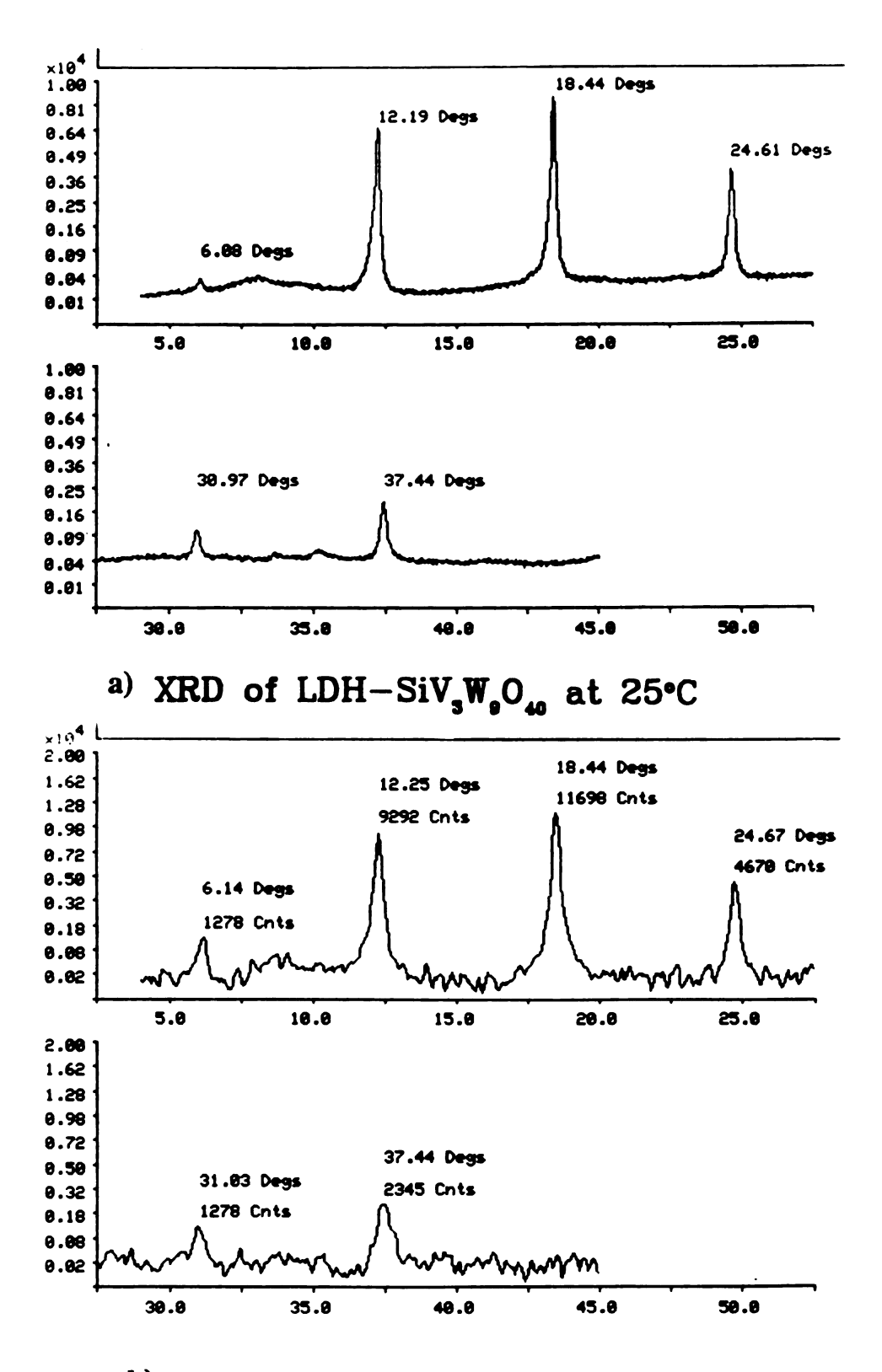
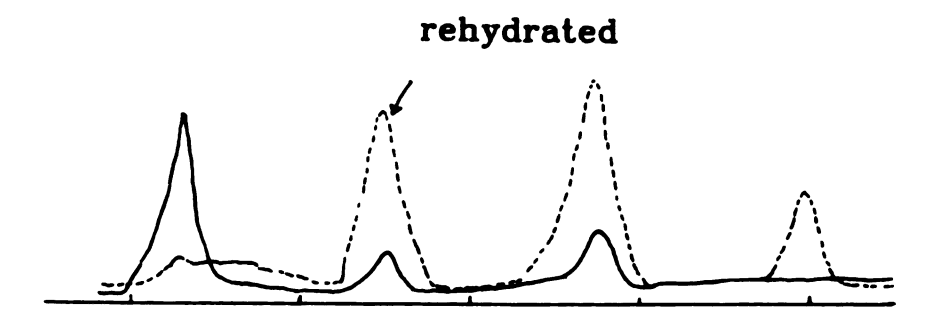


Fig. 46. DSC and TGA of LDH-H2W  $_{\rm 12}{\rm O}_{\rm 40}.$ 

Fig. 47. XRD pattern of LDH-SiV<sub>3</sub>W<sub>9</sub>O<sub>40</sub> at different temperatures. a) 25°C, b) 165°C, c) 220°C: dotted line for the dehydrated sample, solid line for the rehydrated sample, d) 250°C, e) 360°C and f) 500°C.

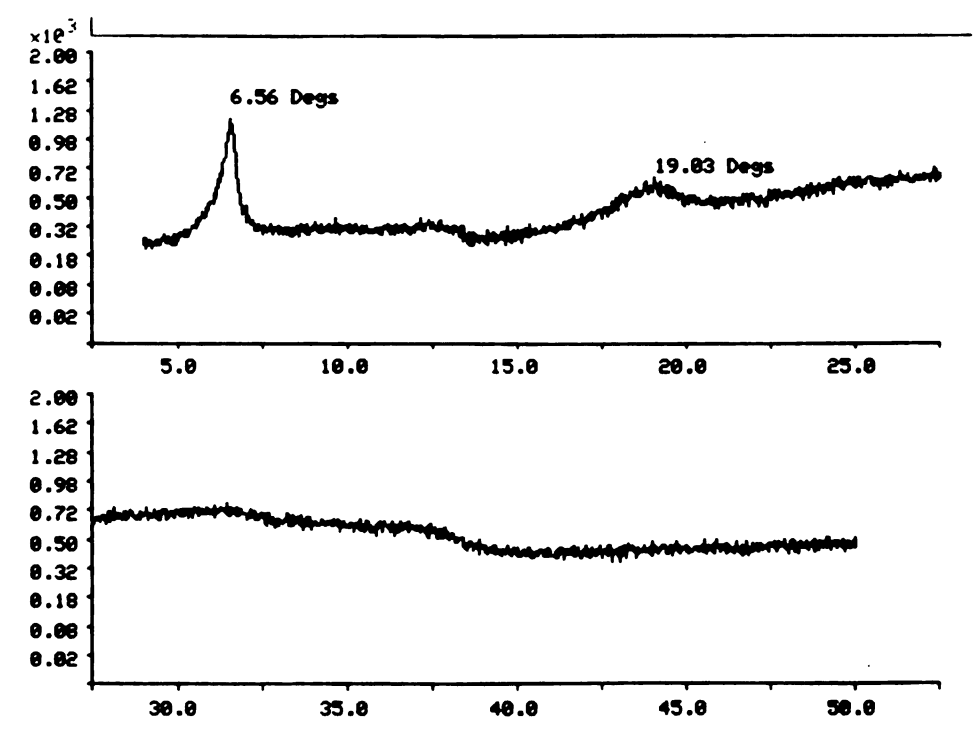


b) XRD of LDH-SiV<sub>3</sub>W<sub>9</sub>O<sub>40</sub> at 165°C

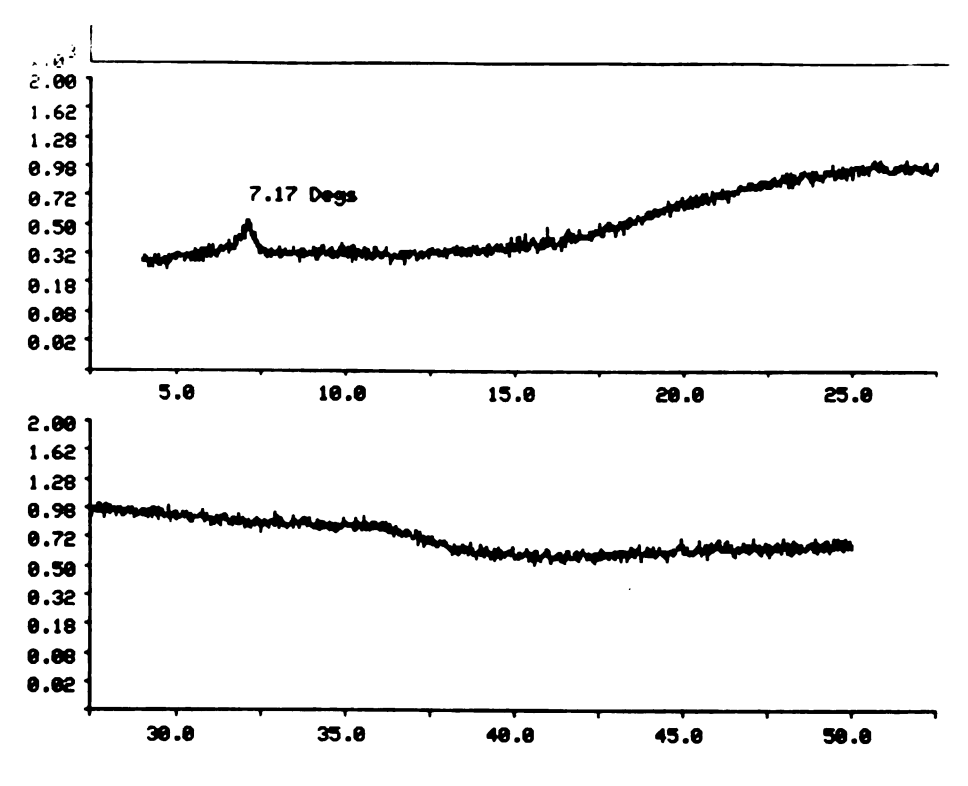




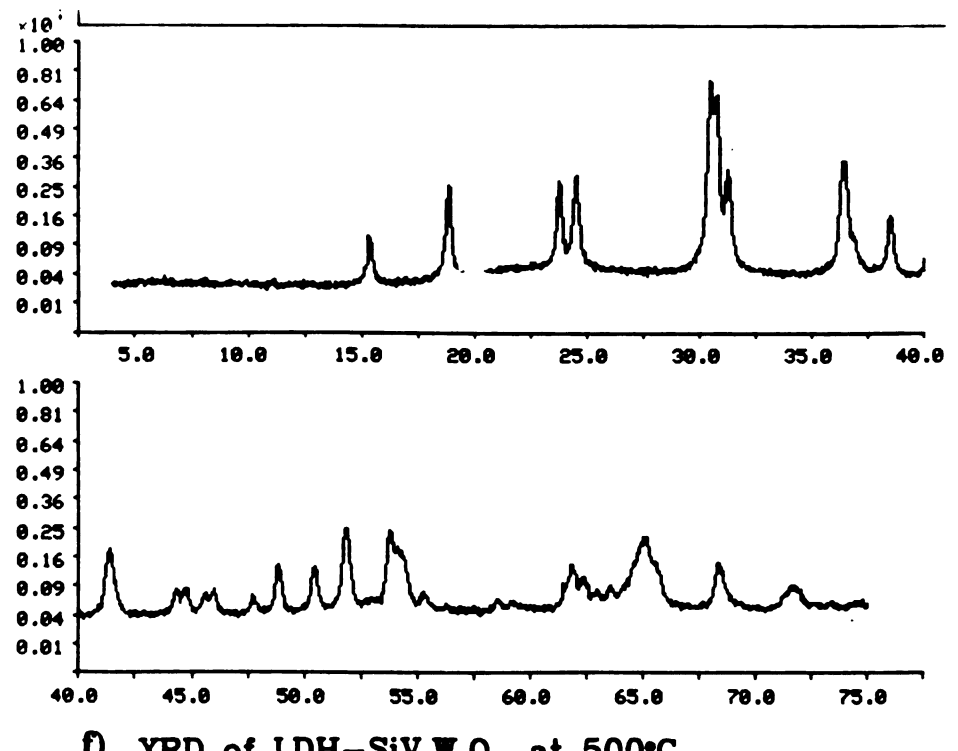
## c) XRD of LDH-SiV, $W_{\bullet}O_{40}$ at 220°C



d) XRD of LDH-SiV,  $W_0O_{40}$  at 250°C



## e) XRD of LDH-SiV, W,O, at 360°C



XRD of LDH-SiV, W,O, at 500°C

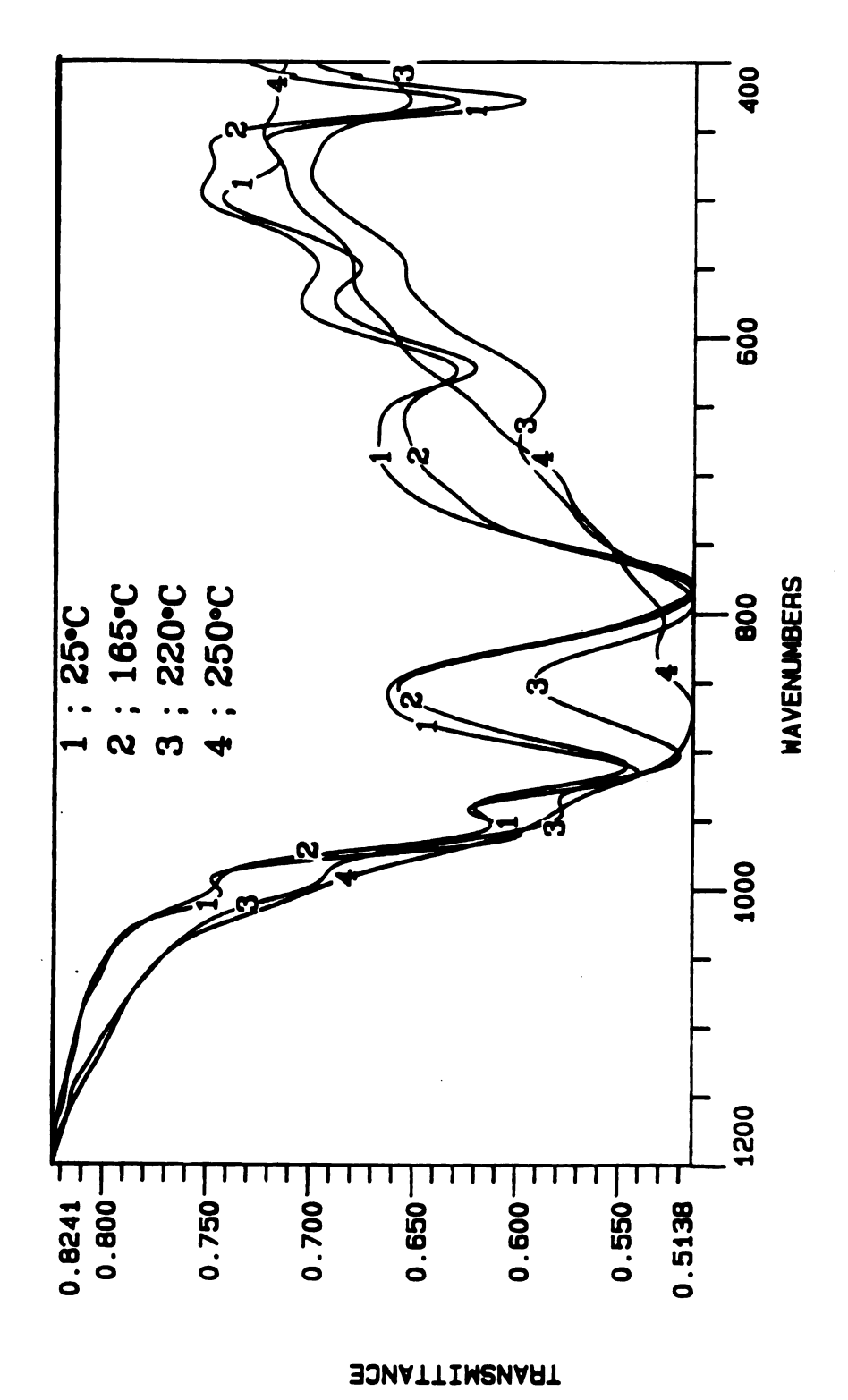


Fig. 48. Ir spectra of LDH-SiV<sub>3</sub>W<sub>9</sub>O<sub>40</sub> at different temperatures.

spectra of the sample heated to 250°C is consistent with a single band centered at 870 cm<sup>-1</sup>. At 500°C, new crystalline inorganic phases appear.

The DSC and TGA data are shown in Fig. 49. The dehydration process occurs up to 200°C, followed by dehydroxylation of the host lattice beyond this point up to 365°C. An exothermic process starts at 460°C and new crystalline inorganic phases are observed by XRD.

**LDH-BV(IV)W11O40**: This complex is stable up to 225°C and the rehydration of heated sample is possible, as illustrated in Fig. 50. Beyond 225°C, the POM in the gallery BV(IV)W11O40 is decomposed and according to the ir spectrum and XRD pattern amorphous phase results. As in the other cases, in the amorphous phase there is one band centered at  $862 \text{ cm}^{-1}$ , as shown in Fig. 51. The ir spectra at higher temperatures are also shown in Fig. 51. There is only one unidentified peak at  $2\theta = 7.24^{\circ}$  in the specimen heated to  $360^{\circ}$ C, as shown in Fig. 50. At  $470^{\circ}$ C, new crystalline inorganic phases appear.

The DSC and TGA data showing phase changes are given in Fig. 52. The dehydration of lattice water occurs up to 227°C, followed by dehydroxylation of the lattice between 285°C and 355°C. An exothermic process related to the formation of new crystalline inorganic phases starts at 442°C.

LDH-BCo(II)W11O39: This complex is stable up to  $200^{\circ}$ C and below this point, the rehydration of the heated sample is possible, as shown in Fig. 53. The decomposition of BCo(II)W11O39 in the gallery is observed beyond this point and verified by the ir spectra shown in Fig. 54. As in the other LDH-POMs cases, the ir spectrum at  $250^{\circ}$ C shows only one \*absorption band centered at 842 cm<sup>-1</sup>. Thermal decomposition of these LDH-POMs typically results in an amorphous phase with an absorption band positioned at 855 cm<sup>-1</sup>. In the specimen heated to  $250^{\circ}$ C there is only one unidentified XRD peak at  $20 = 7.03^{\circ}$ . The XRDs of LDH-BCo(II)W11O39 at different temperatures are shown

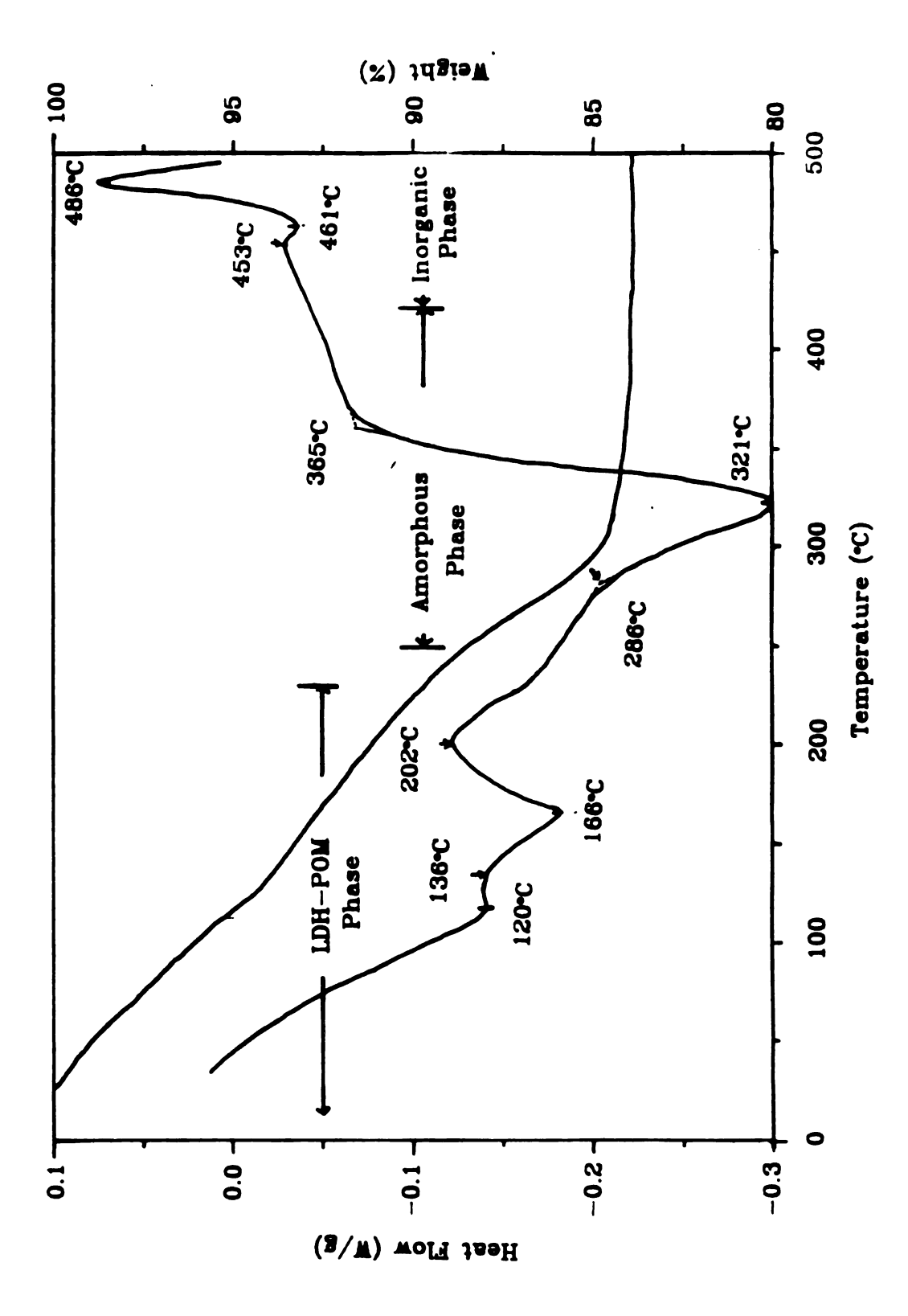
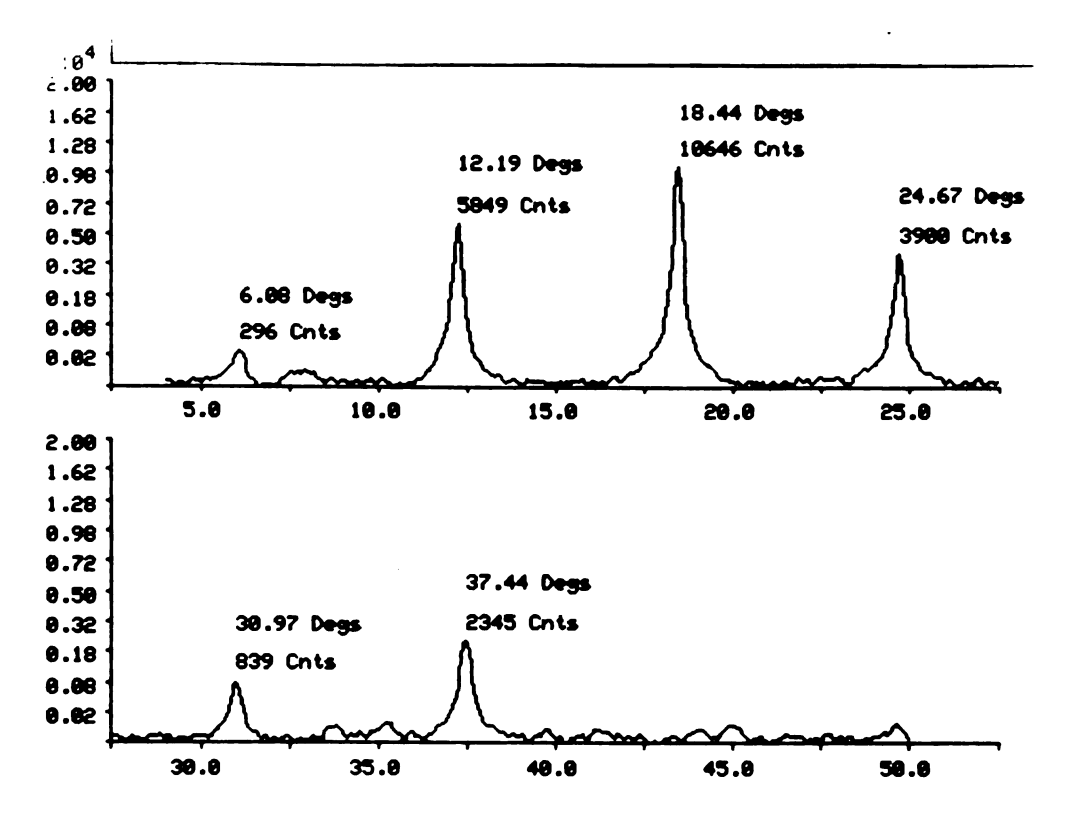
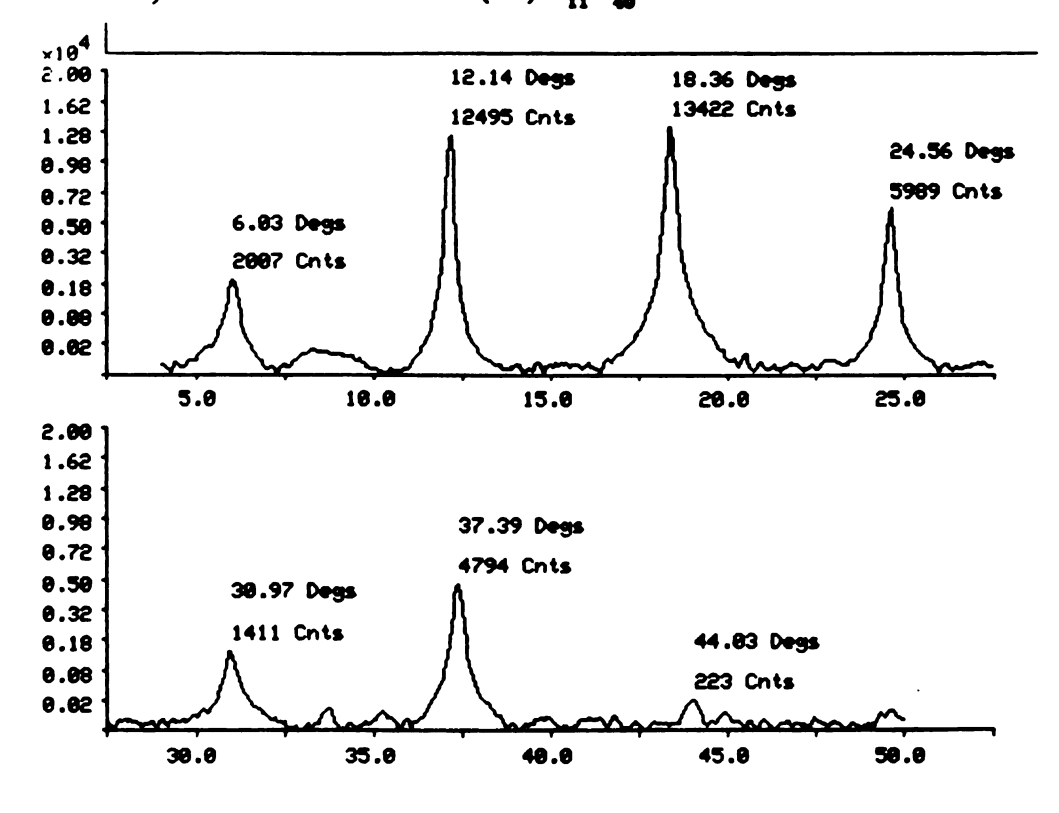


Fig. 49. DSC and TGA of LDH-SiV<sub>3</sub>W<sub>9</sub>O<sub>40</sub>.

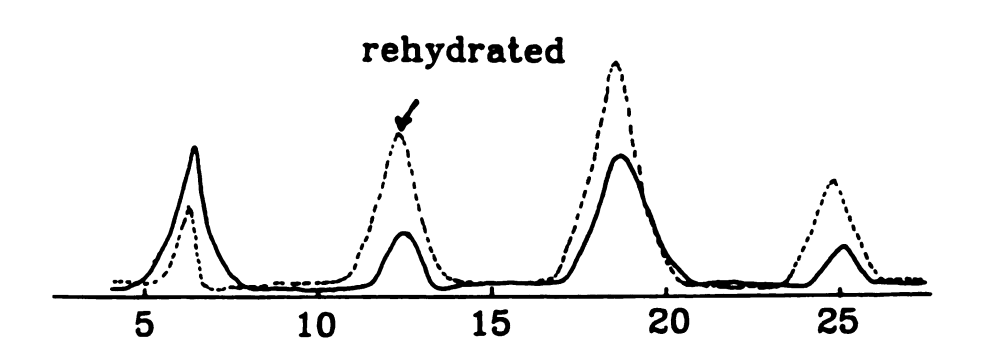
Fig. 50. XRD pattern of LDH-BVW<sub>11</sub>O<sub>40</sub> at different temperatures. a) 25°C, b) 150°C, c) 225°C: dotted line for the rehydrated sample, solid line for the dehydrated sample, d) 255°C, e) 360°C and f) 470°C.

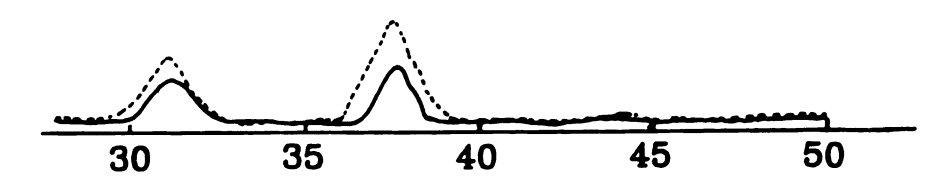




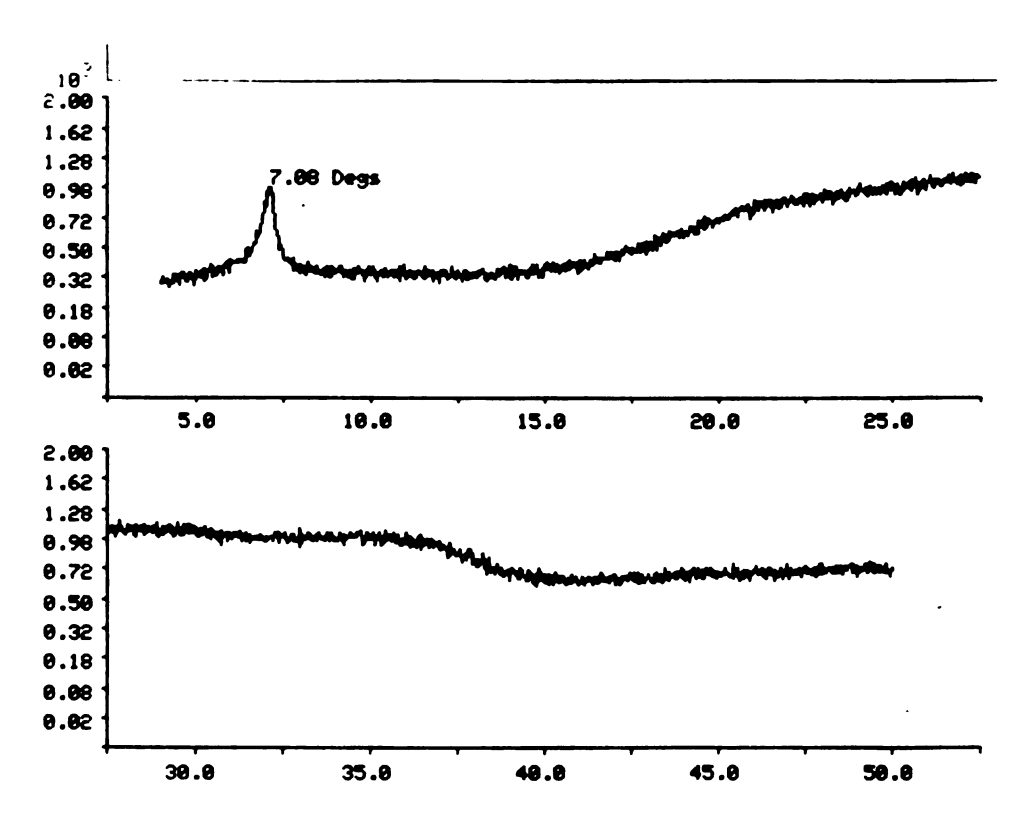


b) XRD of LDH-BV(IV) $W_{11}O_{40}$  at 150°C

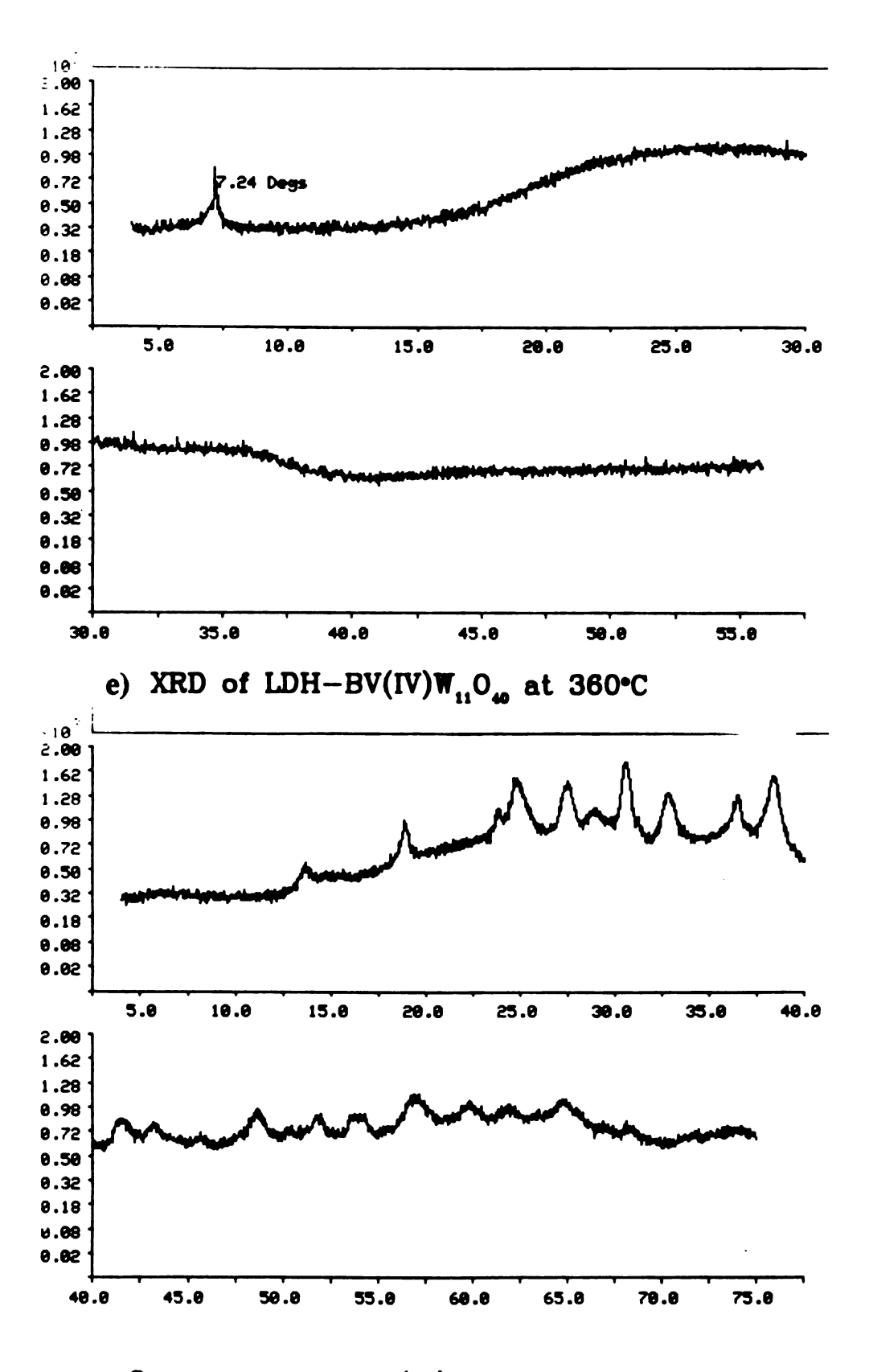




c) XRD of LDH-BV(IV) $\mathbf{W}_{11}O_{40}$  at 225°C



d) XRD of LDH-BV(IV) $W_{11}O_{40}$  at 255°C



f) XRD of LDH-BV(IV) $W_{11}O_{40}$  at 470°C

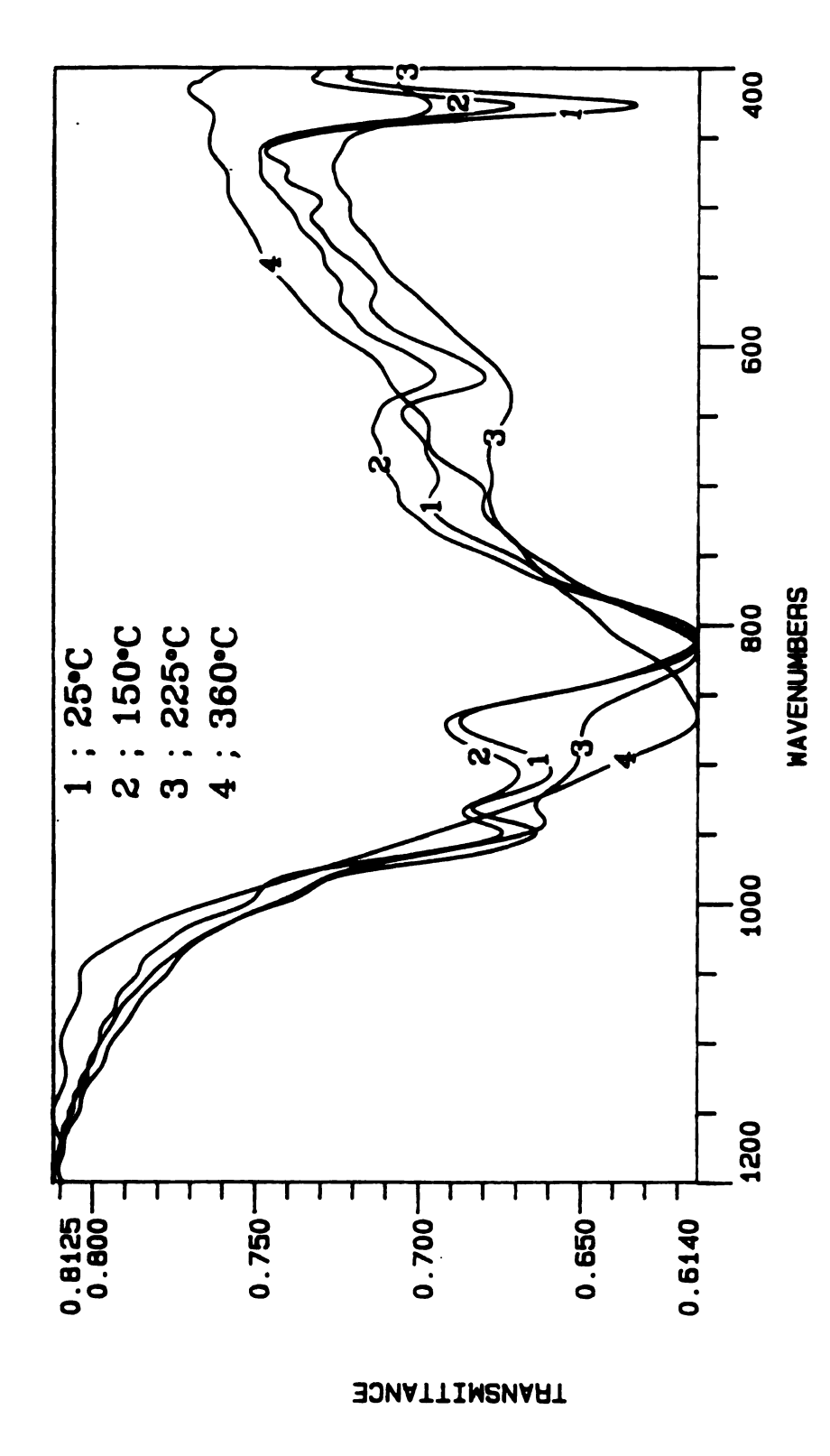


Fig. 51. Ir spectra of LDH-BVW $_{11}$ O $_{40}$  at different temperatures.

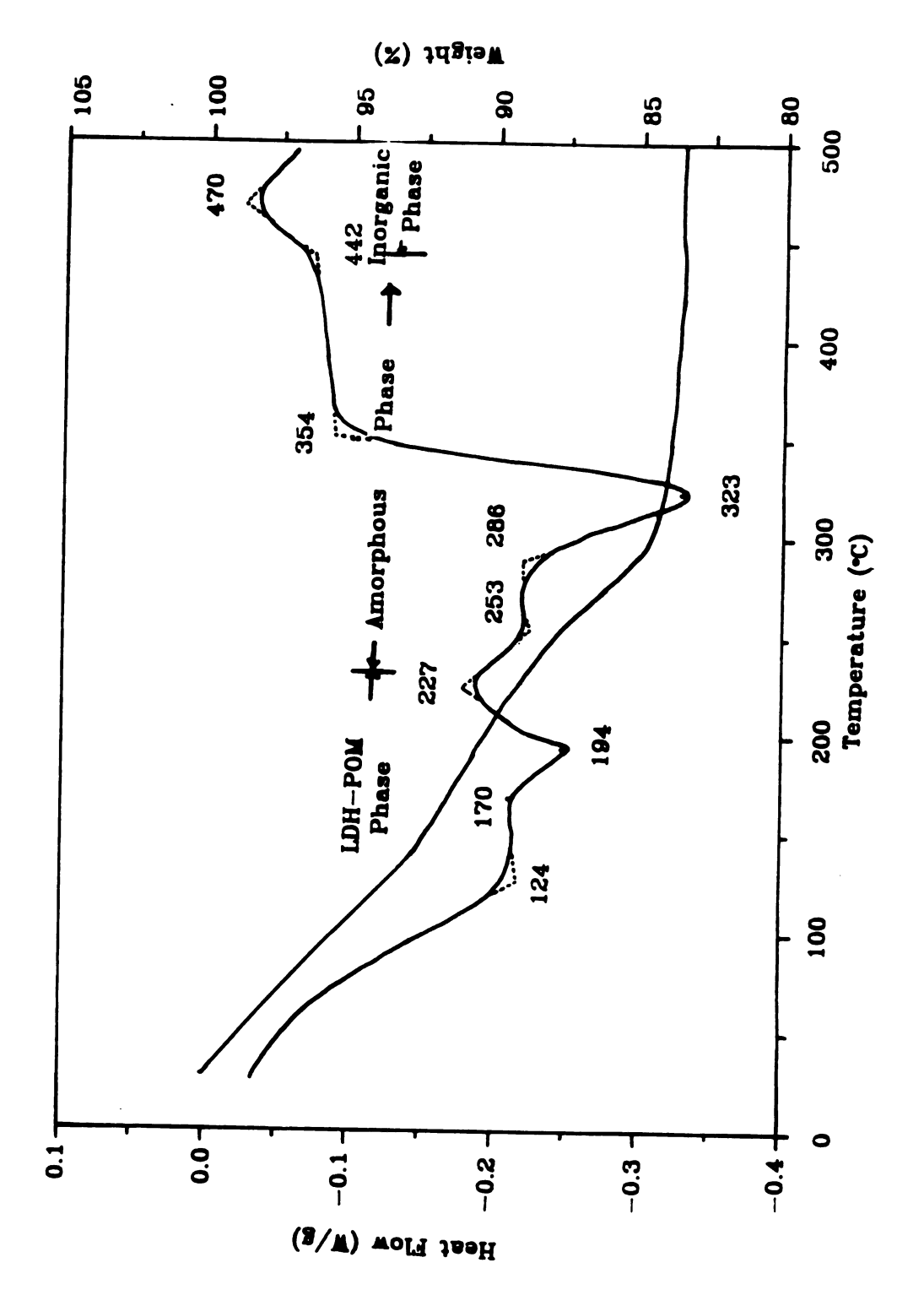
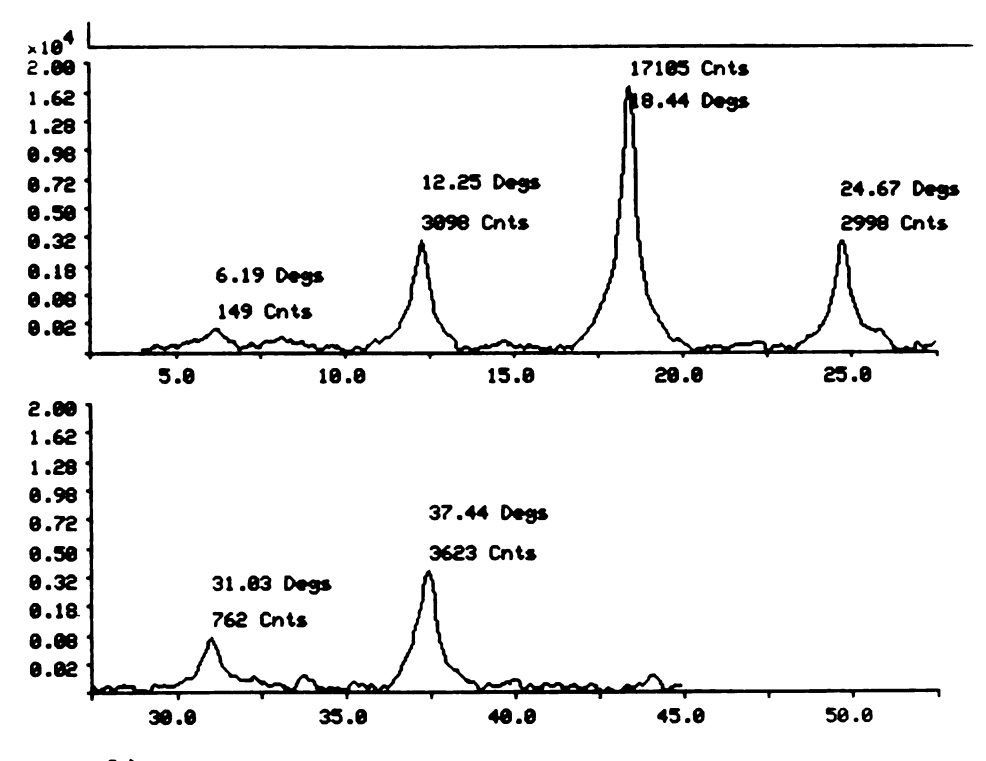
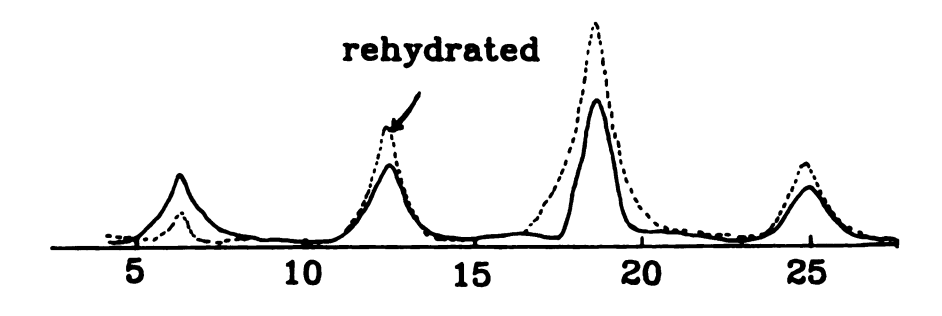


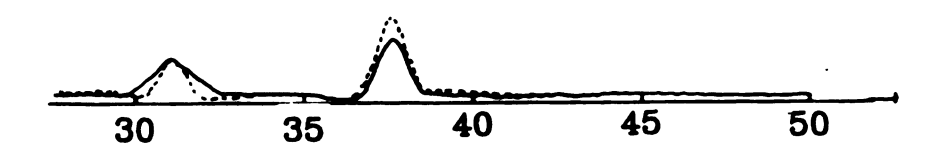
Fig. 52. DSC and TGA of LDH-BVW  $_{11}\mathrm{O}_{40}.$ 

Fig. 53. XRD pattern of LDH-BCoW<sub>11</sub>O<sub>39</sub> at different temperatures. a) 25°C, b) 185°C: dotted line for the rehydrated sample, solid line for the dehydrated sample, c) 200°C: dotted line for the rehydrated sample, solid line for the dehydrated sample, d) 250°C, e) 360°C and f) 500°C.

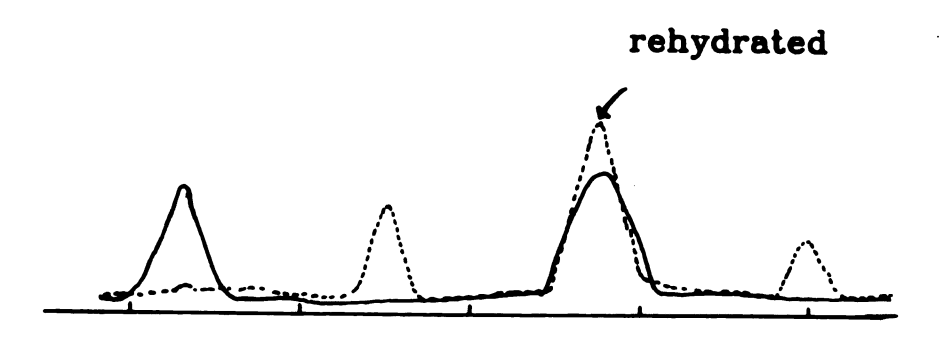


b) XRD of LDH-BCo(II)W<sub>11</sub>O<sub>40</sub> at 25°C

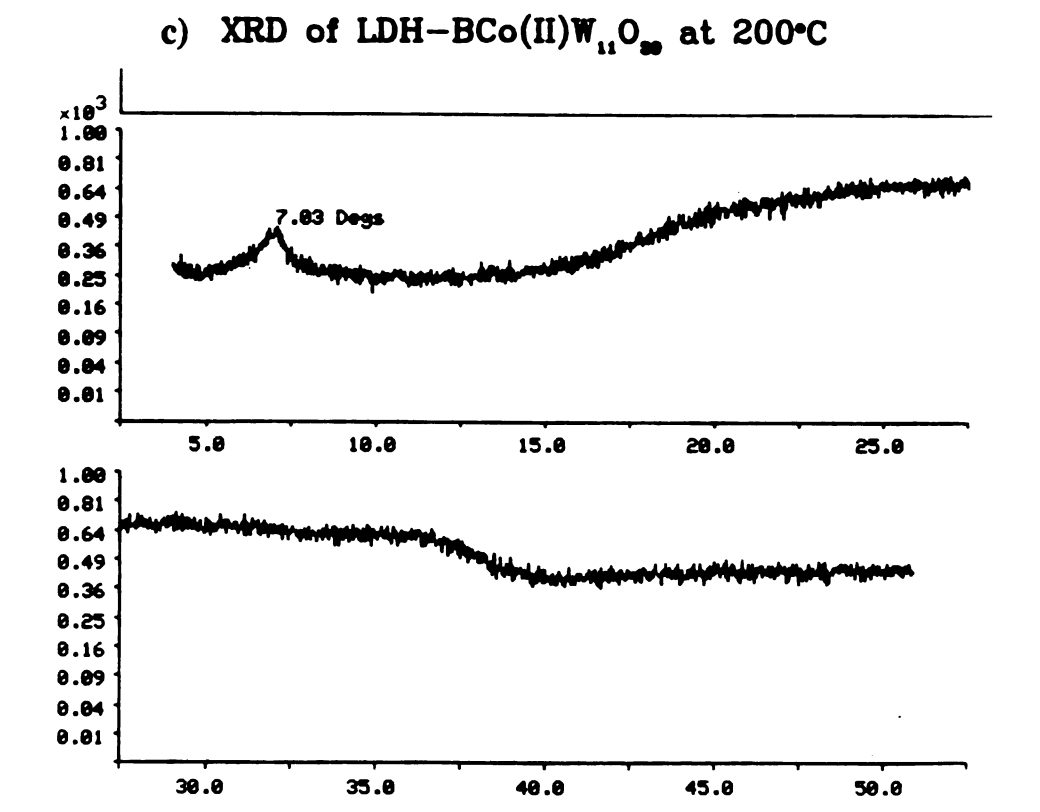




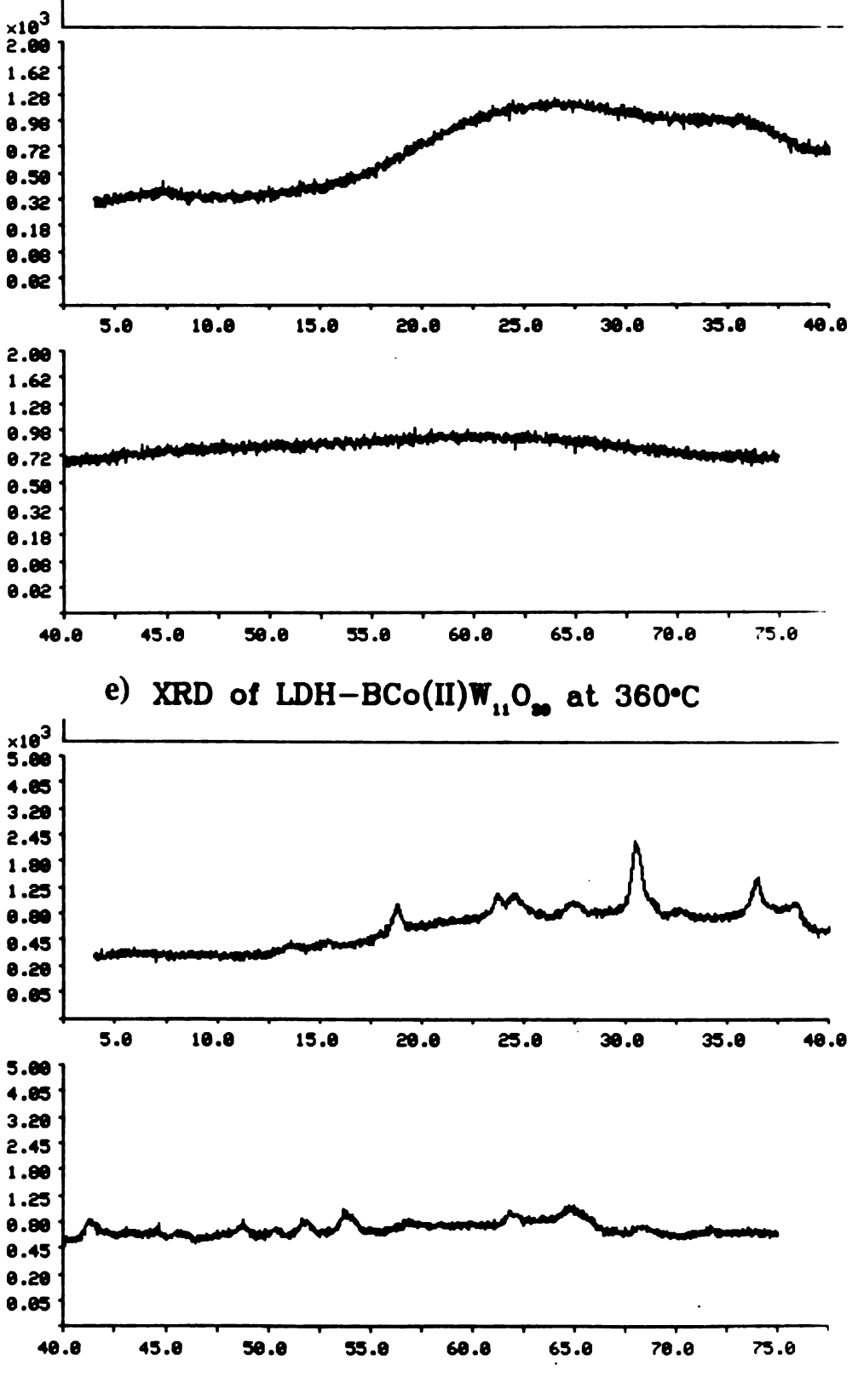
a) XRD of LDH-BCo(II)W<sub>11</sub>O<sub>20</sub> at 185°C







d) XRD of LDH-BCo(II) $W_{11}O_{50}$  at 250°C



f) XRD of LDH-BCo(II)W<sub>11</sub>O<sub>20</sub> at 500°C

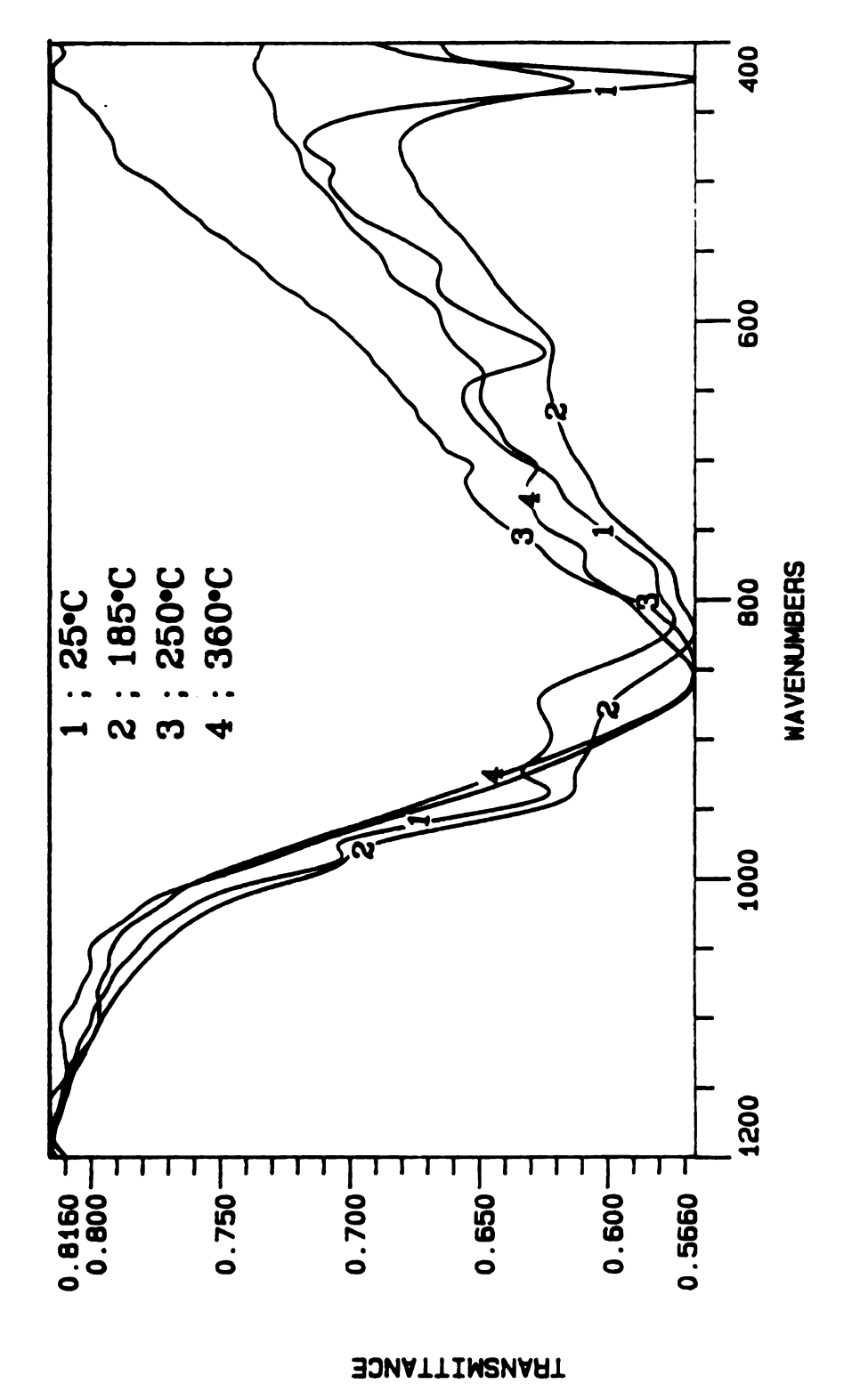


Fig. 54. Ir spectra of LDH-BCoW11039 at different temperatures.

in Fig. 53. At 360°C a complete amorphous phase appear. At 500°C new crystalline inorganic phases are observed.

The DSC and TGA results showing phase changes are presented in Fig. 55. The dehydration process occurs up to 225°C, followed by the dehydroxylation of the host lattice up to 365°C. A small exothermic peak starting at 450°C indicates the onset of new inorganic phase formation.

**LDH-BCu(II)W11O39**: This complex is stable up to 190°C. Rehydration of the heated sample is possible, as shown in Fig. 56. The BCu(II)W11O39 in the gallery decomposes at 230®C, as verified by changes in the ir spectra shown in Fig. 57 and in the XRD pattern at 230°C shown Fig. 56. As in the other cases, there is only one ir absorption band centered at 835 cm<sup>-1</sup> below 1000 cm<sup>-1</sup>. The XRD pattern of the 230°C specimen shows two unidentified peaks at  $2\theta = 6.63^{\circ}$  and  $19.08^{\circ}$ . Heating beyond this point results in complete formation of an amorphous phase. At 500°C, new crystalline inorganic phases appear, as shown in Fig. 56.

The DSC and TGA of LDH-BCu(II)W11O39 are provided in Fig. 58. The dehydration process occurs up to 230°C, followed by dehydroxylation of the host layer up to 360°C. There is a very small exothermic peak starting at 450°C, which corresponds to new inorganic phase formation.

LDH-PMo2W9O39: This complex is stable at 205°C and also shows the reversible rehydration process, as indicated by their XRD pattern in Fig. 59. Its ir spectrum, as given in Fig. 60, shows that the intensity of an absorption band around 427 cm<sup>-1</sup> decreases substantially upon heating, reflecting to some extent layer network degradation. At 340°C an amorphous phase is formed, as shown in the XRD pattern in Fig. 59. As in the other cases, the ir spectrum at the amorphous region shows no fine absorption structure with only one band centered at 860 cm<sup>-1</sup>. At 500°C the crystalline inorganic phases appear, as shown in the XRD pattern of the 500°C material.

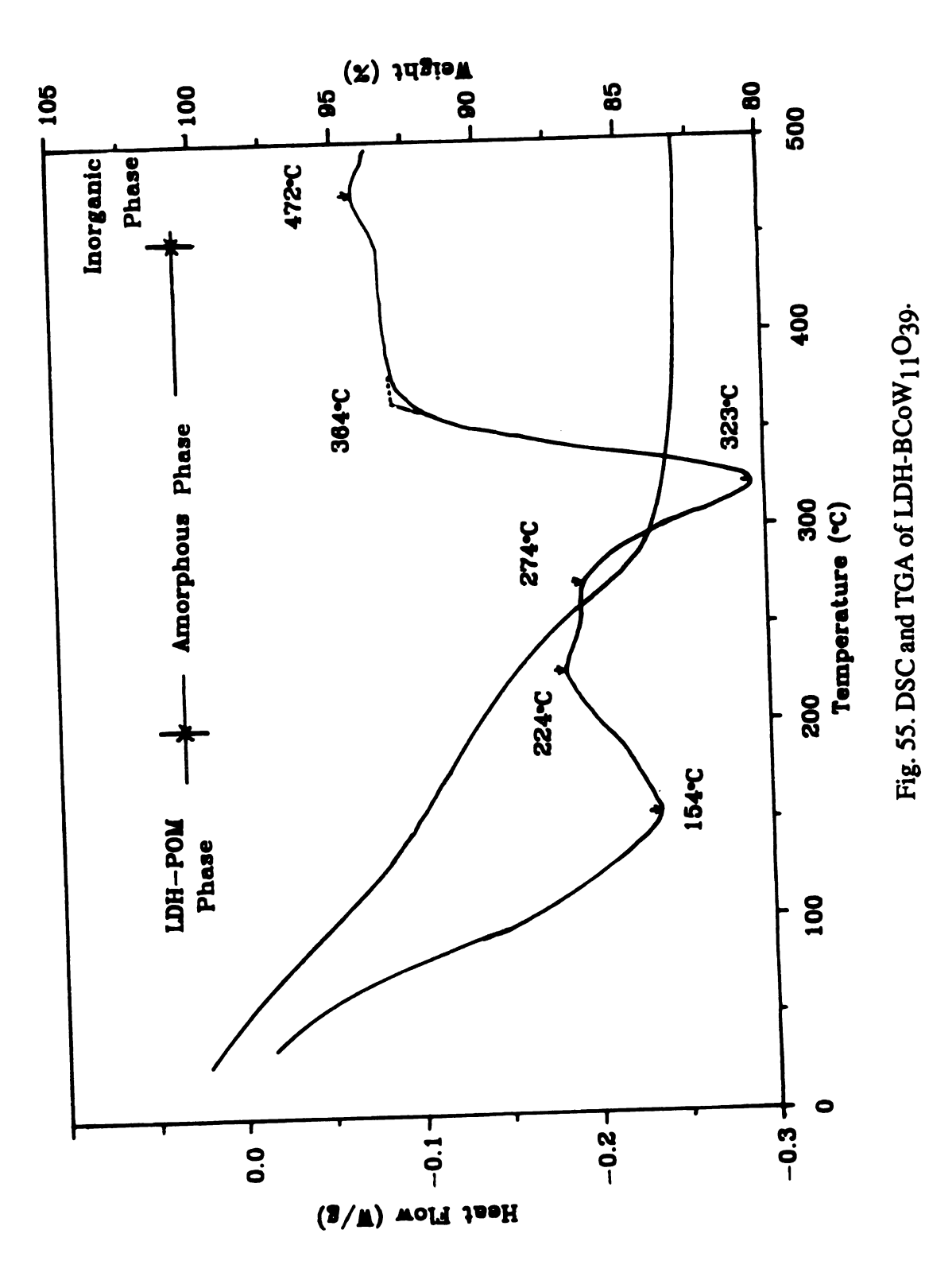
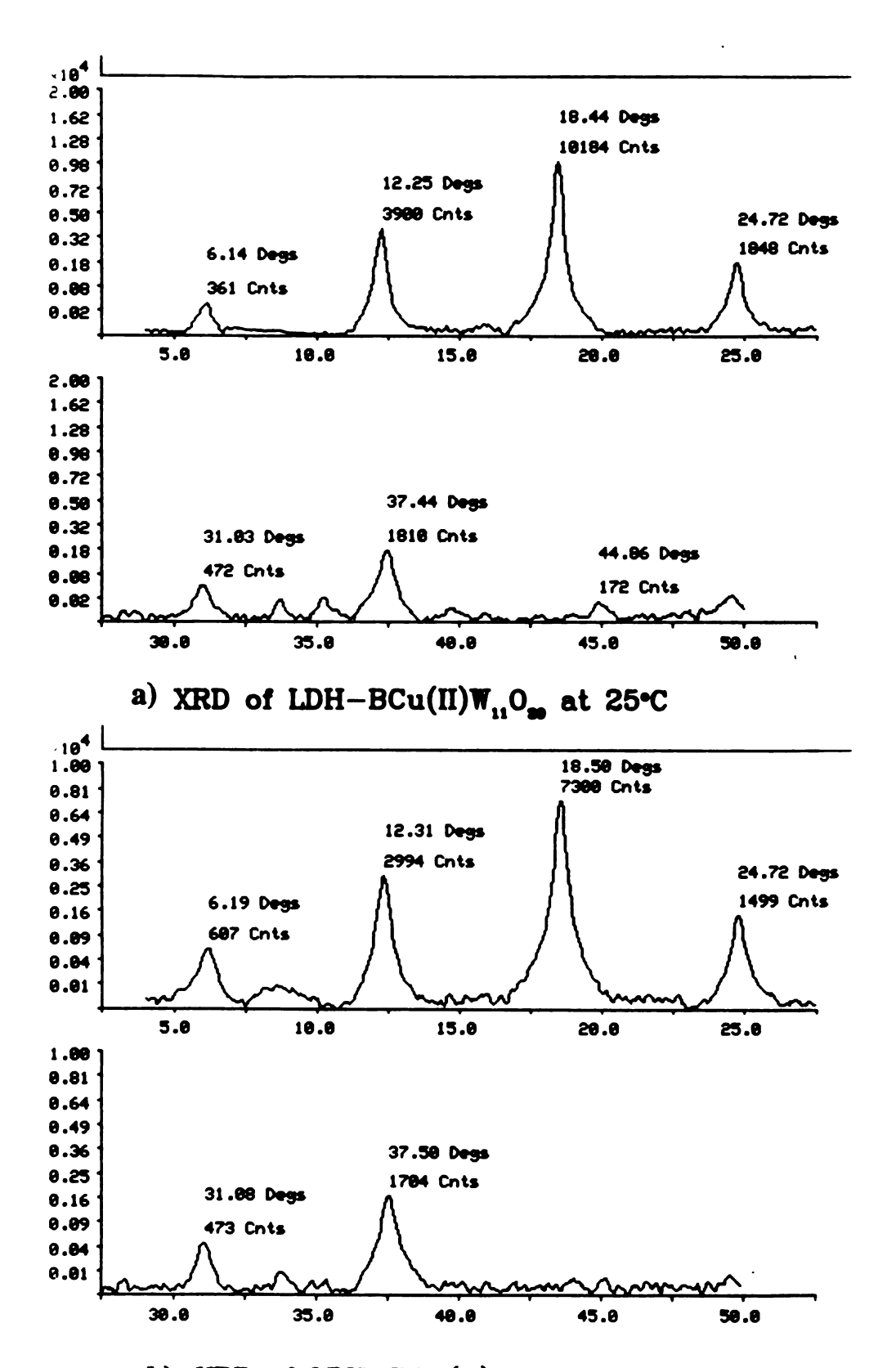
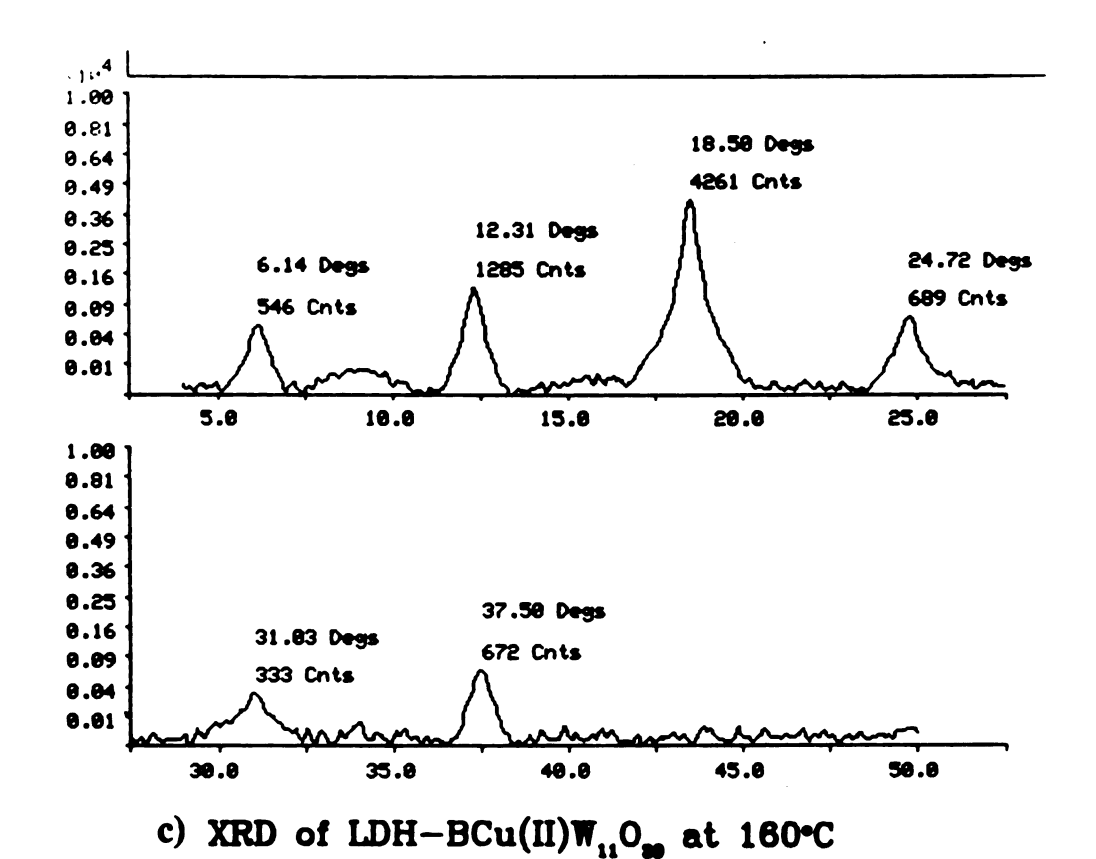
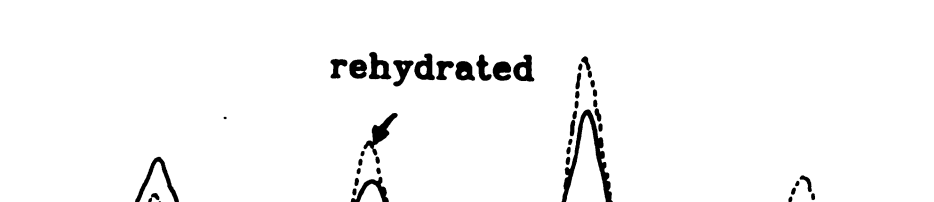


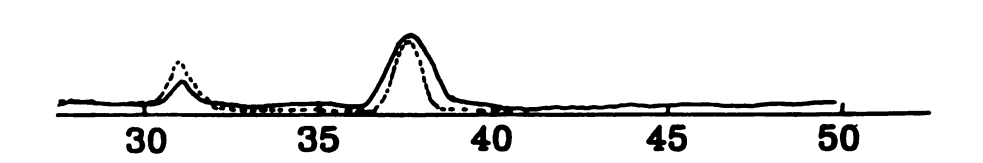
Fig. 56. XRD pattern of LDH-BCuW<sub>11</sub>O<sub>39</sub> at different temperatures. a) 25°C, b) 125°C, c) 160°C, d) 190°C: dotted line for the rehydrated sample, solid line for the dehydrated sample, e) 230°C and f) 500°C.



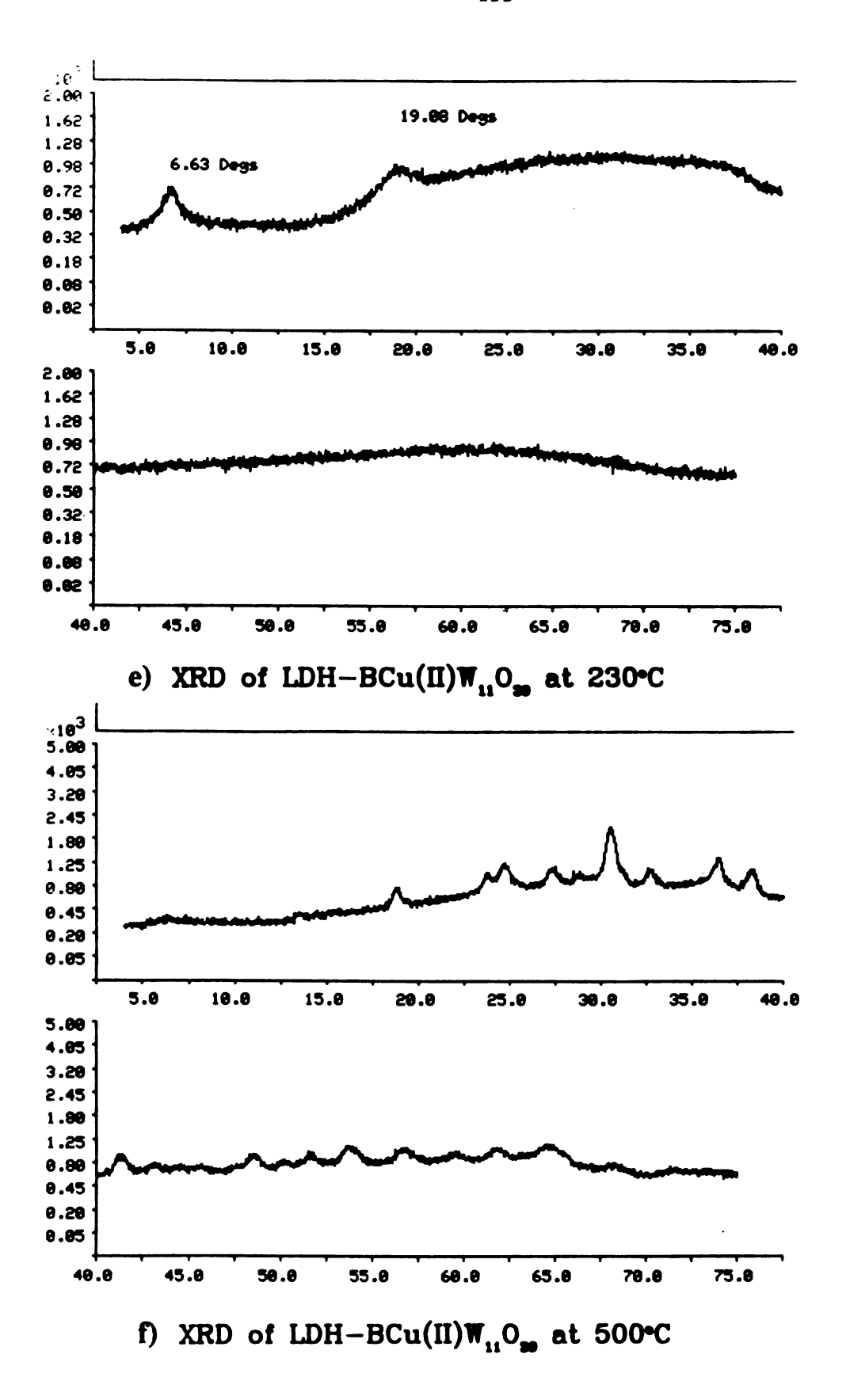
b) XRD of LDH-BCu(II)W<sub>11</sub>O<sub>20</sub> at 125°C







d) XRD of LDH-BCu(II)W<sub>11</sub>O<sub>20</sub> at 190°C



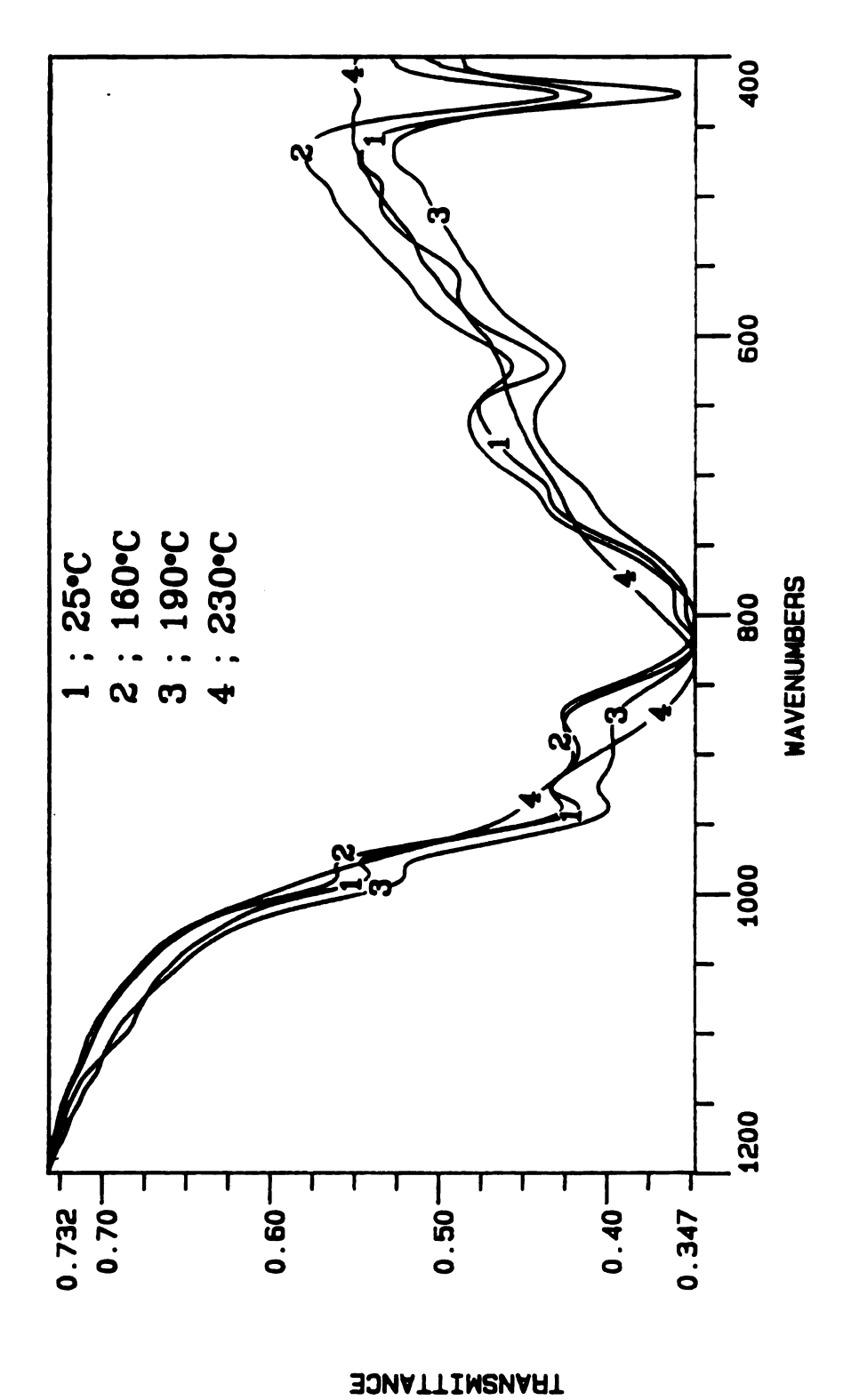


Fig. 57. Ir spectra of LDH-BCuW $_{11}$ O $_{39}$  at different temperatures.

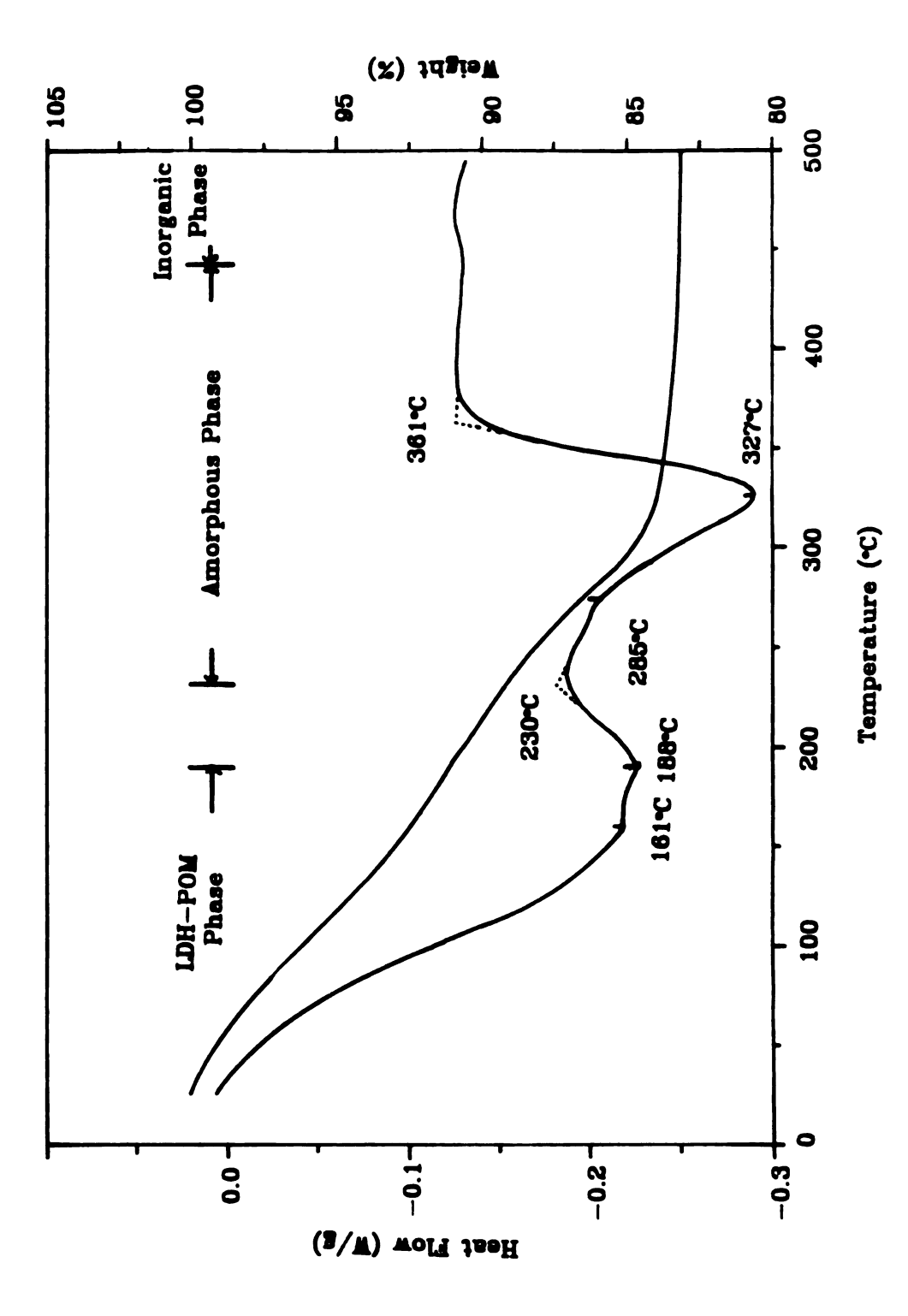
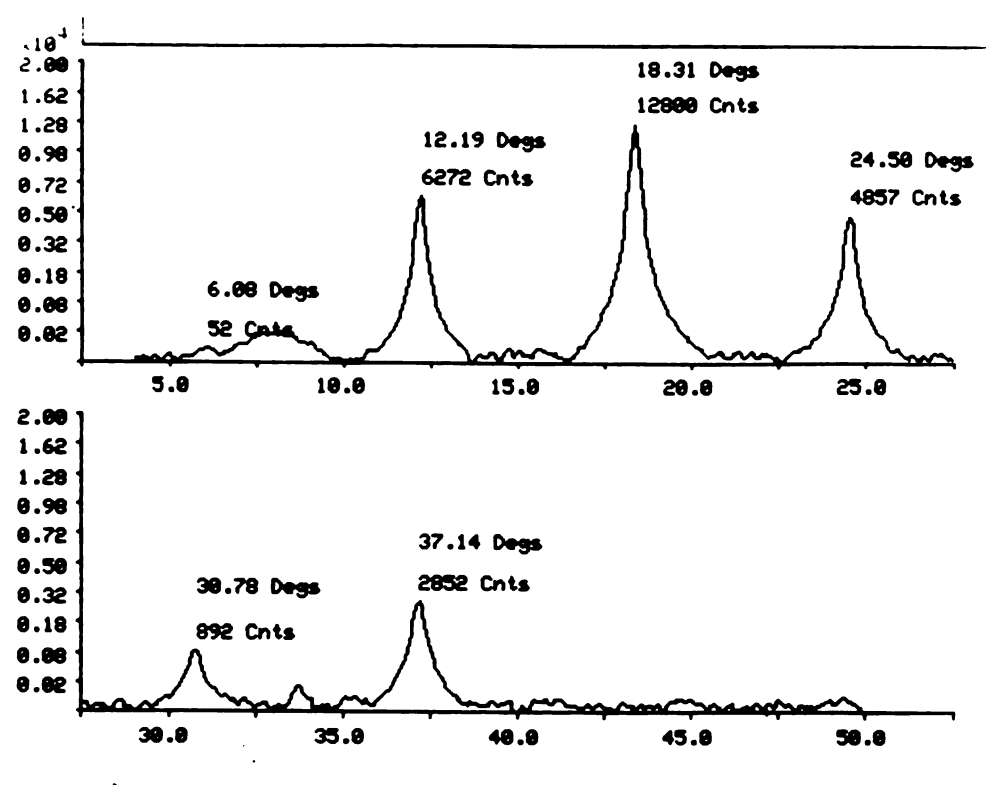
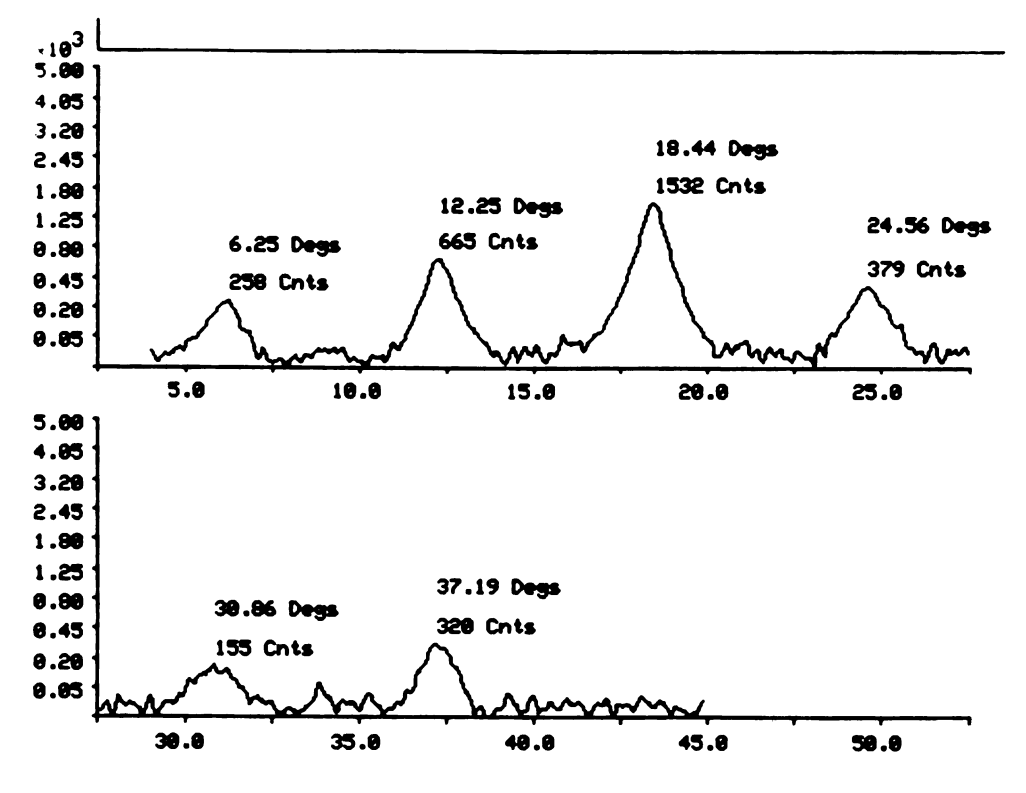


Fig. 58. DSC and TGA of LDH-BCuW<sub>11</sub>0<sub>39</sub>.

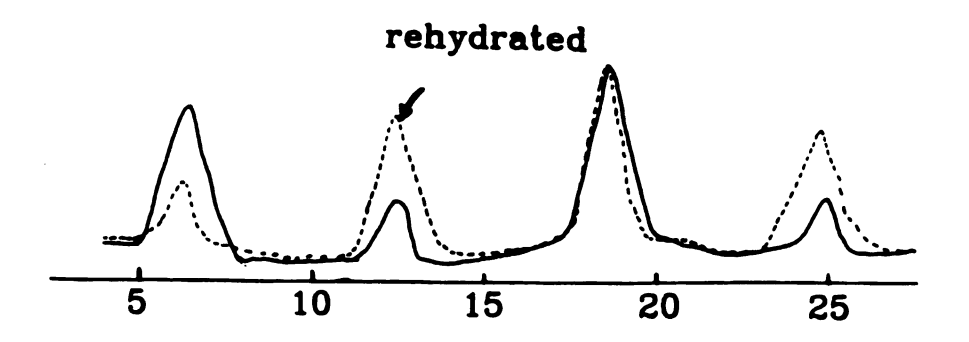
Fig. 59. XRD pattern of LDH-PMo<sub>2</sub>W<sub>9</sub>O<sub>39</sub> at different temperatures. a) 25°C, b) 150°C, c) 205°C: dotted line for the rehydrated sample, solid line for the dehydrated sample, d) 340°C, and e) 500°C.

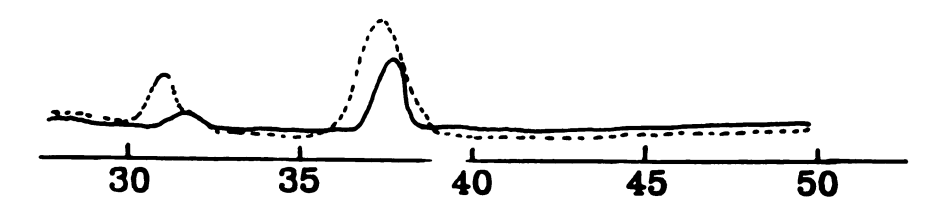




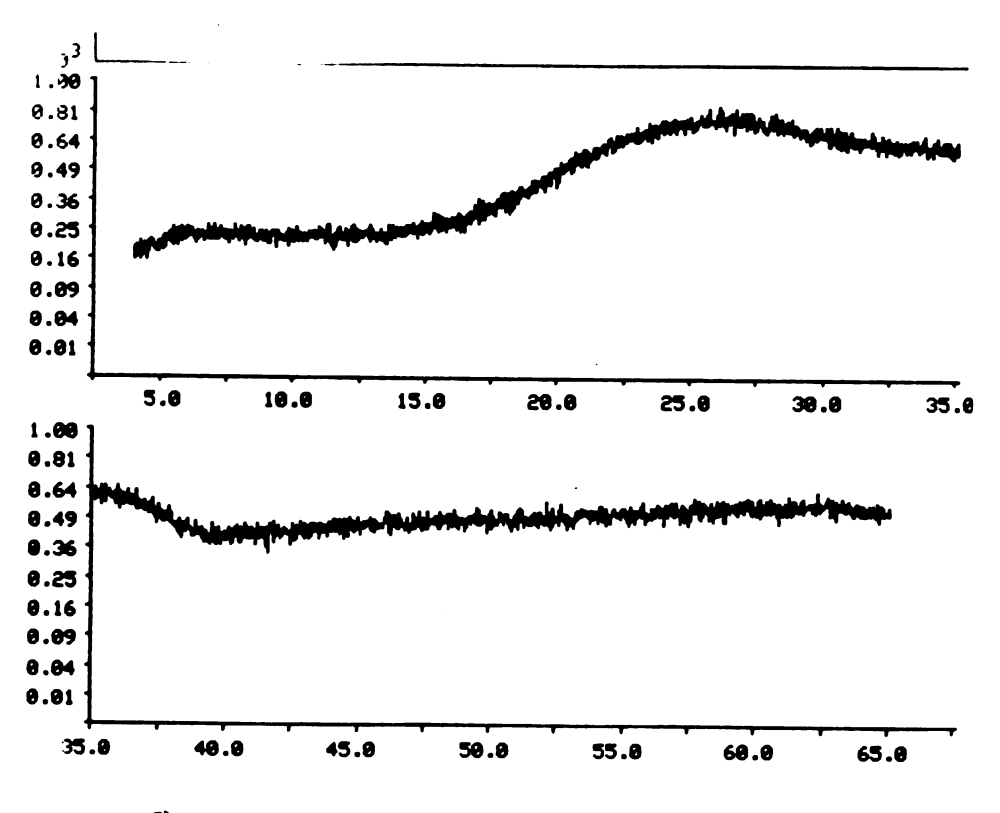


b) XRD of LDH-PMo, W.O. at 150°C

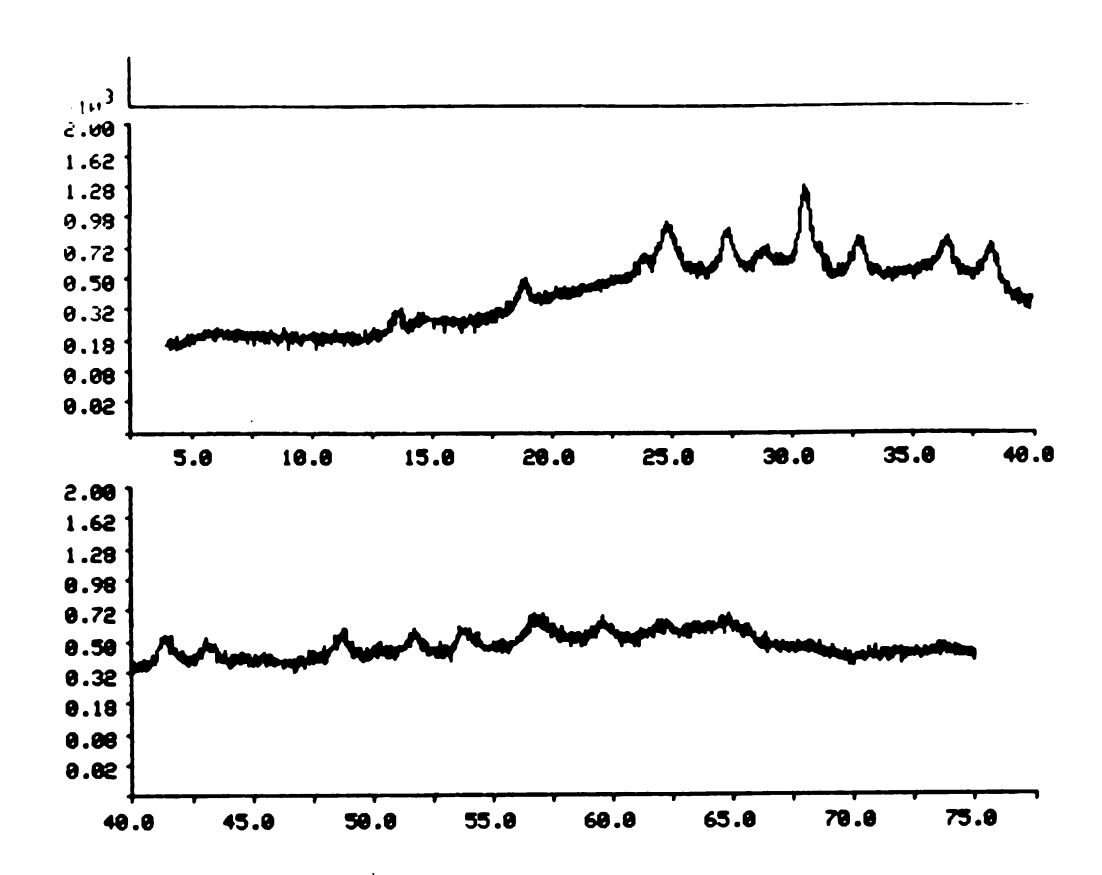




c) XRD of LDH-PMo, WO, at 205°C



d) XRD of LDH-PMo<sub>2</sub>W<sub>9</sub>O<sub>30</sub> at 340°C



e) XRD of LDH-PMo<sub>2</sub>W<sub>0</sub>O<sub>30</sub> at 500°C

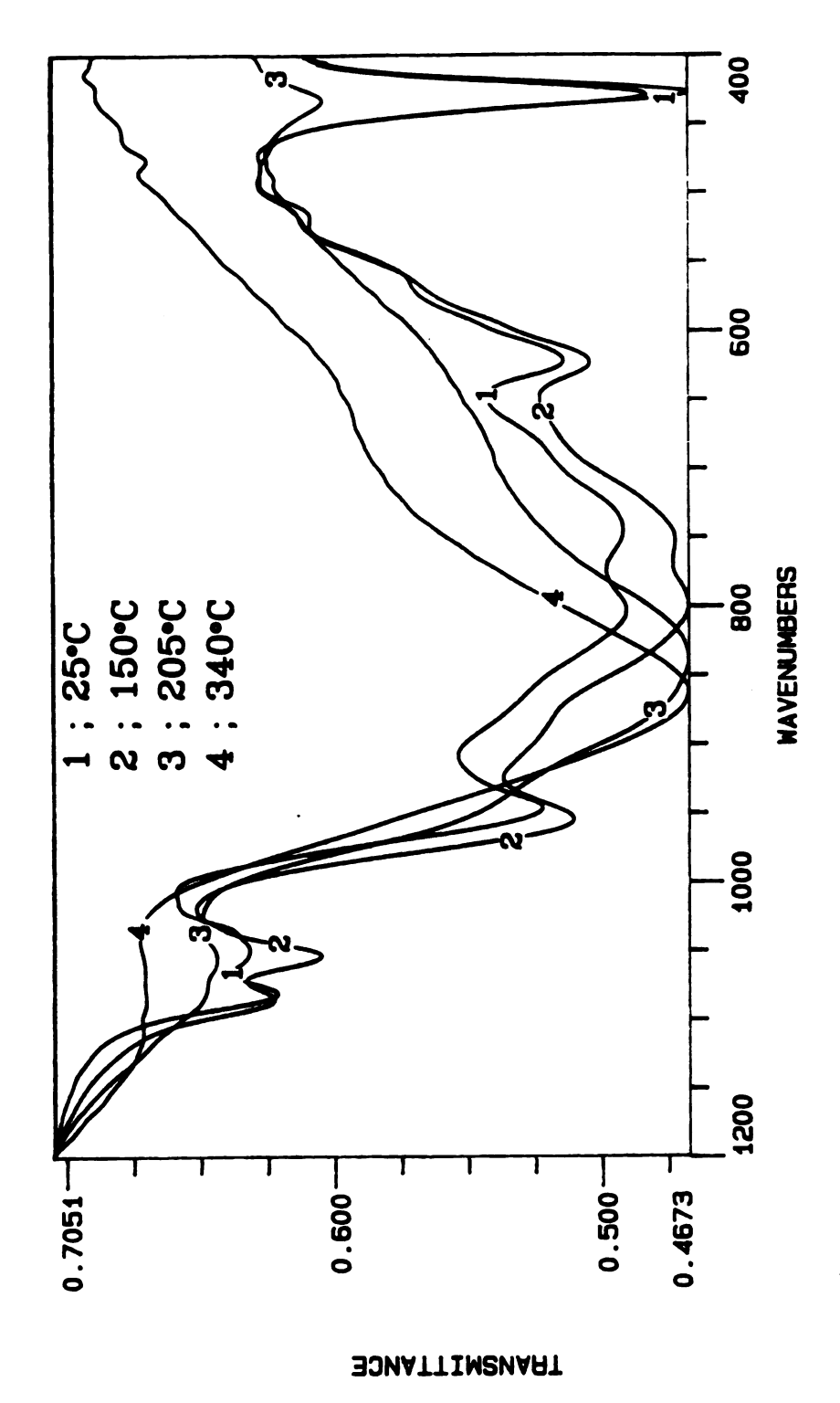


Fig. 60. Ir spectra of LDH-PMo2W9O39 at different temperatures.

The DSC and TGA of LDH-PMo<sub>2</sub>W<sub>9</sub>O<sub>39</sub> are shown in Fig. 61. The dehydration process occurs up to 205°C, followed by dehydroxylation of the layer up to 340°C. There is a small exothermic peak starting at about 450°C which corresponds to the process of new crystalline inorganic phase formation.

LDH-SiFe(SO<sub>3</sub>)W<sub>11O<sub>39</sub></sub>: This complex is stable up to 200°C and rehydration is possible below this point shown in Fig. 62. The XRD pattern of the specimen heated to  $268^{\circ}$ C shows only one unidentified small peak at  $2\theta = 7.17^{\circ}$ . Its ir spectrum shows only one absorption band centered at 863 cm<sup>-1</sup> without a band around 427 cm<sup>-1</sup>, indicative of degradation of both the POM in the gallery and the hydroxyl layer, as shown in Fig. 63. An amorphous phase is observed until new crystalline inorganic phases appear at  $500^{\circ}$ C.

The DSC and TGA of LDH-SiFe(SO<sub>3</sub>)W<sub>11</sub>O<sub>39</sub> are provided in Fig. 64. The dehydration process occurs up to 207°C, followed by dehydroxylation of hydroxyl layer up to 338°C. At 450°C new crystalline inorganic phases appear.

LDH-SiW11O39: This system is stable at 180°C. Rehydration of heated samples is possible, as indicated by their XRD pattern shown in Fig. 65. The decomposition of both the hydroxyl layer and the POM in the gallery occurs beyond 180°C, as shown in the ir spectra provided in Fig. 66. At 300°C LDH-SiW11O39 becomes amorphous; new crystalline inorganic phases appear at 500°C, as shown in Fig. 65

The DSC and TGA of LDH-SiW<sub>11</sub>O<sub>39</sub> are provided in Fig. 67. The dehydration process occurs up to 227°C, followed by the dehydroxylation of layer up to 356°C. An exothermic peak starting at 450°C corresponds to the onset of new crystalline inorganic phases formation.

LDH-BW11039: This complex is stable at 210°C. Rehydration of heated samples is possible below this point, as shown by XRD patterns in Fig. 68. At 260°C, the LDH-BW11039 turns into an amorphous phase; new crystalline inorganic phases appear at 500°C. As in the other cases, the ir spectrum Fig. 69 of an amorphous material shows

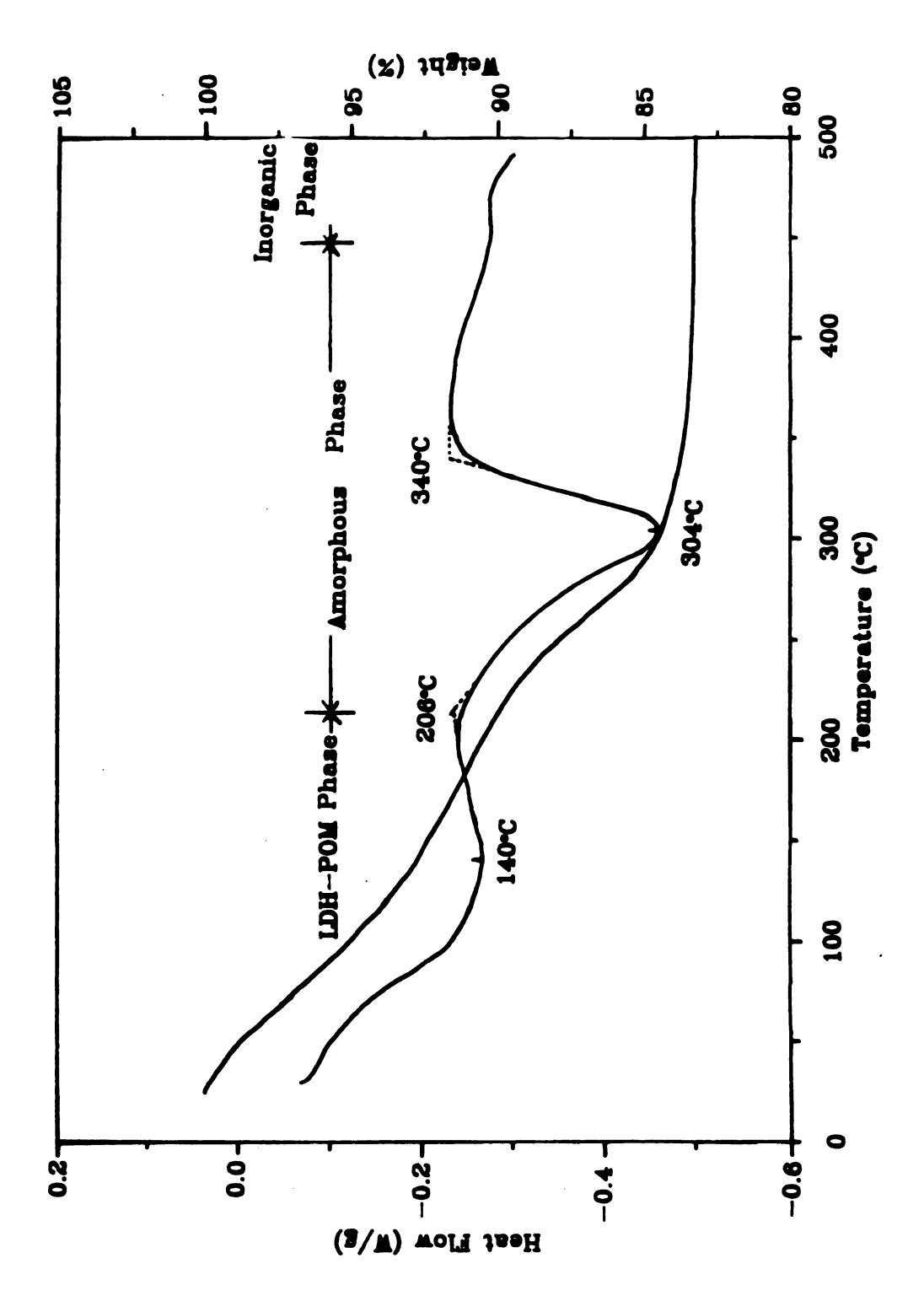
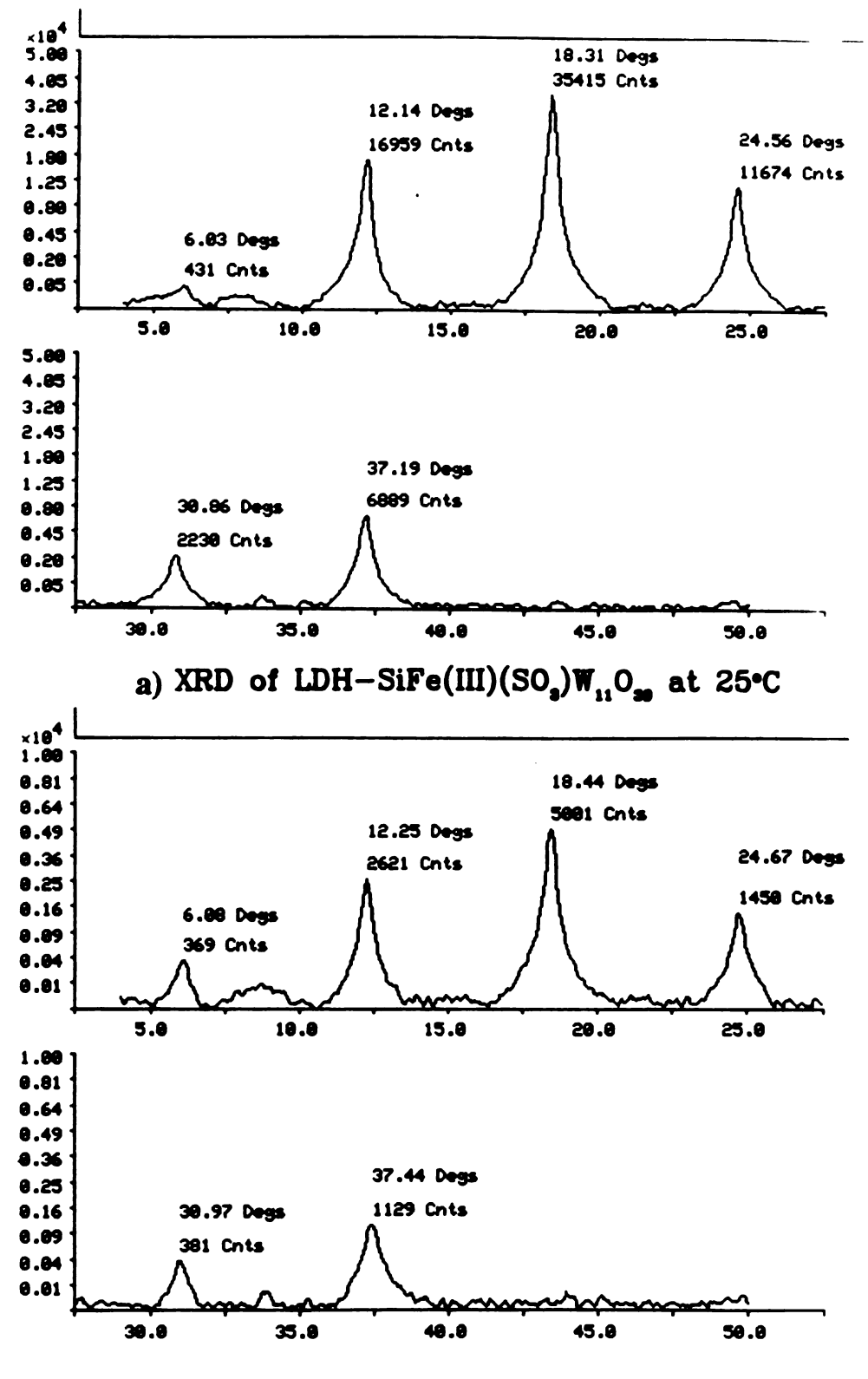
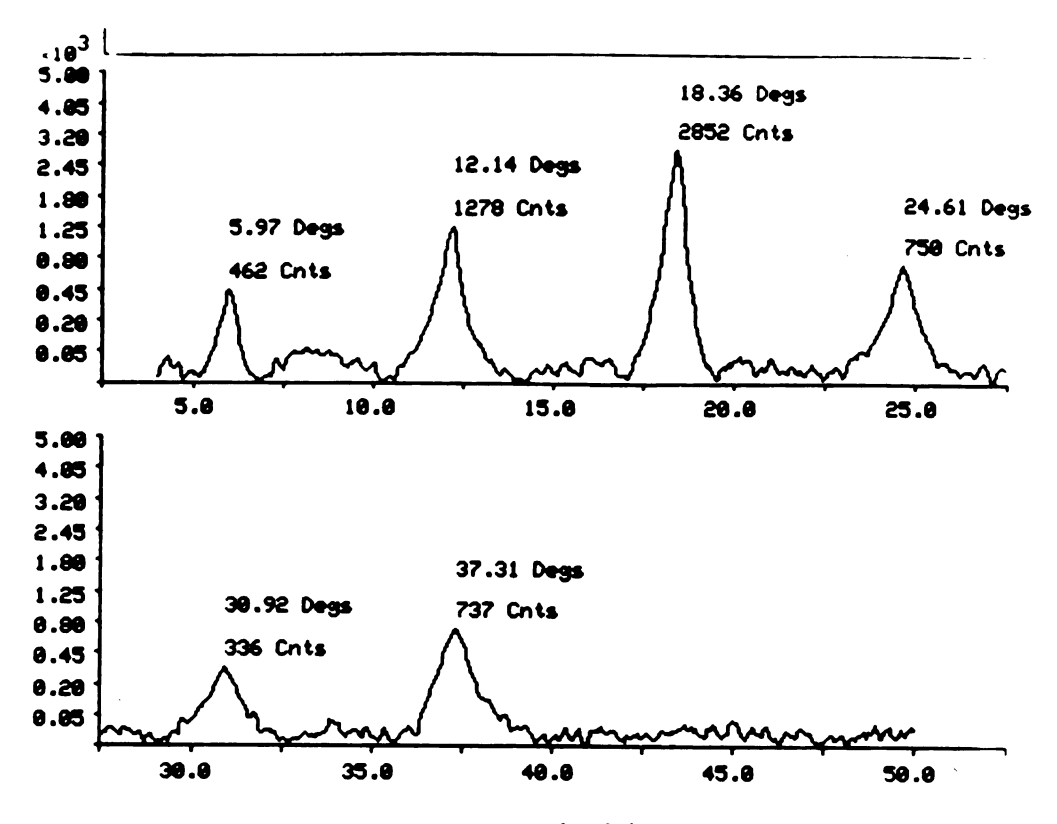


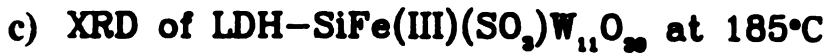
Fig. 61. DSC and TGA of LDH-PMo<sub>2</sub>W<sub>9</sub>O<sub>39</sub>.

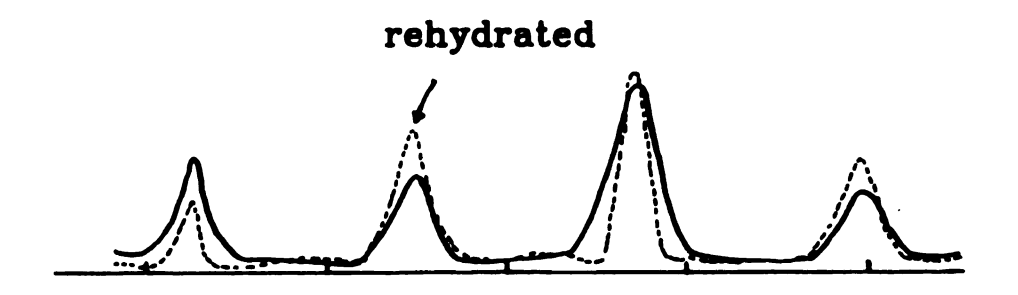
Fig. 62. XRD pattern of SiFe(SO<sub>3</sub>)W<sub>11</sub>O<sub>39</sub> at different temperatures. a) 25°C, b)  $150^{\circ}$ C, c)  $185^{\circ}$ C, d)  $200^{\circ}$ C: dotted line for the rehydrated sample, solid line for the dehydrated sample, e)303°C and f)  $500^{\circ}$ C.



b) XRD of LDH-SiFe(III)(SO<sub>3</sub>)W<sub>11</sub>O<sub>30</sub> at 150°C

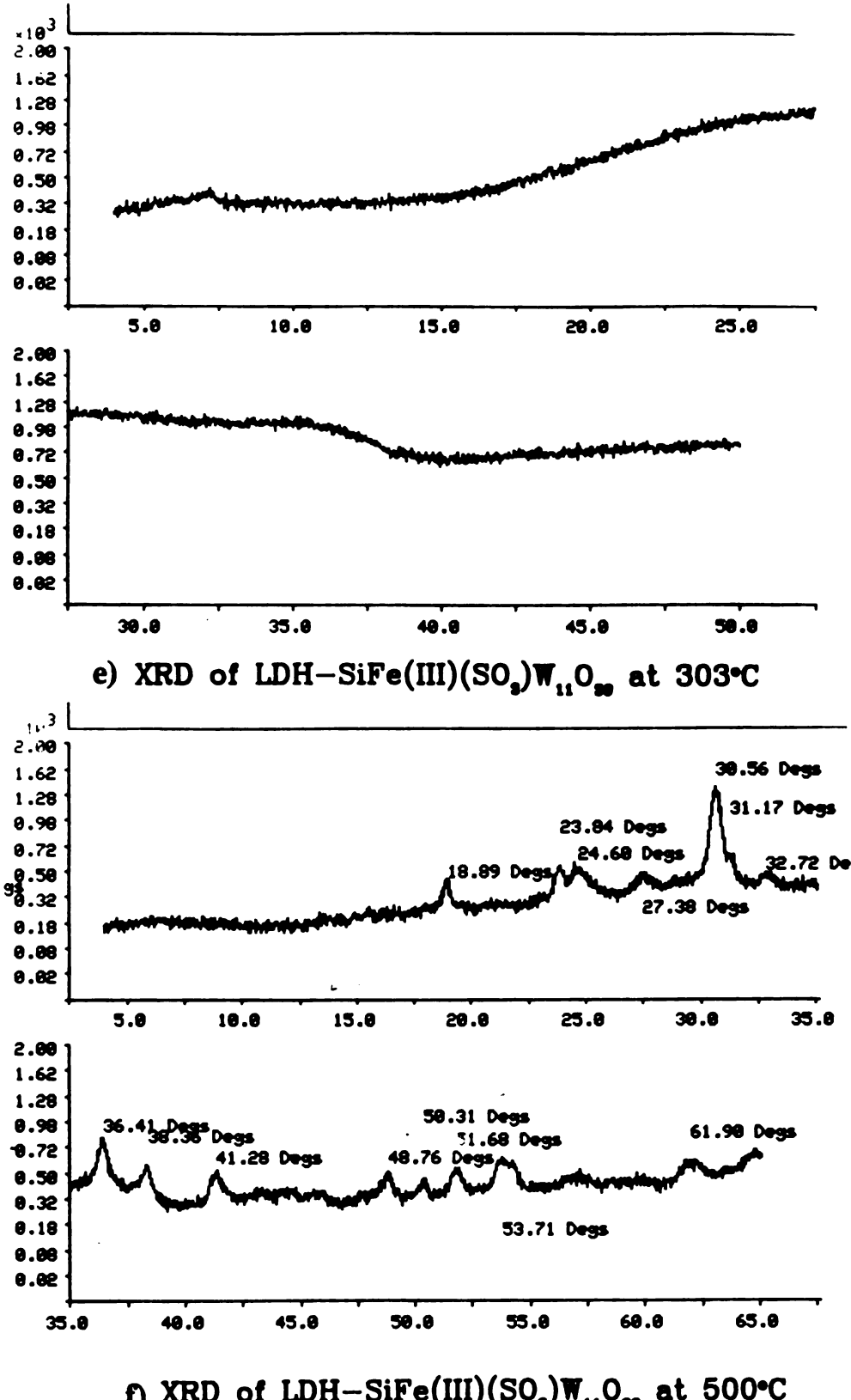








d) XRD of LDH-SiFe(III)(SO<sub>s</sub>)W<sub>11</sub>O<sub>se</sub> at 200°C



f) XRD of LDH-SiFe(III)(SO<sub>s</sub>)W<sub>11</sub>O<sub>se</sub> at 500°C

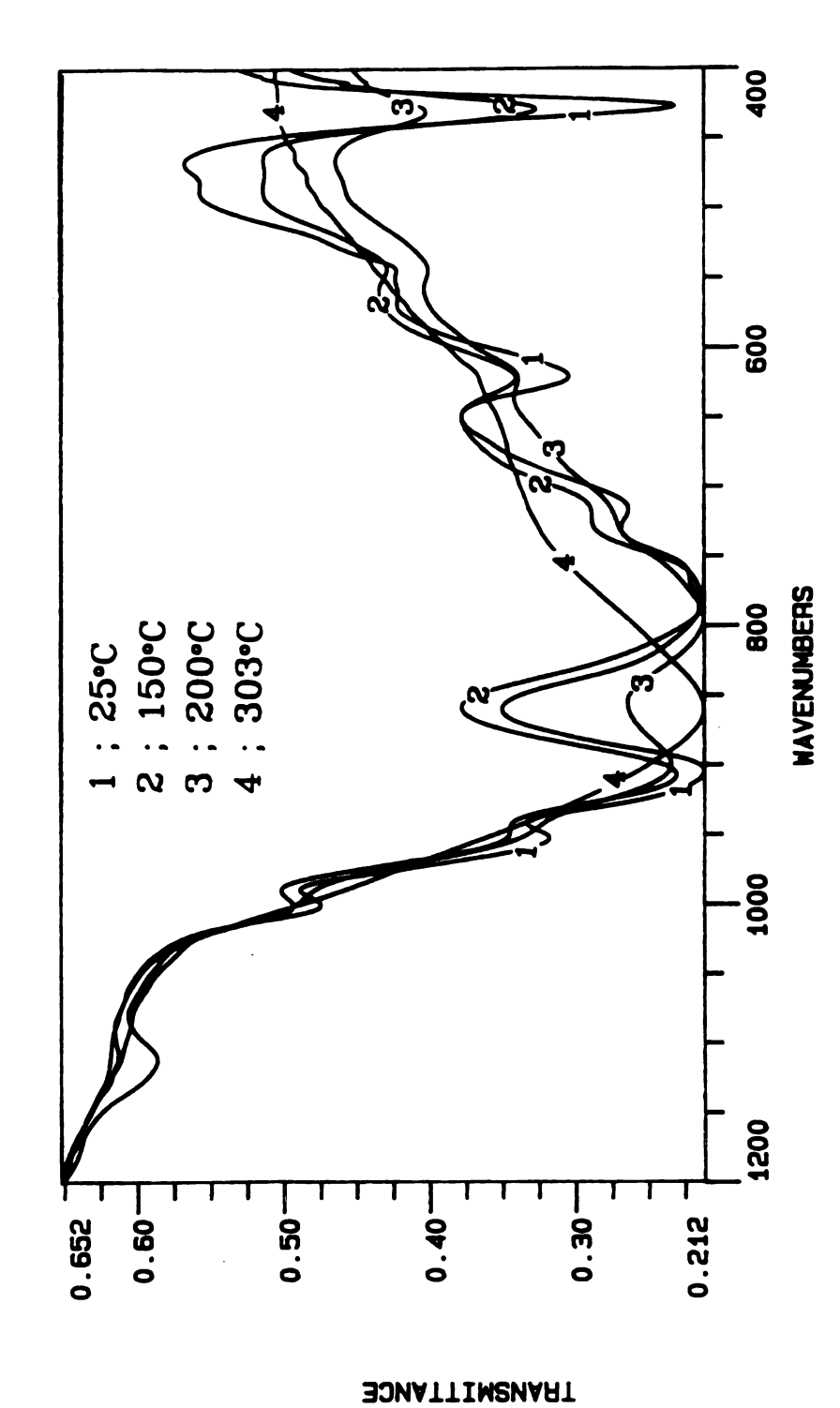


Fig. 63. Ir spectra of LDH-SiFe(SO<sub>3</sub>)W<sub>11</sub>O<sub>39</sub> at different temperatures.

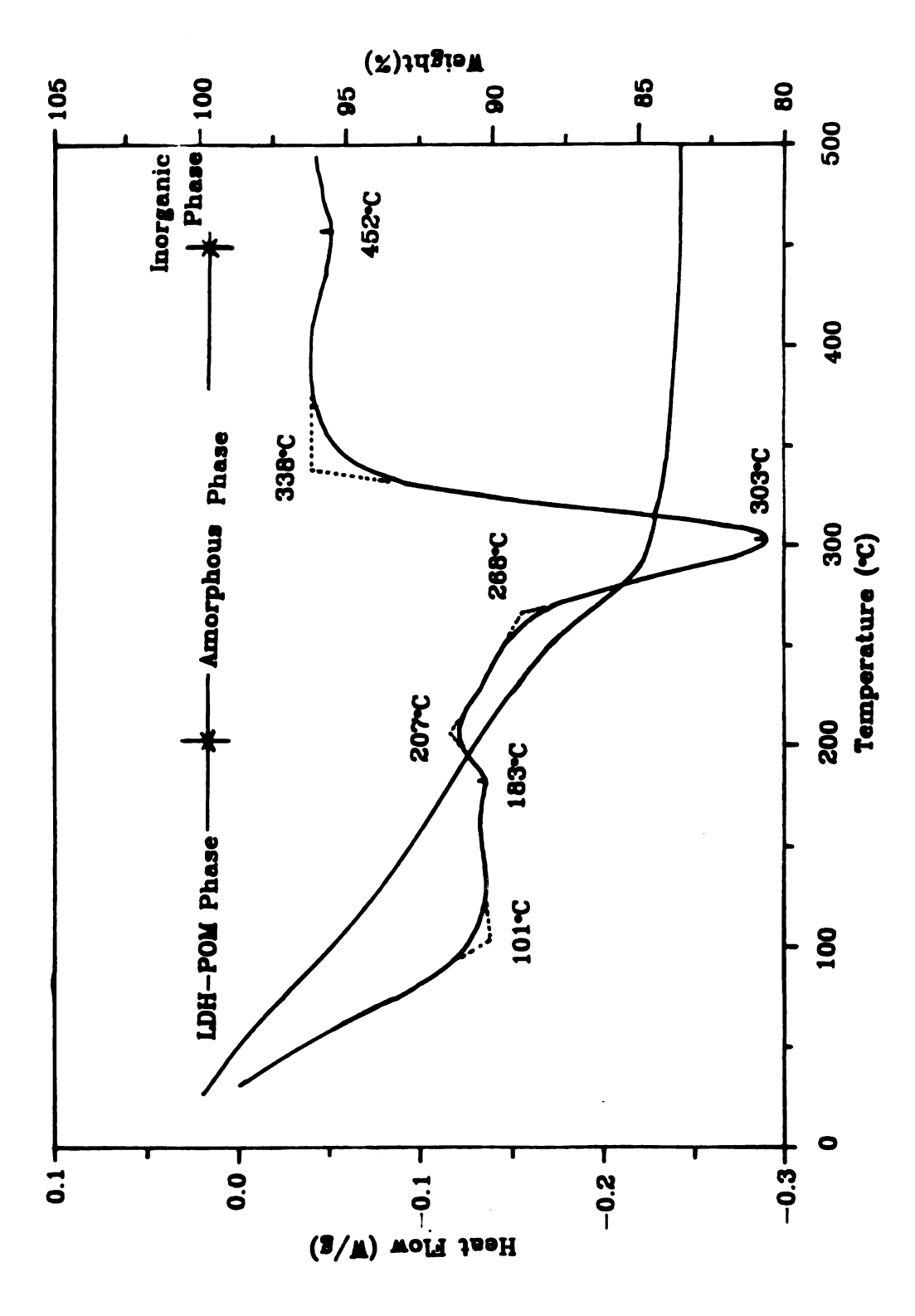
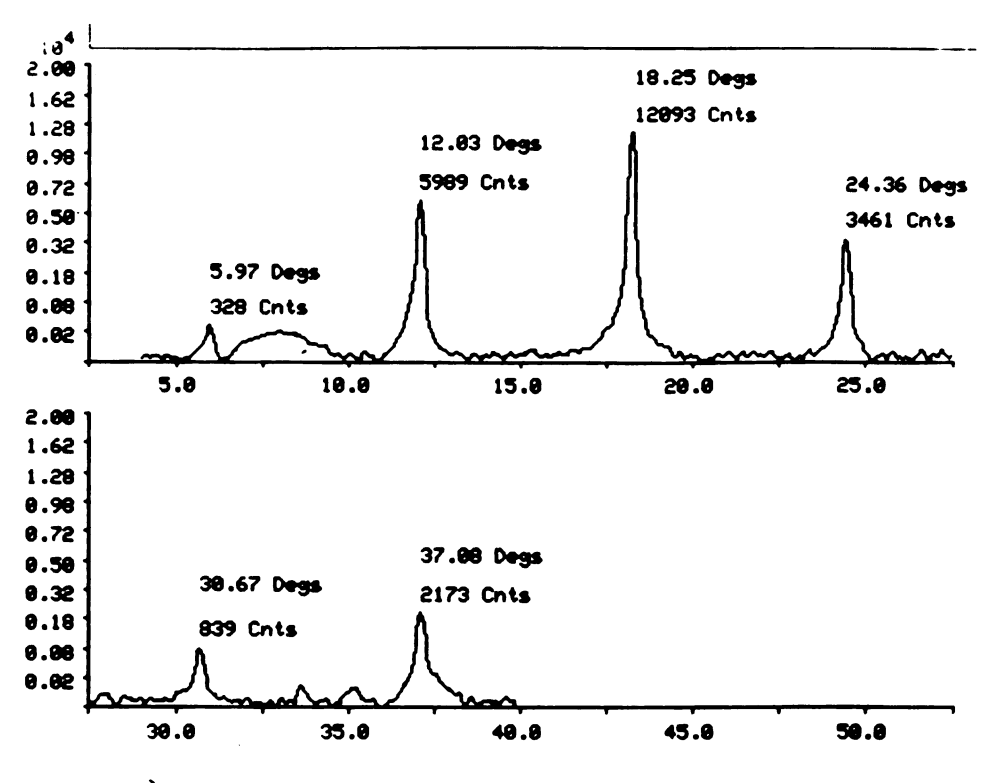


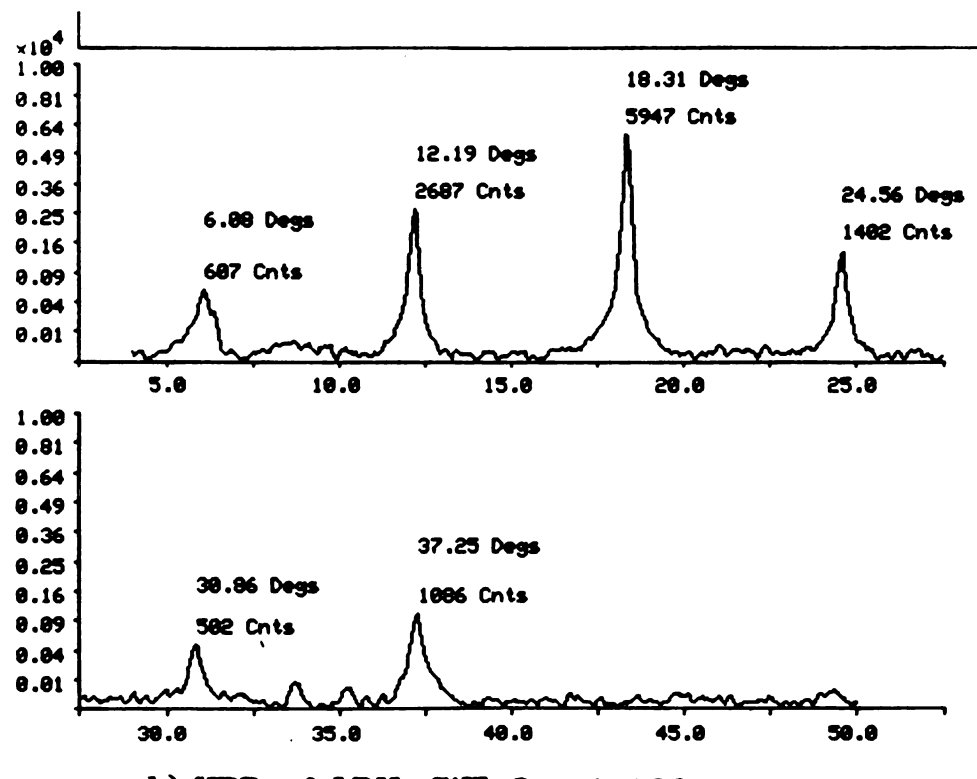
Fig. 64. DSC and TGA of LDH-SiFe(SO<sub>3</sub>)W<sub>11</sub>O<sub>39</sub>.

Fig. 65. XRD pattern of LDH-SiW11O39 at different temperatures. a) 25°C, b) 160°C, c) 180°C: dotted line for the rehydrated sample, solid line for the dehydrated sample, d) 230°C, e) 300°C and f) 500°C.

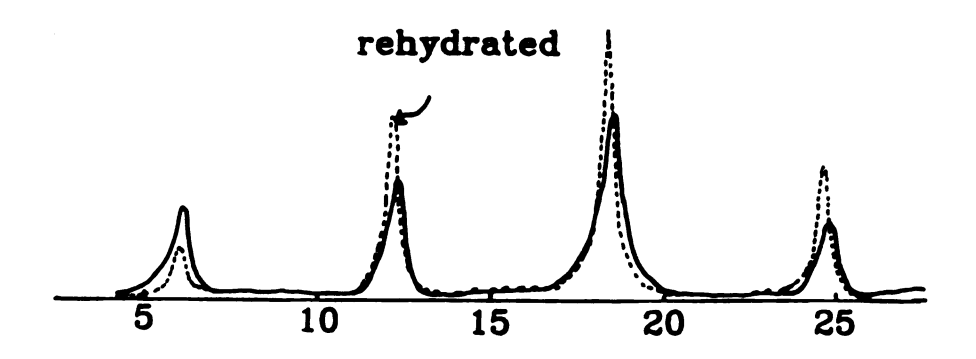


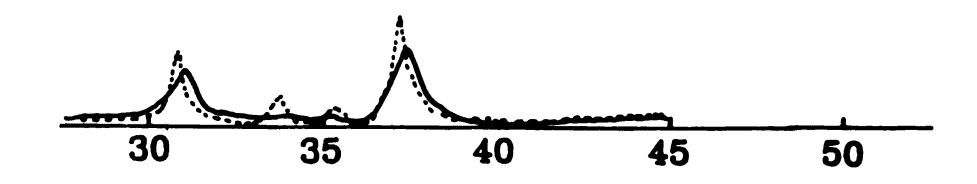
a) XRD of LDH-SiW<sub>11</sub>O<sub>20</sub> at 25°C

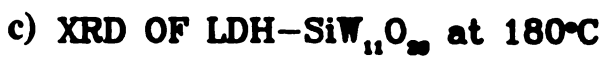
) 160°C

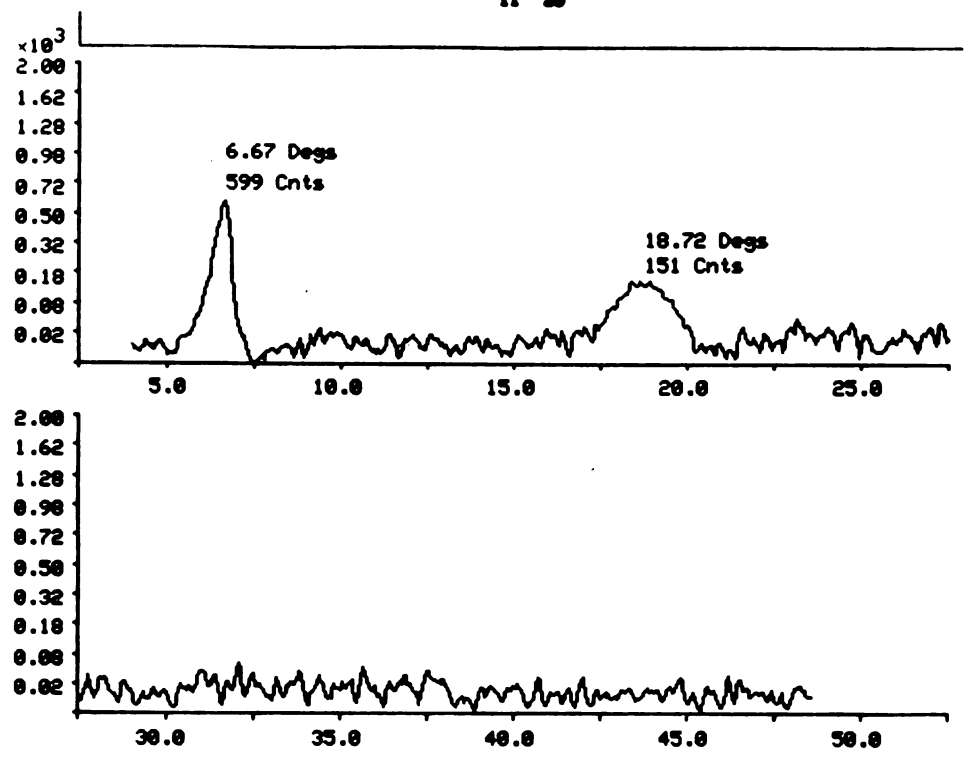


b) XRD of LDH-SiW<sub>11</sub>O<sub>20</sub> at 160°C

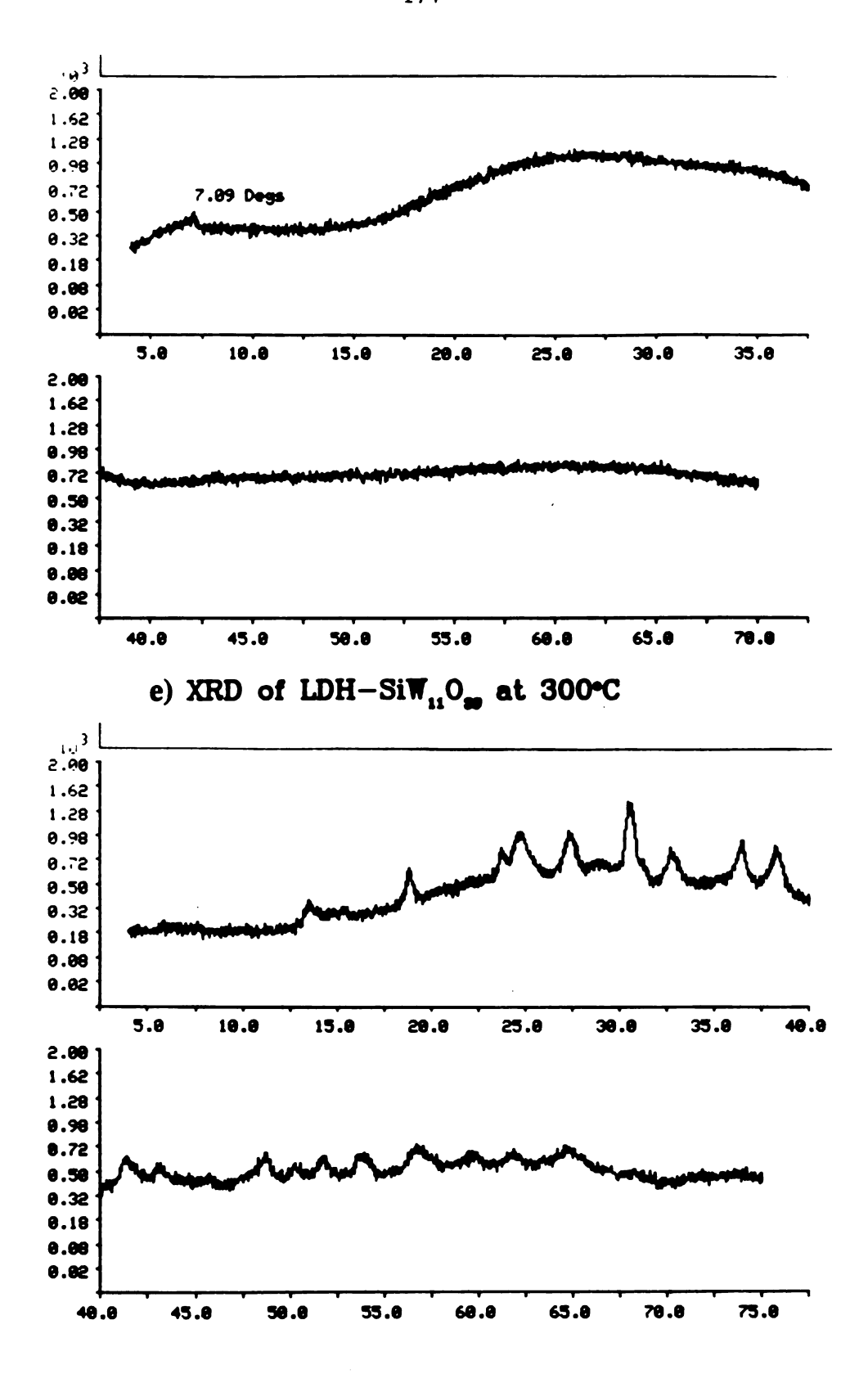








d) XRD of LDH-Si $W_{11}O_{20}$  at 230°C



f) XRD of LDH-SiW<sub>11</sub>O<sub>20</sub> at 500°C

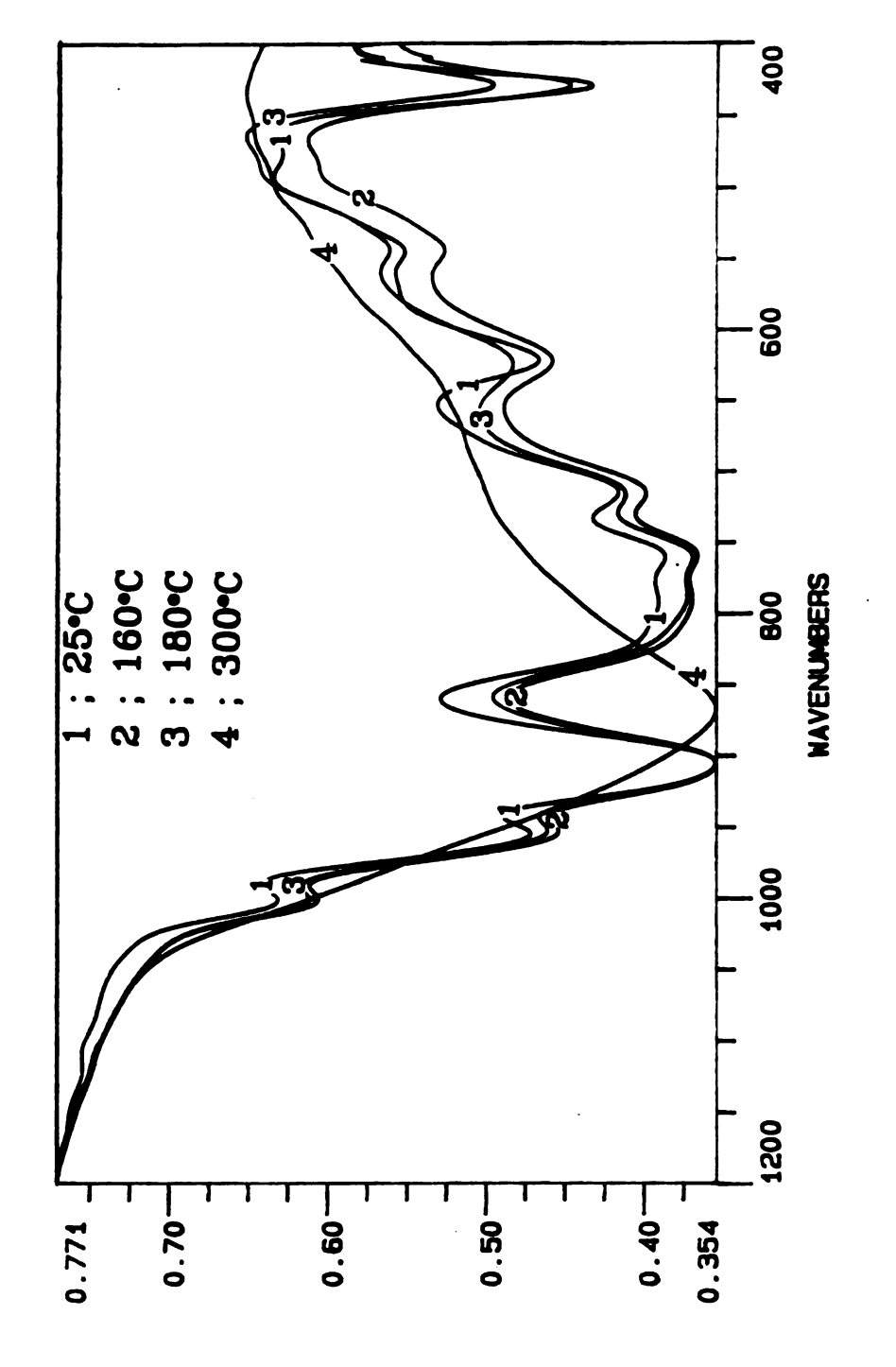


Fig. 66. Ir spectra of LDH-SiW<sub>11</sub>O<sub>39</sub> at different temperatures.

100

THANSMITTANCE

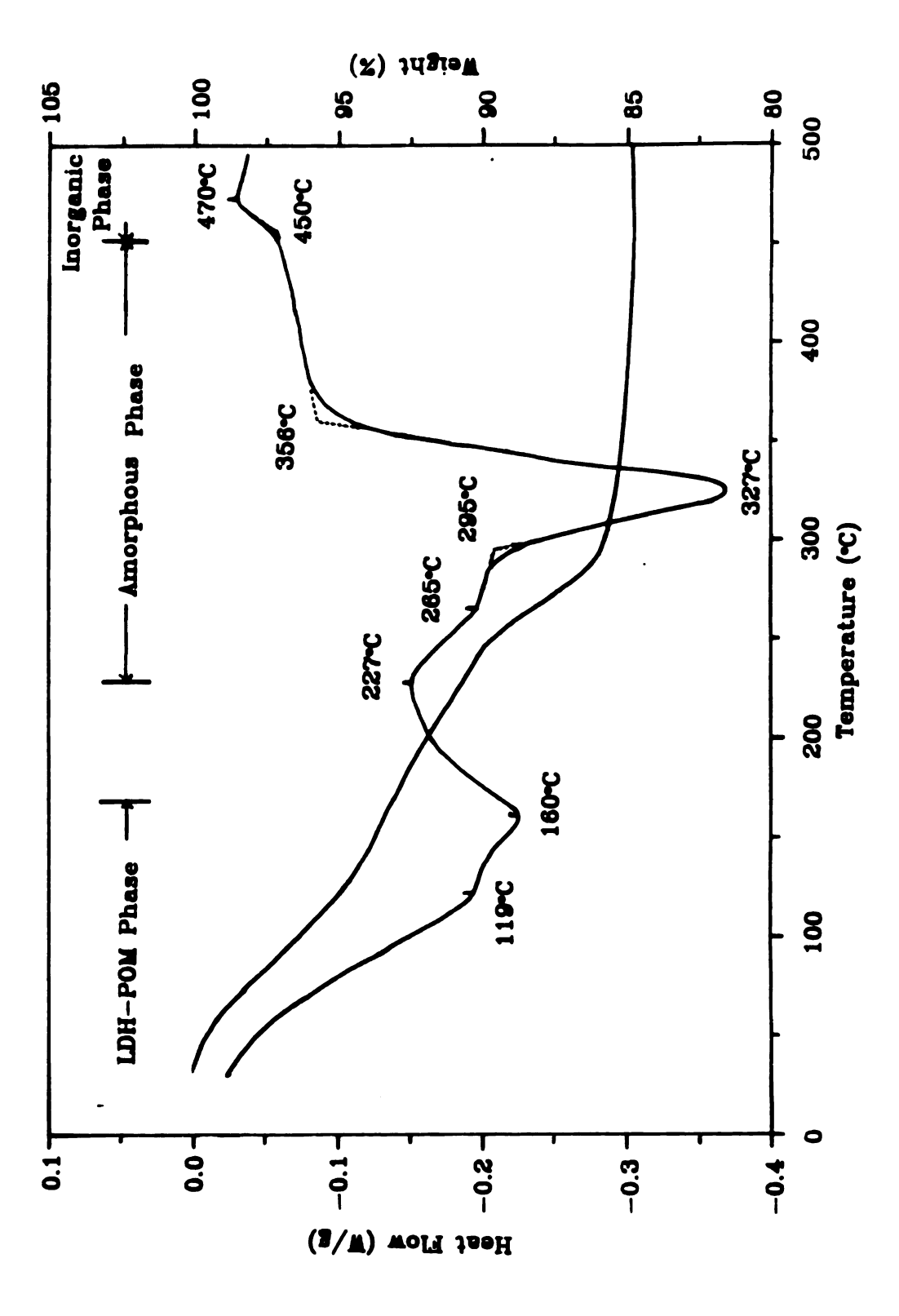
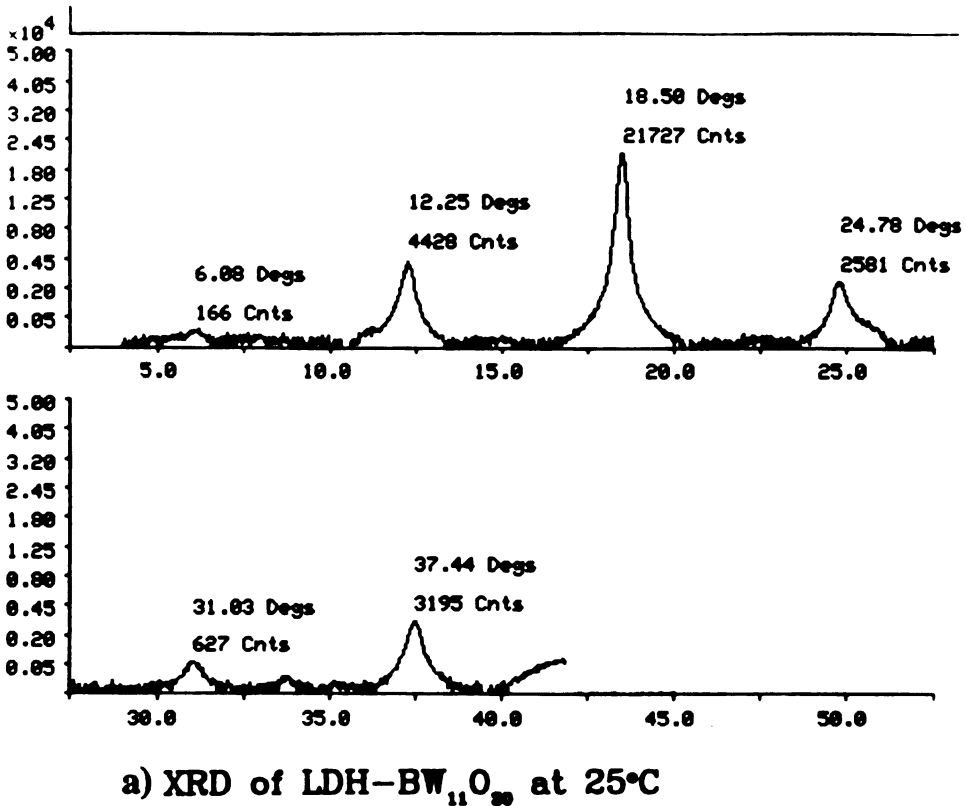
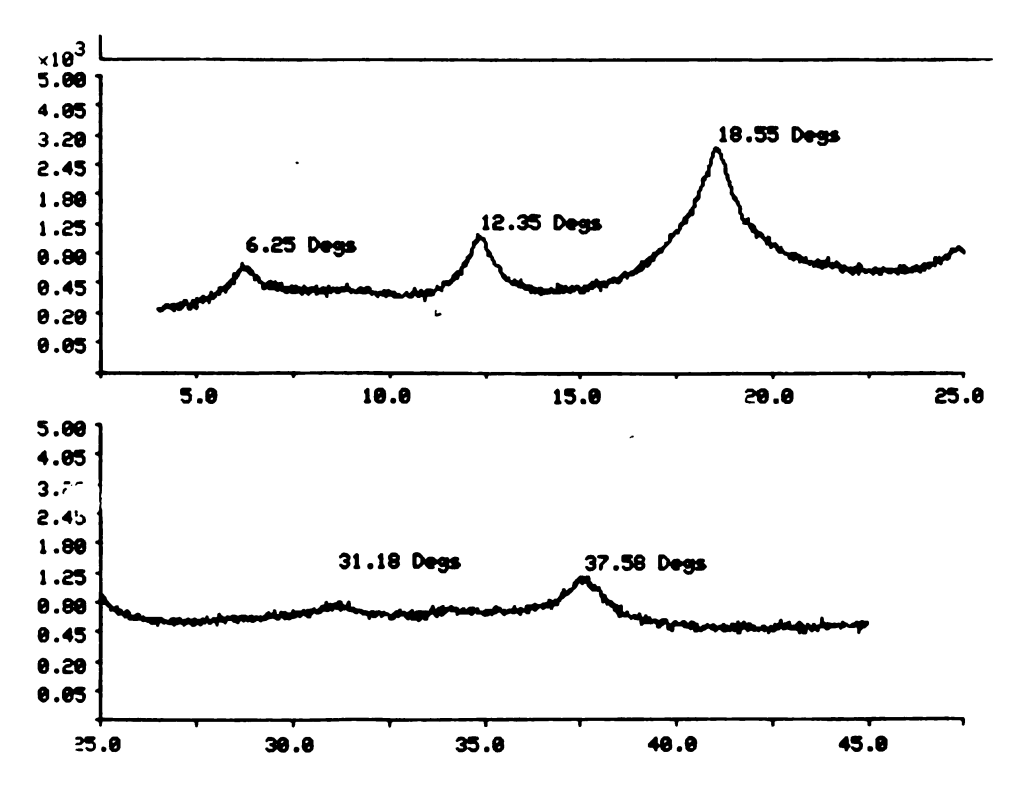


Fig. 67. DSC and TGA of LDH-SiW  $_{11}\mathrm{O}_{39}$ .

Fig. 68. XRD pattern of LDH-BW<sub>11</sub>O<sub>39</sub> at different temperatures. a) 25°C, b) 150°C, c) 180°C: dotted line for the rehydrated sample, solid line for the dehydrated sample, d) 210°C, e) 260°C and f) 500°C.

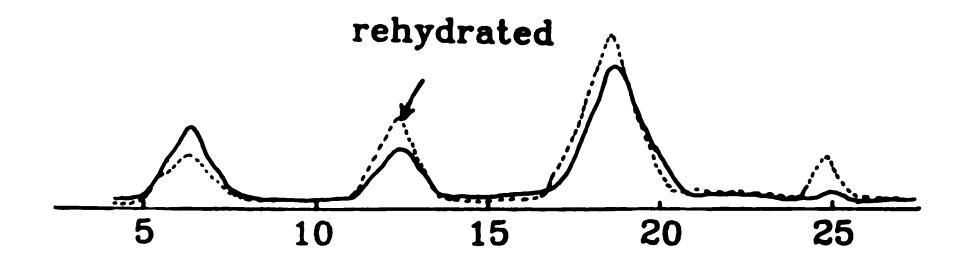


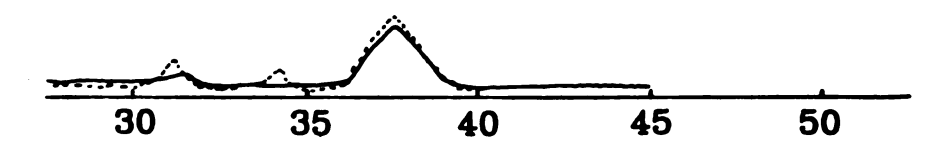


b) XRD of LDH-BW<sub>11</sub>O<sub>30</sub> at 150°C

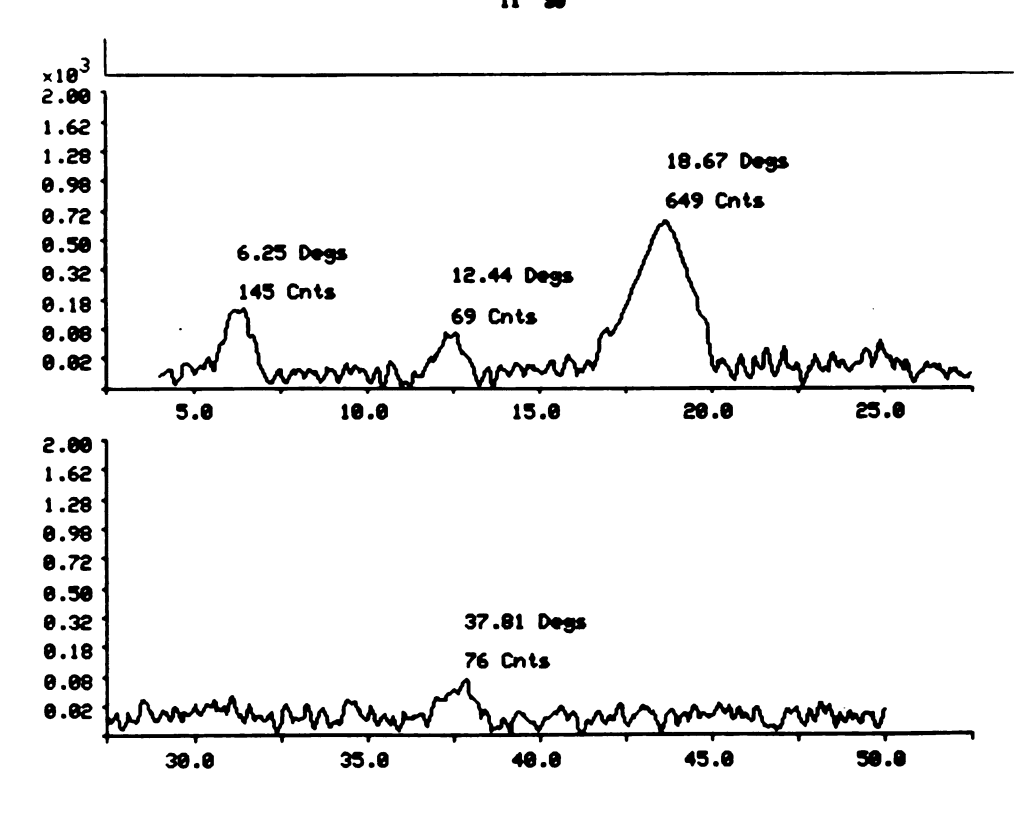
5°C, b) 150°C

ared sample i

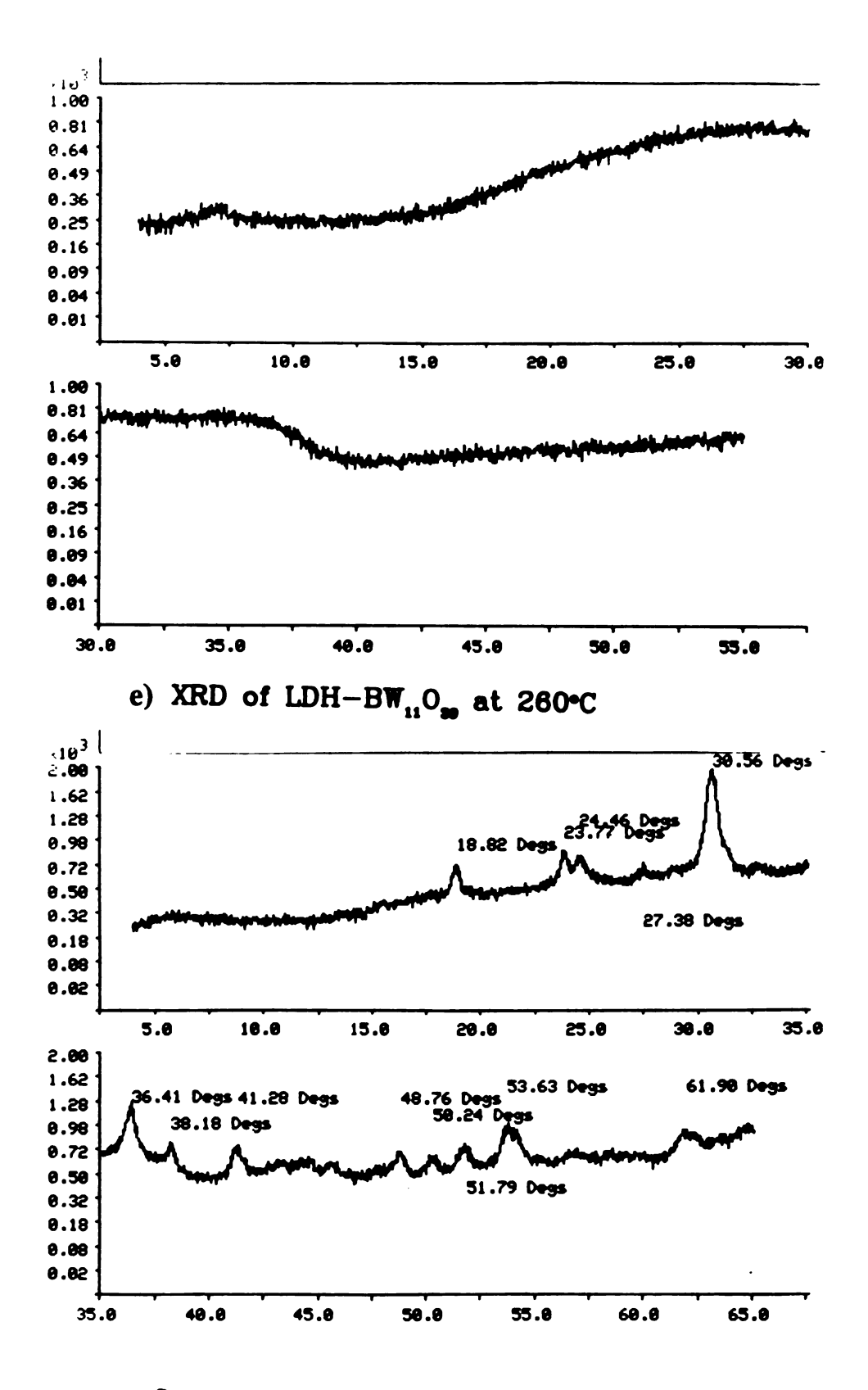




c) XRD of LDH-BW<sub>11</sub>O<sub>30</sub> at 180°C



d) XRD of LDH-BW<sub>11</sub>O<sub>se</sub> at 210°C



f) XRD of LDH-BW<sub>11</sub>O<sub>30</sub> at 500°C

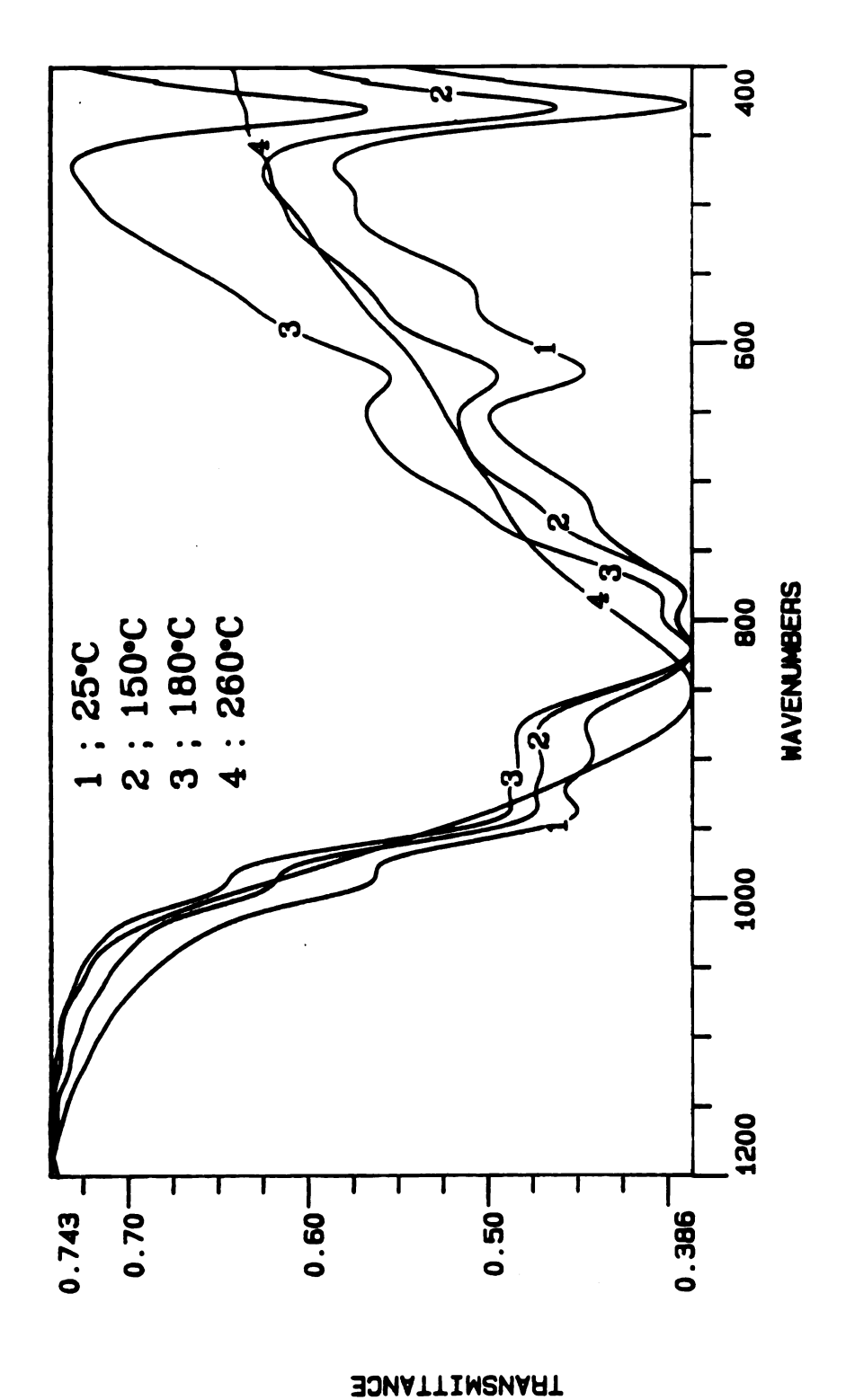


Fig. 69. Ir spectra of LDH-BW11039 at different temperatures.

only one absorption band centered at 855 cm<sup>-1</sup> without the band around 427 cm<sup>-1</sup>, which is attributed to the Zn-OH-Al lattice vibration. Thus, species in an amorphous region do not contain an Al-O-Zn network.

The DSC and TGA of LDH-BW11O39 are provided in Fig. 70. The dehydration process occurs up to 208°C, followed by dehydroxylation of the hydroxyl layer up to 342°C. At 450°C new crystalline inorganic phases appear.

**LDH-Co<sub>2</sub>W<sub>12</sub>O<sub>42</sub>**: This system is stable to  $180^{\circ}$ C. Rehydration of sample heated to  $180^{\circ}$ C is possible as shown by their XRD pattern in Fig. 71. At  $225^{\circ}$ C, The ir spectrum provided in Fig. 72 shows that LDH-Co<sub>2</sub>W<sub>12</sub>O<sub>42</sub> decomposes at  $225^{\circ}$ C. There is only one absorption band centered at 841 cm<sup>-1</sup> as in the other cases. Its XRD pattern shows only one unidentified peak at  $2\theta = 6.9^{\circ}$ . At 320°C It becomes completely amorphous, as shown in its XRD pattern. The ir spectrum of this amorphous material below 1000 cm<sup>-1</sup> shows only one absorption band centered at 856 cm<sup>-1</sup>. At 500°C new crystalline inorganic phases appear.

The DSC and TGA of LDH-Co<sub>2</sub>W<sub>12</sub>O<sub>42</sub> are provided in Fig. 73. Dehydration occurs up to 223°C, followed by dehydroxylation of the hydroxyl layer up to 356°C. At 450°C new crystalline inorganic phases appear.

LDH-PW9O34: When this complex is heated even at 110°C, its XRD pattern shows remarkable peak broadening, as shown in Fig. 74. However, there is no substantial difference in its ir spectrum from that of an unheated samples shown in Fig. 75. Thus, it is obvious that heating causes no structural change in PW9O34 in the gallery by heating. The XRD peak broadening mainly originates from the layer sagging as discussed in a previous section in this chapter. Such a broadened XRD pattern is observed for the 215°C heated specimen; peak broadening is so severe that it is difficult to locate peaks. Rehydration is possible even though recovery of XRD pattern is very slow. Heating at 320°C causes it completely to an amorphous phase. As in the other cases, the ir spectrum below 1000 cm<sup>-1</sup> shows a typical single band centered at 852 cm<sup>-1</sup> below 1000

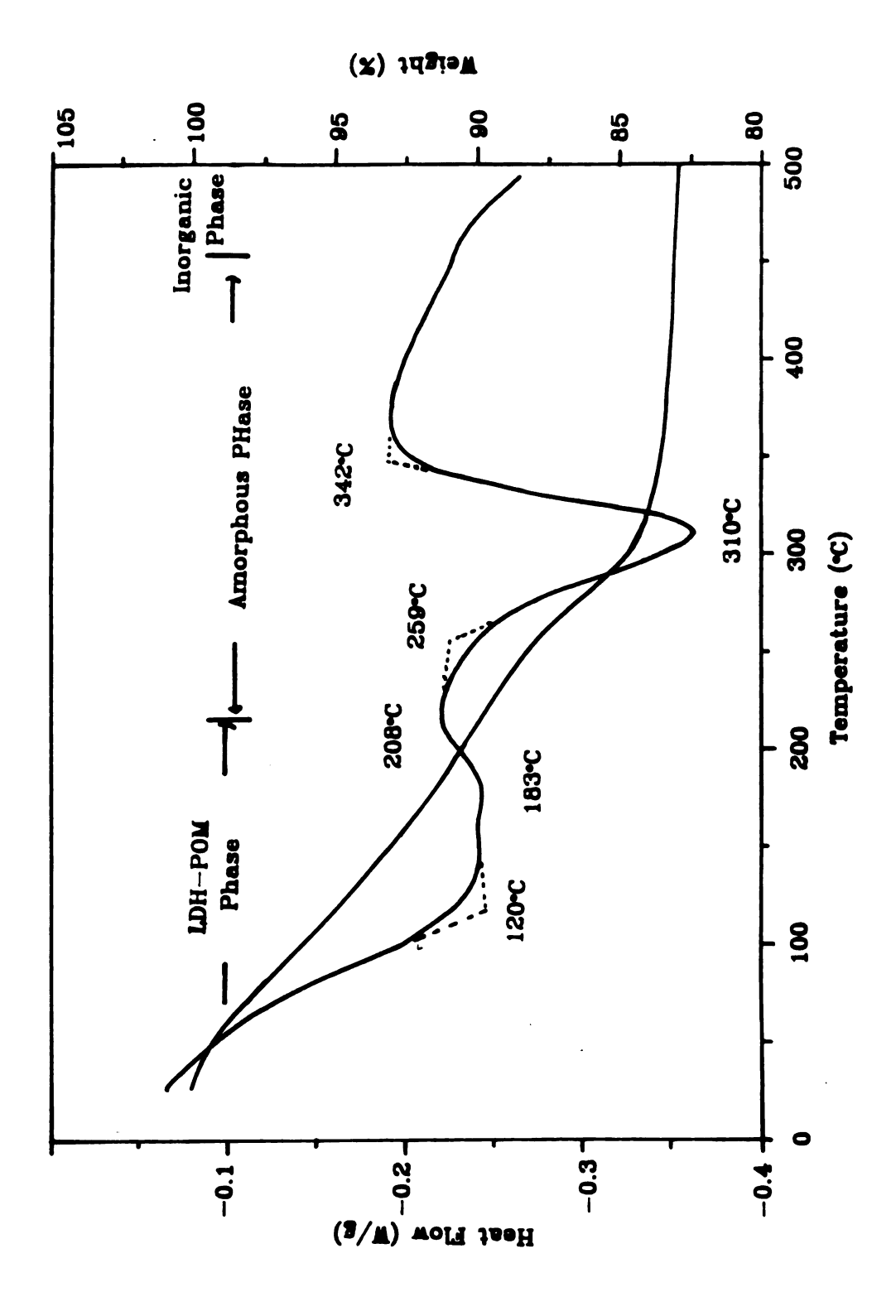


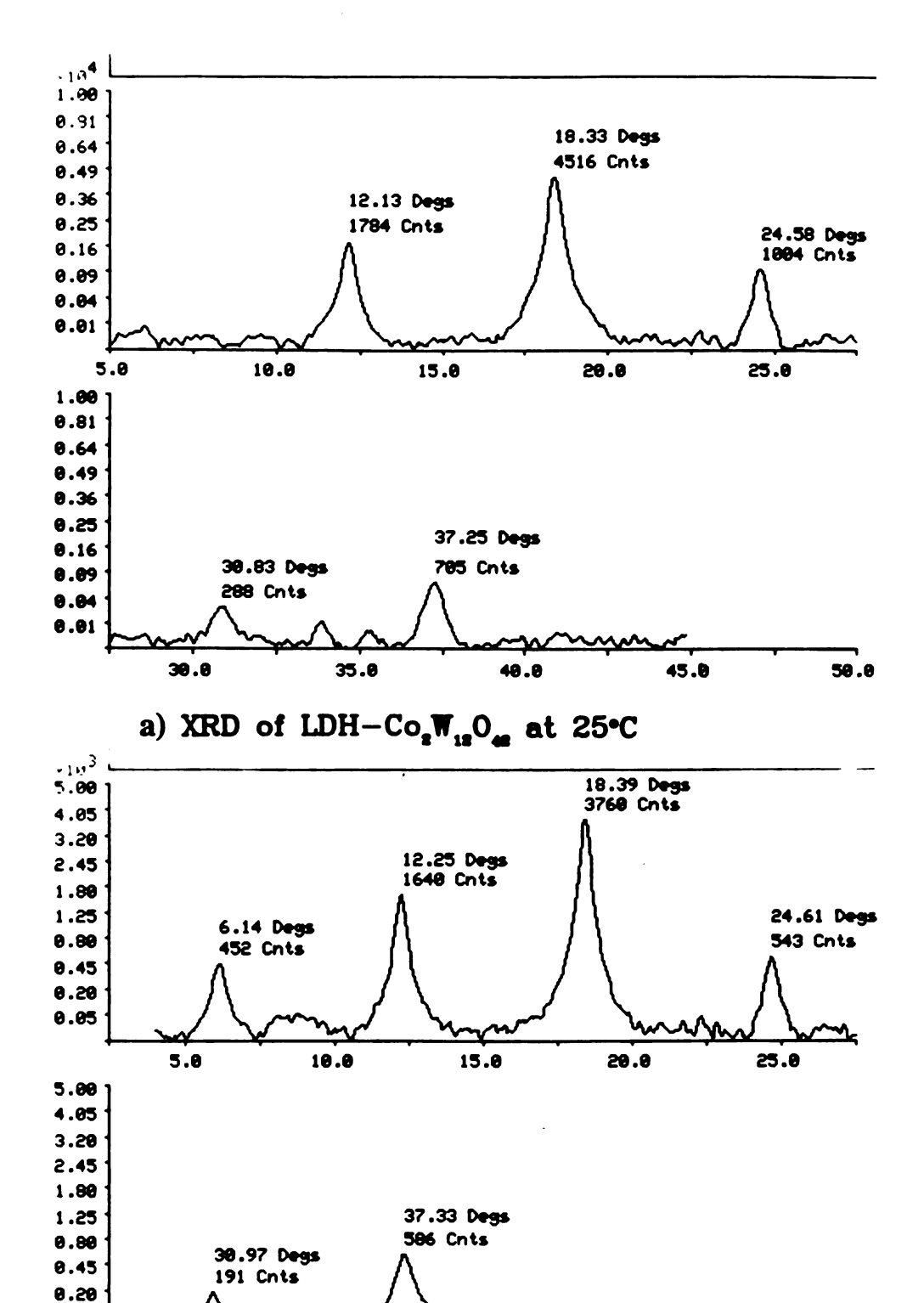
Fig. 70. DSC and TGA of LDH-BW  $_{11}\mathrm{O}_{39}.$ 

Fig

b)1

san

Fig. 71. XRD pattern of LDH-Co<sub>2</sub>W<sub>12</sub>O<sub>42</sub> at different temperatures. a) 25°C, b)120°C, c) 180°C: dotted line for the rehydrated sample, solid line for the dehydrated sample, d) 225°C, e) 320°C and f) 500°C.



b) XRD of LDH-Co<sub>2</sub>W<sub>12</sub>O<sub>48</sub> at 120°C

40.0

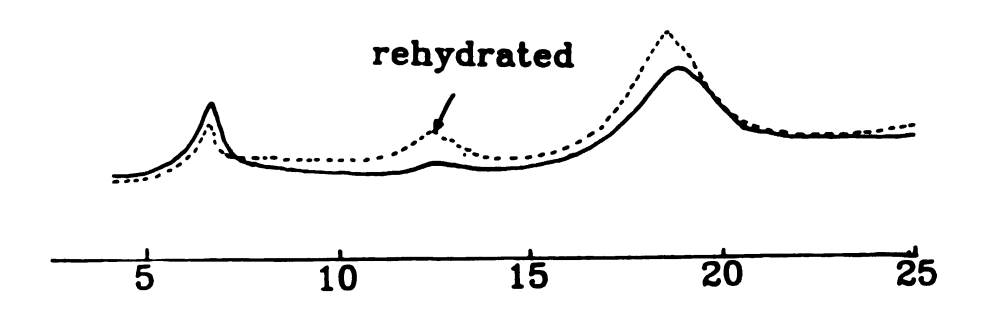
45.0

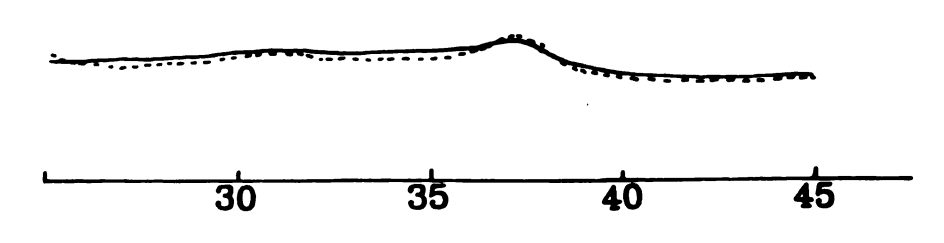
50.0

35.0

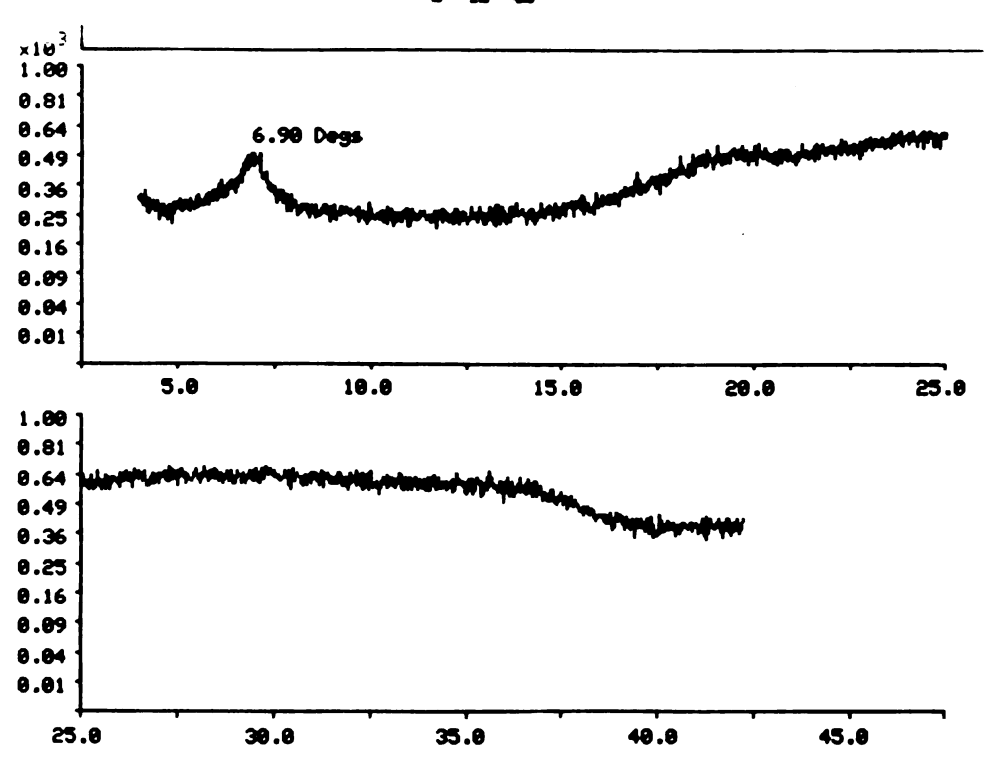
0.05

30.0

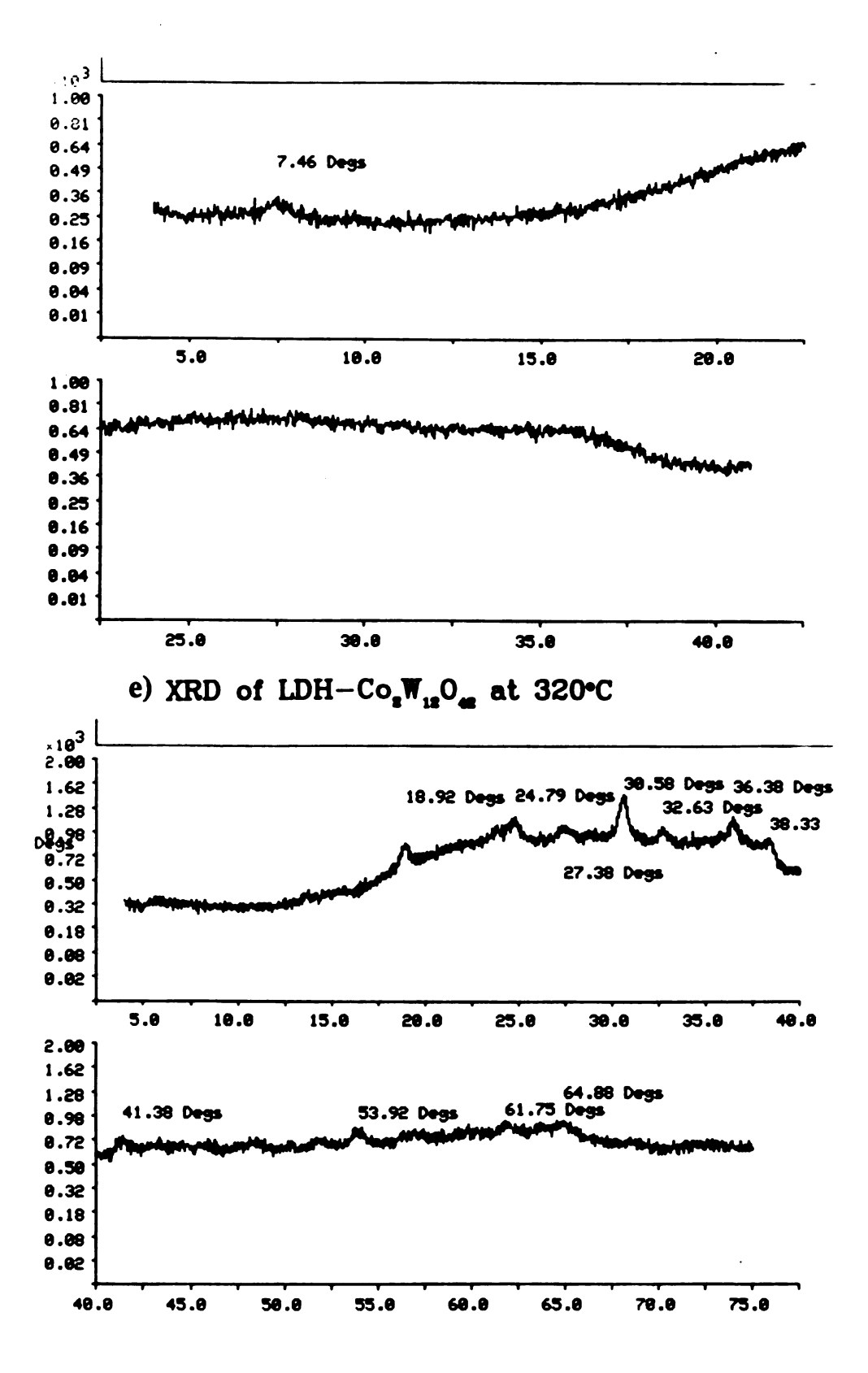




c) XRD of LDH- $Co_2W_{12}O_{ex}$  at 180°C



d) XRD of LDH-Co<sub>2</sub>W<sub>12</sub>O<sub>42</sub> at 225°C



f) XRD of LDH-Co<sub>2</sub>W<sub>12</sub>O<sub>42</sub> at 500°C

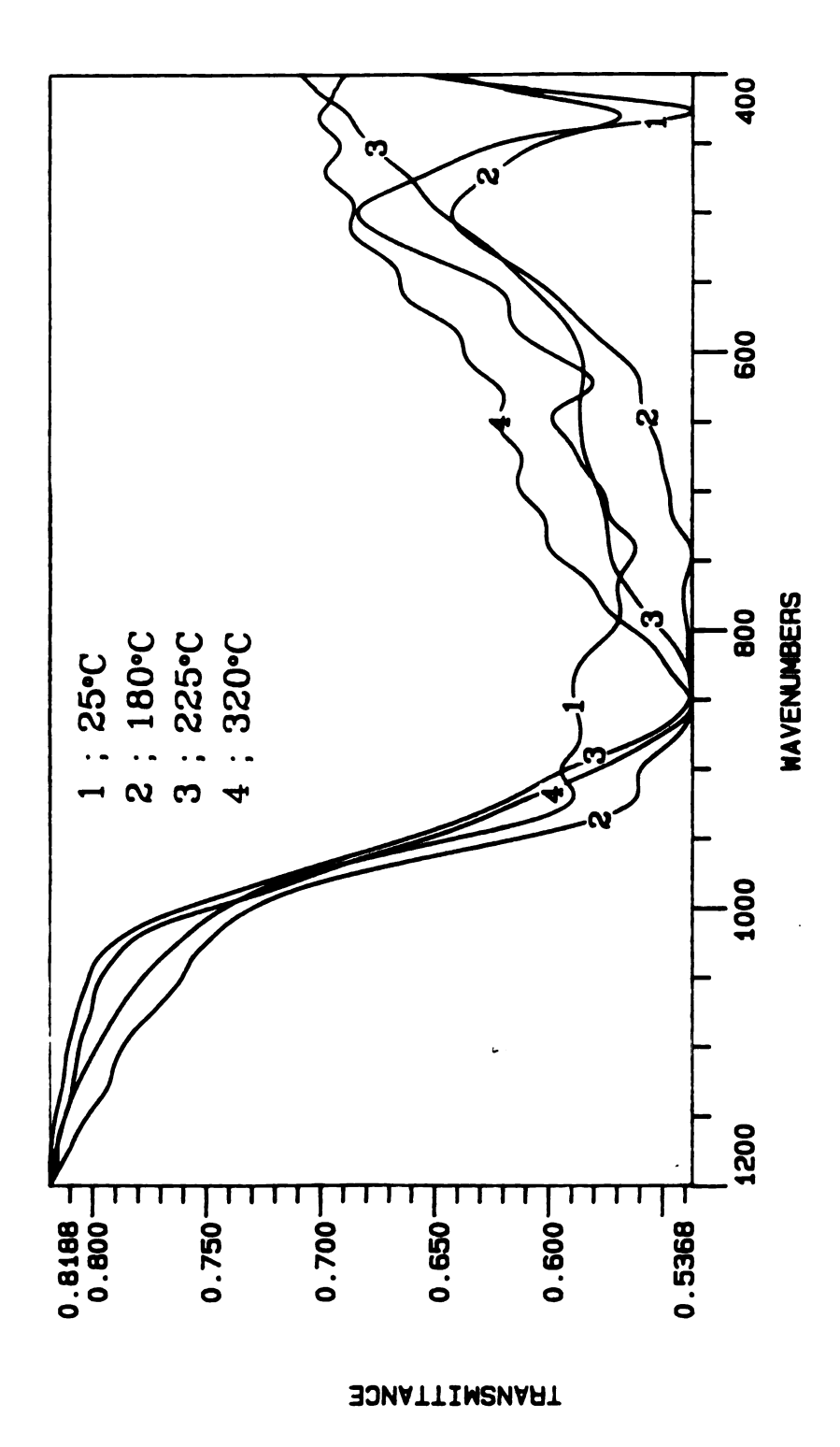


Fig. 72. Ir spectra of LDH-Co<sub>2</sub>W<sub>12</sub>O<sub>42</sub> at different temperatures.

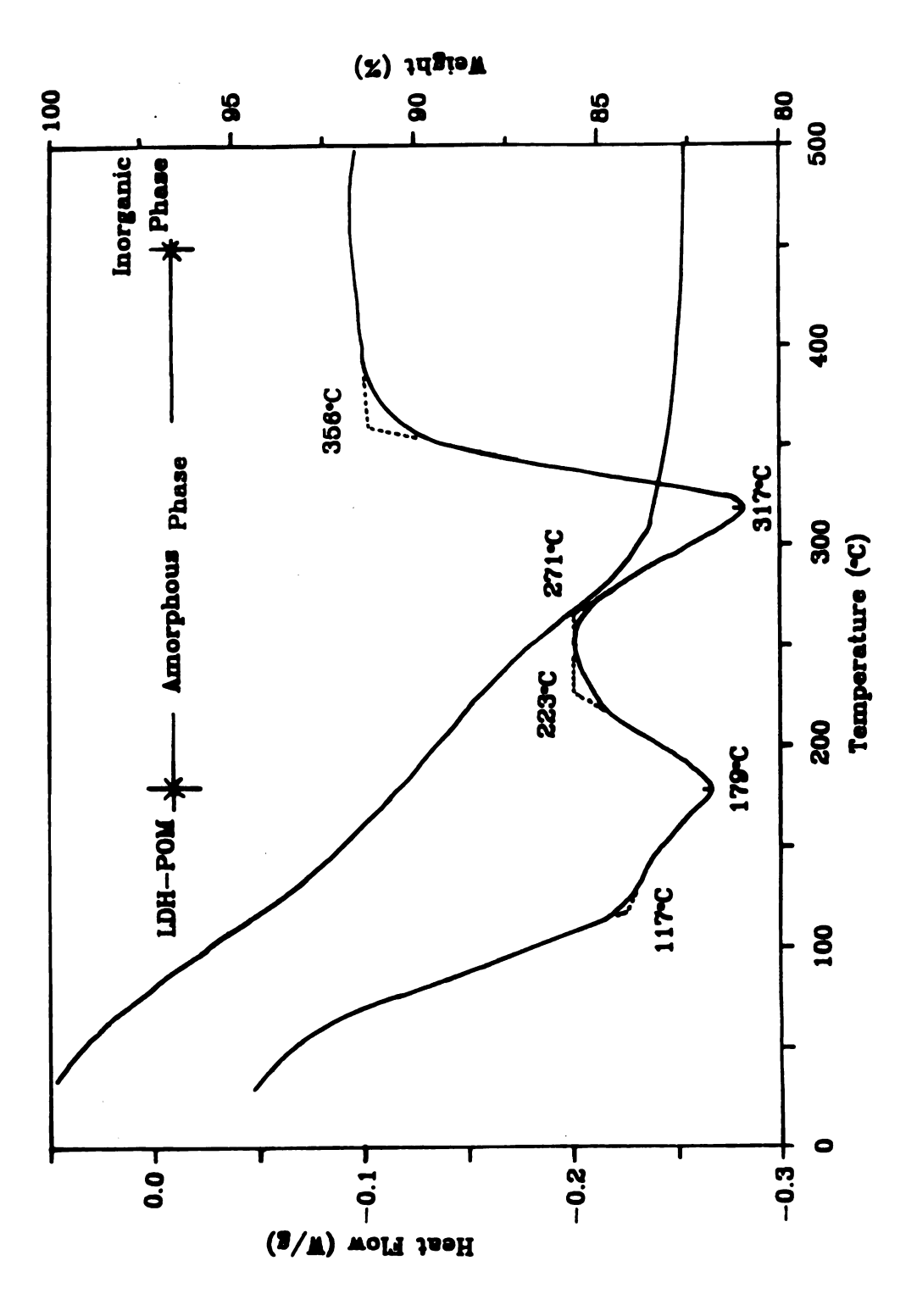
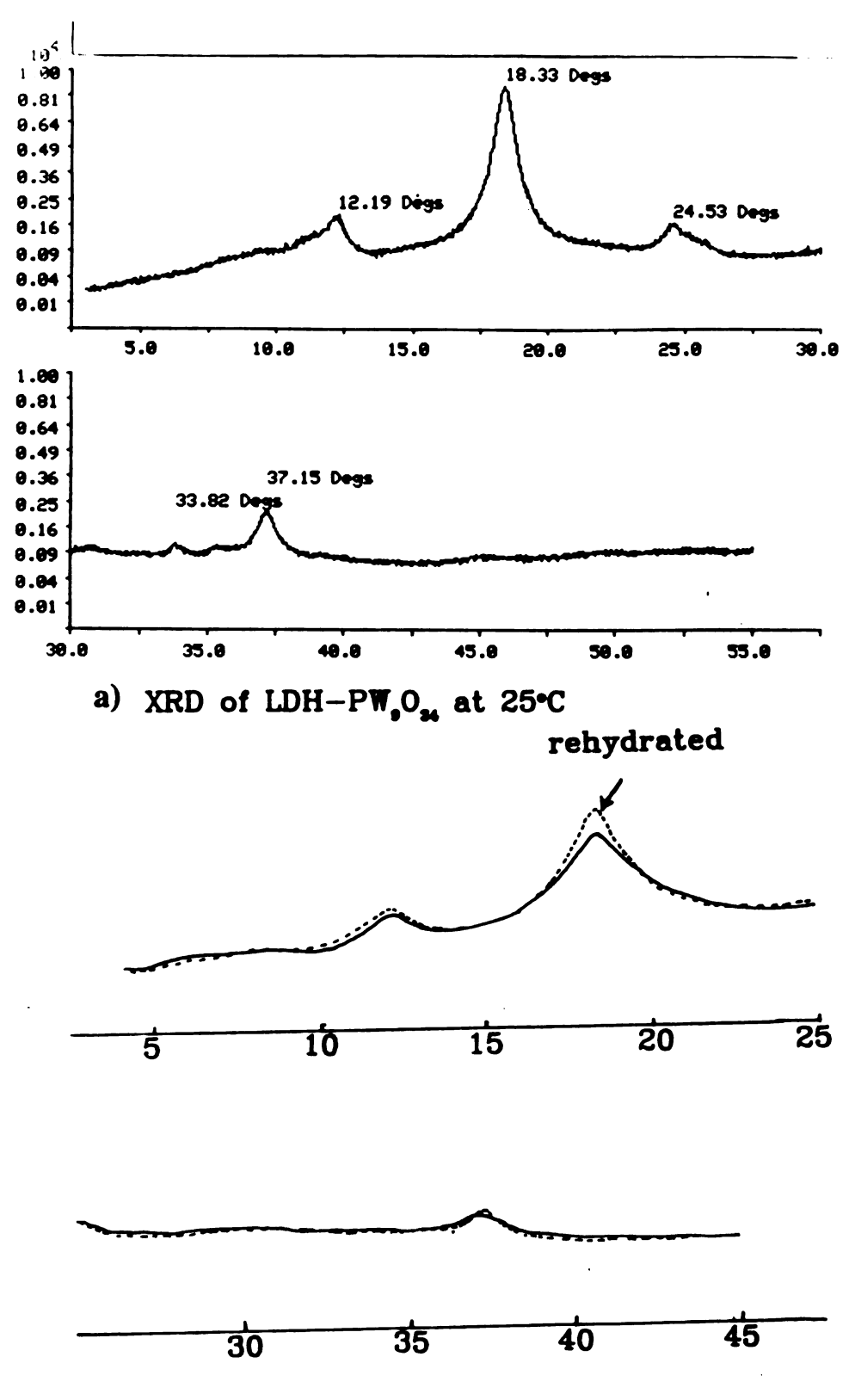
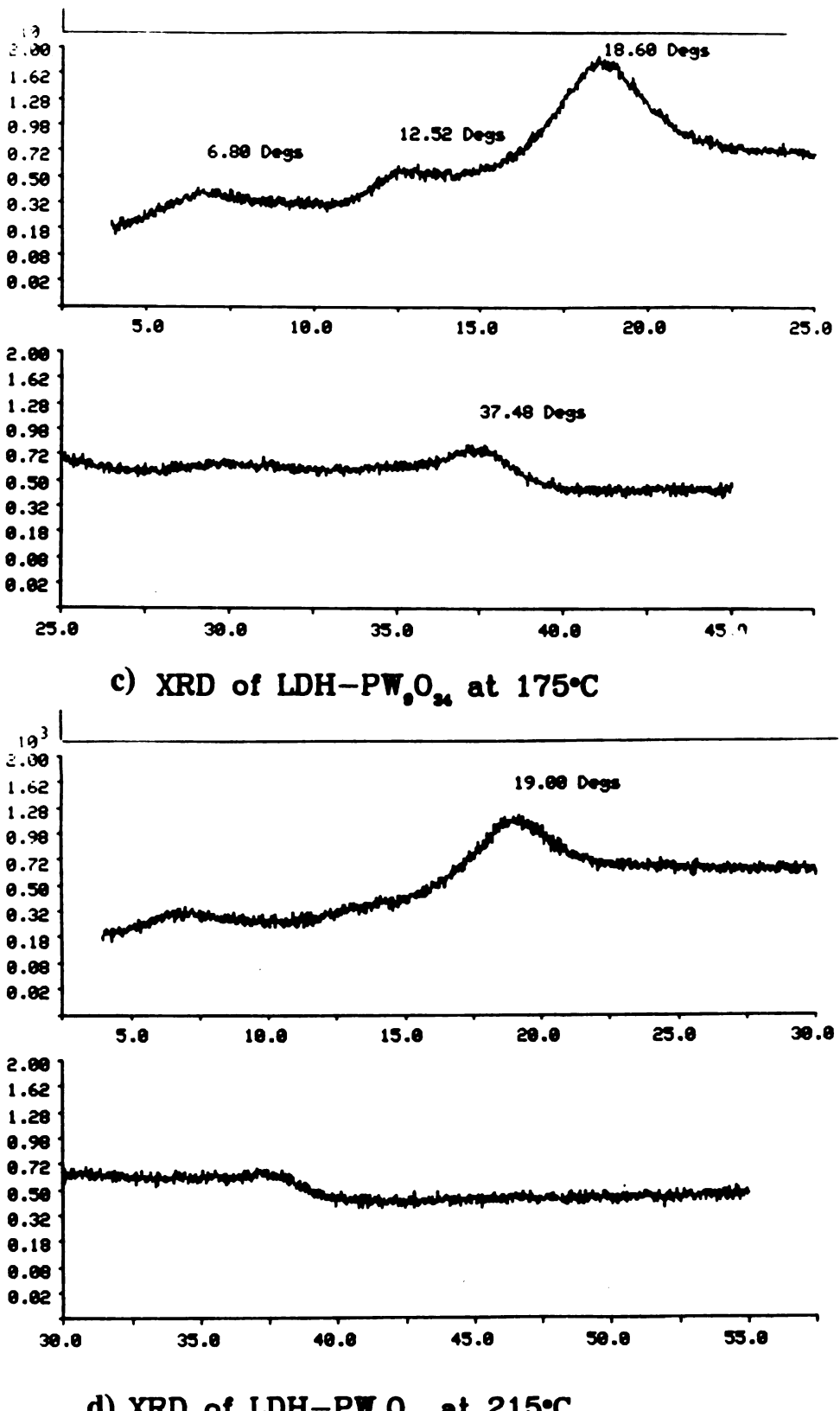


Fig. 73. DSC and TGA of LDH-Co<sub>2</sub>W<sub>12</sub>O<sub>42</sub>.

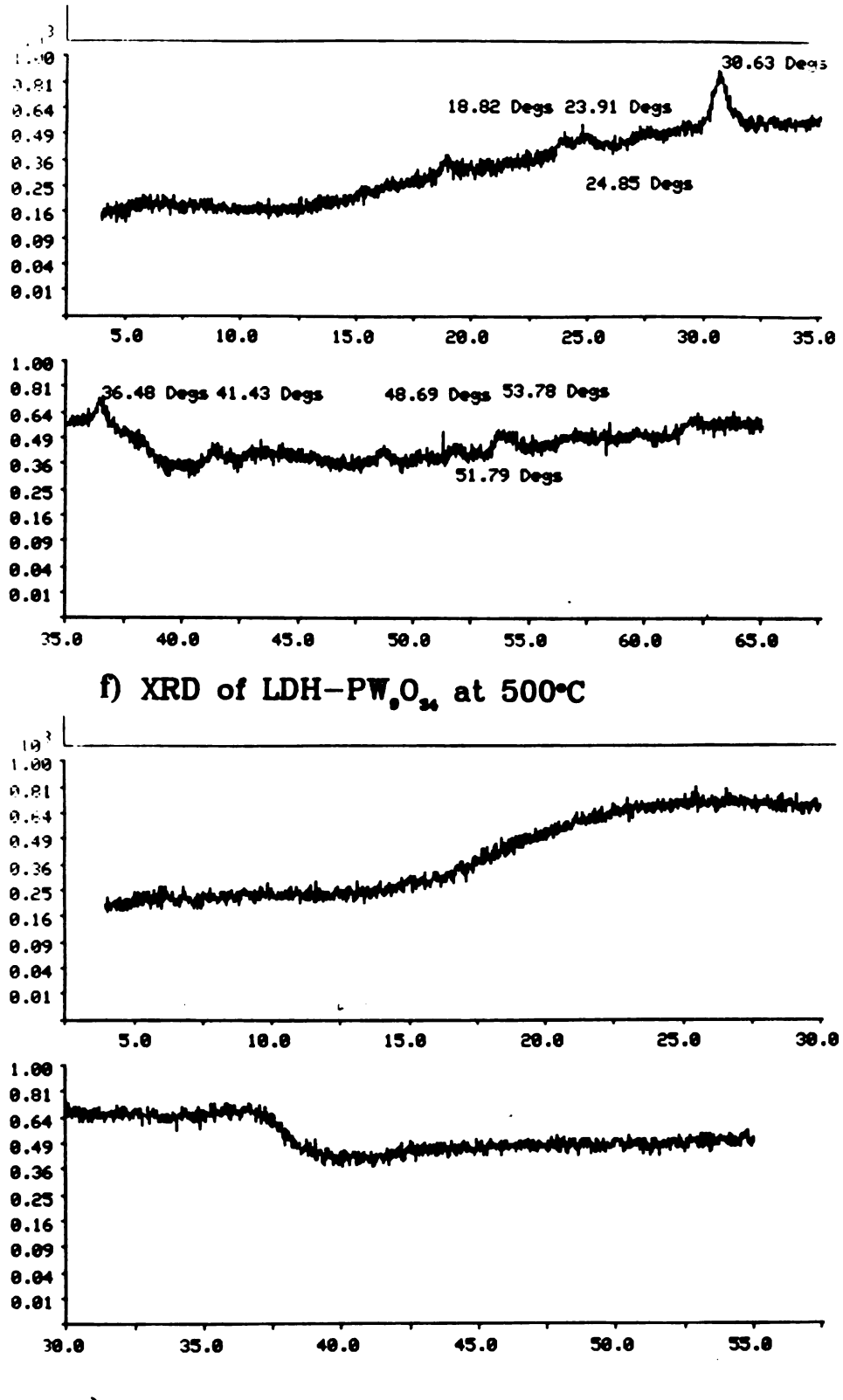
Fig. 74. XRD pattern of LDH-PW<sub>9</sub>O<sub>34</sub> at different temperatures. a) 25°C. b) 110°C: dotted line for the rehydrated sample, solid line for the dehydrated sample, c) 175°C, d) 215°C, e)320°C and f) 500°C.



b) XRD of LDH-PW<sub>0</sub>O<sub>34</sub> at 110°C



d) XRD of LDH-P $\mathbf{W}_{\bullet}$ O<sub>s4</sub> at 215°C



e) XRD of LDH-PW<sub>0</sub>O<sub>34</sub> at 320°C

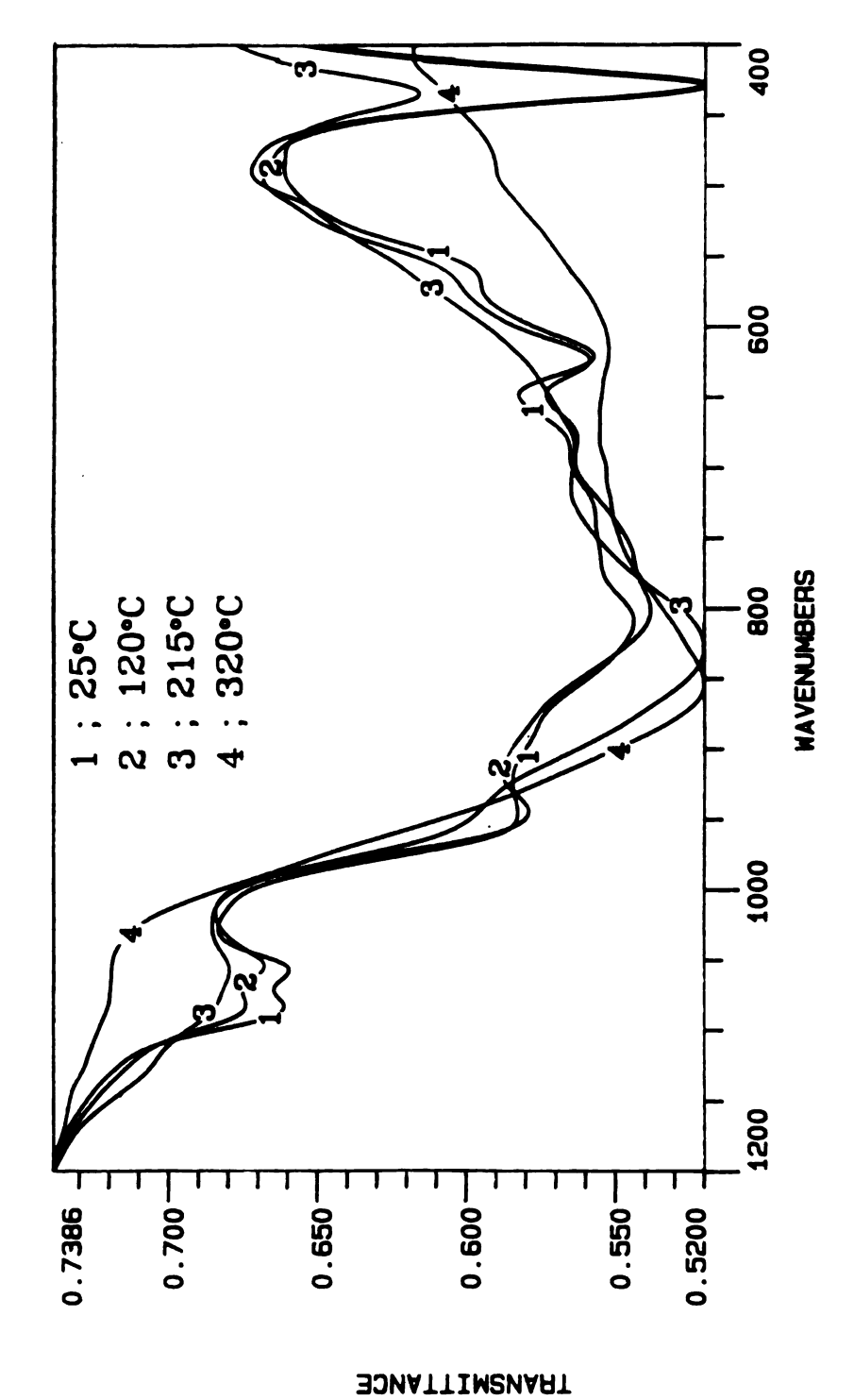


Fig. 75. Ir spectra of LDH-PW9O34 at different temperatures.

cm<sup>-1</sup>. At 500°C new crystalline inorganic phases appear. As the heating temperature increases, the frequency attributed to Al-O-Zn vibrational motion increases: 428 cm<sup>-1</sup> at 25°C, 429 cm<sup>-1</sup> at 110°C, 430 cm<sup>-1</sup> at 150°C, 432 cm<sup>-1</sup> at 175°C and 434 cm<sup>-1</sup> at 215°C.

The DSC and TGA of LDH-PW9O34 are given in Fig. 76. The dehydration process occurs up to 217°C, followed by dehydroxylation of the brucite-like layer up to 350°C. At 450°C new crystalline inorganic phases appear.

LDH-PV14O42: This complex is very thermally unstable even at 125°C. The PV14O42 in the gallery is decomposed at this point, verified by its ir spectrum provided in Fig. 77. However, the hydroxyl layer still remains intact; an absorption band at 429 cm<sup>-1</sup> manifests the preservation of the hydroxyl network. Heating at 120°C changes the XRD pattern to one that is uninterpretable, as shown in Fig. 78. Such decomposed phases remain after heating to 185°C. At 320°C the LDH-PV14O42 turns completely to an amorphous phase, as shown in its XRD pattern in Fig. 78. But unlike the other systems there are two absorption bands centered at 934 cm<sup>-1</sup> and 775 cm<sup>-1</sup>. At 500°C new crystalline inorganic phases appear.

The DSC and TGA of LDH-PV<sub>14</sub>O<sub>42</sub> are provided in Fig. 79. The dehydration of the lattice water and the decomposition of PV<sub>14</sub>O<sub>42</sub> in the gallery occurs up to 180°C, followed by dehydroxylation of the hydroxyl layer up to 374°C. An exothermic peak starting at 450°C indicates the onset of new inorganic phases formation.

LDH-NaP5W30O110: When this system is heated at 120°C, a remarkable change in XRD pattern is observed, as shown in Fig. 80. The first order peak increases, while the second order peak disappears. When the sample heated at 120°C is rehydrated, its XRD pattern is restored to that of an unheated sample. That is, the absent second order peak reappears and the increased intensity of first order peak decreases, as shown in its XRD pattern. However, there is no change in the ir spectrum upon heating at 120°C provided (see Fig. 81), indicative that no structural change has taken place. At 180°C there only

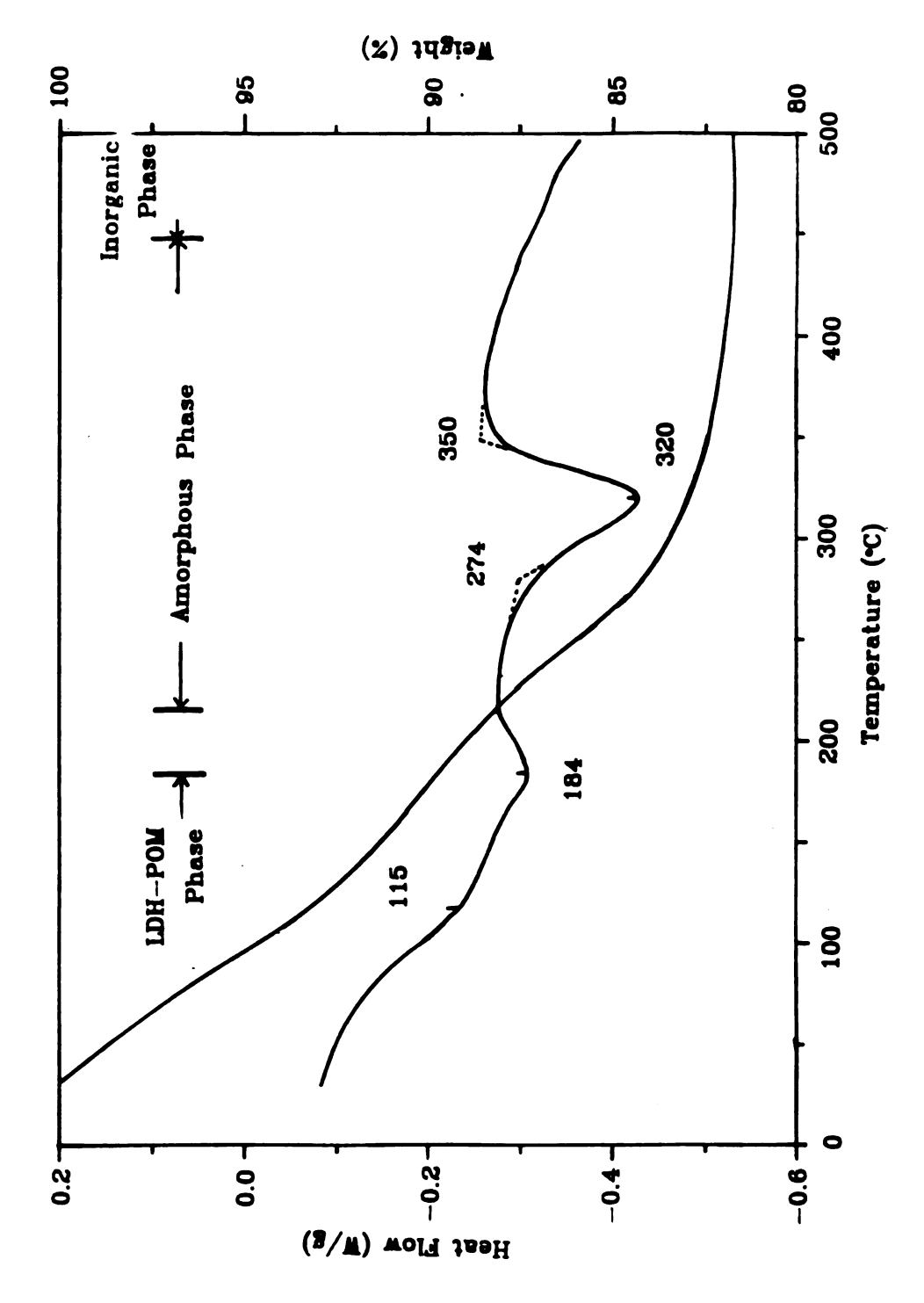


Fig. 76. DSC and TGA of LDH-PW9O34.

1.1

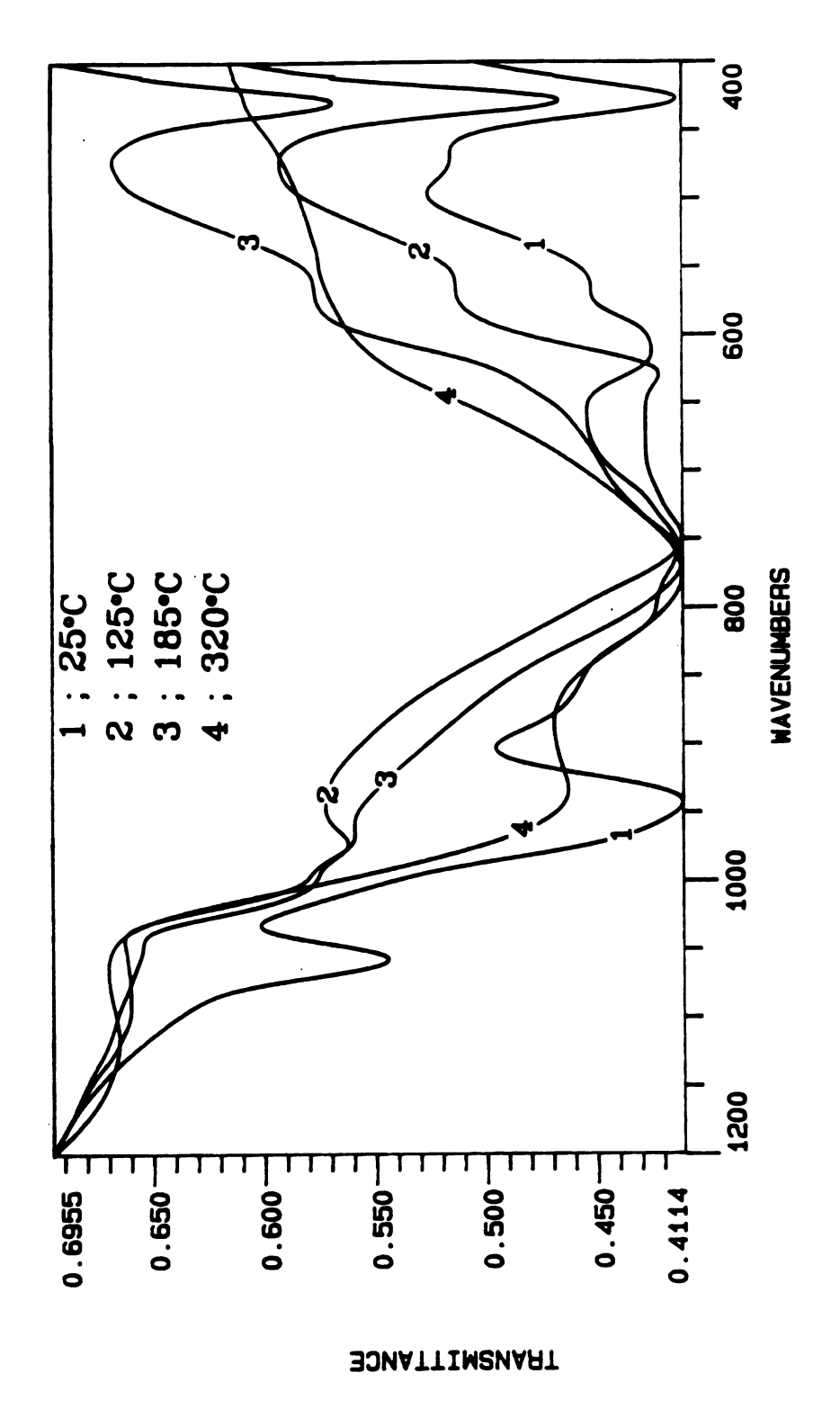
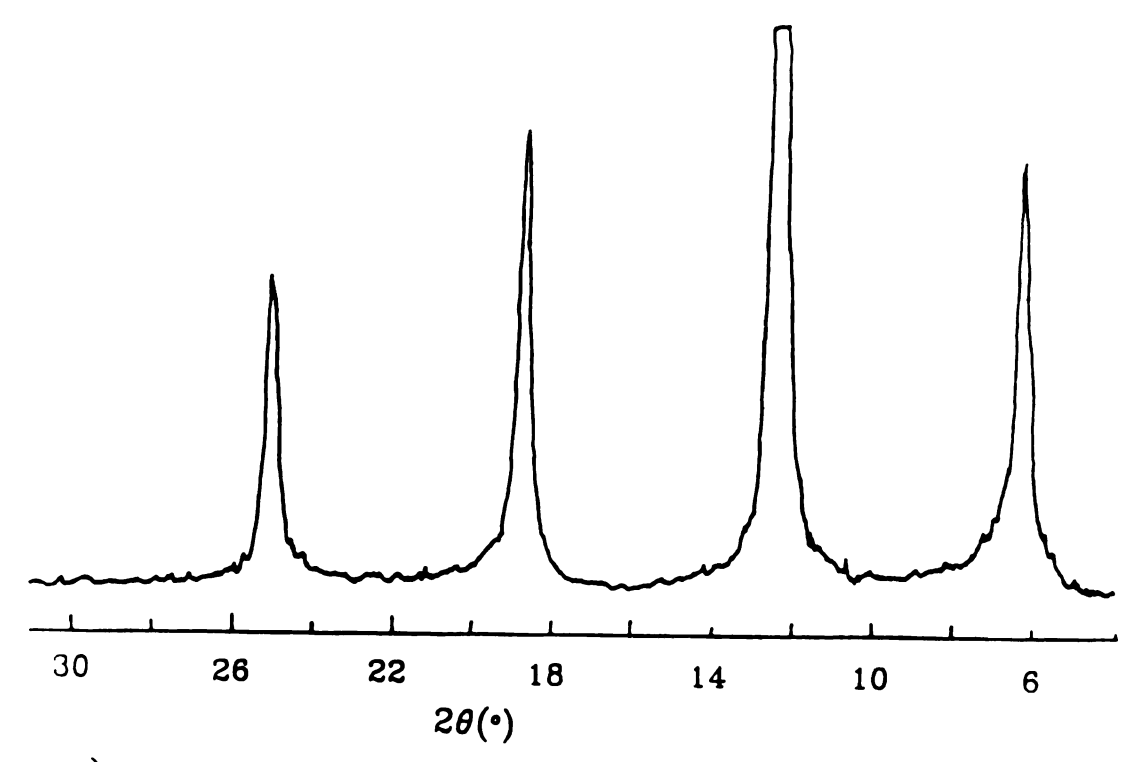


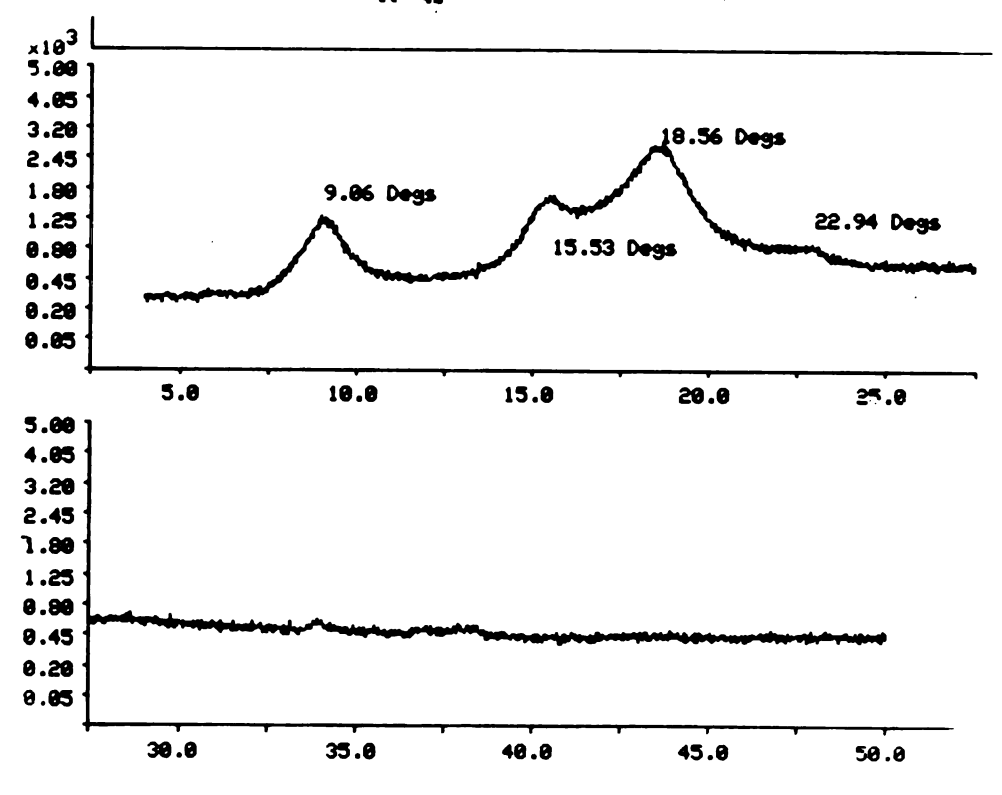
Fig. 77. Ir spectra of LDH-PV<sub>14</sub>O<sub>42</sub>.

		-

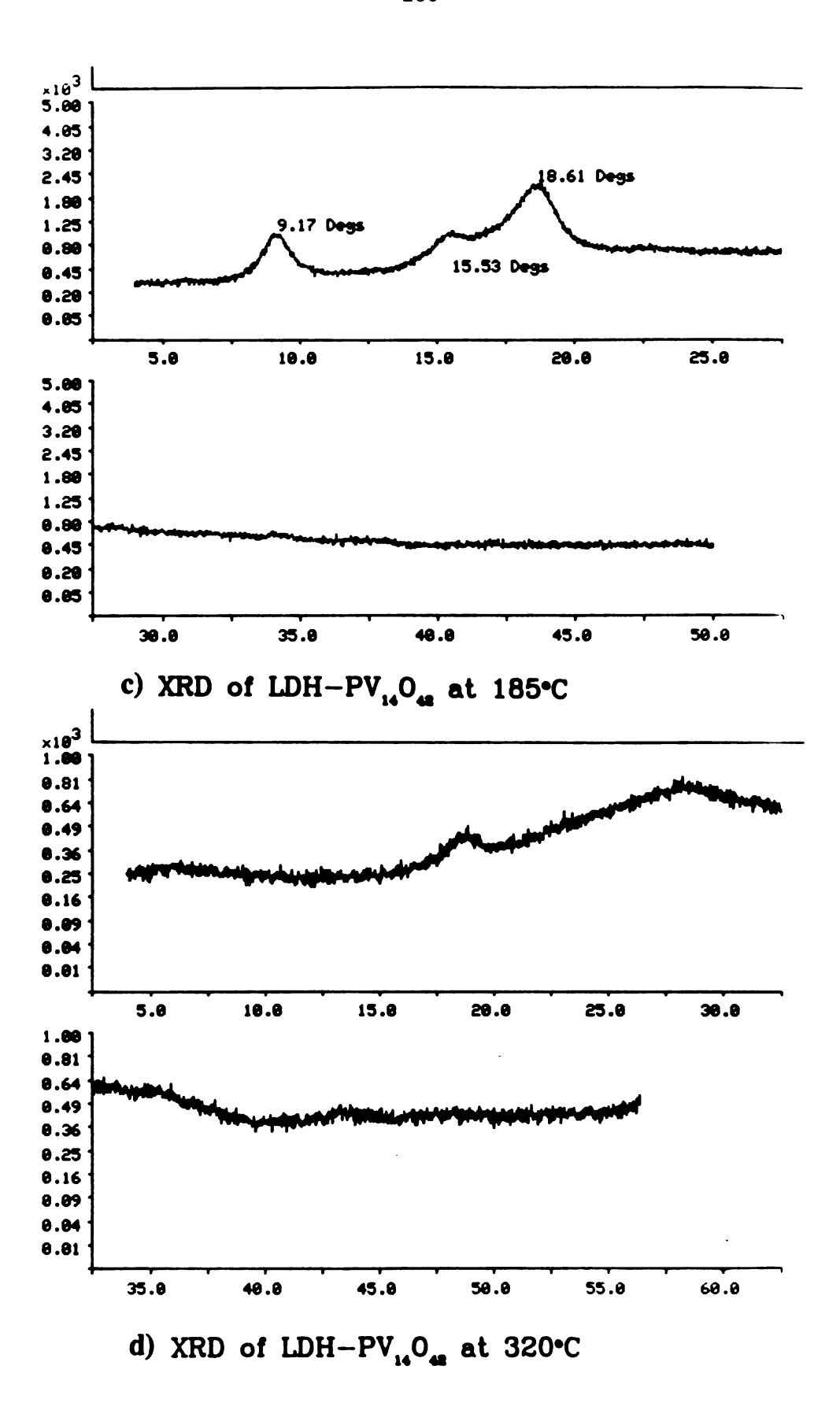
Fig. 78. XRD pattern of LDH-PV<sub>14</sub>O<sub>42</sub> at different temperatures. a) 25°C, b) 125°C, c) 185°C, d) 320°C and e) 500°C.

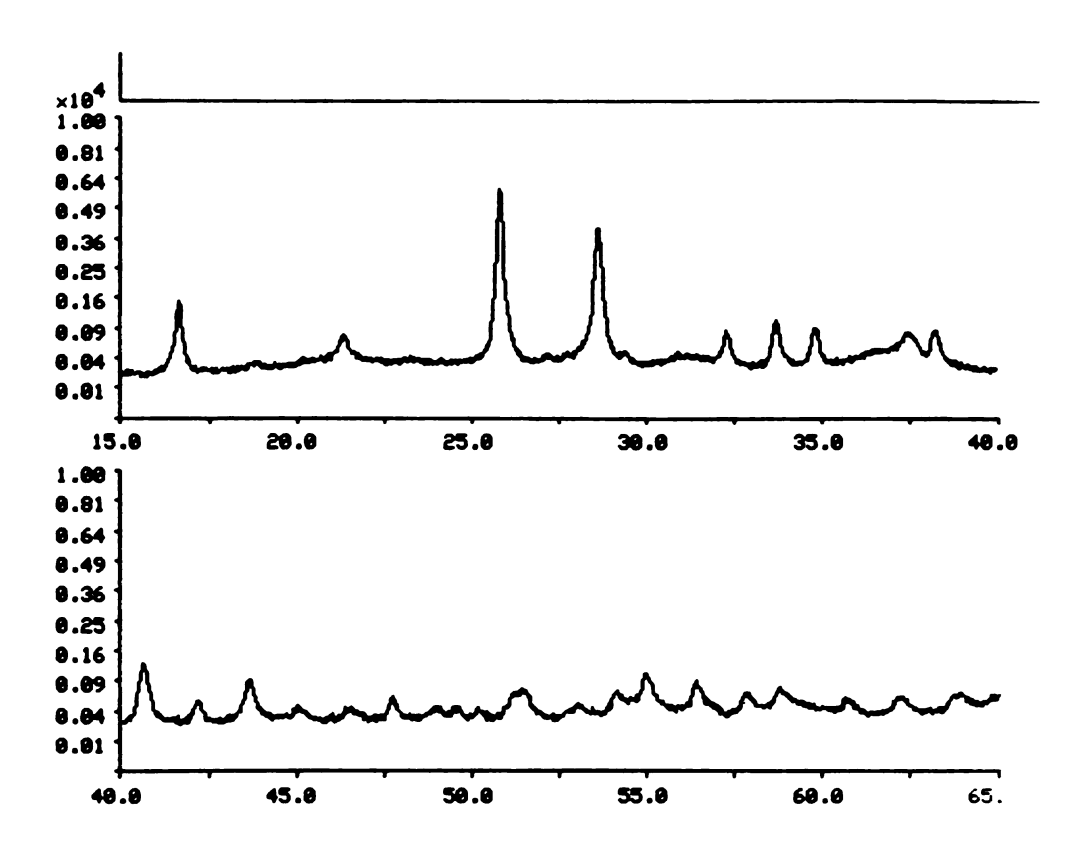


a) XRD of LDH-PV<sub>14</sub>O<sub>42</sub> at 25°C



b) XRD of LDH-PV<sub>14</sub>O<sub>48</sub> at 125°C





e) XRD of LDH-PV<sub>16</sub>O<sub>48</sub> at 500°C

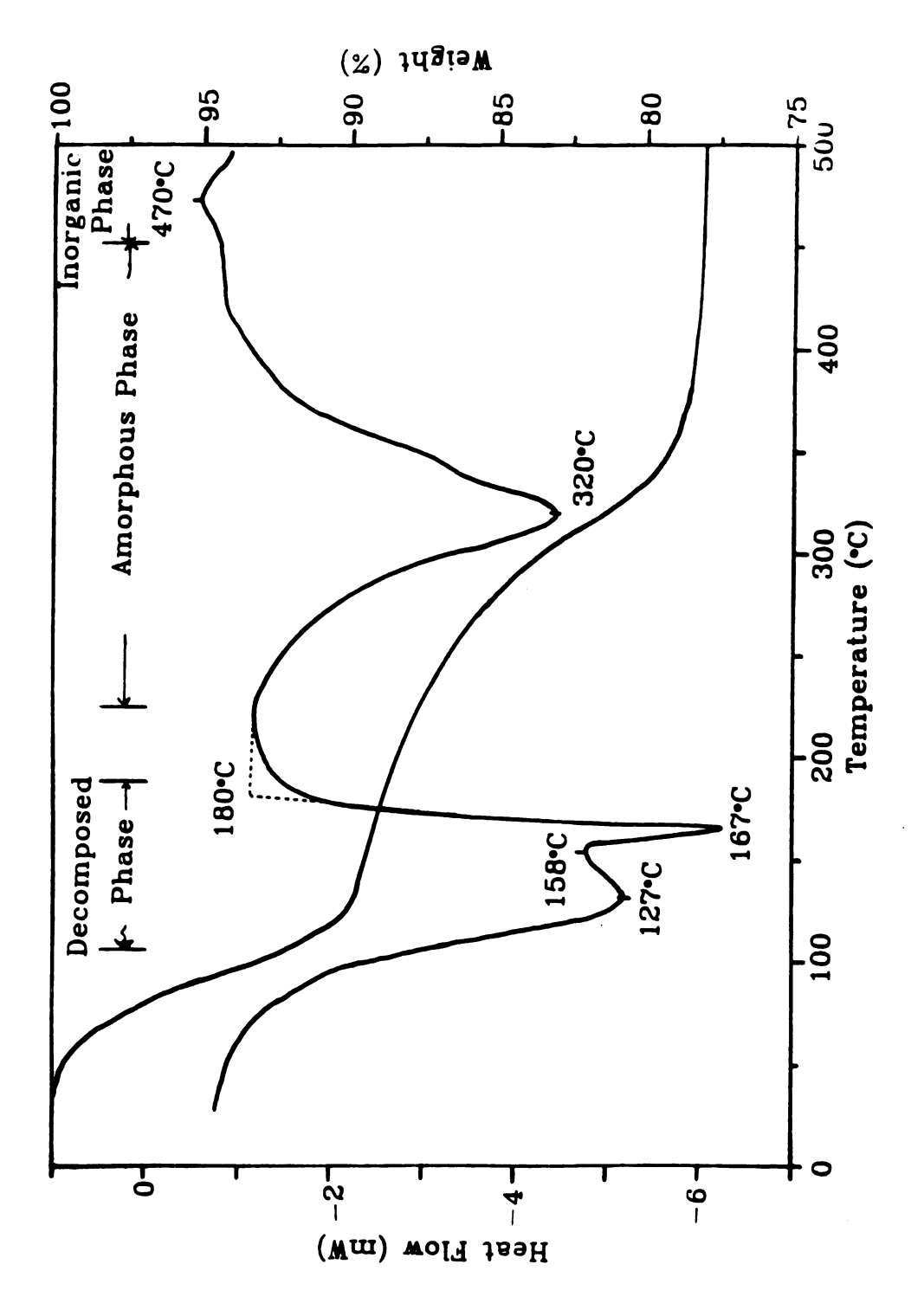
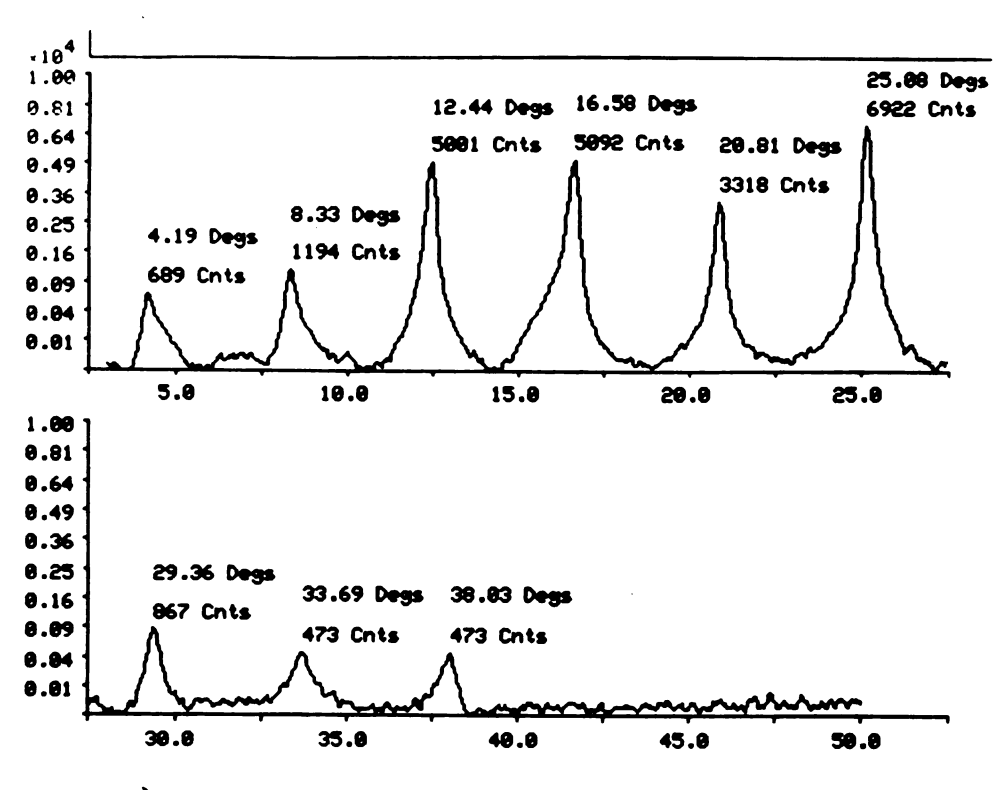


Fig. 79. DSC and TGA of LDH-PV<sub>14</sub>O<sub>42</sub>.

Fig. 80. XRD pattern of LDH-NaP<sub>5</sub>W<sub>30</sub>O<sub>110</sub> at different temperatures. a) 25°C, b)  $120^{\circ}$ C: dotted line for the rehydrated sample, solid line for the dehydrated sample, c)  $180^{\circ}$ C: dotted line for the rehydrated sample, solid line for the dehydrated sample, d)  $250^{\circ}$ C and  $500^{\circ}$ C.

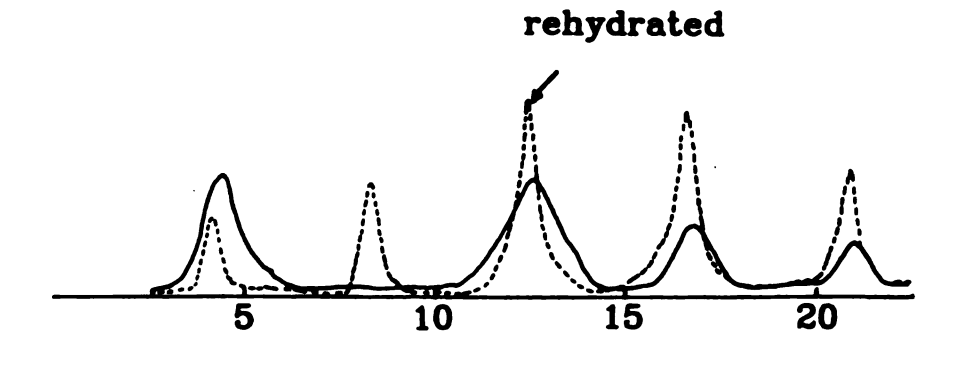


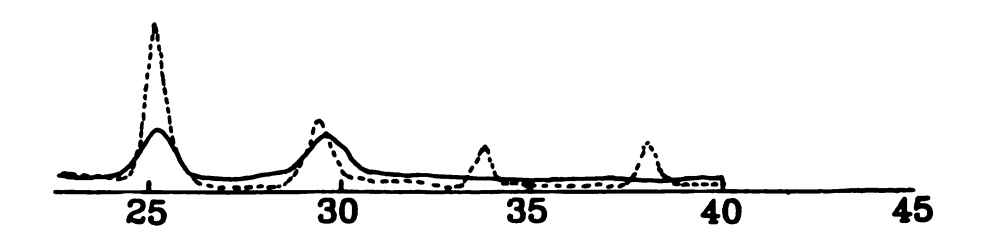
a) XRD of LDH-NaP<sub>8</sub>W<sub>20</sub>O<sub>110</sub> at 25°C

25°C,5

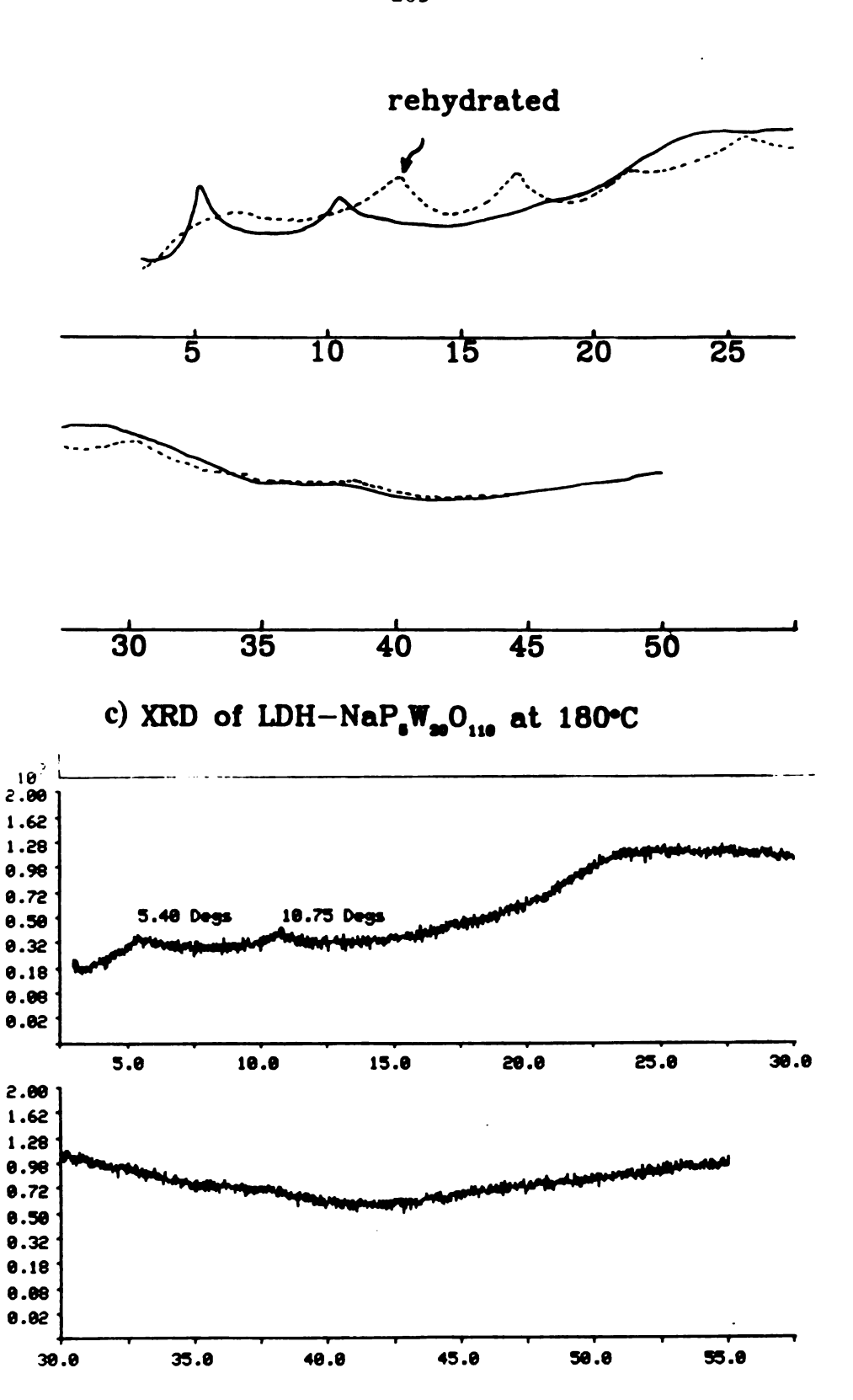
sample.c

sample, û

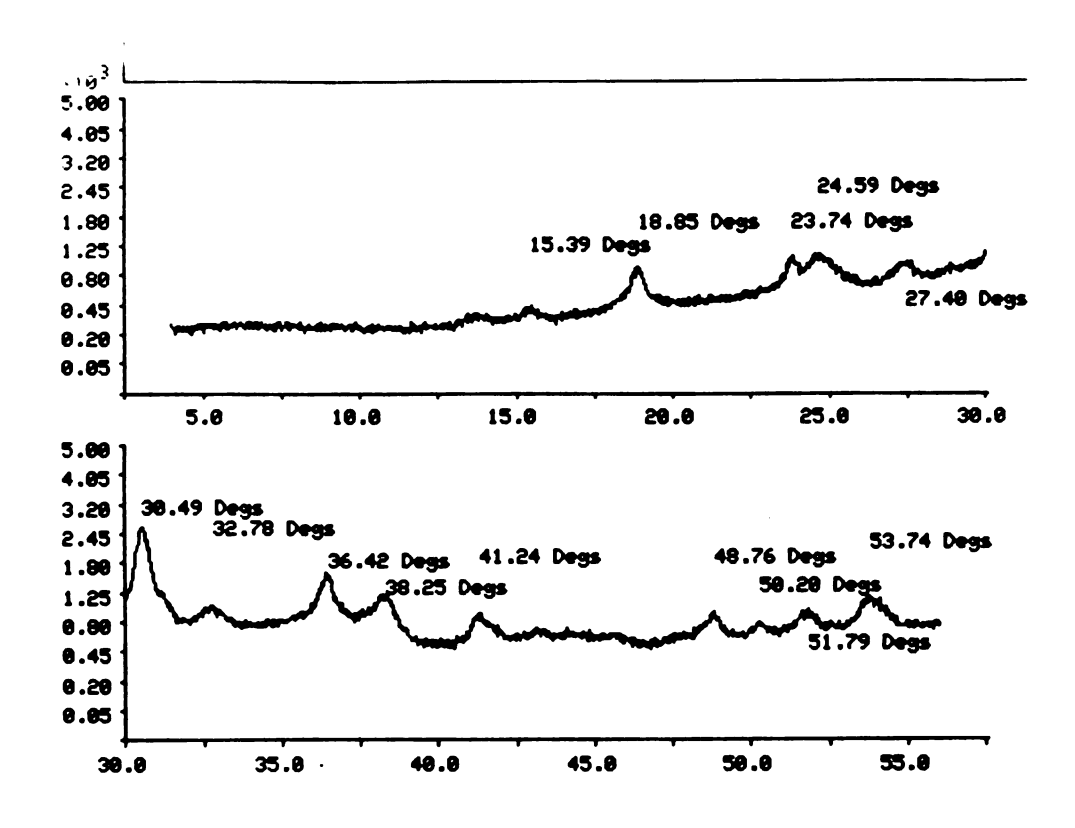




b) XRD of LDH-NaP, W,O110 at 120°C



d) XRD of LDH-NaP<sub>s</sub>W<sub>ss</sub>O<sub>110</sub> at 250°C



e) XRD of LDH-NaP<sub>8</sub> $W_{20}O_{110}$  at 500°C

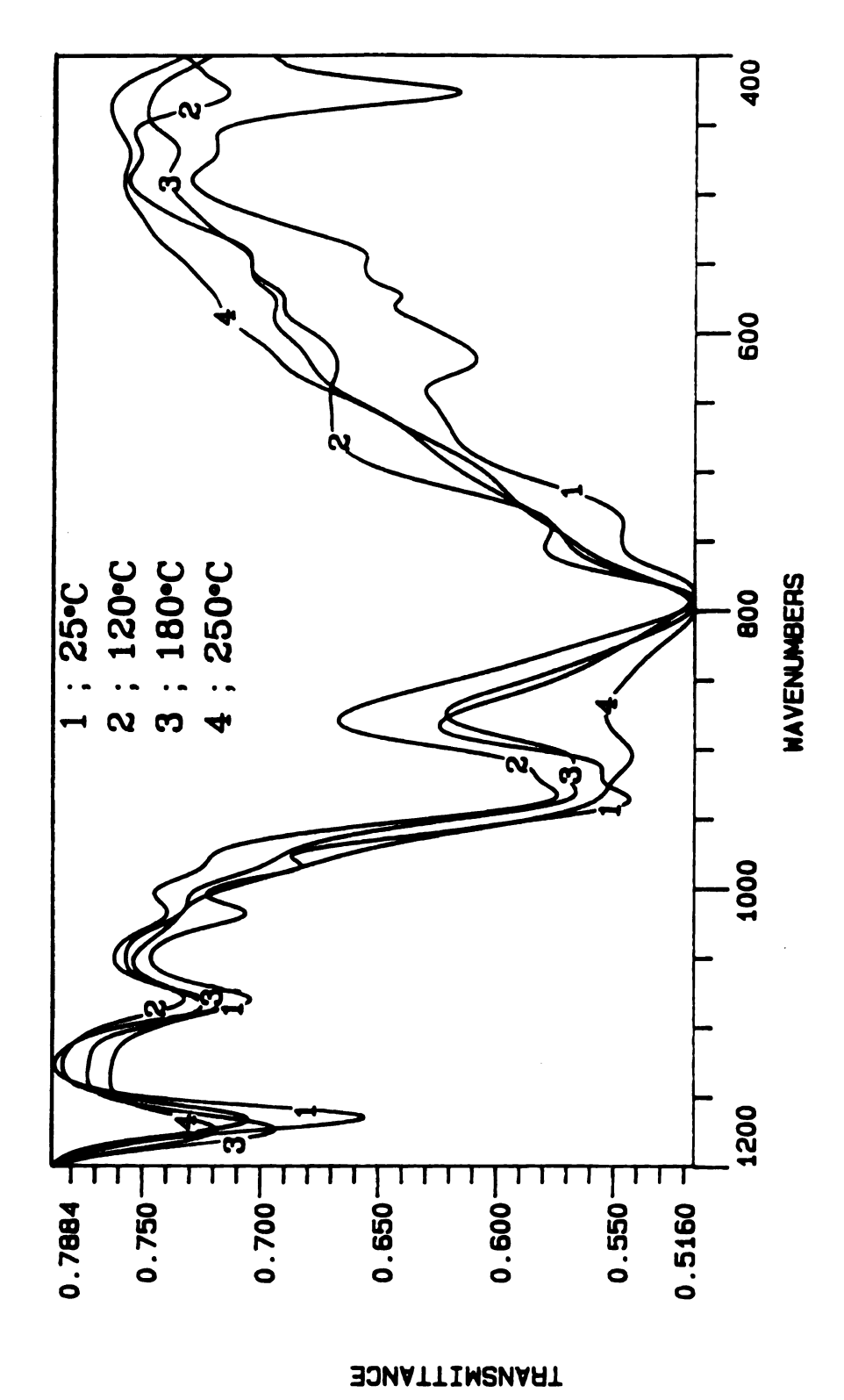


Fig. 81. It spectra of LDH-NaP<sub>5</sub>W $_{30}$ O $_{110}$  at different temperatures.

two peaks at  $2\theta = 5.2^{\circ}$  and  $10.4^{\circ}$  remain. These may be assigned as the first and second order peak, respectively. At  $250^{\circ}$ C, this specimen turns into an almost amorphous phase even though a trace of the LDH-NaP5W30O110 phase remain apparent in its XRD pattern. Its ir spectrum shows evidence of structural change in the NaP5W30O110 in the gallery. New crystalline inorganic phases appear at  $500^{\circ}$ C.

The DSC and TGA of LDH-NaP5W30O110 are given in Fig. 82. The dehydration process occurs up to 176°C, followed by dehydroxylaton of the hydroxyl layer up to 322°C. An exothermic peak starting at 466°C corresponds to the onset of new crystalline inorganic phase formation.

LDH-H2W12O42: This compound is moderately thermally unstable even at low temperature. The XRD pattern of this complex heated at 120°C shows a decomposed phase, as evidenced in Fig. 83. The decomposition of this complex is also easily verified by ir spectroscopy, as illustrated in Fig. 84. A decomposed phase is observed even at 120°C, and the complex turns to an almost amorphous material at 230°C. At 320°C the material is completely amorphous. Its ir spectrum shows one typical simplified absorption band centered at 856 cm<sup>-1</sup> as do other complexes. At 500°C new crystalline inorganic phases appears.

The DSC and TGA of LDH-H<sub>2</sub>W<sub>12</sub>O<sub>42</sub> are provided in Fig. 85. The dehydration process occurs up to 230°C, followed by dehydroxylation of the brucite-like layer to 355°C. At 500°C new crystalline inorganic phase appears.

## F. Adsorption Study of LDH-POMs

The LDH-POMs can be classified according to the charges of POMs in the gallery. The N<sub>2</sub> adsorption isotherms of the representative LDH-POMs are shown in Table 14.

Fig. 86 shows the N<sub>2</sub> adsorption isotherms, providing the isotherm type and the BET (N<sub>2</sub>) surface area. The shape for the first four LDH-POMs, type I, indicates that

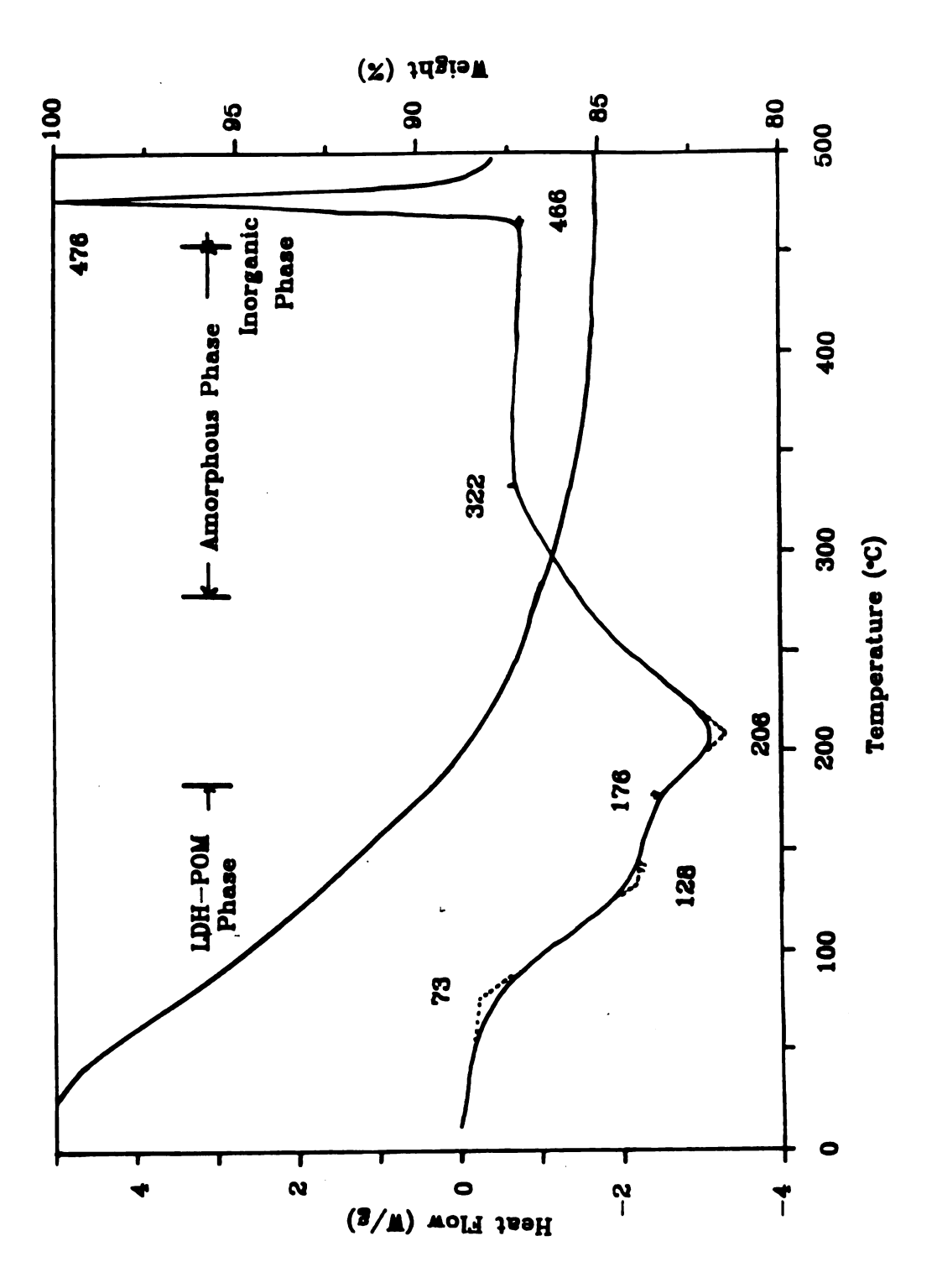
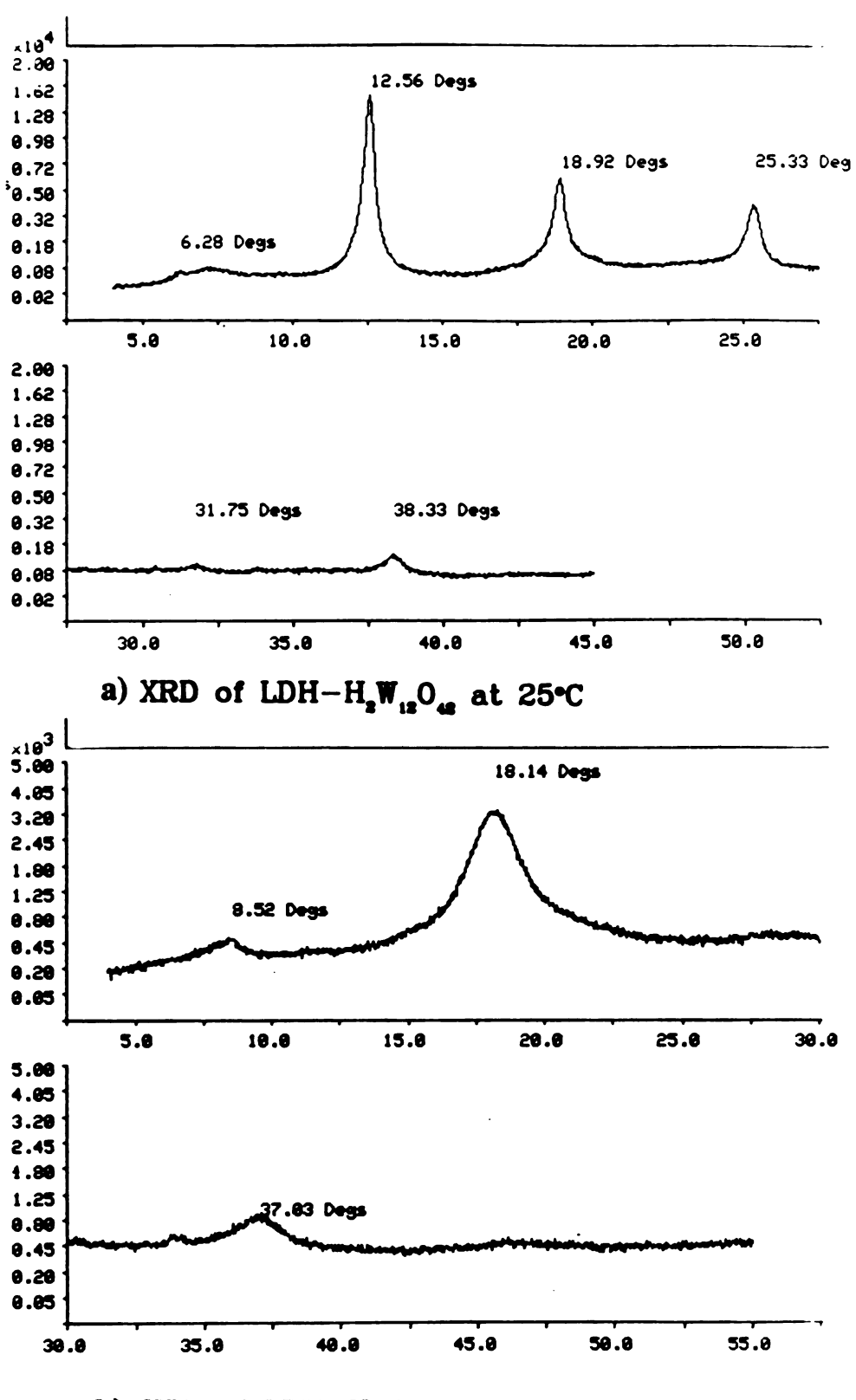
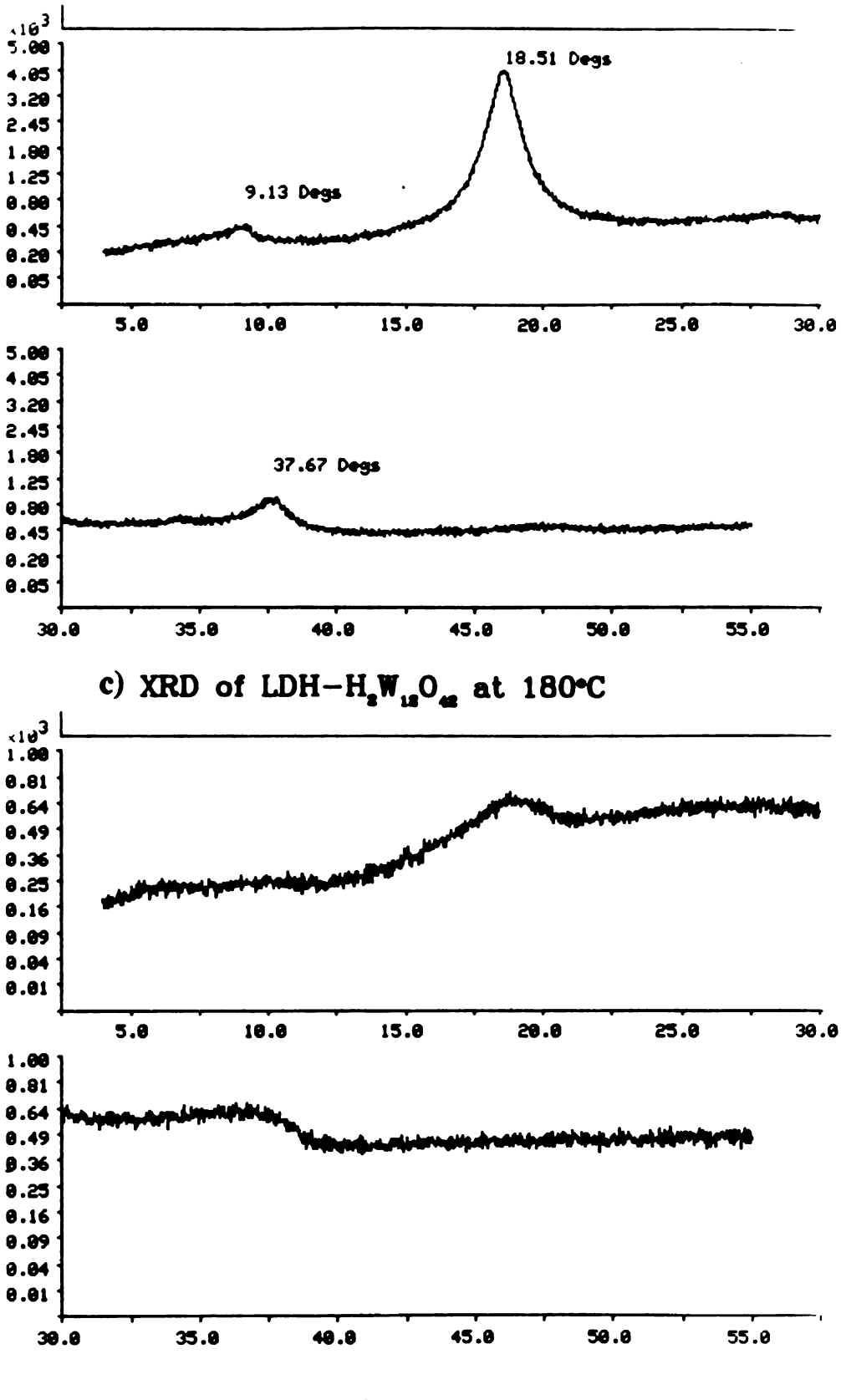


Fig. 82. DSC and TGA of LDH-NaP5W30O110-

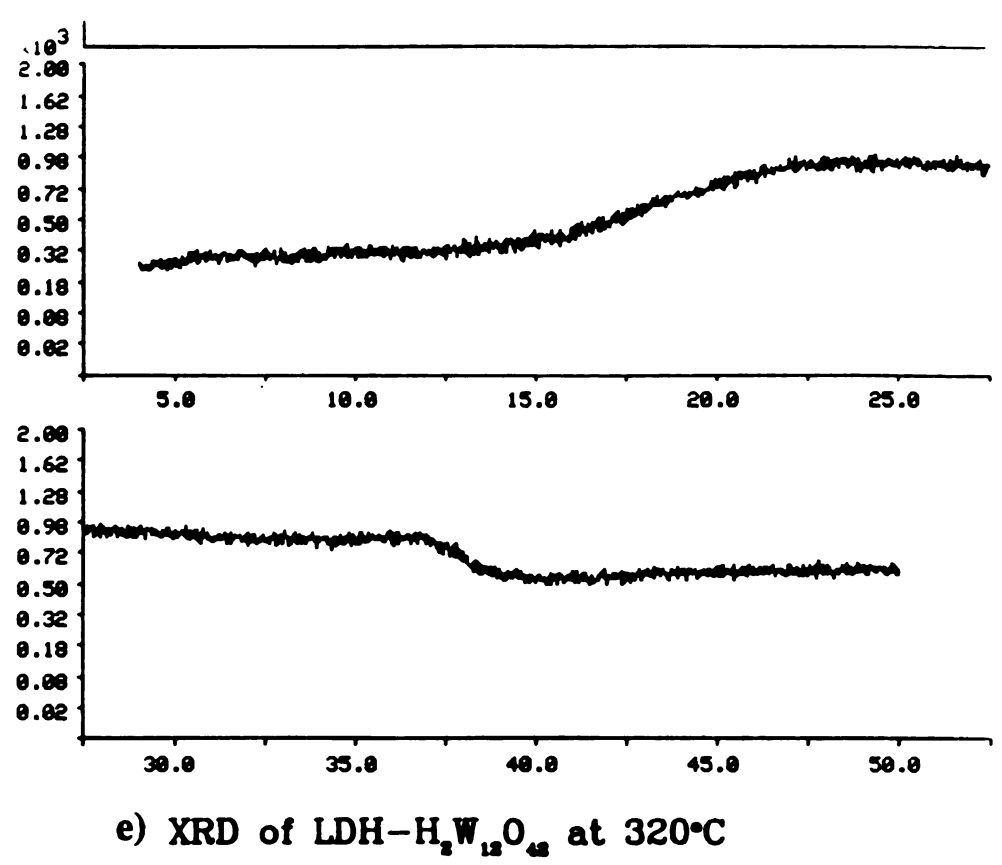
Fig. 83. XRD pattern of LDH- $H_2W_{12}O_{42}$  at different temperatures. a)25°C, b) 120°C, c) 180°C, d) 230°C, e) 320°C and 500°C.

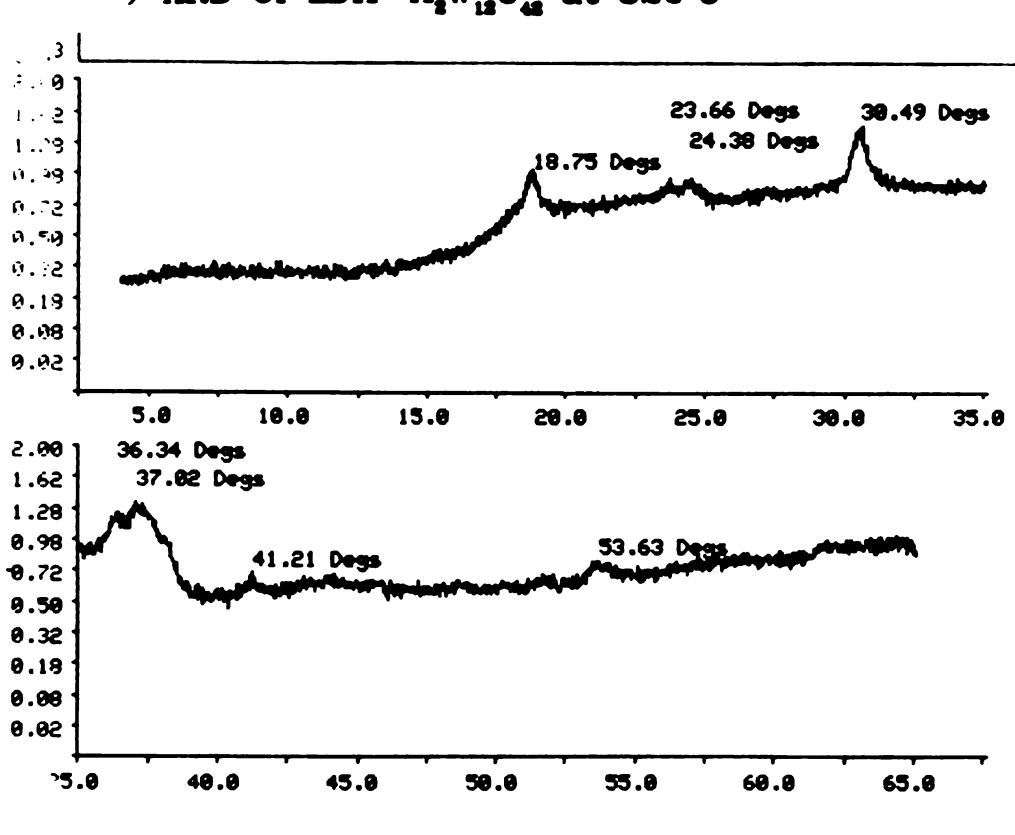


b) XRD of LDH-H<sub>2</sub>W<sub>12</sub>O<sub>42</sub> at 120°C



d) XRD of LDH- $H_2W_{12}O_{42}$  at 230°C





f) XRD of LDH- $H_2W_{12}O_{48}$  at 500°C

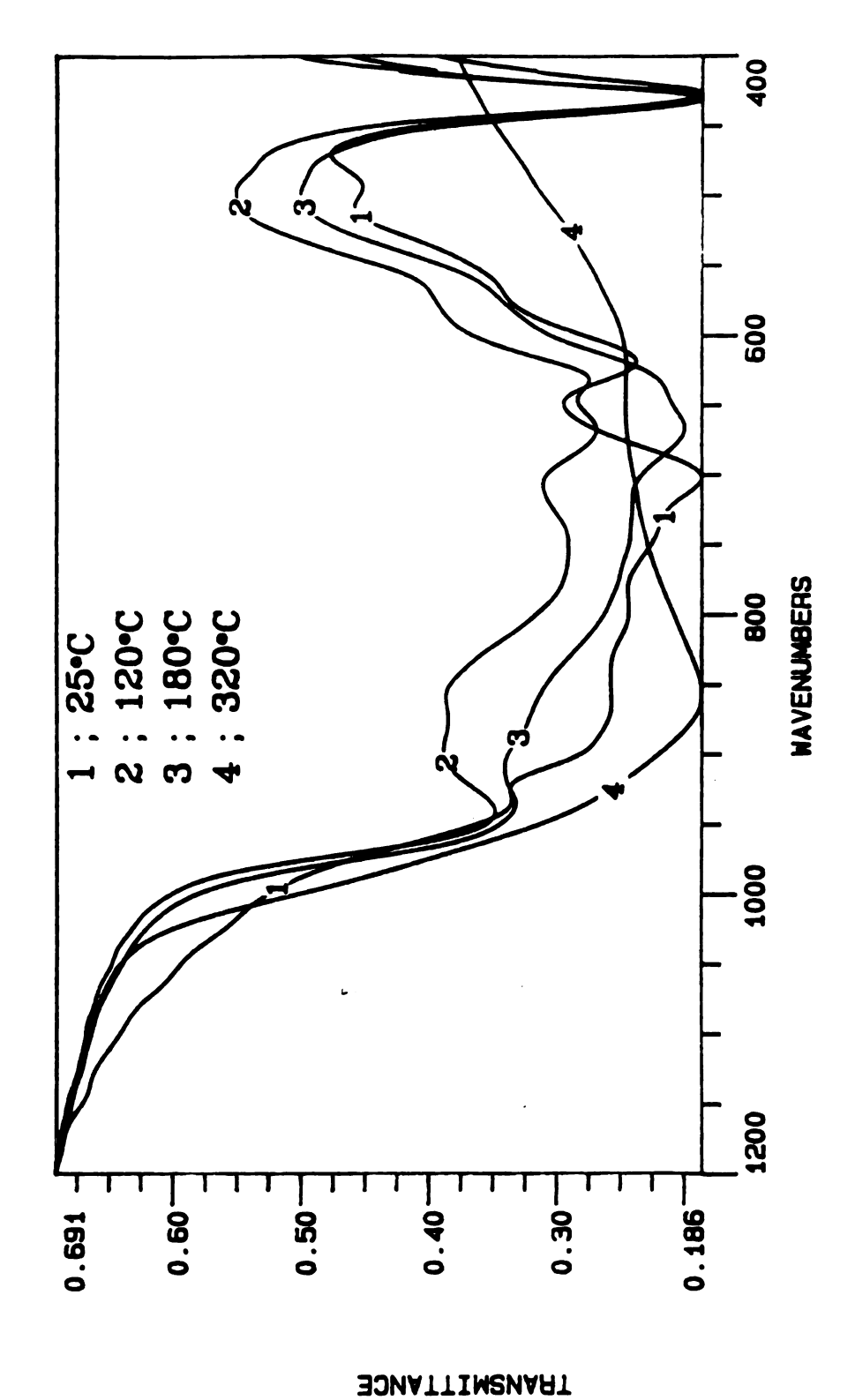


Fig. 84. It spectra of LDH-H<sub>2</sub>W<sub>12</sub>O<sub>42</sub> at different temperatures.

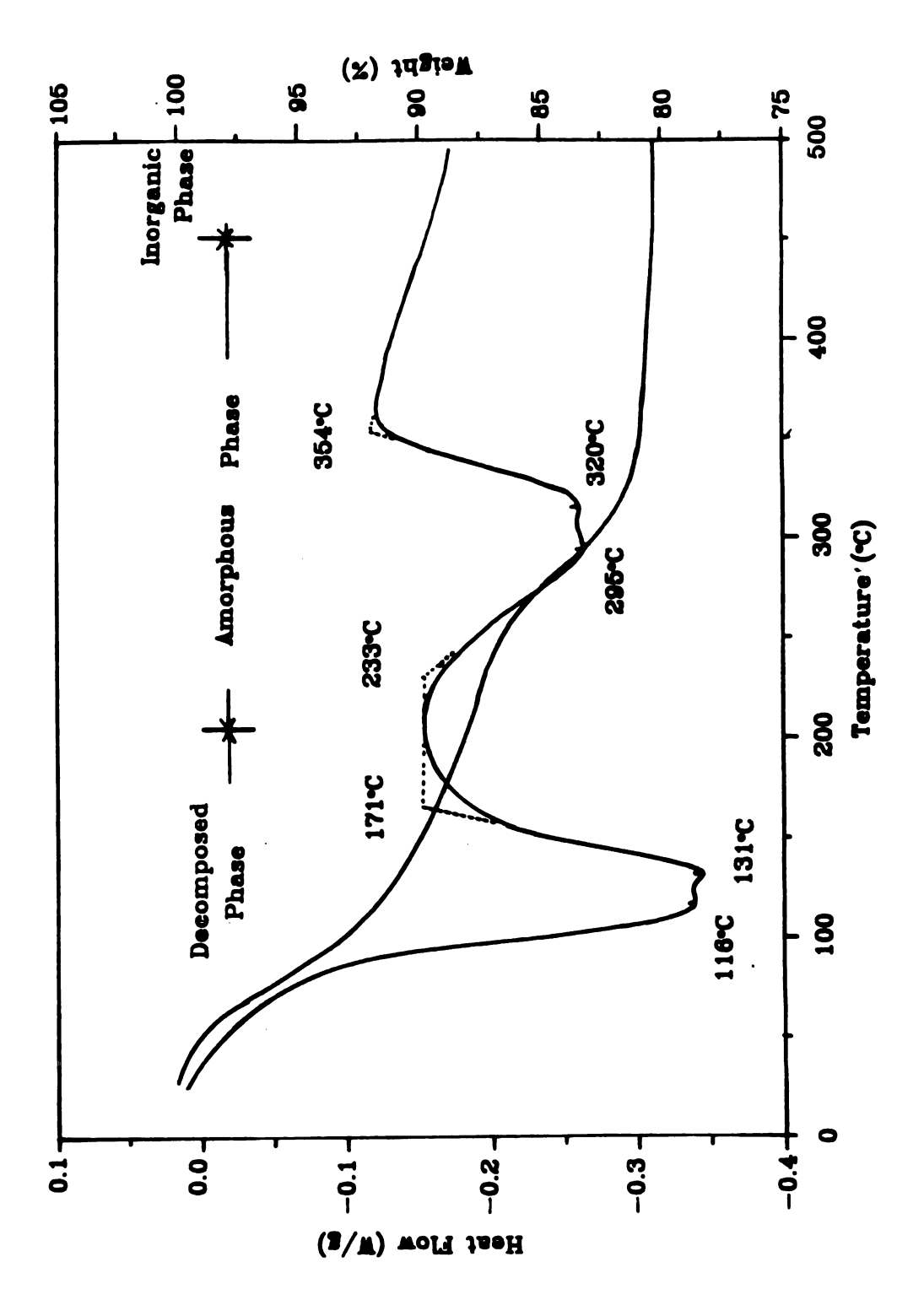


Fig. 85. DSC and TGA of LDH-H<sub>2</sub>W<sub>12</sub>O<sub>42</sub>.

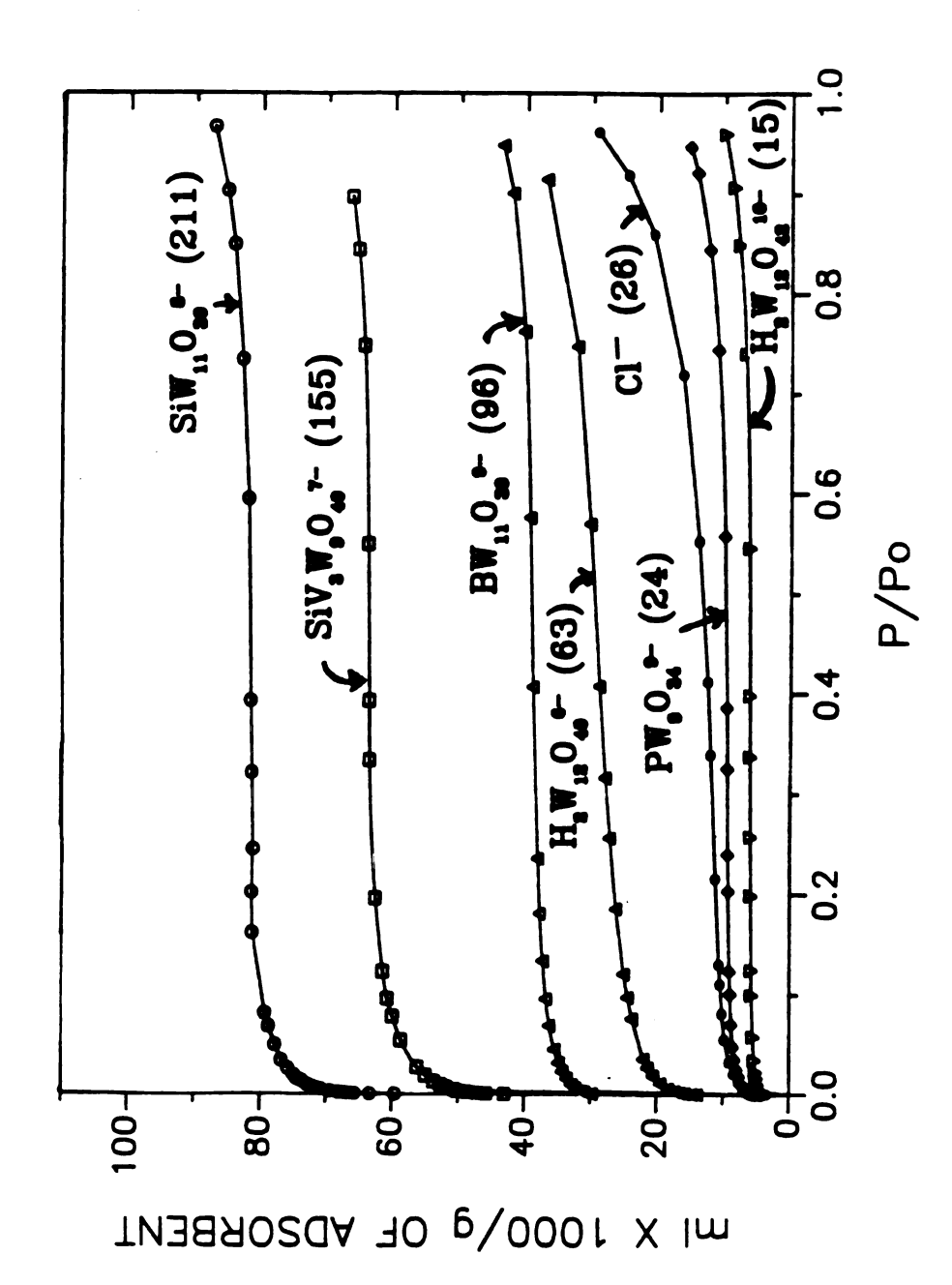
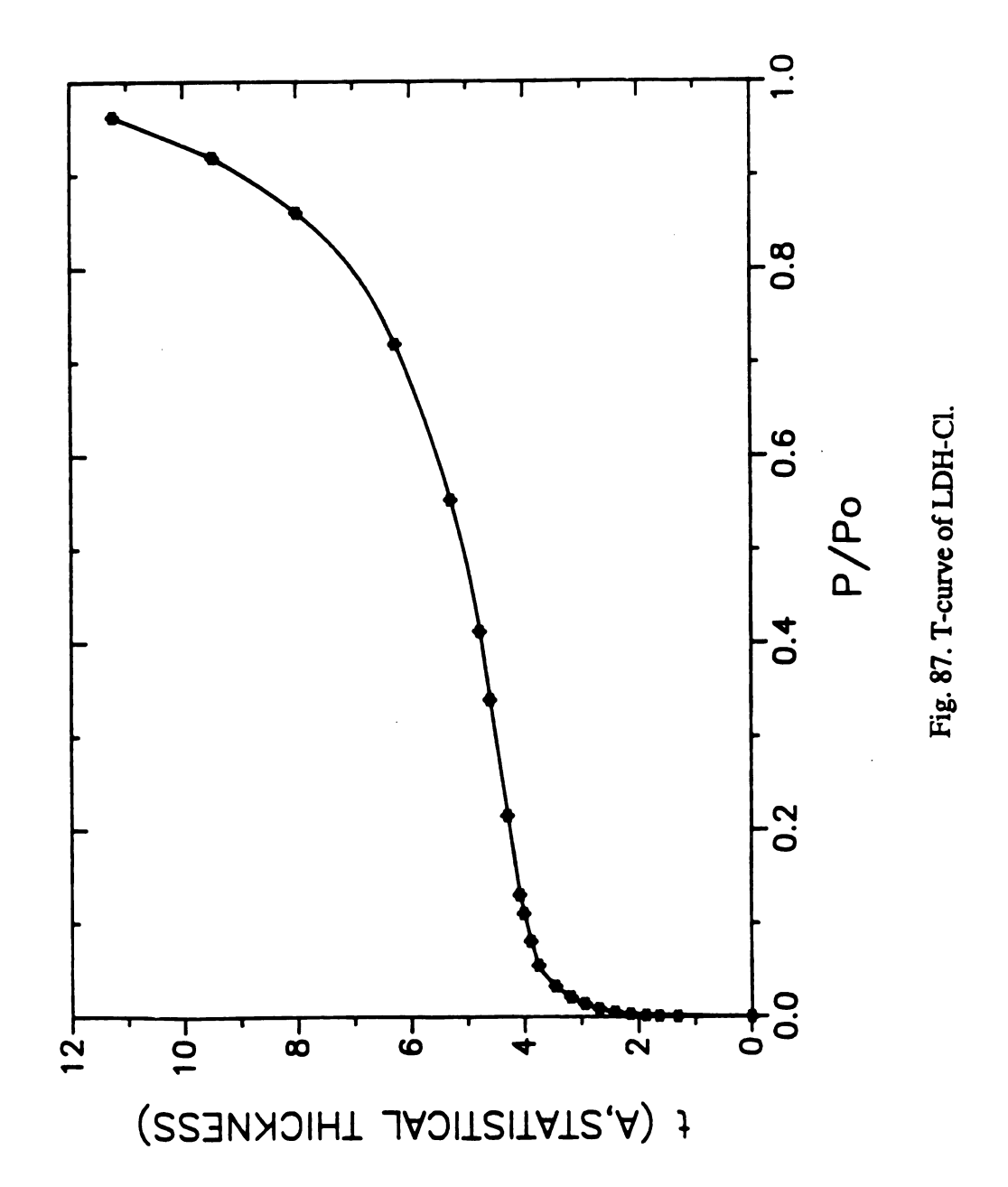


Fig. 86. N<sub>2</sub> adsorption isotherm of LDH-POMs.

Table 14. LDH-POM Intercalates for  $N_2$  Adsorption Studies.

POM	Isotherm Type	Surface Area BET N <sub>2</sub> (m <sup>2</sup> /g)
H <sub>2</sub> W <sub>12</sub> O <sub>40</sub> 6-	I .	63
SiV3W9O40 <sup>7</sup> -	I	155
SiW <sub>11</sub> O <sub>39</sub> 8-	I	211
BW <sub>11</sub> O <sub>39</sub> 9-	I	96
PW9O34 <sup>9</sup> -	II	26
H2W12O4210-	II	15
NaP5W30O110 <sup>14</sup> -	II	8



these systems are microporous materials in which the pores are nearly filled at low p/p<sub>0</sub>. These have relatively high surface areas compared to the other three LDH-POMs whose adsorption isotherm shapes are type II. The latter type II isotherms are typical for nonporous materials. One of lowest adsorptions capacities was observed for LDH-Cl, which is a reference nonporous material used for the t-curve analysis, which is provided in Fig. 87.

The pore volumes of the porous LDH-POMs were obtained from either a D-A or D-R plot and a t-plot. These are shown in Appendix B. All t-plots have the same shape. Such sharp transitions in the t-plot curves indicate that each system has a unique pore size. It can be said that POMs are uniformly distributed in the gallery, thereby providing an unique pore size.

### G. Theoretical Calculation of Surface Area and Pore

#### Volume

Certain POMs can be intercalated in LDH galleries, thereby providing free space in the gallery. The available extra space or area can be estimated in the following way. Here only LDH-POM in which POMs have the Keggin structure are considered.

The general chemical formula of LDH-POMs is

[Zn<sub>2</sub>Al(OH)<sub>6</sub>]<sub>n</sub>POM<sup>n</sup>-, where n is the negative charge carried by POM. The following quantities are defined:

 $S_1$  = area of  $Z_{n_2}Al(OH)_6$  surface in the absence of any gallery ion

 $S_C$  = maximum cross area of POM

The free area created by the intercalation of one molecule of POM in the gallery is equal to  $nS_1 - S_c$ . The molecular weight of  $[Zn_2Al(OH)_6]_nPOM^{n-}$  is equal to 260n + MpOM, where MpOM is the molecular weight of the POM. Assuming that 1) the host layer is perfectly rigid, 2) the repulsive interaction between POMs in the gallery is free and 3) the POM is spherical with  $2r = d(gallery\ height) = 9.6\ Å$ . Then,

$$S(m^2/g) = 6.0 \times 10^3 \times \{nS_1 - (\pi d^2/4)\}/(260n + M_{POM}) - -(1)$$

The calculated values for selective systems including observed ones are tabulated in Table 15. Here, the equation (1) should be greater than zero, Therefore,

$$nS_1 - \pi d^2/4 > 0$$

n > 4.4

Since the area occupied by the POM in the gallery should be less than that provided by the LDH layer ( $nS_1$ ), the above result implies that the minimum charge of a POM with Keggin structure to be intercalated is 4.4. Because of the integrality of molecular charge, the minimum must be 5. However, in this calculation the free area includes all the area available regardless of the size and shape of the free area. For more precise calculation, the assignment of the POMs in the gallery should be taken into account. The most efficient array of the POMs in the given area is a hexagonal one. When the POMs are closely packed hexagonally, the line connecting the nearest three POMs will make an equilateral triangle with an interstice in the center. The area of this equilateral triangle is equal to 0.433 d<sup>2</sup>, corresponding to one half of the area given to one POM. Thus, the area given to one POM is 79.8 Å<sup>2</sup> for d = 9.6 Å, This area consists of the area occupied by one POM as well as the area of the interstice. When the area  $nS_1$  given by the LDH layer is equal to that given to one POM (2 x 0.433 d<sup>2</sup>), the POM molecules in the gallery are most efficiently arranged, so maximum POM number is accommodated by the host layer. Thus,

$$nS_1 = 2 \times 0.433 d^2$$

For d = 9.6 Å and  $S_1 = 16.5 \text{ Å}^2$ , n is equal to 4.8.

In reality, the POMs with 5- charge have not been completely exchanged into the gallery, but only partial exchange has been observed. The observed minimum charge for the complete exchange reaction is 6-. This discrepancy arises from the oversimplification

of the above model. If the repulsive interaction between POMs is considered, the van der Waals radius would increased, and the calculated minimum charge would be greater than 5.

From the above derivation of the minimum charge carried by POM, the average distance between the POMs in the gallery can be also obtained. For the simplicity, let's take the minimum charge is 5-, which corresponds to a value obtained using d = 9.8 Å and the area given to a POM 83.2 Å<sup>2</sup>. As n increases from 5- to 6-, the given area to the POM also increases proportionally. Thus, the resulted area is 99.8 Å<sup>2</sup>. Now, the quantity d corresponds to the distance between the POM. Therefore,

$$2 \times 0.433 d^2 = 99.8$$

d is equal to 10.7 Å. In the same way, the following distances can be obtained for the other n values: n = 7, d = 11.6 Å; n = 8, d = 12.4 Å; n = 9, 13.2 Å; n = 10, 13.9 Å.

The free volume can also be estimated in a following manner. The free space generated by the intercalation of one molecule of POM is V, expressed as below, where the symbols and definitions have the same meaning, except that d is again a d-spacing.

$$V = (d \times nS_1)$$
 - volume occupied by a POM ----(2)

If the shape of POM in the gallery is assumed to be spherical and if the pore volume  $(V_{SD})$  is expressed as a ml/g unit, then

$$V = V_{sp} = 0.6\{16.5 \text{nd} - (\pi d^3/6)\}/(260 n + M_{POM}) ----(3)$$

If the shape of POM in the gallery is cylindrical with height = d(gallery height) and cross area =  $S_C$ , then

$$V = V_{cy} = 0.6\{16.5 \text{nd} - (\pi d^3/4)\}/(260 n + M_{POM}) ----(4)$$

All calculated pore volumes are tabulated along with observed values in Table 15.

As the charge, n, on the POM increases, the calculated pore volume and surface area also increase, because the lateral distance between POMs in the gallery increases. However, the denominators in both equation (3) and (4) also increase with increasing charge. The contribution of the weight term does not change the trend of calculated values: the higher the charges of POMs in the gallery, the larger the surface areas and pore volumes. The observed values of surface area and pore volume increase as the charge on the POM increases only in the range of n = 6 - 8. When n reaches 9, all the values abruptly decrease. Therefore, the maximum value of surface area and pore volume is observed at n = 8. The largest difference in the absolute value between the observed and calculated ones occurs at n = 8. The structure of the POM at n = 8 is no longer a Keggin structure, because one out of 12 W required in the original Keggin structure is missing. The reduction of the lateral diameter of the pillaring POM will contribute extra space in the gallery and result in larger observed than calculated values of both surface area and pore volume.

The big drop in observed surface area and pore volume at n > 8 probably results because one of the assumptions made in the calculation does not hold. The assumption of perfect layer rigidity is not realized in these systems. Imperfect layer rigidity results in layer sagging after the zeolitic water in free space is removed prior to the gas adsorption. Such layer sagging will result in a reduction of the free space, thereby blocking the adsorbate from reaching the gallery space. The dependence of layer sagging on the POM charge densities also is observed in the case of POMs having the same total charge but different size. For the n = 9 case, the 9- charges are delocalized on 39 oxygens in BW11O39 and on 34 oxygens in PW9O34. Therefore, the charge density of the former is lower than that of the latter. The higher charge density and small size of the latter will cause greater layer sagging than the lower charge density POM. The dependence of layer

Table 15. N<sub>2</sub> Gas Adsorption Data and Calculated Values

РОМ	n	Mpok	S	S	>*		>	-
		(g/mole		(8/ <sub>*</sub> m)	V(D-R,D-A) $V(t)$	) V(t)	^*	Vey
						ml x 1000	000	
H <sub>a</sub> W <sub>12</sub> O <sub>40</sub>	9	2848	72.8	63	31.3	23.2	6.39	34.9
SiV <sub>3</sub> W <sub>6</sub> O <sub>40</sub>	7	2500	120.2 155	155	9.69	60.6	0.06	57.7
SiW <sub>11</sub> 0 <sub>36</sub>	8	2753	149.6	211	87.5	77.3	100.2	71.3
BW <sub>11</sub> 0 <sub>30</sub>	6	2657	183.6	96	40.7	35.2	116.0	88.1
PW.034	6	2230	200.7	24	0	0	126.9	96.3

sagging on charge density is also observed in the XRD data for both systems heated at temperatures employed for the adsorption studies. These XRD patterns are in Fig. 68 (c) and Fig. 74 (b). As the charges of POMs increased further, observed values decreased. The details of layer sagging will be discussed in the other section.

The pore volumes calculated on the basis of a cylindrical model are closer to the observed values than those based on a spherical model. Since nitrogen used as an adsorbate in the adsorption study has a finite size, there are dead spaces that nitrogen molecules can not reach. Thus, a cylindrical model, in which the volume occupied by POMs will include some of such dead spaces, will be more realistic than a spherical model, in which the dead spaces are not taken into account.

### G. Photoreactivity of LDH-POMs

Following the scheme of Hill for classifying POM photoreactivity in homogeneous solution, we can classify LDH-POMs by the visual changes which occur during the photoreaction.

Class I: This category of LDH-POMs neither develops any color change even under Ar nor yields any significant photoproduct. The yields are so low even under O<sub>2</sub> that in some cases product production is below reasonable limits of detection. The LDH-POMs containing transition metals are in this category. For example, LDH-SiFe(SO<sub>3</sub>)W<sub>11</sub>O<sub>39</sub>, LDH-BCoW<sub>11</sub>O<sub>39</sub> and LDH-Co<sub>2</sub>W<sub>12</sub>O<sub>42</sub> belong to this class.

Class II: This category of LDH-POMs changes its color to mostly blue under Ar. The original colors are not completely recovered when the reduced LDH-POMs are exposed to air. Even after several days there is still slow recovery of the original color, but complete recovery is not achieved. The LDH-POMs containing V(V) and Mo(IV) belong to this category. Thus, when photoreactions are carried out even under O2, color changes are developed. In the catalytic cycle, the rates of reoxidation of the reduced LDH-POMs

are very slow compared to those of Class III. LDH-PV<sub>14</sub>O<sub>42</sub>, LDH-SiV<sub>3</sub>W<sub>9</sub>O<sub>40</sub> and LDH-PMo<sub>2</sub>W<sub>9</sub>O<sub>39</sub> belong to this category.

Class III: This category of LDH-POMs changes its color from mostly white to blue under an argon atmosphere. When these blue-colored forms are exposed to the air, their colors change back to the original white color. When photoreactions are carried out under O2, no color change develops. Therefore, the catalytic cycle, which involves reduction of LDH-POM by organic substrates, formation of a blue colored LDH-POM and reoxidation of the LDH-POM by O2, is completed without appearance of a color change. For example, LDH-NaP5W30O110, LDH-H2W12O42, LDH-SiW11O39, LDH-PW9O34, LDH-H2W12O40 and LDH-BW11O39 are in this category.

The photoreactivities of LDH-POMs for the oxidation of isopropyl alcohol are summarized in Table 16.

The general trend of photoreactivity in Class III complexes is that the higher the charge on the POMs in the gallery, the greater the reactivity. As discussed in the previous section, the higher the charge on the POM in the gallery, the more free space available between POMs. Therefore, it can be said that the more spaceous the gallery, the more reactive is the system. In the case of LDH-NaP5W30O110, the increase in gallery height provides more space compared to LDH-POMs of the Keggin-type. Therefore, for the Class III systems, the greater the free space within the gallery, the higher the photoreactivity. This observation is contradictory to Fox's result in which the higher the charges or the larger the sizes of POMs, the lower the reactivities. The photoreactivities of LDH-POMs have been observed to be very much different from those of homogeneous POM solutions. It has been claimed that a pre-association complex formation between the organic substrate and POM should precede photoactivation and that the photoreactivities depend on the stabilities of these complexes. The rate of formation of the pre-association complex in the LDH-POM will be dependent upon the mobility of the organic substrate within the free space in the gallery. It is certain that the

Table 16. Photochemical Reactivities of LDH-POMs

		Tur	Turnover number	er
POM	Charge	Ar	o	O <sub>s</sub> /Ar
NaP.W.O.	14	17.9	31.4	1.8
H <sub>8</sub> W <sub>18</sub> O <sub>48</sub>	10	8.0	17.5	9.0
PV,04	6	4.7	11.7	2.5
SiW <sub>11</sub> 0 <sub>20</sub>	8	2.4	12.0	5.0
PW.O.	6	3.3	8.3	2.5
H,W,O,	9	•	10.3	-
Siv, Wo.	4	1.6	8.0	4.9
PMo,W,O,	7	1.2	7.8	6.5
BVW <sub>11</sub> O <sub>46</sub>	4	2.0	3.9	1.9
BW <sub>11</sub> O <sub>20</sub>	6	1	1.2	1
SiFe(SO <sub>3</sub> )W <sub>11</sub> O <sub>32</sub>	4		1.3	ī
BCoW <sub>11</sub> 0 <sub>36</sub>	4	-	1.1	ì
Co <sub>8</sub> W <sub>18</sub> O <sub>48</sub>	8	-	1	1
BCuW <sub>11</sub> 0 <sub>20</sub>	2	1	1	1

more spaceous the gallery is, the faster the organic substrate will travel through it. Therefore, higher reactivity will be observed in the high charged system containing a large POM rather than in a low charged system with small sized POM. The increased space also facilitates diffusion of products from the reaction site out of the gallery. The ability of product to leave easily minimizes back electron transfer from the reduced POM to product or other transient species. Therefore, both easy access of reactant and easy leaving of product in the gallery make the system well suited for high photoreactivities. Fox has also claimed that the photoreactivities of POM depend on the heteroatom of the POMs, as well as on their reduction potentials. The same observation has been made for the LDH-POMs. For example, the following order of photoreactivity was observed: PW9O34 > H2W12O40 > SiV3W9O40 > Co2W12O42. Therefore, the photoreactivities of LDH-POMs depend on the electrochemical properties of POMs, as in the homogeneous solution. When the photoreactivities of LDH-POMs under Ar are compared with those under O2, the highest ratio of (turnover # under O2/turnover # under Ar) is observed in LDH-H2W12O40. A trace of product was produced under Ar, while under O<sub>2</sub> a large quantity of product was obtained as shown in Table. 16. The behavior of this system shows that reoxidation of reduced POM in the gallery by O2 is highly efficient even though the total yield is lower than that in other systems which have more free space in the gallery due to the high charge of POM, e.g., LDH-H2W12O42. Therefore, this system illustrates that the photoreactivities of LDH-POMs associate strongly with the electrochemical properties of POMs.

The LDH-POMs in which boron is a heteroatom are very photochemically unreactive compared to those in which P is the heteroatom.

Class I system shows almost no photoreactivity, perhaps because insufficient number of photons is available to carry out photoreaction on the W-O centers due to the high absorption of photons by the transition metals.

# H. Swelling Properties of LDH-POMs

It is known that LDH-A intercalation compounds, in which A is a general inorganic anion, do not swell in any solvent. However, LDH-Or derivatives, in which Or is an organic anion, for example, alkyl sulfate, can be swelled by polar organic solvents, as was mentioned in the introduction.

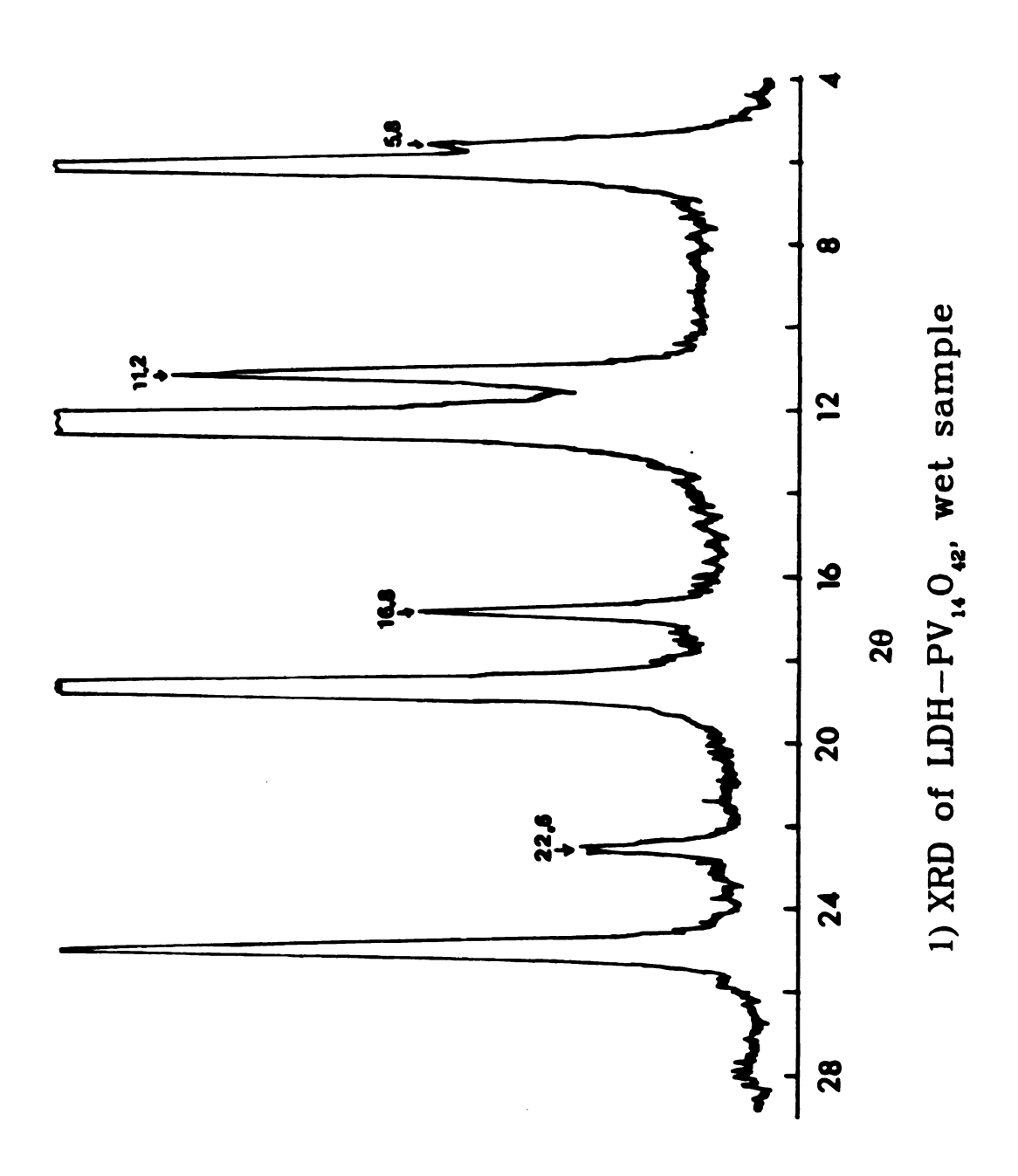
The LDH-POM derivatives show unique, but limited swelling by water, in contrast to the conventional LDH-A. Wet samples of LDH-PV14O42 and LDH-NaP5W30O110 were examined by XRD as shown in Fig. 88. There were two phases present in each sample. One phase gives a high d spacing corresponding to the swelled phase, the other exhibits a low d-spacing, corresponding to the non-swelled phase. The differences in d-spacings of the two hydrated phases in LDH-PV14O42 and LDH-NaP5W30O110 are 1.5 Å and 2.3 Å, respectively. These values correspond to one and two monolayers of water, respectively. This unusual swelling property of LDH-POMs can provide insights into the ion exchange mechanism for LDH-A with POMs and will be discussed later.

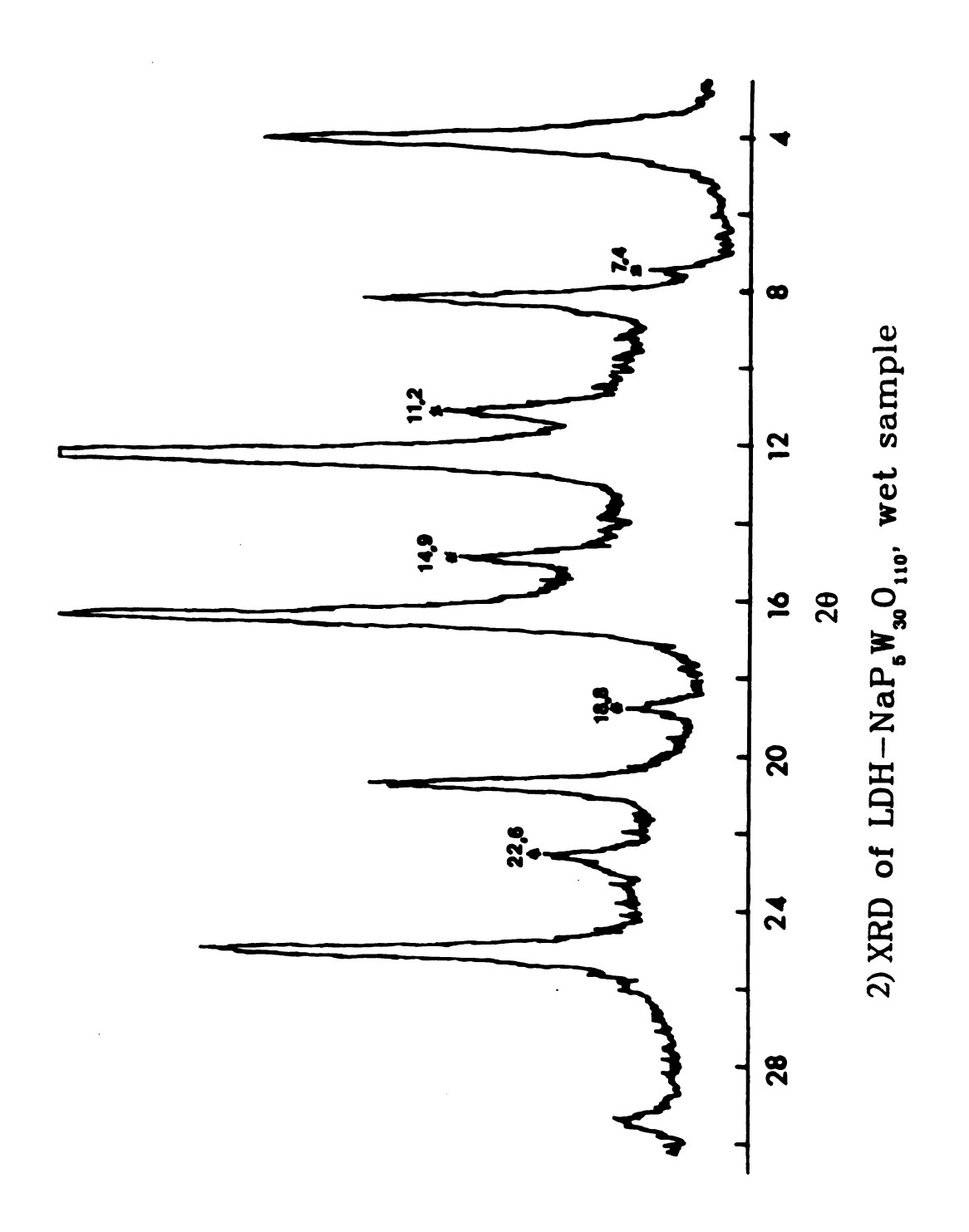
## I. Proposed Mechanism of Ion Exchange Reaction.

Three important observations can be used to support a mechanism for the ion exchange reaction of LDH-NO3 with POMs. First of all, the ion exchange reaction takes places only in neutral or acidic solution. Secondly, the LDH layer is not strictly rigid. Finally, LDH-POMs can be swelled over a limited range, for example, 1 - 2 monolayers of water, whereas LDH-NO3 is not swellable.

LDH layers have broken edge sites in which the aluminums are coordinatively unsaturated. Such edges may have chemical property similar to those of aluminum hydroxide whose colloidal particles carry positive charge at acidic and neutral condition and negative charge at basic condition.<sup>37</sup> Therefore, negatively charged POMs will electrostatically interact with positively charged edges of LDH layer at acidic and neutral

Fig. 88. XRD pattern for wet samples of 1) LDH-PV  $_{14}\text{O}_{42}$  and 2) LDH-NaP5W30O110.

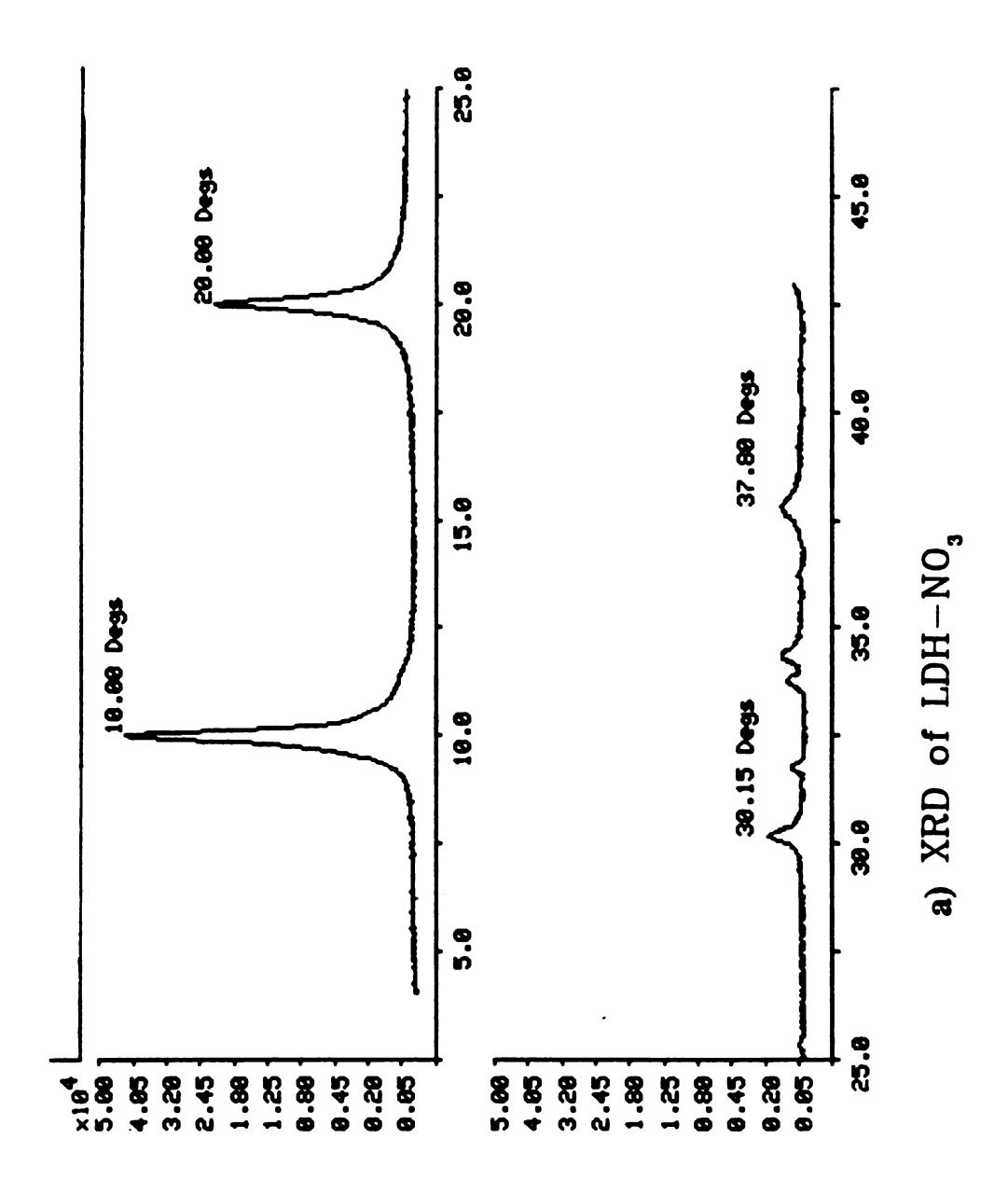


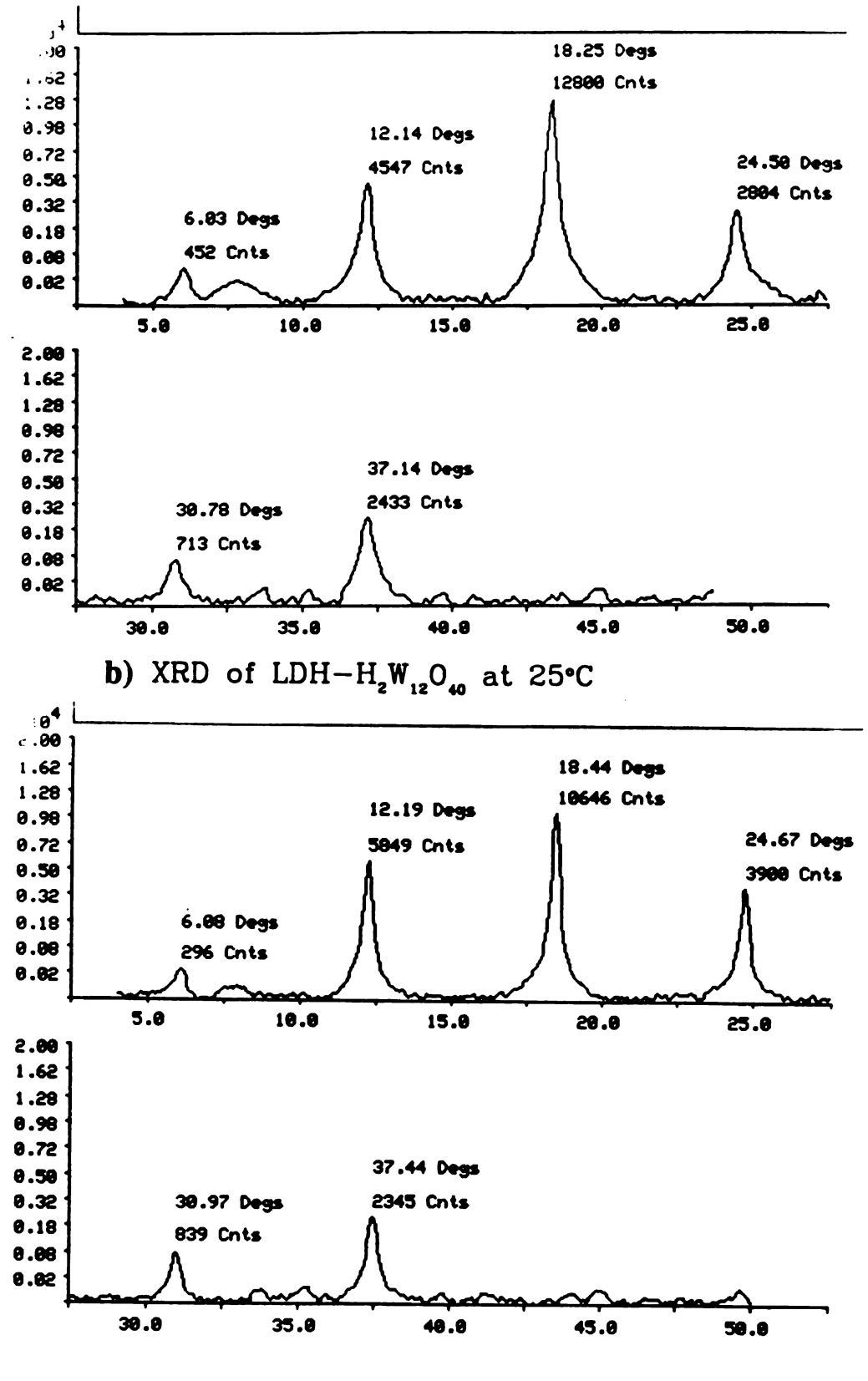


conditions. It is obvious that the interaction will be stronger with highly charged POMs than with lower charged POMs. POMs will consequently bind to the edge of the layer. Exchange of NO3 with edge-bound POMs will take place. Once POMs replace NO3 at the edge of the layer, two phases coexist. One is a LDH-POM phase and the other is a LDH-NO3 phase. The LDH-POM is the only swellable phase and thereby only it can provide sufficient space for easy access of incoming POMs into the gallery to replace NO3. The flexibility of the LDH layer helps the whole system accommodate two different phases in the same gallery. As the reaction proceeds, the LDH-POM phase extends toward the center of the particles and the exchange reaction becomes more favorable because the preformed LDH-POM phase will help the exchange reaction to proceed due to the swellability of this phase. Consequently, the LDH-POM phase plays the role of a catalyst by facilitating the exchange reaction.

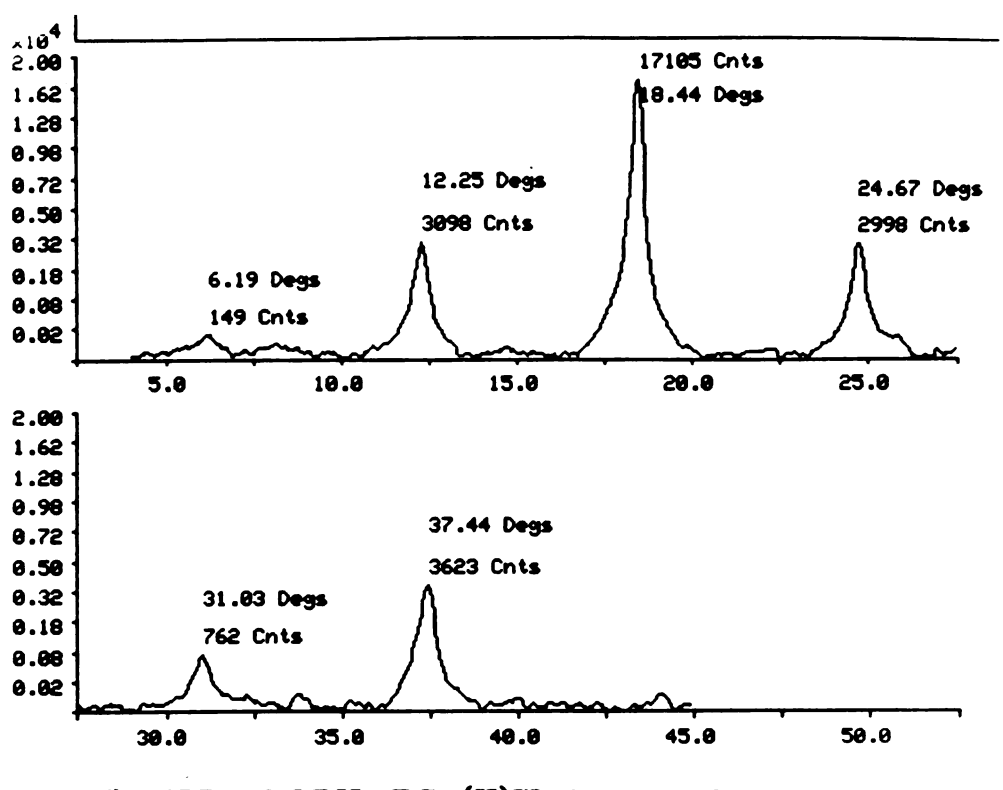
Appendix A: XRD pattern of LDH-NO<sub>3</sub> and LDH-POMs at 25°C.

(a) LDH-NO<sub>3</sub>, b) LDH-H<sub>2</sub>W<sub>12</sub>O<sub>40</sub>, c) LDH-BV(IV)W<sub>11</sub>O<sub>40</sub>, d) LDH-BCoW<sub>11</sub>O<sub>39</sub>, e) LDH-BCuW<sub>11</sub>O<sub>39</sub>, f) LDH-SiFe(SO<sub>3</sub>)W<sub>11</sub>O<sub>39</sub>, g) LDH-SiV<sub>3</sub>W<sub>9</sub>O<sub>40</sub>, h) LDH-PMo<sub>2</sub>W<sub>9</sub>O<sub>39</sub>, i) LDH-SiW<sub>11</sub>O<sub>39</sub>, j) LDH-BW<sub>11</sub>O<sub>39</sub>, k) LDH-PW<sub>9</sub>O<sub>34</sub>, l) LDH-Co<sub>2</sub>W<sub>12</sub>O<sub>42</sub>, m) LDH-PV<sub>14</sub>O<sub>42</sub>, n) LDH-NaP<sub>5</sub>W<sub>30</sub>O<sub>110</sub> and o) LDH-H<sub>2</sub>W<sub>12</sub>O<sub>42</sub>.

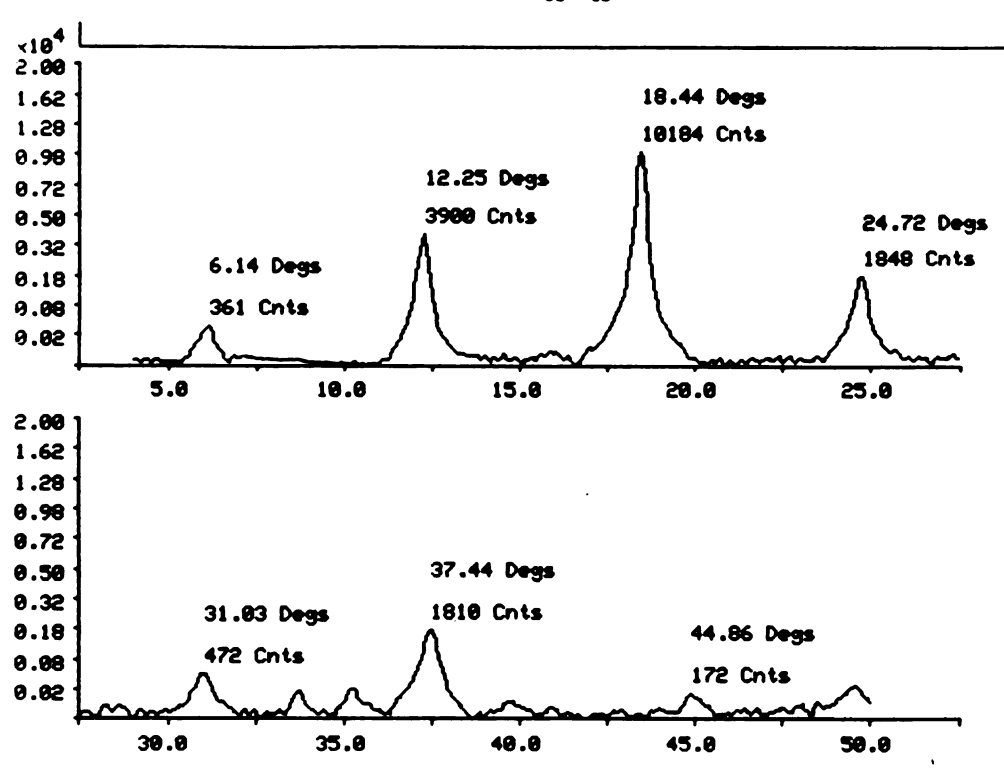




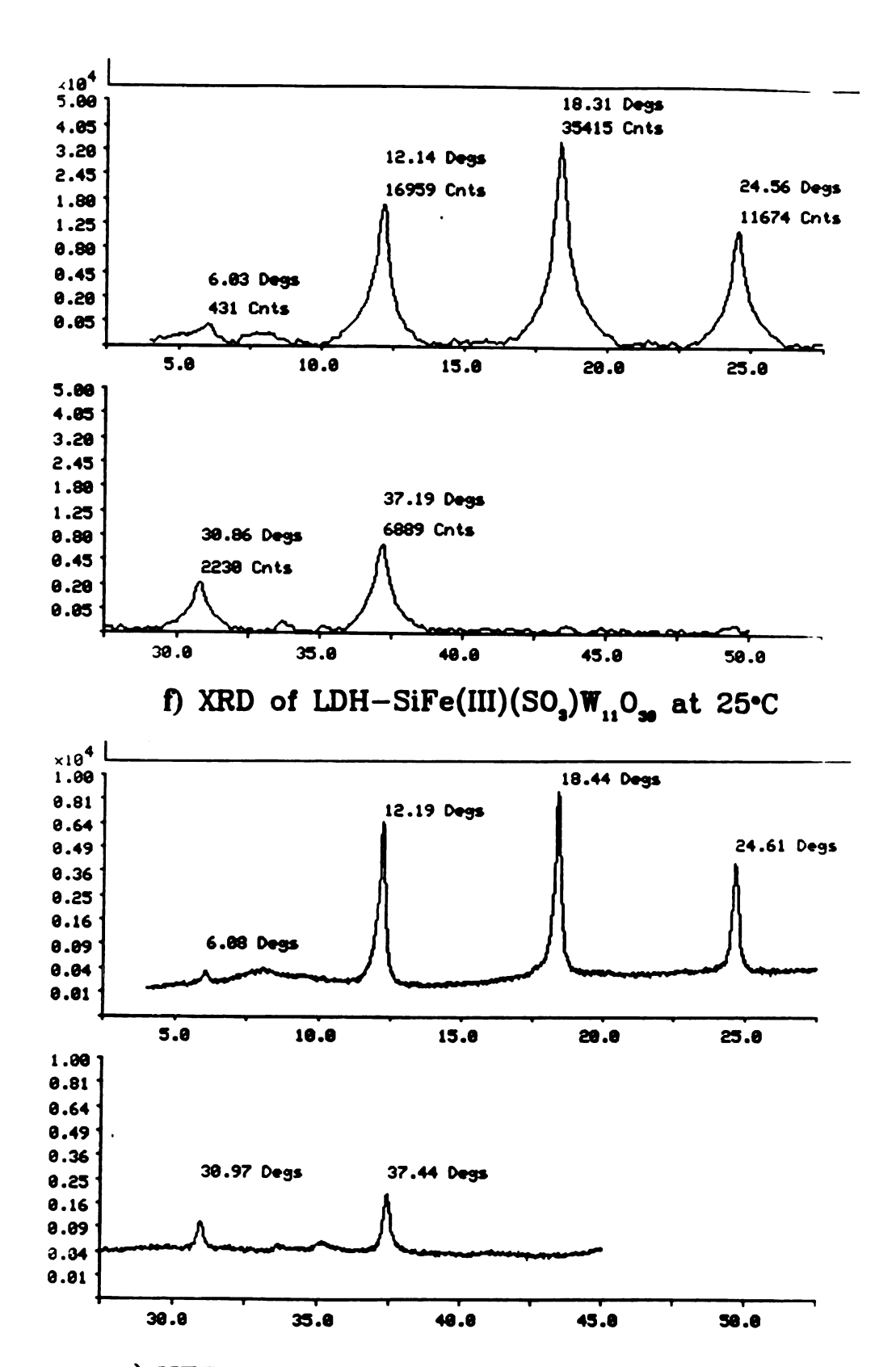
c) XRD of LDH-BV(IV)W<sub>11</sub>O<sub>40</sub> at 25°C



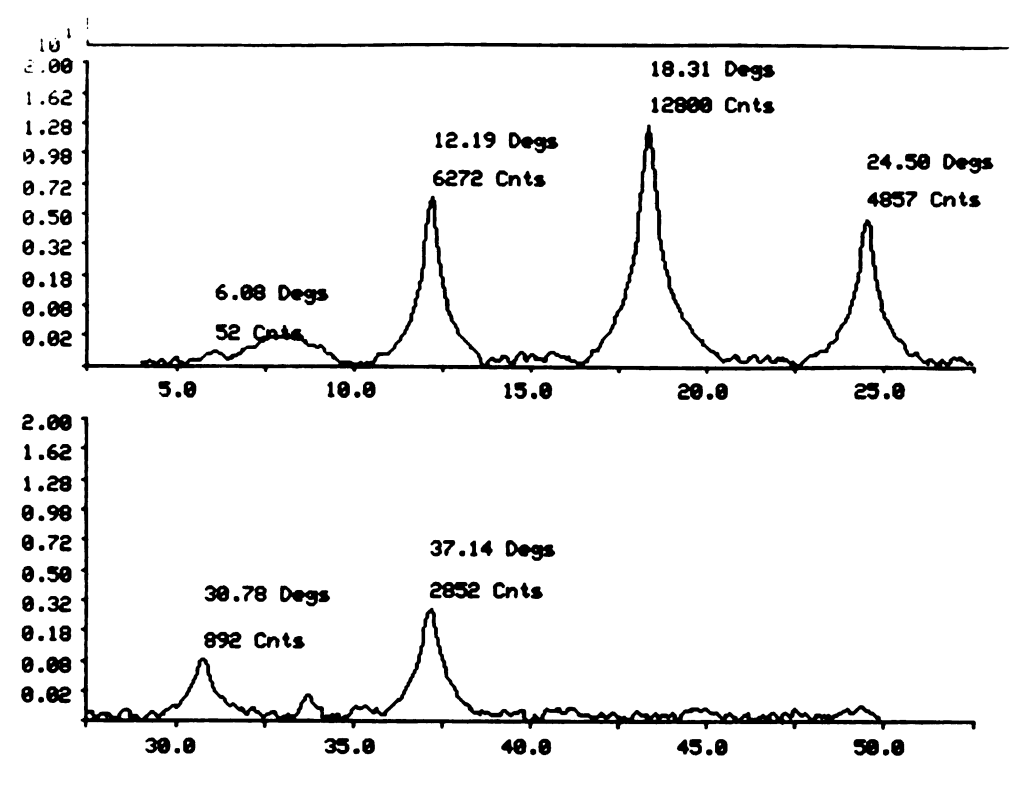
d) XRD of LDH-BCo(II)W<sub>11</sub>O<sub>40</sub> at 25°C



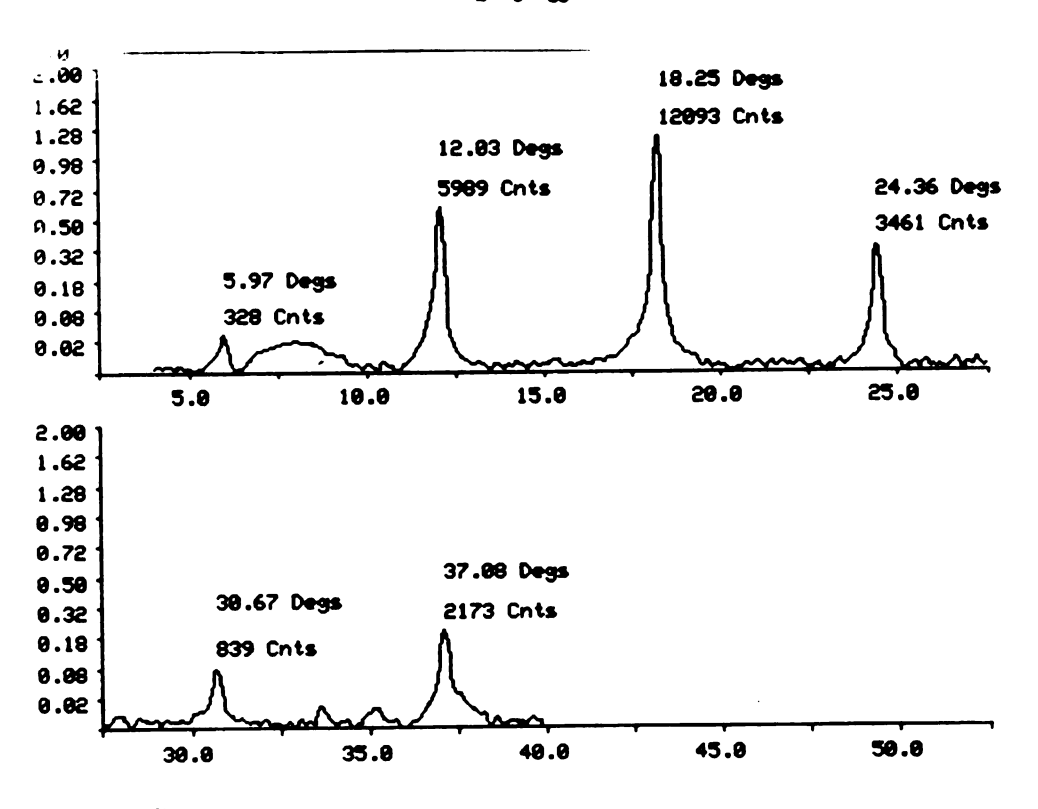
e) XRD of LDH-BCu(II)W110, at 25°C



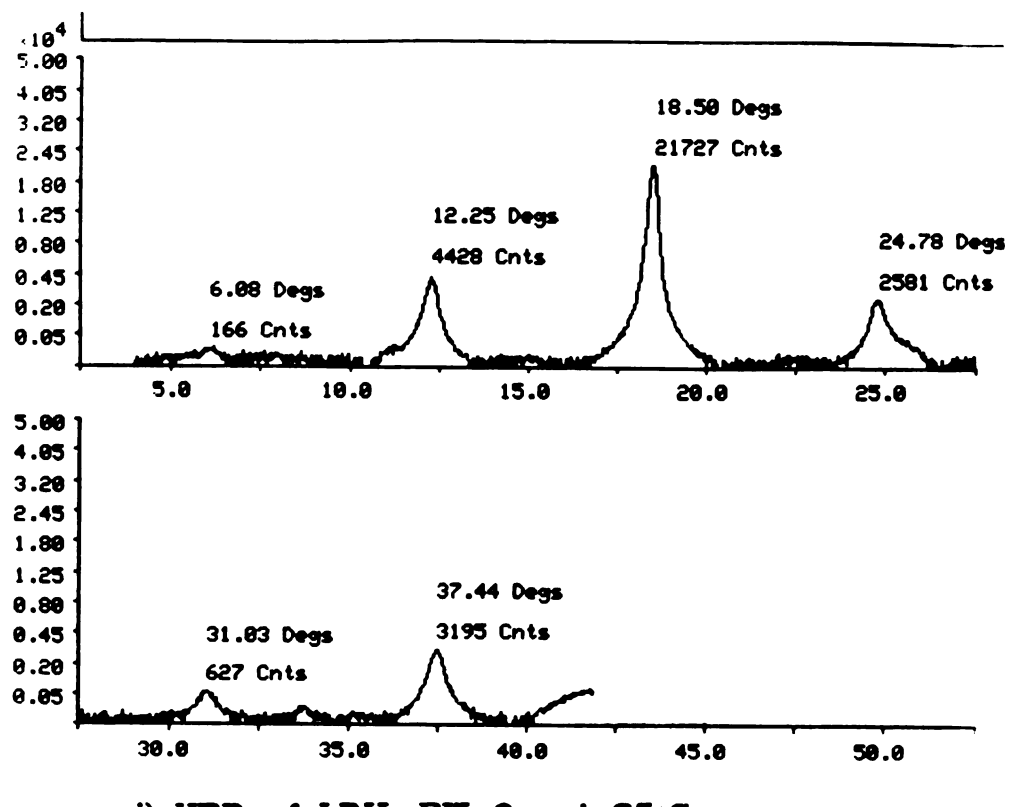
g) XRD of LDH-SiV $_3$ W $_9$ O $_{40}$  at 25°C

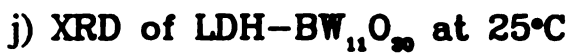


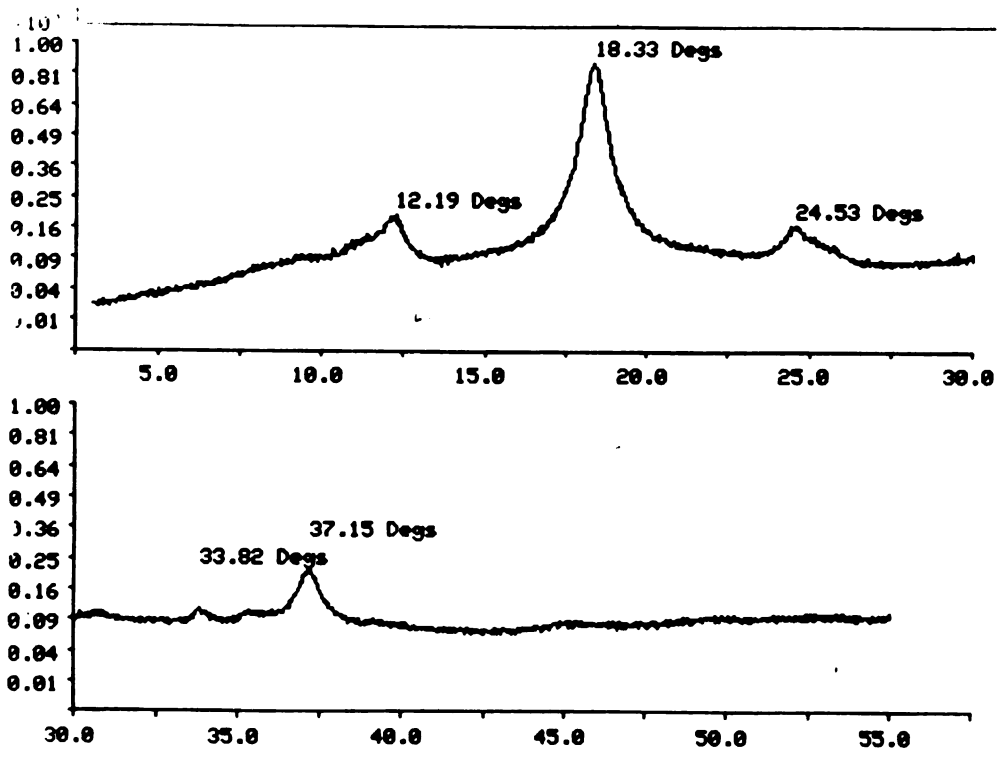
## h) XRD of LDH-PMo<sub>2</sub>W<sub>0</sub>O<sub>30</sub> at 25°C



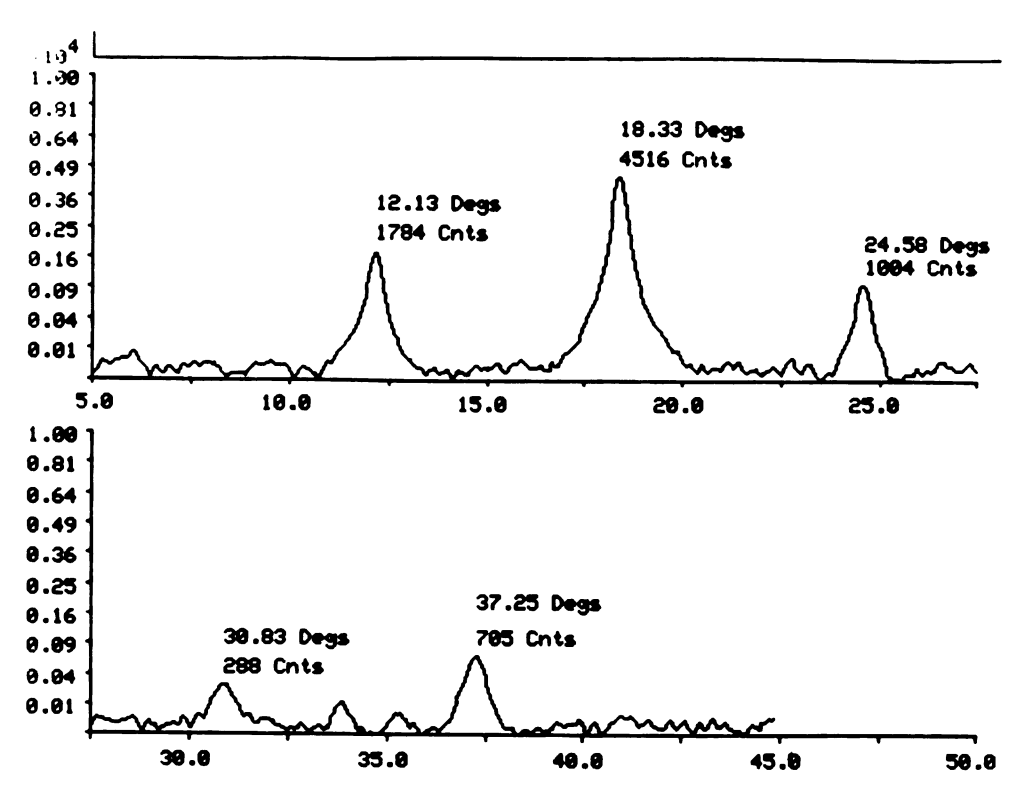
i) XRD of LDH-SiW<sub>11</sub>O<sub>20</sub> at 25°C

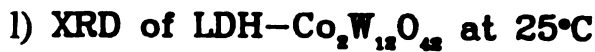


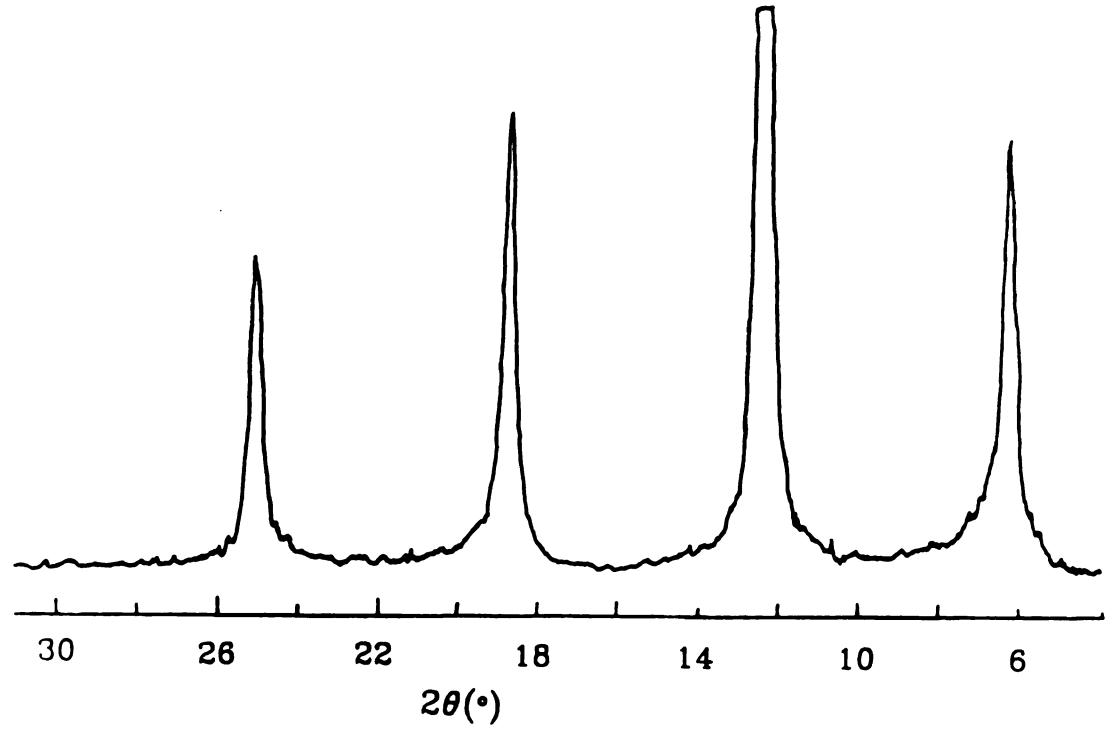




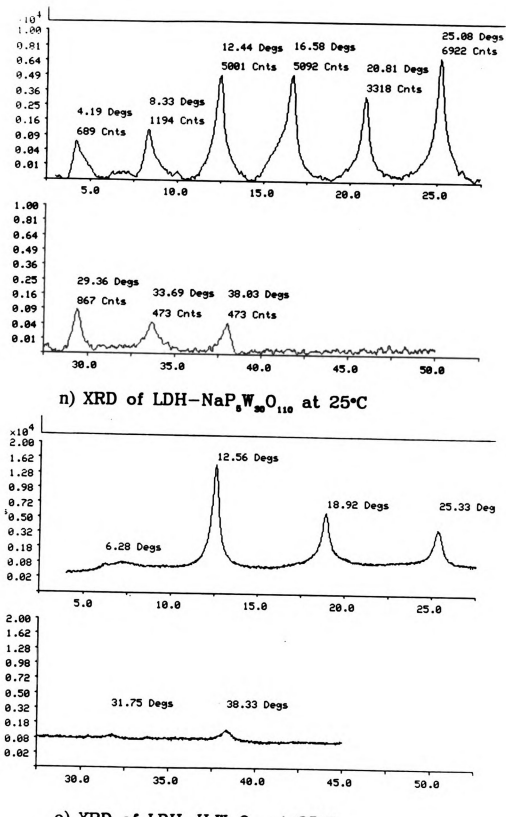
k) XRD of LDH-PW<sub>0</sub>O<sub>24</sub> at 25°C







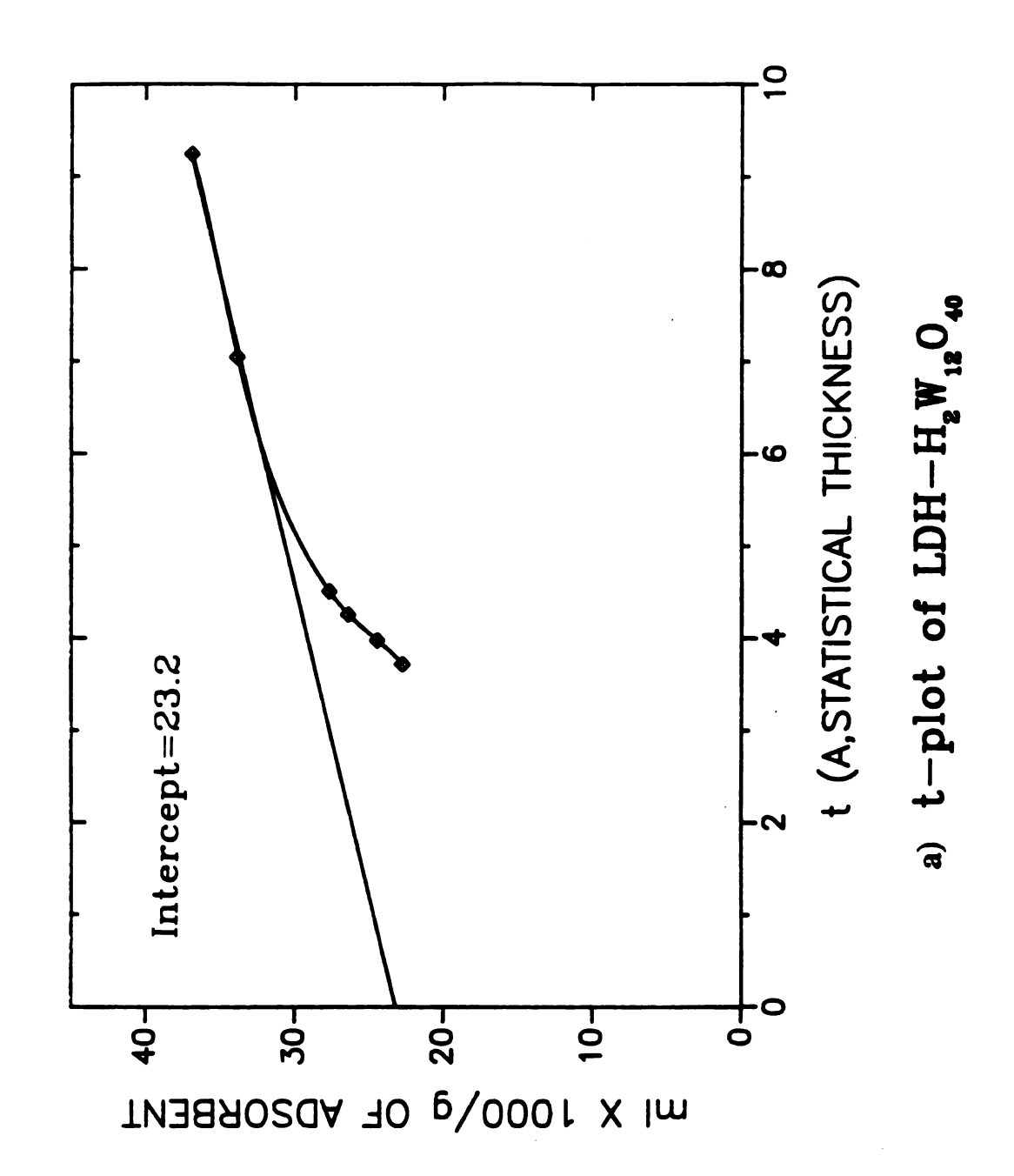
m) XRD of LDH-PV $_{14}$ O $_{42}$  at 25°C

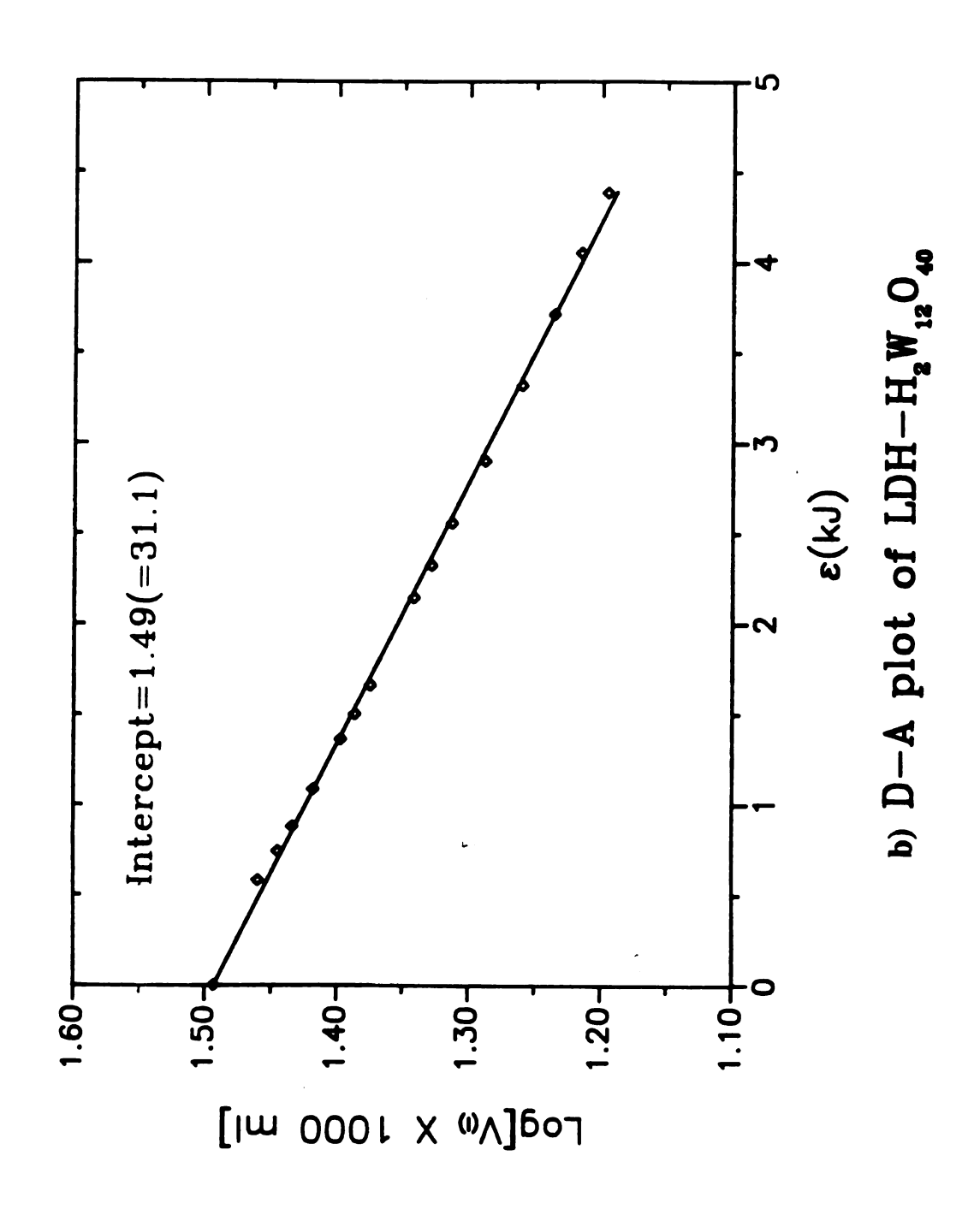


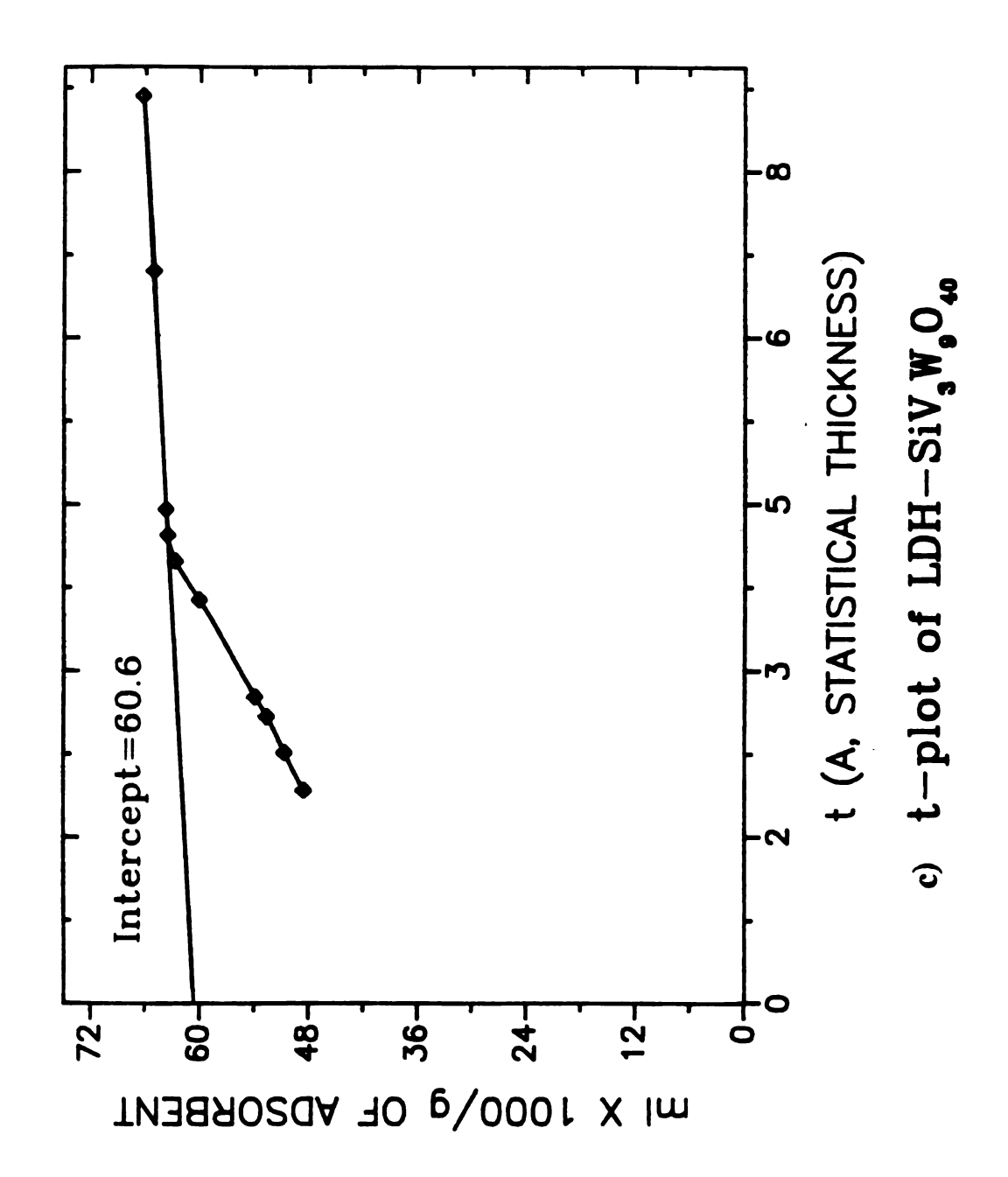
o) XRD of LDH-H2W12O42 at 25°C

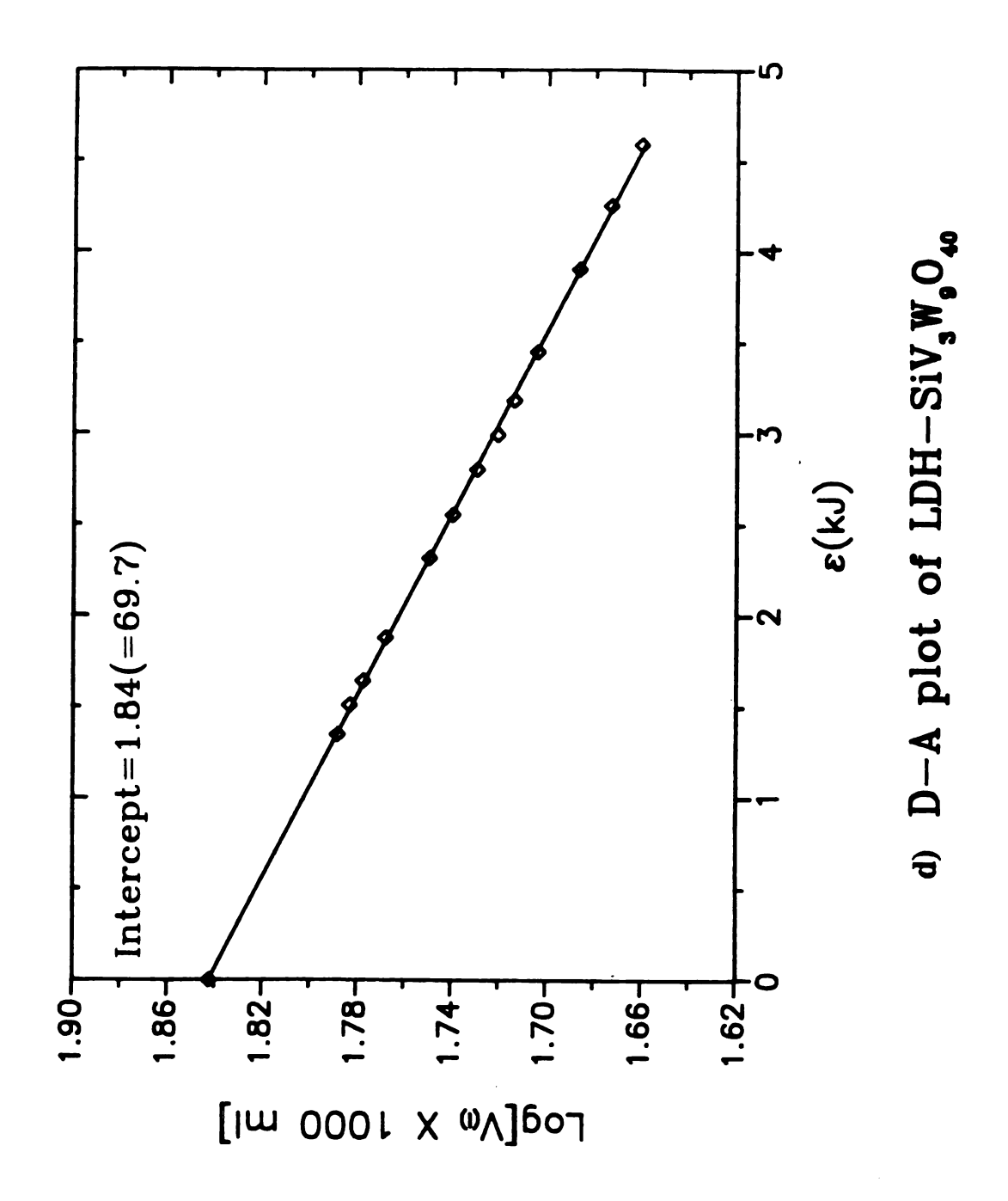
Appendix B: T-plots and D-R or D-A plots of LDH-POMs.

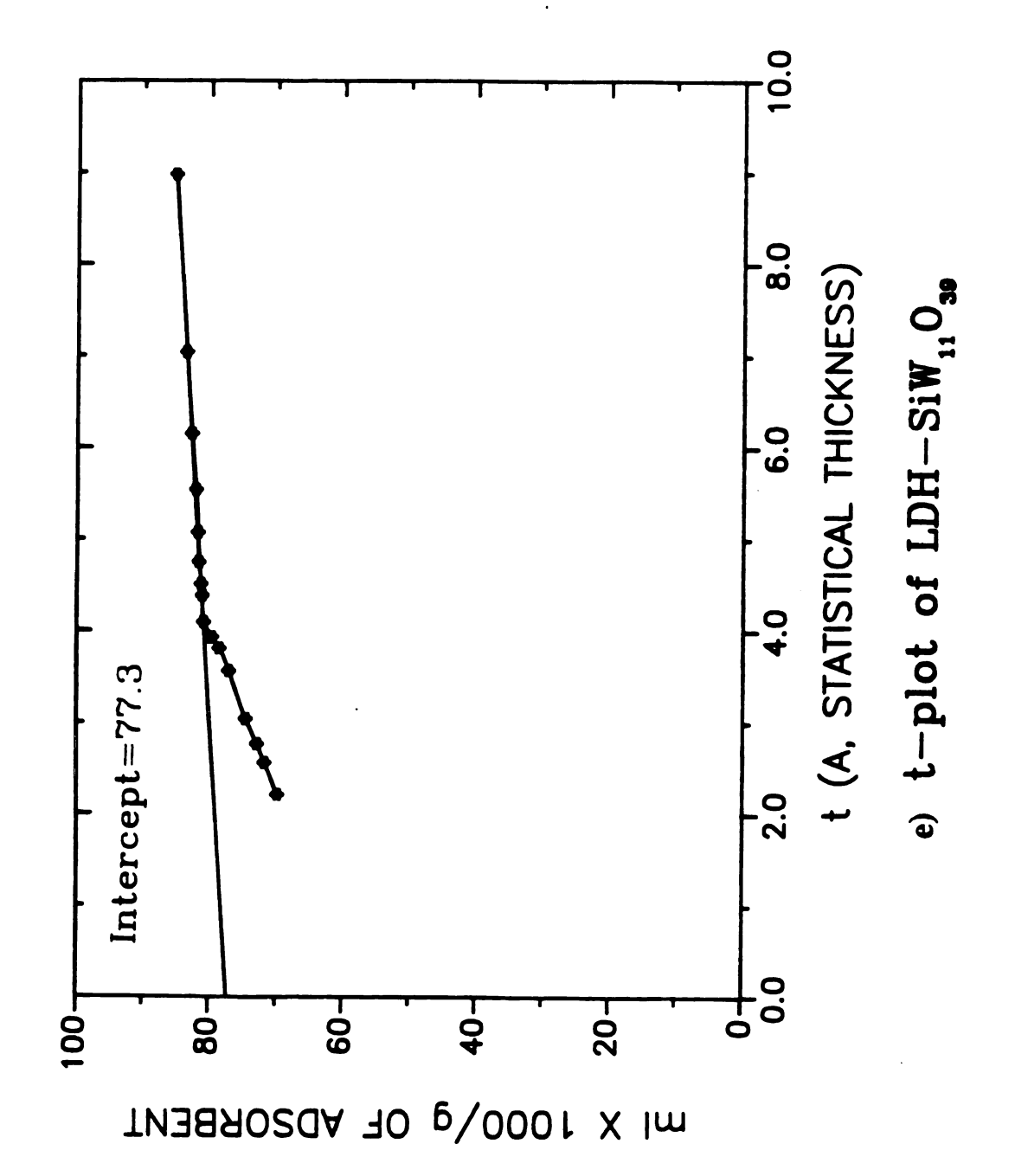
- a) t-plot of LDH-H2W12O40. b) D-A plot of LDH-H2W12O40.
- c) t-plot of LDH-SiV3W9O40. d) D-A plot of LDH-SiV3W9O40.
- e) t-plot of LDH-SiW11O39. f) D-R plot of LDH-SiW11O39.
- g) t-plot of LDH-BW11O39. h) D-A plot of LDH-BW11O39.

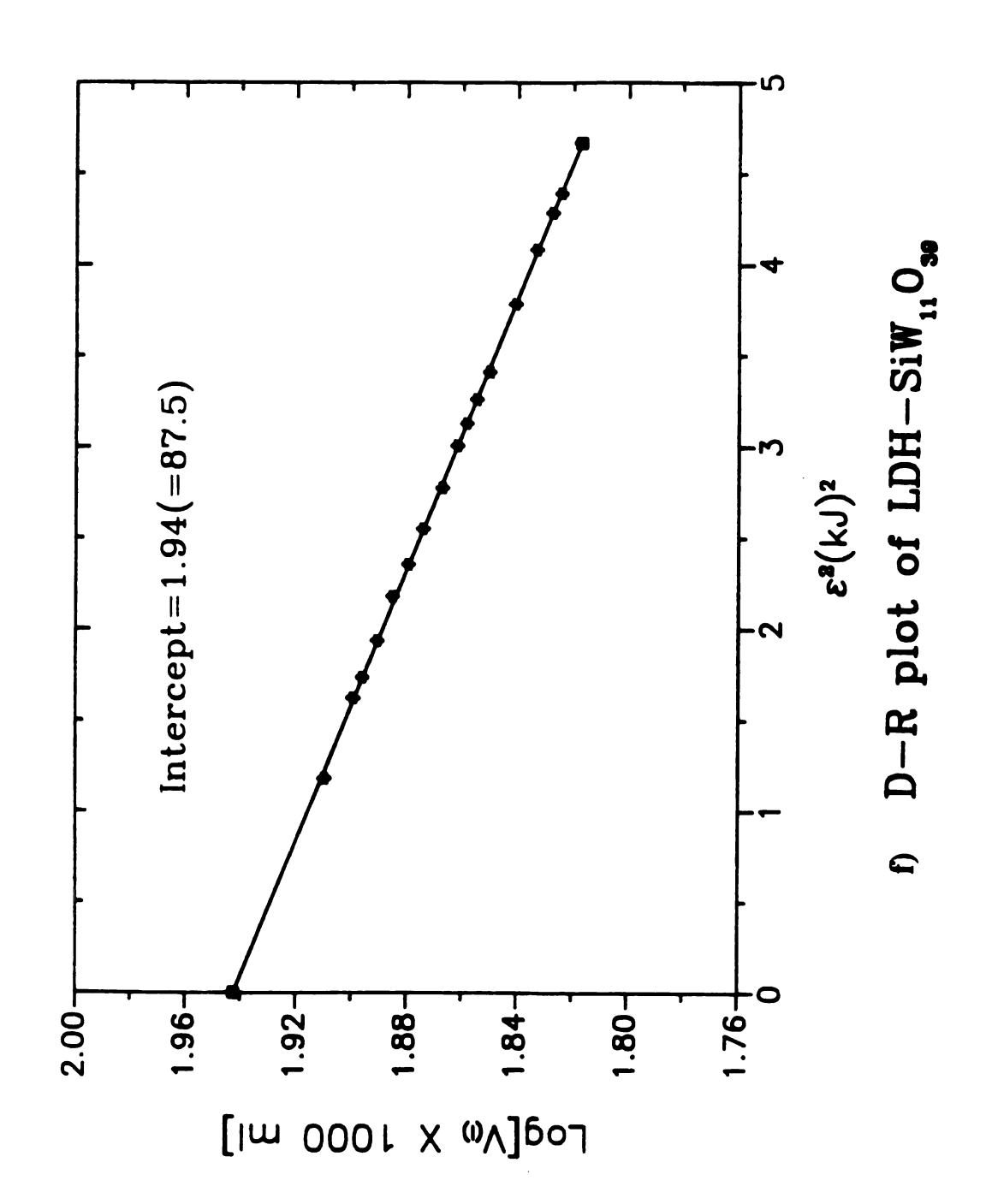


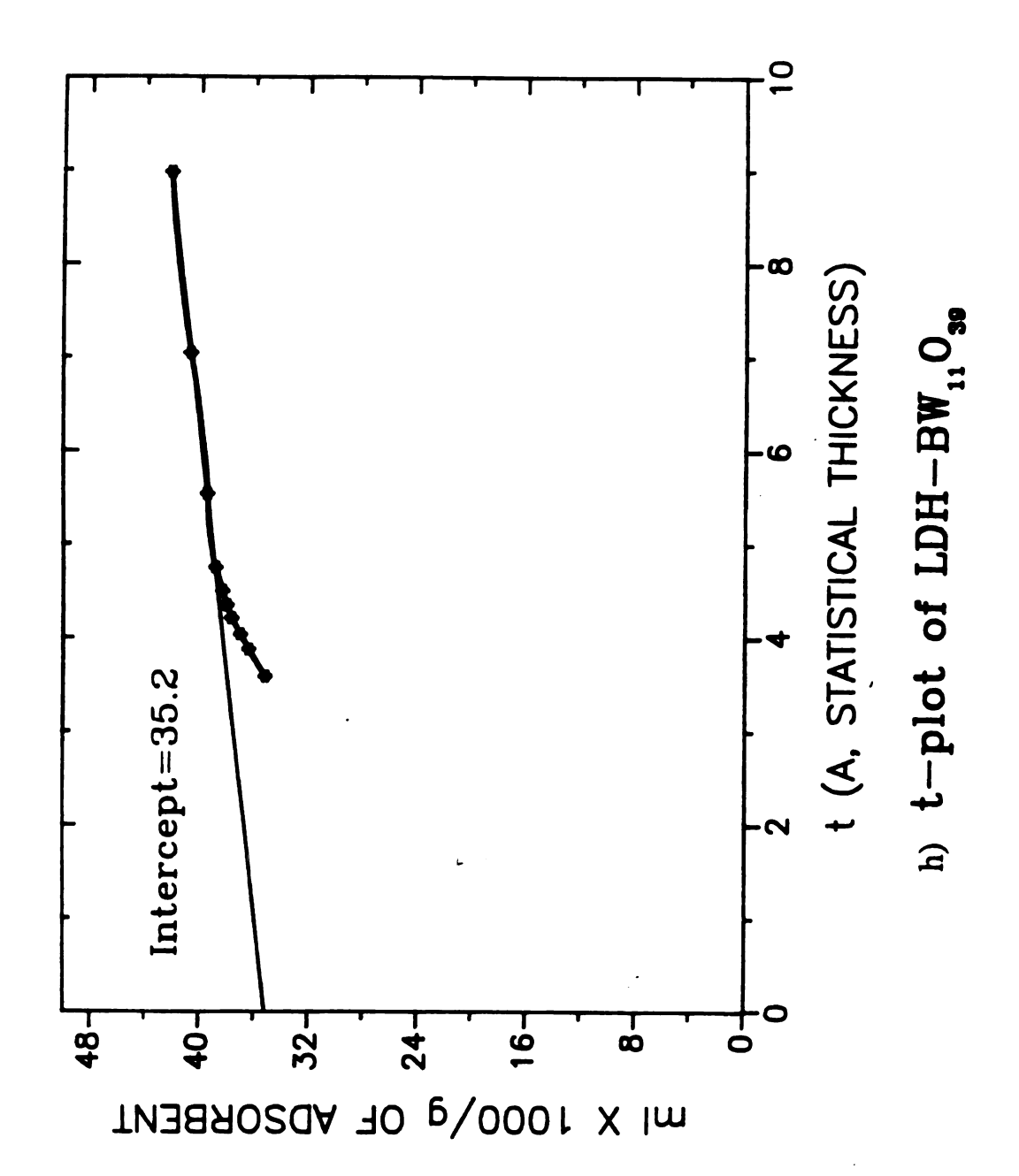


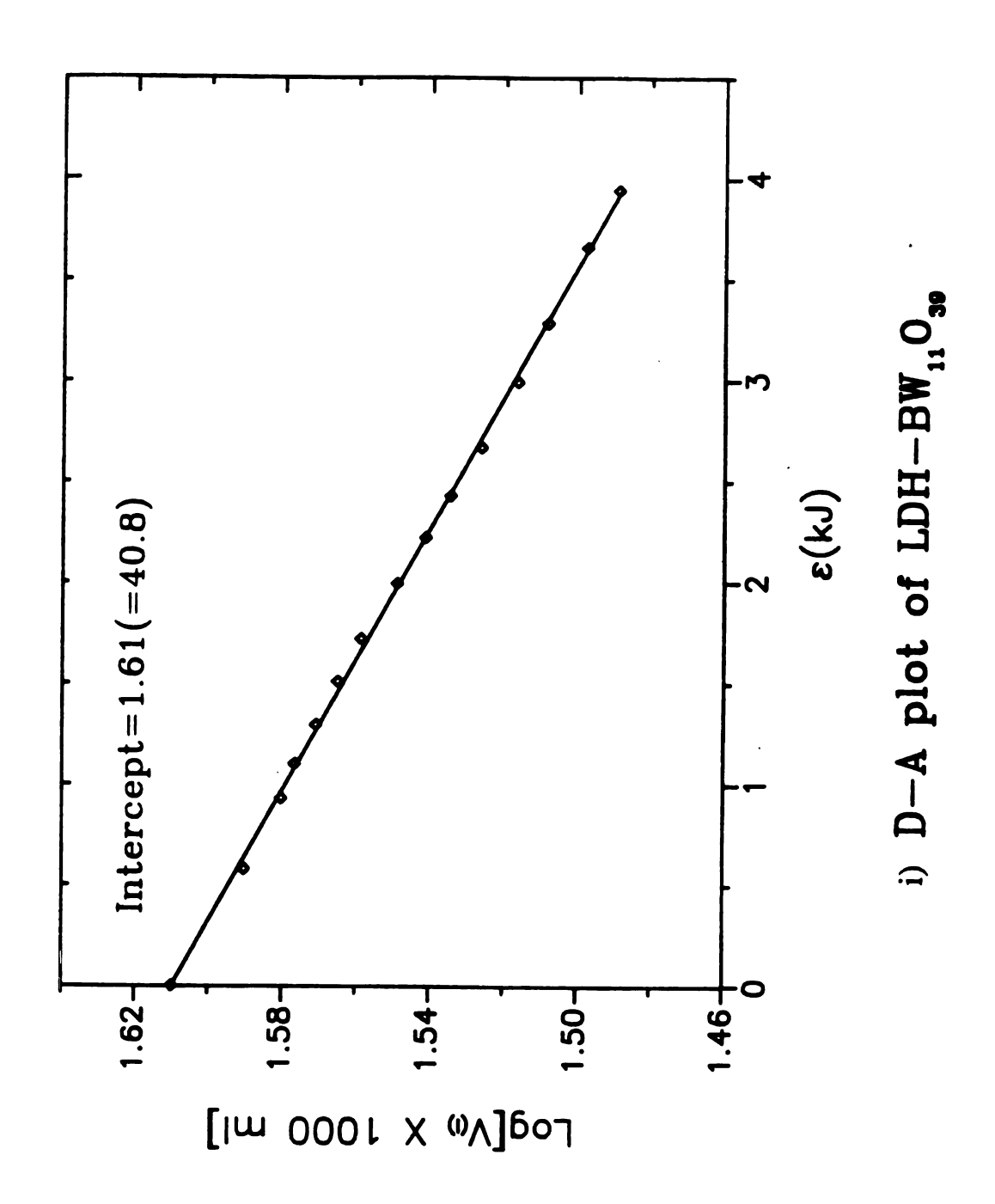












## References

- 1. Barrer, R.M.; Mcleod, D.M., Trans. Faraday Soc., 1955, 51, 1290.
- 2. Mortland, M.M.; Berkheiser, V.E., Clays Clay Miner., 1976, 24, 60.
- 3. Shabtai, T.; Frydman, N.; Lazar, R., "Preceeding of the 6th International Congress on Catalysis" (1976) London, The Chemical Society, London, 1977, 660.
- 4. Knudson, M.I.; McAtee, J.L., Clays Clay Miner., 1973 21, 19.
- 5. Trynor, M.F.; Mortland, M.M.; Pinnavaia, T.J., Clays Clay Miner., 1978, 26, 319.
- 6. Brindley, G.W.; Sempels, R.E., Clay Miner., 1977, 12, 229.
- 7. Yamanaka, S.; Brindley, G.W., Clays Clay Miner., 1978, 26, 107.
- 8. Lahav, N.; Shani, U.; Shabtai, J., Clays Clay Miner., 1978, 26, 107.
- 9. Vaughan, D.E.W.; Lussier, R.J., "Preprints, 5th, International Conference on Zeolites:, Naples, Italy, 1980, June 2-6.
- 10. Brindley, G.W.; Yamanaka, S., Clays Clay Miner., 1979 64, 830.
- 11. Ocelli, M.L.; Tindwa, R.M., Clays Clay Miner., 1983, 31, 22.
- 12. Cheng, S.; Peng, G.W.; Clearfield, A., *Ind. Eng. Chem. Prod. Res. Dev.*, **1984**, <u>23</u>, 219.
- 13. Dines, M.B.; Griffith, P.C., J. Phy. Chem., 1982, 86, 571,
- 14. Dines, M.G.; DiGiacomo, P.M.; Callahan, K.P.; Griffith, P.C.; Lane, R.H.; Cooksey, R.E., in "Catalytically Modified Surface in Catalysis and Electrocatalysis", J.S. Miller, 1982, ACS Symposium Series 192, Washington, DC..
- 15. Taylor, H.F.W., Miner. Mag., 1973 29, 376.
- 16. Miyata, S.; Kumura, T., Chem. Lett., 1973, 843.
- 17. Brown, G.; Gastuche, M.C., Clay Miner., 1967, 7, 193.
- 18. Kwon, T.; Tsigdinos, G.A.; Pinnavaia, T.J., J. Am. Chem. Soc., 1988, 110, 3653.

- 19. Fordel, C., Amer. Min., 1941, 26, 295.
- 20. Allmann, R.; Lohse, H., Neues Jb. Miner. Monatsh, 1966 161.
- 21. Ingram, L.; Taylor, H.F.W., Min. Mag., 1967, 36, 465.
- 22. Taylor, H.F.W., Min. Mag., 1973, 39, 377.
- 23. Allman, R., Acta Cryst., 1968. B24, 972.
- 24. Feitchnecht, W., Helv. Chem. Acta, 1942, 25, 555.
- 25. Gastuche, M.C.; Brown, G.; Mortland, M.M., Clay Miner., 1967, 7, 177.
- 26. a) Miyata, S.; Ikada, A., Clays Clay Miner., 1977, 25, 14.
  - b) Miyata, S., Clays Clay Miner., 1980, 28, 50.
  - c) Miyata, S, Clays Clay Miner., 1975, 23, 369.
- 27. Roy, D.M.; Roy, R.; Osborn, E.F., Am. J. Sci., 1953, 251, 337.
- 28. Taylor, R.M., Clay Miner., 1984, 19, 591.
- 29. Bish, D.L., Bull. B.R.G.M. (2), 1978, 298.
- 30. Miyata, S., Clays Clay Miner., 1983, 31, 305.
- 31. Glaeser, R.; Mering, J., C.R. Hebd. Seanc. Acad. Sci., Paris, 1968, 267, 436.
- 32. Norrish, K., Trans. Faraday Soc., 1954, 18, 120.
- 33. Bradley, W.F.; Grim, R.E.; Clark, G.F., Z. Kristallogr. Kristallgeom., 1937, 97, 260.
- 34. a) Hendicks, S.B.; Nelson, R.A.; Alexander, L.T. J. Am. Chem. Soc., 1940, 62, 1457.
  - b) Mcakenzie, R.M, Clay Miner. Bull., 1950, 1, 115.
- 35. Hendicks, S.B.: Jefferson, M.E., Amer. Miner., 1960, 23, 863.
- 36. MacEwan, D.M.C., Clays Clay Miner., 1960, 9, 431.
- 37. van Olphen, H., " An Introduction to Clay Colloid Chemistry" 2nd Ed., Wiley, New York, 1977.
- 38. Norrish, K., Discuss. Faraday Soc., 1954, 18, 120.
- 39. Squet, H.; De LA Callie, C.; Pezerat, H., Clays Clay Miner., 1975, 23, 1.

- 40. Dosch, W.; zur Strassen, H., Zement-Kalk-Gips, 1967, 20, 392.
- 41. Boehm, H.B.; Steinle, J.; Vieweger, C., Angew. Chem. Intd. Ed. Eng., 1977, 16, 265.
- 42. a) Weiss, A., Angew. Chem. Int. Ed. Engl., 1963, 2, 134.
  b) Lagaly, G., Angew. Chem. Int. Ed. Engl., 1976, 15, 575.
- 43. Brindley, G.W.; Kikkwa, S., Clays Clay Miner., 1980, 28, 87
- 44. Miyata, S.; Okada, A., Clays Clay Miner., 1977, 25, 14.
- 45. Miyata, S., Clays Clay Miner., 1975, 23, 369.
- 46. Rouxhet, P.G.; Taylor, H.F., Chimia, 1969, 23, 480.
- 47. Miyata, S.; Kumura, T., Japan, 7,329,478; Chem. Abstr., 19xx, 80; 85257p.
- 48. Miyata, S.; Takada, M.; Okada, A., Ger. Offen., 2,222,473; Chem. Abst., 19xx, 81, 54438q.
- 49. Miyata, S.; Kuroda, M, Ger. Offen., 2,950,489; Chem. Abst., 19xx, 93, 96250a.
- 50. Miyata, S., Clays Clay Miner., 1980, 28, 50.
- 51. Herman, R.G.; Klier, K.; Simons, G.W.; Finn, B.P.; Bulko, J.B.; Kobylinski, T.P., *J. Catal.*, **1979**, 56, 407.
- 52. Reichle, W.T., J. Catal., 1985, 94, 547.
- 53. Martin, K.J.; Pinnavaia, T.J., J. Am. Chem. Soc., 1986, 108, 541.
- 54. Itaya, K.; Chang, H.C.; Uchida, I., *Inorg. Chem.*, 1987, 26, 24.
- 55. Pope, M.P., "Heteropoly and Isopoly Oxometalates", Springer, New York, 1983.
- 56. Day, V.W.; Klemoerer, W.G., *Nature*, 1985, 228, 533.
- 57. Krebs, B., Acta Crystallogr., Sec. B, 1972, 28, 2222
- 58 Kihlborg, L., Ark. Kemi., 1963, 21, 3
- 59. Keggin, J.F., *Nature*, 1933, 131, 908.
- 60. Teze, A.; Herve, G., J. Inorg. Nucl. Chem., 1977, 39, 2151.
- 61. Kerpet, D.L.," The early Transition Elements", Academic Press, New York, 1972, pp.54.

- 62. Kazansky, L.P.; Potapovaand, I.V.; Spitsyn, V.I., *Proc. 3rd Internat. Conf. Chemistry and Uses of Molybdenum*, Ann Arbor, MI, **1979**, pp.67.
- 63. Copaux, H., Bull. Soc. Chim. France, 1908, 3, 101
- 64. Teze, A.; Herve, G., J. Inorg. Nucl. Chem., 1977, 39, 999.
- 65. Massart, R.; Contant, R.; Fruchart, M.J.; Ciabrini, J.P.; Fournier, M., *Inorg. Chem.*, 1980, 16, 2916.
- 66. a) Kehrmann, A., Z. Anorg. Chem., 1892, 1, 423.
  - b) Souchay, P., Ann. Chim., 1947, 2, 203.
  - c) Contant, R.; Fruchart, J.M.; Teze, A., C. R. Acad. Sci. Ser.C, 1974, 278, 199.
- 67. Herve, G.; Teze, A., C. R. Acad. Sci., Ser.C, 1974, 278, 1417.
- 68. Baker, L.C.W.; Baker, V.E.S.; Eriks, K.; Pope, M.T.; Shibata, M.; Rollins, O.W., Fang, J.H.; Koh, L.L., J. Am. Chem. Soc. 1966, 88, 2329.
- 69. Bradley, A.J.; Illigworth, J.W., *Pro. Roy. Soc.*, A, **1936**, <u>157</u>, 113.
- 70. Fournier, M., Doctoral Thesis, Universite Pierre et Marie Curie, Paris, 1976.
- 71. Fuchs, J.; Jahr, K.F., Z. Naturforsch., 1974, 23b, 1380
- 72. Meikleijohn, P.T.; Pope, M.T.; Prados, R.A., J. Am. Chem. Soc., 1974, 96, 6779.
- 73. Salamonn-Bertho, G.; Lefebvre, J., C.R. Acad. Sci., Ser. C, 1975, 280, 1199.
- 74. Zonnevijlle, F.; Tourne, C.M.; Tourne, G.F., Inorg. *Chem.*, 1982, 21, 2742, 2751.
- 75. Baker, L.c.W.; Figgis, J.S., J. Am. Chem. Soc., 1970 92, 3794.
- 76. Beltyukova, S.V.; Poluektov, N.S.; Kravchenko, T.B.; Kononenko, L.I., *Dokl. Phys. Chem.*, **1978**, 238, 165[1369]
- 77. Malik, S.A.; Weakley, T.J.R., J. Chem. Soc., A, 1968, 2647.
- 78. Rippan, R.; Puscasu, M., Z. Anorg. Chem., 1968, <u>358</u>, 83.
- 79. Teze, A.; Herve, G., J. Inorg. Nucl. Chem., 1977, 39, 2151.
- 80. Teze, A.; Souchy, P., C.R. Acad. Sci., Ser. C, 1973, 276, 1525.
- 81. Tourne, C.; Tourne, G., Bull. Soc. Chim. Fr., 1969, 1124,

- 82. Tourne, C.M.; Tourne, G.; Malik, S.A.; Weakley, T.J.R., J. Inorg. Nucl. Chem., 1970, 32, 3875.
- 83. Hoof, D.L.; Pope, M.T., unpublished work.
- 84. Bushey, P.A., M.S. Thesis, Georgetown University, 1974.
- 85. Wendel, C.H.; Pope, M.T., unpublished work.
- 86. Brown, D.H., J. Chem. Soc., 1962, 4408.
- 87. Weakley, T.J.R., J. Chem. Soc., Dalton Trans., 1973,341.
- a) Baker, L.C.W.; Figis, J.S., J. Am. Chem. Soc., 1970, 92, 3794.
  b) Landis, A.L., ph D. Thesis, Georgetown University, 1977; Diss. Abst., 38B, 4225.
- 89. Herve, G.; Teze, A., Inorg. Chem., 1977, 16, 2115.
- 90. Peacock, R.D.; Weakley, T.J.R., J. Chem. Soc. A, 1971, 1836.
- 91. Botar, A.V.; Weakley, T.J.R., Rev. Roum. Chim., 1973, 18, 1155.
- 92. Marcu, G.; Rusu, M.; Botar, A.V., Rev. Roum. Chim., 1974, 19, 827.
- 93. Termes, S.C.; Pope, M.T., Transit. Met. Chem., 1978, 3, 103.
- 94. Tourne, C.; Tourne, G., Rev. Chim. Mineral, 1977, 14, 83.
- 95. Kosyakov, V.N.; Timofeev, G.A.; Erin, E.A.; Andreev, V.I.; Kopytov, V.V.; Simakin, G.A., Sov. Radiochem., 1977, 19, 418[511].
- 96. Saprykin, A.S.; Spitsyn, V.I.; Krot, N.N., Dokl. Chem., 1976, 226, 114[853].
- 97. Saprykin, A.S.; Spitsyn, V.I.; Orlova, M.M.; Zhuravleva, O.P.; Krot, N.N., Sov. Radiochem., 1978, 20, 207[247].
- 98. Marcu, G.; Botar, A.; Rusu, M., Roum. Chem. 1977, 24, 1465.
- 99. Itzal, S.M.; Malik, S.A., Inorg. Chim. Acta, 1977, 22, L29.
- 100. Spitsyn, V.I.; Orlova, M.M; Saprykina, O.P.; Saprykin, A.S.; Krot, N.N, Russ. J. Inorg. Chem., 1977, 22, 1355[2508].
- 101. Peacock, R.D.; Weakley, T.J.R., J. Chem. Soc. 1971, A, 1836.
- 102. Kuruscev, T.; Sargeson, A.M.; West, B.O., J. Phys. Chem, 1957, 61, 1559.

- 103. Baker, L.C.W.; Pope, M.T., J. Am. Chem. Soc., 1960, 82, 4176.
- 104. Evans. H.T.Jr., *Perspect. Struct. Chem.*, 1971, 4, 1.
- 105. Barcza, L.; Pope, M.T., J. Phys. Chem., 1973, 77, 1795.
- 106. Klemperer, W.G.; Shum, W., J. Am. Chem. Soc., 1978, 100, 4891.
- 107. Day, V.W.; Klemperer, W.G.; Schwartz, C., J. Am. Chem. Soc., 1987, 109, 6030.
- 108. Finke, R.G.; Rapko, B.; Saxton, R.J.; Domaille, P.J.; J. Am. Chem. Soc., 1986, 108, 2947.
- 109. Papaconstantinou, E.; Dimotikali, D.; Politou, A. Inorg. Chim. Acta, 1980, 46, 155.
- 110. Papaconstantinou, E., J. Chem. Soc. Chem. Commun., 1982, 12
- 111. Hill, C.L.; Bouchard, D.A., J. Am. Chem. Soc., 1985, 107, 5148.
- 112. Prosser-McCartha, C.M.; Kadkhodayan, M.; Williamston, M.M.; Bouchard, D.A.; Hill, C.L., J. Chem. Soc. Chem. Commun., 1986, 1747.
- 113. Fox, M.A.; Cardona, R.; Gaillard, E., J. Am. Chem. Soc., 1987, 109, 6347.
- 114. Papaconstantinou, E., J. Chem. Soc, Faraday Trans., 1982, 1, 78, 2769.
- 115. Dubinin, M.M., Prog. Surf. Membr. Sc., 1975, 1.
- 116. a) Dubinin, M.M.; Zaverina, E.D.; Radushkevich, L.V., Zh. Fiz. Khim., 1947, 21., 1351.
  - b) Radushkevich, L.V., Zh. Fiz. Khim., 1949, 23, 1410.
- 117. Marsh, H.; Rand, B., J. Colloid Interface Sci., 1969, 33, 101.
- 118. Dubinin, M.M.; Astakhov, V.A., Adv. Chem. Ser., 1970, 102, 69.
- 119. Mikhail, R.S.; Brunauer, S.; Bodor, E.E, J. Colloid Interface Sci., 1968, 26, 45.
- 120. Massart, R.; Contant, R.; Fruchart, J.M., Ciabrini, J.P.; Fournier, M., *Inorg. Chem.*, 1977, 16, 2916.
- 121. Weakley, T.J.R., J. Chem. Soc., Dalton, 1973, 343.
- 122. Teze, A.; Herve, G., J. Inorg. Nucl. Chem., 1977, 39, 999.
- 123. Dommaille, P.J., J. Am. Chem. Soc., 1984, 106, 7677.

- 124. Zonnevijlle, F.; Tourne, C.M.; Tourne, G.F., *Inorg. Chem.*, 1983, 22, 1198.
- 125. Zonnevijlle, F.; Tourne, C.M.; Tourne, G.F., *Inorg. Chem.*, 1983, 21, 1198.
- 126. Baker, L.C.W.; McCutcheon, T.P., J. Am. Chem. Soc., 1956, 78, 4503.
- 127. Mooney, R.W.; Chiola, V.; Hoffman, C.W.W.; Vandertpool, C.D., J. Electrochem. Soc., 1962, 1179.
- 128. Evans Jr., H.T.; Rollins, O.W., Acta Cryst. 1976, B32, 1565.
- a) Preyssler, C., Bull. Soc. Chim. Fr., 1970, 30.
  b) Alizadeh, M.H.; Hamalker, S.P.; Jeannin, Y.; Martin-Frere, J.; Pope, M.P., J. Am. Chem. Soc., 1985, 107, 2662.
- 130. Altenau, J.J.; Pope, M.T.; Prados, R.A.; So, H., *Inorg. Chem.*, 1975, 14, 417.
- 131. Nomiya, K.; Kato, K.; Miwa, M., Polyhedron, 1986, 5, 811.
- 132. Finke, R.G.; Rapko, B.; Saxton, R.J.; Domaille, P. J. Am. Chem. Soc., 1986, 108, 2947.
- a) Howarth, O.W.; Jarrold, M., J. Chem. Soc., Dalton, 1978, 503.
  b) Kazanskii, L.P.; Spitsyn, V.I., Dokl. Acad. Nauk SSSR, 1975, 223, 721[381].
- 134. Kazanskii, L.P.; Fedotov, M.A.; Spitsyn, V.P., *Dokl. Phys. Chem.*, 1977, 234, 617[1376].
- 135. Hernandez-Moreno, J.; Ulibarri, M.A.; Rendon, J.L.; Serna, J., *Phys. Chem. Miner.*, 1985, 12, 34.
- 136. a) Thouvent, R.; Fournier, M.; Franck, R.; Rocchiccioli-Deltcheff, C., *Inorg. Chem.*, 1984, 23, 598.
  - b) Rocchiccioli-Deltcheff, C.; Fournier, M.; Franck, R.; Thouvenot, R., Inorg. Chem. 1983, 22, 207.
  - c) Rocchiccioli-Deltcheff, C.; Thouvenot, R, J. Chem. Research (s), 1977, 46.
  - d) Rocchiccioli-Deltcheff, C.; Thouvenot, R.; Franck, R., Spectro Chim. Acta, 1976, 32A, 587.

- e) Rocchiccioli-Deltcheff, C.; Thouvenot, R., C. R. Acad. Sc. Paris, Ser. C, 1974, 278, 857.
- f) Thouvenot, R.; Rocchiccioli-Deltcheff, C.; Souchay, P., C. R. Acad. Sc. Paris, Ser. C, 1974, 278, 455.
- 137. Kazanskii, L.P., Bull. Acad. Sci. USSR, Div. Chem. Sci., 1975, 24, 432[502].
- 138. Contant, R., Can. J. Chem. 1987, 65, 568.
- 139. Kato, R.; Kobayashi, A.; Sasaki, Y., Inorg. Chem., 1982, 21, 240.
- 140. Kiss, B.A., Acta Chim. Acad. Sc. Hungaricae, Tomus, 1973, 75(4), 351.
- 141. Katsoulis, D.E.; Pope, M.T., J. Am. Chem. Soc., 1984, 106, 2737.